

**STRUCTURE, MAGNETIC AND ELECTROCHEMICAL
PROPERTIES OF $\text{BiFe}_{1-x}\text{M}_x\text{O}_3$ (M = Co, Ni, Cu)
NANOPARTICLES PREPARED BY
A SIMPLE SOLUTION METHOD**

Jessada Khajonrit



**A Thesis Submitted in Partial Fulfillment of the Requirements for the
Degree of Doctor of Philosophy in Applied Physics
Suranaree University of Technology
Academic Year 2016**

โครงสร้าง สมบัติทางแม่เหล็กและสมบัติทางไฟฟ้าเคมีของอนุภาคนาโน
กลุ่ม $\text{BiFe}_{1-x}\text{M}_x\text{O}_3$ ($\text{M} = \text{Co}, \text{Ni}, \text{Cu}$) เตรียมโดยวิธีสารละลายอย่างง่าย



วิทยานิพนธ์นี้เป็นส่วนหนึ่งของการศึกษาตามหลักสูตรปริญญาวิทยาศาสตรดุษฎีบัณฑิต
สาขาวิชาฟิสิกส์ประยุกต์
มหาวิทยาลัยเทคโนโลยีสุรนารี
ปีการศึกษา 2559

**STRUCTURE, MAGNETIC AND ELECTROCHEMICAL
PROPERTIES OF $\text{BiFe}_{1-x}\text{M}_x\text{O}_3$ (M = Co, Ni, Cu) NANOPARTICLES
PREPARED BY A SIMPLE SOLUTION METHOD**


Suranaree University of Technology has approved this thesis submitted in partial fulfillment of the requirements for the Degree of Doctor of Philosophy.

Thesis Examining Committee



(Assoc. Prof. Dr. Prapan Manjumn)

Chairperson




(Prof. Dr. Santi Maensiri)

Member (Thesis Advisor)



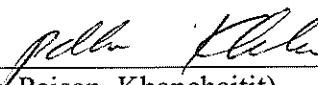
(Asst. Prof. Dr. Montree Sawangphruk)

Member



(Assoc. Prof. Dr. Rattikorn Yimnirun)

Member




(Dr. Paisan Khanchaitit)

Member



(Prof. Dr. Sukit Limpijumnong)

Vice Rector for Academic Affairs
and Innovation



(Prof. Dr. Santi Maensiri)

Dean of Institute of Science

เจษฎา ขจรฤทธิ์ : โครงสร้าง สมบัติทางแม่เหล็กและสมบัติทางไฟฟ้าเคมีของอนุภาคนาโน กลุ่ม $\text{BiFe}_{1-x}\text{M}_x\text{O}_3$ ($\text{M} = \text{Co}, \text{Ni}, \text{Cu}$) เตรียมโดยวิธีสารละลายอย่างง่าย (STRUCTURE, MAGNETIC AND ELECTROCHEMICAL PROPERTIES OF $\text{BiFe}_{1-x}\text{M}_x\text{O}_3$ ($\text{M} = \text{Co}, \text{Ni}, \text{Cu}$) NANOPARTICLES PREPARED BY A SIMPLE SOLUTION METHOD) อาจารย์ที่ปรึกษา : ศาสตราจารย์ ดร.สันติ แม้นศิริ, 242 หน้า.

ในงานวิจัยนี้ได้ทำการสังเคราะห์อนุภาคนาโน $\text{BiFe}_{1-x}\text{M}_x\text{O}_3$ ($\text{M} = \text{Co}, \text{Ni}, \text{Cu}$) ที่ $x = 0, 0.05, 0.1, 0.2$ และ 0.3 ด้วยวิธีสารละลายอย่างง่าย โดยได้ทำการศึกษาลักษณะเฉพาะโดยใช้เทคนิค XRD SEM XANES และ Gas absorption และได้ทำการศึกษาสมบัติทางแม่เหล็กและสมบัติทางไฟฟ้าเคมีโดยใช้เทคนิค VSM และ CV GCD และ EIS ตามลำดับ ผลการศึกษาโครงสร้างด้วยเทคนิค XRD พบว่า มีเฟสหลักของ BiFeO_3 ในทุกตัวอย่างและมีเฟสเจือปนของเฟสอื่น ๆ เช่น $\text{Bi}_2\text{Fe}_4\text{O}_9$, CoFe_2O_4 , Co_3O_4 และ NiFe_2O_4 ในบางตัวอย่าง การเพิ่มขึ้นของปริมาณการเจือไอออนของ Co Ni และ Cu ได้ทำให้ขนาดผลึกและขนาดอนุภาคลดลง ผลจากการศึกษาสถานะประจุของ Bi Fe Co Ni และ Cu ด้วยเทคนิค XANES พบว่า มีประจุ Bi^{3+} , Fe^{3+} , Co^{2+} , Co^{3+} , Ni^{2+} และ Cu^{3+} การศึกษาสมบัติทางแม่เหล็กพบว่า การเจือ Co Ni และ Cu ที่ปริมาณสูงขึ้นมีผลทำให้ค่าแมกนีไทเซชันอิ่มตัว (M_s) มีค่าเพิ่มขึ้น ซึ่งเป็นผลเนื่องมาจากการลดลงของขนาดอนุภาคซึ่งทำให้สัดส่วนของพื้นที่ผิวต่อปริมาตรเพิ่มขึ้นและทำให้สปินไม่ชดเชย (Uncompensated spin) ที่ผิวต่อโมเมนต์แม่เหล็กของอนุภาคเพิ่มขึ้น การเจือ Co Ni และ Cu ที่ปริมาณสูงขึ้นสามารถเพิ่มค่าสภาพบังคับ (H_c) เนื่องจากการลดลงของขนาดอนุภาค นอกจากนี้ การมีอยู่ของเฟสเจือปน CoFe_2O_4 , Co_3O_4 และ NiFe_2O_4 ได้ส่งผลต่อค่าแมกนีไทเซชันอิ่มตัวและค่าสภาพบังคับของตัวอย่างที่เจือด้วย Co และ Ni ตามลำดับ วงฮิสเทอรีซิสของวัสดุ BiFeO_3 และวัสดุ BiFeO_3 ที่เจือด้วย Ni และ Cu แสดงพฤติกรรมทางแม่เหล็กแบบเฟอร์โรแบบอ่อน ยกเว้น วัสดุ BiFeO_3 ที่เจือด้วย Co ซึ่งแสดงพฤติกรรมทางแม่เหล็กแบบเฟอร์โรในช่วงอุณหภูมิระหว่าง 50 ถึง 350 เคลวิน ค่าแมกนีไทเซชันอิ่มตัว ค่าสภาพบังคับ และค่าแมกนีไทเซชันคงค้าง (M_r) มีค่าเพิ่มขึ้นเมื่ออุณหภูมิลดลง พฤติกรรมทางแม่เหล็กที่เกิดขึ้นนี้สอดคล้องกับผลจากการศึกษาด้วย กฎของคูรี-ไวส์ ซึ่งพบว่า ไอออนแม่เหล็กต่าง ๆ ในทุกตัวอย่างมีการจัดเรียงแบบสปินสูง อันตรกิริยาแม่เหล็กแบบแอนติเฟอร์โรได้แสดงให้เห็นในทุกตัวอย่าง ยกเว้นในบางตัวอย่างของวัสดุ BiFeO_3 ที่เจือด้วย Co นอกจากนี้ เมื่ออุณหภูมิลดลง พบว่าค่าแมกนีไทเซชันอิ่มตัว ค่าสภาพบังคับ และค่าแมกนีไทเซชันคงค้าง (M_r) มีค่าเพิ่มขึ้น ผลจากการศึกษาผลของอุณหภูมิกับค่าแมกนีไทเซชันของ ZFC และ FC พบว่า ทุกตัวอย่างมีค่าอุณหภูมิจำกัดที่ทำให้แมกนีไทเซชันของวัสดุเปลี่ยนแปลงทิศทาง (T_B) มากกว่า

350 เคลวิน ยกเว้น BiFeO_3 และ $\text{BiFe}_{0.95}\text{Cu}_{0.05}\text{O}_3$ ซึ่งพบว่ามีค่า T_B ประมาณ 250 เคลวิน การศึกษาสมบัติไฟฟ้าเคมีของอนุภาคนาโนซึ่งได้ประดิษฐ์เป็นขั้วไฟฟ้า (Electrode) พบว่า ทุกขั้วไฟฟ้าได้แสดงพฤติกรรมของตัวเก็บประจุแบบซูโคคาร์ปาซิเตอร์ ขั้วไฟฟ้าของ $\text{BiFe}_{0.95}\text{Cu}_{0.05}\text{O}_3$ ได้แสดงประสิทธิภาพที่เพิ่มมากขึ้น โดยมีค่าที่สูงที่สุดของค่าการเก็บประจุไฟฟ้าเคมีจำเพาะเท่ากับ 451.82 ฟารัดต่อกรัม และ 233.41 ฟารัดต่อกรัม ซึ่งวัดด้วยวิธี CV และ วิธี GCD ตามลำดับ ค่าความหนาแน่นพลังงานจำเพาะเท่ากับ 73.03 วัตต์ชั่วโมงต่อกิโลกรัม ค่าความหนาแน่นกำลังงานจำเพาะเท่ากับ 6413.41 วัตต์ต่อกิโลกรัม นอกจากนี้ การเจือด้วย Co และ Ni ที่ $x = 0.05$ และการเจือด้วย Cu ที่ $x = 0.05$ ถึง 0.2 สามารถเพิ่มค่าการเก็บรักษาการเก็บประจุ (Capacity retention) ได้เพิ่มขึ้นอย่างไรก็ตาม เมื่อเพิ่มปริมาณการเจือ อัตราเร็วในการสแกนและความหนาแน่นของกระแสสูงขึ้น พบว่าค่าการกักเก็บประจุไฟฟ้าเคมีจำเพาะ ความหนาแน่นพลังงานจำเพาะและความหนาแน่นกำลังงานจำเพาะของขั้วไฟฟ้าของวัสดุ BiFeO_3 ที่เจือด้วย Co Ni และ Cu ที่ประดิษฐ์ขึ้นมีค่าลดลง ซึ่งน่าจะเป็นผลเนื่องมาจากการลดลงของพฤติกรรมการเก็บประจุ จำนวนของบริเวณเร่ง (Active site) ของปฏิกิริยารีดอกซ์และสัมประสิทธิ์การแพร่ การเพิ่มขึ้นของขนาดของรูพรุนมีโซพอร์และการมีอยู่ของเฟสเจือปนในตัวอย่างต่าง ๆ

มหาวิทยาลัยเทคโนโลยีสุรนารี

สาขาวิชาฟิสิกส์
ปีการศึกษา 2559

ลายมือชื่อนักศึกษา ภวเรศดา ขจรภักดิ์
ลายมือชื่ออาจารย์ที่ปรึกษา ศ.ดร.วิทย์

JESSADA KHAJONRIT : STRUCTURE, MAGNETIC AND
ELECTROCHEMICAL PROPERTIES OF $\text{BiFe}_{1-x}\text{M}_x\text{O}_3$ (M = Co, Ni, Cu)
NANOPARTICLES PREPARED BY A SIMPLE SOLUTION METHOD.
THESIS ADVISOR : PROF. SANTI MAENSIRI, D.Phil. 242 PP.

MAGNETIC PROPERTIES/ELECTROCHEMICAL PROPERTIES/SIMPLE
SOLUTION METHOD/ $\text{BiFe}_{1-x}\text{M}_x\text{O}_3$ (M = Co, Ni, Cu) NANOPARTICLES

In this work, $\text{BiFe}_{1-x}\text{M}_x\text{O}_3$ (M = Co, Ni, Cu) nanoparticles with $x = 0, 0.05, 0.1, 0.2,$ and 0.3 were synthesized by a simple solution method. The nanoparticles were characterized by XRD, SEM, XANES, and Gas absorption. The magnetic and electrochemical properties of the nanoparticles were studied by using VSM and CV, GCD, and EIS, respectively. The XRD results indicated the main phase of BiFeO_3 in all samples and impurity phases of $\text{Bi}_2\text{Fe}_4\text{O}_9$, CoFe_2O_4 , Co_3O_4 , and NiFe_2O_4 in some samples. Increasing of Co, Ni, and Cu doping concentration led to the decrease of the crystallite size and particle size of BiFeO_3 -based nanoparticles. The XANES results indicated that the valence states of Bi, Fe, Co, Ni, and Cu were in the Bi^{3+} , Fe^{3+} , Co^{2+} , Co^{3+} , Ni^{2+} , and Cu^{3+} . The study of the magnetic properties revealed that the increases of Co, Ni, and Cu doping concentration at Fe site of BiFeO_3 caused the increase of M_s due to effect of particle size reduction resulting in the increase of surface-volume ratio and the contribution of uncompensated spin at the surface to the total magnetic moment of the particle. Increasing of Co, Ni, and Cu doping concentrations can improve the H_c values due to the decrease of the crystallite sizes of the BiFeO_3 -based particles. Moreover, the presences of secondary phases of the CoFe_2O_4 , Co_3O_4 , and NiFe_2O_4

nanoparticles affected the M_s and H_c values in Co and Ni-doped BiFeO_3 samples, respectively. The hysteresis loops of undoped BiFeO_3 , Ni, and Cu-doped BiFeO_3 samples exhibit a weak ferromagnetism at 50-350 K, except Co-doped BiFeO_3 samples are ferromagnetic. This corresponds to the Curie-Weiss's law fitting results, which indicates that all magnetic ions in all samples are in the high spin configuration. Antiferromagnetic interactions were observed in all samples, except some Co doping samples. The M_s , H_c , and M_r values in the doped samples increased with decrease of temperature. The results of temperature dependence of the ZFC and FC magnetization showed that T_B of all samples are higher than 350 K, except undoped BiFeO_3 and $\text{BiFe}_{0.95}\text{Cu}_{0.05}\text{O}_3$ samples ($T_B \sim 250$ K). The study of the electrochemical properties of the fabricated nanoparticles electrodes showed that all electrodes exhibited pseudocapacitor behavior. The $\text{BiFe}_{0.95}\text{Cu}_{0.05}\text{O}_3$ electrode showed the improved performance with the highest specific capacitances of 451.82 F/g and 233.41 F/g for the CV and GCD measurements, respectively, energy density of 73.03 Wh/Kg and power density of 6413.41 W/Kg. Moreover, the Co and Ni doping with $x = 0.05$ and Cu doping with $x = 0.05-0.2$ can improve capacity retention. However, the specific capacitance, energy and power density of fabricated Co, Ni, and Cu doped BiFeO_3 electrodes decreased with increasing the doping concentration, scan rate and current density. This is possibly resulted in the reductions of capacitive behavior, number of active sites of redox reaction, diffusion coefficient, increase of mesopore size, and presence of the secondary phase in the samples.

School of Physics

Academic Year 2016

Student's Signature Jessada Khajonrit

Advisor's Signature 

ACKNOWLEDGEMENTS

There are many people, to whom I would like to express my sincere word of acknowledgments. First of all, I would like to extend my thanks to a number of people who have contributed so much to my PhD at Suranaree University. First of all, I would like to convey my deepest appreciation to my supervisor, Prof. Dr. Santi Maensiri who has given me constant encouragement, great opportunity, invaluable guidance not only a scientific expertise, but also a view of life, patience and understanding throughout the whole period of my PhD candidature. I would like to thank my thesis examination committee members, Assoc. Prof. Dr. Rattikorn Yimnirun, Asst. Prof. Dr. Montree Sawangphruk, Assoc. Prof. Dr. Prapan Manyum and Dr. Paisan Khanchaitit for serving on my Ph.D. in reading and providing me with valuable comments. In addition, I would like to express my sincerest appreciation to the School of Physics, Suranaree University of Technology, Department of physics (Khon Kaen University) for magnetic properties measurement, The Synchrotron Light Research Institute for XANES facilities. I am grateful to the Nanotechnology Center, National Science and Technology Development Agency, Ministry of Science and Technology, through the Center of Excellence Network for the financial support. I would like to thank to AMP group members for their friendship during work. Finally, I give my special appreciation to my family, it is no exaggeration to say that I could not complete the PhD without their boundless help, love, care, and support that I have receiving from them over all the years of my life.

Jessada Khajonrit

CONTENTS

	Page
ABSTRACT IN THAI.....	I
ABSTRAC IN ENGLISH.....	III
ACKNOWLEDMENTS.....	V
CONTENTS.....	VI
LIST OF TABLES.....	X
LIST OF FIGURES.....	XV
LIST OF ABBREVIATIONS.....	XXIV
CHAPTER	
I INTRODUCTION.....	1
1.1 Principle and reason.....	1
1.2 Objectives of the dissertation.....	5
1.3 Limitation of the study.....	5
1.4 Location of research.....	6
1.5 Expected results.....	6
1.6 Outline of thesis.....	6
II LITERATURE REVIEWS.....	8
2.1 Fundamentals of BiFeO ₃	8
2.1.1 Structure of BiFeO ₃	8
2.1.2 Magnetism of BiFeO ₃	10

CONTENTS (Continued)

	Page
2.1.3 Phase decomposition and impurity for BiFeO ₃	15
2.2 Study of Synthesis of BiFeO ₃ -based nanoparticle.....	17
2.3 Study of magnetic and electrochemical properties of BiFeO ₃	19
2.3.1 Study of magnetic properties of BiFeO ₃	19
2.3.2 Study of electrochemical properties of BiFeO ₃	26
2.4 Theoretical Approach.....	29
2.4.1 Magnetic properties of materials.....	29
2.4.2 Electrochemical properties of materials.....	36
III EXPERIMENTAL PROCEDURE.....	49
3.1 Sample preparation.....	50
3.1.1 Synthesis of BiFe _{1-x} M _x O ₃ (M = Co, Ni, Cu) nanoparticles.....	50
3.1.2 Fabrication of the BiFe _{1-x} M _x O ₃ (M = Co, Ni, Cu) nanoparticle electrodes.....	51
3.2 Material characterization.....	54
3.2.1 X-ray diffraction (XRD).....	54
3.2.2 Scanning electron microscopy (SEM).....	57
3.2.3 Transmission electron microscopy (TEM).....	59
3.2.4 X-ray absorption near-edge spectroscopy (XANES).....	60
3.2.5 Gas absorption techniques.....	62
3.2.6 Magnetic measurements.....	65

CONTENTS (Continued)

	Page
3.3 Electrochemical measurements.....	67
3.3.1 Cyclic voltammetry.....	70
3.3.2 Galvanostatic charge-discharge.....	74
3.3.3 Electrochemical impedance spectroscopy (EIS).....	75
IV RESULTS AND DISCUSSION.....	78
4.1 Co-doped BiFeO ₃ nanoparticles.....	79
4.1.1 Structural and morphology characterization.....	79
4.1.2 Magnetic properties of the Co-doped BiFeO ₃ nanoparticles....	97
4.1.3 Electrochemical properties of Co-doped BiFeO ₃ nanoparticles.....	109
4.2 Ni-doped BiFeO ₃ nanoparticles.....	125
4.2.1 Structural and morphology characterization.....	125
4.2.2 Magnetic properties of the Ni-doped BiFeO ₃ nanoparticles.....	141
4.2.3 Electrochemical properties of Ni-doped BiFeO ₃ nanoparticles.....	151
4.3 Cu-doped BiFeO ₃ nanoparticles.....	167
4.3.1 Structural and morphology characterization.....	167
4.3.2 Magnetic properties of the Cu-doped BiFeO ₃ nanoparticles.....	184

CONTENTS (Continued)

	Page
4.3.3 Electrochemical properties of Cu-doped BiFeO ₃ nanoparticles.....	193
V CONCLUSIONS AND SUGGESTIONS.....	209
5.1 The structure and morphology characterization.....	209
5.2 The Magnetic properties.....	211
5.3 The Electrochemical properties.....	213
5.4 Suggestions.....	216
REFERENCES.....	218
APPENDIX.....	239
CURRICULUM VITAE.....	242

LIST OF TABLES

Table	Page
2.1	Lists of reports for magnetic properties of BiFeO ₃ based nanoparticles.....20
2.2	Summary of the various metal oxide electrodes.....45
2.3	Electrolytes that are used often.....48
3.1	List of materials used as starting materials for BiFe _{1-x} M _x O ₃ (M = Co, Ni, and Cu) nanoparticles preparation, quoting their source and purity.....51
4.1	List of Crystallite size (D), lattice parameters (a, c), unit cell volume (V), crystal density (ρ), phase composition of BiFeO ₃ , Bi ₂ Fe ₄ O ₉ , CoFe ₂ O ₄ , and Co ₃ O ₄ , residuals of the weighted pattern (R _{wp}) and pattern (R _p), and goodness of fit (GOF) of BiFe _{1-x} Co _x O ₃ with x = 0, 0.05, 0.1, 0.2, and 0.3 nanoparticles.....82
4.2	Absorption edges and oxidation states at Bi M ₅ -edge of all Co-doped BiFeO ₃ samples along with the standard samples.....92
4.3	Absorption edges and oxidation states at Fe K-edge of all Co-doped BiFeO ₃ samples along with the standard samples.....93
4.4	Absorption edges and oxidation states at Co K-edge of all Co-doped BiFeO ₃ samples along with the standard samples.....93
4.5	Specific surface area (S _{BET}), mean pore diameter (D _{MP}), total pore volume (V _{TP}), meso pore diameter (D _{BJH}), particle size (D _{BET}) of BiFe _{1-x} Co _x O ₃ (x = 0, 0.05, 0.1, 0.2, and 0.3) nanoparticles.....96

LIST OF TABLES (Continued)

Table	Page
4.6	Coercivity (H_c), saturation magnetization (M_s), and remanant magnetization (M_r) values of $\text{BiFe}_{1-x}\text{Co}_x\text{O}_3$ ($x = 0, 0.05, 0.1, \text{ and } 0.2$) samples at different temperatures.....101
4.7	Coercivity (H_c), saturation magnetization (M_s), and remanant magnetization (M_r) values of $\text{BiFe}_{1-x}\text{Co}_x\text{O}_3$ ($x = 0.3$) samples at different temperatures.....102
4.8	Effective magnetic moment (μ_{eff}), Curie-Weiss temperature (θ) obtained from Curie-Weiss law's fitting results for Co-doped BiFeO_3108
4.9	Specific capacitances, number of active sites (N), and diffusion coefficients (D) $\text{BiFe}_{1-x}\text{Co}_x\text{O}_3$ ($x = 0, 0.05, \text{ and } 0.1$) samples at various scan rates.....114
4.10	Specific capacitances, numbers of active sites (N), and diffusion coefficients of $\text{BiFe}_{1-x}\text{Co}_x\text{O}_3$ ($x = 0.1, 0.2, \text{ and } 0.3$) samples at various scan rates.....115
4.11	Specific capacitances, energy densities, and power densities of $\text{BiFe}_{1-x}\text{Co}_x\text{O}_3$ ($x = 0, 0.05, \text{ and } 0.1$) samples at various current densities....119
4.12	Specific capacitances, energy densities, and power densities of $\text{BiFe}_{1-x}\text{Co}_x\text{O}_3$ ($x = 0.2 \text{ and } 0.3$) sample at various current densities.....120
4.13	List of crystallite sizes (D), lattice parameters (a, c), unit cell volume (V), crystal density (ρ), phase composition of BiFeO_3 , $\text{Bi}_2\text{Fe}_4\text{O}_9$, and NiFe_2O_4 , residuals of the weighted pattern (R_{wp}) and pattern (R_p), and goodness of fit (GOF) of $\text{BiFe}_{1-x}\text{Ni}_x\text{O}_3$ ($x = 0, 0.05, 0.1, 0.2, \text{ and } 0.3$) nanoparticles.....127
4.14	Absorption edges and oxidation states at Bi M_5 -edge of all Ni-doped BiFeO_3 samples along with the standard samples.....136

LIST OF TABLES (Continued)

Table	Page
4.15	Absorption edges and oxidation states at Fe <i>K</i> -edge of all Ni-doped BiFeO ₃ samples along with the standard samples.....137
4.16	Absorption edges and oxidation states at Ni <i>K</i> -edge of all Co-doped BiFeO ₃ samples along with the standard samples.....137
4.17	Specific surface area (<i>S</i> _{BET}), mean pore diameter (<i>D</i> _{MP}), total pore volume (<i>D</i> _{TP}), particle size (<i>D</i> _{BET}) of BiFe _{1-x} Ni _x O ₃ (<i>x</i> = 0, 0.05, 0.1, 0.2, and 0.3) nanoparticles.....140
4.18	Coercivity (<i>H</i> _c), saturation magnetization (<i>M</i> _s), and remanant magnetization (<i>M</i> _r) values of BiFe _{1-x} Ni _x O ₃ (<i>x</i> = 0, 0.05, 0.1, and 0.2) samples at different temperatures.....145
4.19	Coercivity (<i>H</i> _c), saturation magnetization (<i>M</i> _s) and remanant magnetization (<i>M</i> _r) values of BiFe _{1-x} Ni _x O ₃ (<i>x</i> = 0.3) samples at different temperatures.....146
4.20	Effective magnetic moment (<i>μ</i> _{eff}), Curie-Weiss temperature (<i>θ</i>) obtained from Curie-Weiss law fitting results for Ni-doped BiFeO ₃150
4.21	Specific capacitances, number of active sites (<i>N</i>), and diffusion coefficients (<i>D</i>) of BiFe _{1-x} Ni _x O ₃ (<i>x</i> = 0, 0.05, and 0.1) samples at various scan rates.....155
4.22	Specific capacitances, numbers of active site (<i>N</i>), and diffusion coefficients of BiFe _{1-x} Ni _x O ₃ (<i>x</i> = 0.1, 0.2, and 0.3) samples at various scan rates.....156
4.23	Specific capacitances, energy densities, and power densities of BiFe _{1-x} Ni _x O ₃ (<i>x</i> = 0, 0.05, and 0.1) samples at various current densities.....160

LIST OF TABLES (Continued)

Table	Page
4.24	Specific capacitances, energy densities, and power densities of $\text{BiFe}_{1-x}\text{Ni}_x\text{O}_3$ ($x = 0.2$ and 0.3) sample at various current densities.....161
4.25	List of crystallite sizes (D), lattice parameters (a , c), unit cell volume (V), crystal density (ρ), phase composition of BiFeO_3 and $\text{Bi}_2\text{Fe}_4\text{O}_9$, residuals of the weighted pattern (R_{wp}) and pattern (R_p), and goodness of fit (GOF) of $\text{BiFe}_{1-x}\text{Cu}_x\text{O}_3$ ($x = 0, 0.05, 0.1, 0.2,$ and 0.3) nanoparticles.....170
4.26	Absorption edges and oxidation states at Bi M_5 -edge of all Cu-doped BiFeO_3 samples along with the standard samples.....179
4.27	Absorption edges and oxidation states at Fe K -edge of all Cu-doped BiFeO_3 samples along with the standard samples.....180
4.28	Absorption edges and oxidation states at Cu K -edge of all Cu-doped BiFeO_3 samples along with the standard samples.....180
4.29	Specific surface area (S_{BET}), mean pore diameter (D_{MP}), total pore volume (V_{TP}), meso pore diameter (D_{BH}), particle size (D_{BET}) of $\text{BiFe}_{1-x}\text{Cu}_x\text{O}_3$ ($x = 0, 0.05, 0.1, 0.2,$ and 0.3) nanoparticles.....183
4.30	Coercivity (H_c), saturation magnetization (M_s), and remanant magnetization (M_r) values of $\text{BiFe}_{1-x}\text{Cu}_x\text{O}_3$ ($x = 0, 0.05, 0.1,$ and 0.2) samples at different temperatures.....187
4.31	Coercivity (H_c), saturation magnetization (M_s) and remanant magnetization (M_r) values of $\text{BiFe}_{1-x}\text{Cu}_x\text{O}_3$ ($x = 0.3$) samples at different temperatures.....188

LIST OF TABLES (Continued)

Table		Page
4.32	Effective magnetic moment (μ_{eff}), Curie-Weiss temperature (θ) obtained from Curie-Weiss law fitting results for Cu-doped BiFeO_3	192
4.33	Specific capacitances, number of active sites (N) and diffusion coefficients (D) of $\text{BiFe}_{1-x}\text{Cu}_x\text{O}_3$ ($x = 0, 0.05, \text{ and } 0.1$) samples at various scan rates.....	198
4.34	Specific capacitances, numbers of active site (N), and diffusion coefficient of $\text{BiFe}_{1-x}\text{Cu}_x\text{O}_3$ ($x = 0.1, 0.2, \text{ and } 0.3$) samples at various scan rates.....	199
4.35	Specific capacitance, energy densities, and power densities of $\text{BiFe}_{1-x}\text{Cu}_x\text{O}_3$ ($x = 0, 0.05, \text{ and } 0.1$) samples at various current densities.....	203
4.36	Specific capacitances, energy densities, and power densities of $\text{BiFe}_{1-x}\text{Cu}_x\text{O}_3$ ($x = 0.2 \text{ and } 0.3$) sample at various current densities.....	204

LIST OF FIGURES

Figure	Page
1.1	Ragone plot of various energy storage devices.....3
2.1	Schematic view of crystal structure of bulk BiFeO ₃9
2.2	Scheme of the antiferromagnetic structure of BiFeO ₃ , the magnetic moments describe a cycloid with a period of 64 nm.....11
2.3	The much difference between Field-cooled (FC) and zero-field-cooled (ZFC) magnetization is consistent with a spin-glass state.....12
2.4	Ferromagnetic hysteresis due to uncompensated surface spins in BiFeO ₃ nanocrystals.....15
2.5	Compositional phase diagram of Bi ₂ O ₃ -Fe ₂ O ₃ system.....17
2.6	(a) Temperature dependence of the magnetization for BiFeO ₃ nanoparticles of varying sizes, showing zero field cooling (ZFC) and field cooling (FC) curves. (b) Expanded plots of ZFC and FC curves for BiFeO ₃ nanoparticles with diameters of 245 and the bulk.....21
2.7	(a) VSM measurement of different BiFeO ₃ nanoparticles synthesized from 450 to 600 °C and (b) the partially enlarged curve of BiFeO ₃ powders synthesized at 600 °C.....22
2.8	(a) The CV curves of BiFeO ₃ electrodes at different scanning rates (b) The charge and discharge curve of BiFeO ₃ electrode.....27

LIST OF FIGURES (Continued)

Figure	Page
2.9 Cyclic voltammograms of BiFeO ₃ nanorods on AAO at different scan rates.....	28
2.10 Demonstration of the magnetic moment associated with (a) an orbiting electron and (b) a spinning electron.....	30
2.11 Hysteresis loop of a ferromagnetic behavior.....	36
2.12 Schematic diagram of a supercapacitor device.....	38
2.13 Flow-chart describing the different types of capacitors.....	38
2.14 The principle charge storage mechanism of (a) EDLC (b) Pseudocapacitor.....	39
3.1 Schematic diagram of fabrication of the electrode and measuring electrochemical parameters.....	52
3.2 Diagram showing preparation and characterization of BiFe _{1-x} M _x O ₃ (M = Co, Ni, and Cu) nanoparticles.....	53
3.3 Bragg diffraction by crystal planes.....	55
3.4 X-ray diffractometer.....	56
3.5 Diagram of major components of SEM.....	58
3.6 Scanning electron microscope.....	58
3.7 Transmission Electron Microscopes.....	60
3.8 The IUPAC classification of adsorption isotherms.....	63
3.9 Schematic diagram of the vibrating sample magnetrometer (VSM).....	67
3.10 Experimental set up of electrochemical measurements consist of personal computer, potentiostat/galvanostat and electrochemical cell.....	68

LIST OF FIGURES (Continued)

Figure	Page
3.11	View of measurement and set up of the Nova 1.10 software.....69
3.12	Cyclic voltammogram of three different electrochemical capacitors: ideal, resistive, faradaic capacitors.....71
4.1	XRD patterns of $\text{BiFe}_{1-x}\text{Co}_x\text{O}_3$ ($x = 0, 0.05, 0.1, 0.2,$ and 0.3) nanoparticles.....80
4.2	Rietveld refinement of XRD data for (a) BiFeO_3 (b) Co-doped BiFeO_3 ($x = 0.05$) nanoparticles.....83
4.3	Rietveld refinement of XRD data for Co-doped BiFeO_3 nanoparticles: (a) $x = 0.1$ (b) $x = 0.2$84
4.4	Rietveld refinement of XRD data for Co-doped BiFeO_3 ($x = 0.3$) nanoparticles.....85
4.5	SEM images of $\text{BiFe}_{1-x}\text{Co}_x\text{O}_3$ nanoparticles: (a) $x = 0$, (b) $x = 0.05$, (c) $x = 0.1$, (d) $x = 0.2$, and (e) $x = 0.3$86
4.6	Bright field TEM images (left), high-resolution (HRTEM) TEM images (middle) and corresponding selected areas electron diffraction (SAED) patterns (right) of $\text{BiFe}_{1-x}\text{Co}_x\text{O}_3$ nanoparticles: (a) $x = 0$, (b) $x = 0.05$, (c) $x = 0.1$, (d) $x = 0.2$, and (e) $x = 0.3$88
4.7	XANES spectra of $\text{BiFe}_{1-x}\text{Co}_x\text{O}_3$ ($x = 0, 0.05, 0.1, 0.2,$ and 0.3) nanoparticles: (a) Bi M_5 -edge and (b) Fe K -edge.....91
4.8	XANES spectra at Co K -edge of $\text{BiFe}_{1-x}\text{Co}_x\text{O}_3$ ($x = 0, 0.05, 0.1, 0.2,$ and 0.3) nanoparticles.....92

LIST OF FIGURES (Continued)

Figure	Page
4.9	N ₂ adsorption-desorption isotherms (a) and pore-size distribution (b) of the BiFe _{1-x} Co _x O ₃ nanoparticles.....95
4.10	Variations of crystallite size calculated by XRD and particle size calculated from BET of BiFe _{1-x} Co _x O ₃ nanoparticles as a function of Co content (%)......96
4.11	Magnetization hysteresis loops at different temperature of BiFe _{1-x} Co _x O ₃ nanoparticles: (a) x = 0, (b) x = 0.05, (c) x = 0.1, (d) x = 0.2, and (e) x = 0.3. (f) Variations in saturation magnetization as a function of Co content (%)......100
4.12	ZFC/FC curves and fitting the data to the Curie-Weiss law (inset) for (a) BiFeO ₃ and (b) BiFe _{0.95} Co _{0.05} O ₃ nanoparticles.....106
4.13	ZFC/FC curves and fitting the data to the Curie-Weiss law (inset) for (a) BiFe _{0.9} Co _{0.1} O ₃ and (b) BiFe _{0.8} Co _{0.2} O ₃ nanoparticles.....107
4.14	ZFC/FC curves and fitting the data to the Curie-Weiss law (inset) for BiFe _{0.7} Co _{0.3} O ₃ nanoparticles.....108
4.15	CV curves of the BiFe _{1-x} Co _x O ₃ nanoparticles: (a) x = 0, (b) x = 0.05, (c) x = 0.1, (d) x = 0.2, and (e) x = 0.3. (f) Specific capacitance vs scan rate.....113
4.16	Galvanostatic charge-discharge curves of the BiFe _{1-x} Co _x O ₃ nanoparticles: (a) x = 0, (b) x = 0.05, (c) x = 0.1, (d) x = 0.2, and (e) x = 0.3. (f) Specific capacitance vs current density.....117

LIST OF FIGURES (Continued)

Figure	Page
4.17	Ragone plot showing energy densities and power densities relationship of BiFeO ₃ and Co-doped BiFeO ₃ electrodes.....118
4.18	Capacity retention (%) of the BiFe _{1-x} Co _x O ₃ electrodes after 500 cycles at 10A/g current density.....121
4.19	Nyquist plots of the BiFe _{1-x} Co _x O ₃ (x = 0, 0.05, 0.1, 0.2, and 0.3) electrodes.....123
4.20	Equivalent circuit of the BiFe _{1-x} Co _x O ₃ electrodes: (a) x = 0, (b) x = 0.05, (c) x = 0.1, (d) x = 0.2, and (e) x = 0.3.....124
4.21	XRD patterns of BiFe _{1-x} Ni _x O ₃ (x = 0, 0.05, 0.1, 0.2, and 0.3) nanoparticles.....125
4.22	Rietveld refinement of XRD data for (a) BiFeO ₃ (b) Ni-doped BiFeO ₃ x = 0.05 nanoparticles.....128
4.23	Rietveld refinement of XRD data for Ni-doped BiFeO ₃ nanoparticles (a) x = 0.1 (b) x = 0.2.....129
4.24	Rietveld refinement of XRD data for Ni-doped BiFeO ₃ (x = 0.3) nanoparticles.....130
4.25	SEM images of BiFe _{1-x} Ni _x O ₃ nanoparticles: (a) x = 0, (b) x = 0.05, (c) x = 0.1, (d) x = 0.2, and (e) x = 0.3.....131

LIST OF FIGURES (Continued)

Figure	Page
4.26	Bright field TEM images (left), high-resolution (HRTEM) TEM images (middle) and corresponding selected areas electron diffraction (SAED) patterns (right) of $\text{BiFe}_{1-x}\text{Ni}_x\text{O}_3$ nanoparticles: (a) $x = 0$, (b) $x = 0.05$, (c) $x = 0.1$, (d) $x = 0.2$, and (e) $x = 0.3$
	133
4.27	XANES spectra of $\text{BiFe}_{1-x}\text{Ni}_x\text{O}_3$ ($x = 0, 0.05, 0.1, 0.2, \text{ and } 0.3$) nanoparticles: (a) Bi M_5 -edge and (b) Fe K -edge.....
	135
4.28	XANES spectra at Ni K -edge of $\text{BiFe}_{1-x}\text{Ni}_x\text{O}_3$ ($x = 0, 0.05, 0.1, 0.2, \text{ and } 0.3$) nanoparticles.....
	136
4.29	N_2 adsorption-desorption isotherms (a) and pore-size distribution (b) of the $\text{BiFe}_{1-x}\text{Ni}_x\text{O}_3$ nanoparticles.....
	139
4.30	Variations of crystallite size calculated by XRD and particle size calculated from BET of $\text{BiFe}_{1-x}\text{Ni}_x\text{O}_3$ nanoparticles as a function of Ni content (%).....
	140
4.31	Magnetization hysteresis loops at different temperature of $\text{BiFe}_{1-x}\text{Ni}_x\text{O}_3$ nanoparticles: (a) $x = 0$, (b) $x = 0.05$, (c) $x = 0.1$, (d) $x = 0.2$, and (e) $x = 0.3$. (f) Variations in saturation magnetization as a function of Ni content (%).....
	144
4.32	ZFC/FC curves and fitting the data to the Curie-Weiss law (inset) for (a) BiFeO_3 and (b) $\text{BiFe}_{0.95}\text{Ni}_{0.05}\text{O}_3$ nanoparticles.....
	148
4.33	ZFC/FC curves and fitting the data to the Curie-Weiss law (inset) for (a) $\text{BiFe}_{0.9}\text{Ni}_{0.1}\text{O}_3$ and (b) $\text{BiFe}_{0.8}\text{Ni}_{0.2}\text{O}_3$ nanoparticles.....
	149

LIST OF FIGURES (Continued)

Figure	Page
4.34 ZFC/FC curves and fitting the data to the Curie-Weiss law (inset) for BiFe _{0.7} Ni _{0.3} O ₃ nanoparticles.....	150
4.35 CV curves of the BiFe _{1-x} Ni _x O ₃ nanoparticles: (a) x = 0, (b) x = 0.05, (c) x = 0.1, (d) x = 0.2, and (e) x = 0.3. (f) Specific capacitance vs scan rate.....	154
4.36 Galvanostatic charge-discharge curves of the BiFe _{1-x} Ni _x O ₃ nanoparticles: (a) x = 0, (b) x = 0.05, (c) x = 0.1, (d) x = 0.2, and (e) x = 0.3. (f) Specific capacitance vs current density.....	159
4.37 Ragone plot showing energy densities and power densities relationship of BiFeO ₃ and Ni-doped BiFeO ₃ electrodes.....	162
4.38 Capacity retention (%) of the BiFe _{1-x} Ni _x O ₃ electrodes after 500 cycles at 10A/g current density.....	164
4.39 Nyquist plots of the BiFe _{1-x} Ni _x O ₃ (x = 0, 0.05, 0.1, 0.2, and 0.3) electrodes.....	165
4.40 Equivalent circuit of the BiFe _{1-x} Ni _x O ₃ electrodes: (a) x = 0, (b) x = 0.05, (c) x = 0.1, (d) x = 0.2, and (e) x = 0.3.....	166
4.41 XRD patterns of BiFe _{1-x} Cu _x O ₃ (x = 0, 0.05, 0.1, 0.2, and 0.3) nanoparticles.....	169
4.42 Rietveld refinement of XRD data for (a) BiFeO ₃ (b) Cu-doped BiFeO ₃ x = 0.05 nanoparticles.....	171
4.43 Rietveld refinement of XRD data for Cu-doped BiFeO ₃ nanoparticles (a) x = 0.1 (b) x = 0.2.....	172

LIST OF FIGURES (Continued)

Figure	Page
4.44 Rietveld refinement of XRD data for Cu-doped BiFeO ₃ nanoparticles x = 0.3.....	173
4.45 SEM images of BiFe _{1-x} Cu _x O ₃ nanoparticles: (a) x = 0, (b) x = 0.05, (c) x = 0.1, (d) x = 0.2, and (e) x = 0.3.....	174
4.46 Bright field TEM images (left), high-resolution (HRTEM) TEM images (middle) and corresponding selected areas electron diffraction (SAED) patterns (right) of BiFe _{1-x} Cu _x O ₃ nanoparticles: (a) x = 0, (b) x = 0.05, (c) x = 0.1, (d) x = 0.2, and (e) x = 0.3.....	176
4.47 XANES spectra of BiFe _{1-x} Cu _x O ₃ (x = 0, 0.05, 0.1, 0.2, and 0.3) nanoparticles: (a) Bi M ₅ -edge and (b) Fe K-edge.....	178
4.48 XANES spectra at Cu K-edge of BiFe _{1-x} Cu _x O ₃ (x = 0, 0.05, 0.1, 0.2, and 0.3) nanoparticles.....	179
4.49 N ₂ adsorption-desorption (a) isotherms and pore-size distribution (b) of the BiFe _{1-x} Cu _x O ₃ nanoparticles.....	182
4.50 Variations of crystallite size calculated by XRD and particle size calculated from BET of BiFe _{1-x} Cu _x O ₃ nanoparticles as a function of Cu content (%)......	183
4.51 Magnetization hysteresis loops at different temperature of BiFe _{1-x} Co _x O ₃ nanoparticles: (a) x = 0, (b) x = 0.05, (c) x = 0.1, (d) x = 0.2, and (e) x = 0.3. (f) Variations in saturation magnetization as a function of Co content (%)......	186

LIST OF FIGURES (Continued)

Figure	Page
4.52	ZFC/FC curves and fitting the data to the Curie-Weiss law (inset) for (a) BiFeO ₃ and (b) BiFe _{0.95} Cu _{0.05} O ₃ nanoparticles.....190
4.53	ZFC/FC curves and fitting the data to the Curie-Weiss law (inset) for (a) BiFe _{0.9} Cu _{0.1} O ₃ and (b) BiFe _{0.8} Cu _{0.2} O ₃ nanoparticles.....191
4.54	ZFC/FC curves and fitting the data to the Curie-Weiss law (inset) for BiFe _{0.7} Cu _{0.3} O ₃ nanoparticles.....192
4.55	CV curves of the BiFe _{1-x} Cu _x O ₃ nanoparticles: (a) x = 0, (b) x = 0.05, (c) x = 0.1, (d) x = 0.2, and (e) x = 0.3. (f) Specific capacitance vs scan rate.....197
4.56	Galvanostatic charge-discharge curves of the BiFe _{1-x} Cu _x O ₃ nanoparticles: (a) x = 0, (b) x = 0.05, (c) x = 0.1, (d) x = 0.2, and (e) x = 0.3. (f) Specific capacitance vs current density.....201
4.57	Ragone plot showing energy densities and power densities relationship of BiFeO ₃ and Cu-doped BiFeO ₃ electrodes.....202
4.58	Capacity retention (%) of the BiFe _{1-x} Cu _x O ₃ electrodes after 500 cycles at 10 A/g current density.....205
4.59	Nyquist plots of the BiFe _{1-x} Cu _x O ₃ (x = 0, 0.05, 0.1, 0.2, and 0.3) electrodes.....207
4.60	Equivalent circuit of the BiFe _{1-x} Cu _x O ₃ electrodes: (a) x = 0, (b) x = 0.05, (c) x = 0.1, (d) x = 0.2, and (e) x = 0.3.....208

LIST OF ABBREVIATIONS

BET	=	Brunauer emmett teller
BJH	=	Barrett-Joyner-Halenda
CV	=	Cyclic voltammetry
EDLC	=	Electric double-layer capacitor
EIS	=	Electrochemical impedance spectroscopy
EXAFS	=	Extended X-ray absorption fine structure
GCD	=	Galvanostatic charge-discharge
H_c	=	Coercivity
M_r	=	Remanent magnetization
M_s	=	Saturation magnetization
NMP	=	N-Methyl-2-pyrrolidone
PVDF	=	Polyvinylidene fluoride
SEM	=	Scanning electron microscopy
TEM	=	Transmission electron microscopy
VSM	=	Vibrating sample magnetometer
XANE	=	X-ray absorption near edge structure
XAS	=	X-ray absorption spectroscopy
XRD	=	X-ray diffraction

CHAPTER I

INTRODUCTION

1.1 Principle and reason

In recent years, research interest in multiferroic materials with a simultaneous coexistence of ferroelectricity and magnetism which has increased due to multifunctional applications such as in data storage, sensors, spintronic and microelectronic devices and many more (Dong *et al.*, 2003). Bismuth ferrite (BiFeO_3), one of the very few and the most interesting multiferroic compound, has been attracting great attention over the past several decades due to its high ferroelectric curie temperature ($T_c \sim 1103 \text{ K}$) and antiferromagnetic neel temperature ($T_N \sim 643 \text{ K}$) in perovskite structure (Catalan and Scott, 2009). However, the magnetization of BiFeO_3 is too weak for many applications. The enhancement of the magnetic properties of BiFeO_3 is also the key to solve these problems (Hill, 2000).

Nanoscale effects on the physical and multiferroic properties of BiFeO_3 are studied because of the potential applications in nanoscale devices (Yang *et al.*, 2012). Several studies have been devoted to the improvement of the magnetic properties of BiFeO_3 through cation substitution realized by B-site (Fe-site) doping, such as nonmagnetic metal ion of Cu (Agrawal *et al.*, 2014) or magnetic ions of Co (Battisha *et al.*, 2015) and Ni (Vanga *et al.*, 2015; Zhao *et al.*, 2013; Kumar and Yadav, 2011)

which can enhance the magnetization. Increasing of Ni content with decreasing in crystallite size of (Nd, Ni) co-doped BiFeO₃ can improve magnetization due to the suppression of spin cycloid structure (Vanga *et al.*, 2015). Size-dependent magnetic properties of BiFeO₃ are strongly correlated with decreasing nanoparticle size below cycloidal spin wavelength of ~62 nm and uncompensated spin at the surface (Park *et al.*, 2007). These factors explain the motivation for this research. Substitution with similar radius ions can be attributed to the size effect of nanostructures which can be considered as candidates for the enhancement of magnetic properties. Hence, in this work, we choose Co, Ni, and Cu ions as the substituents to study and clearly clarify the mechanisms underlying the effects on the magnetic properties of the BiFeO₃-based nanoparticles.

Now-a-days, fast-growing market for portable electronic devices is increasing and there is an urgent demand for environmental-friendly high-power energy storage resources (Zhang *et al.*, 2012). Electrochemical capacitor has been tremendously increased in attention over the past few decades filling the gap between batteries and conventional dielectric capacitors compared and presented in the “ragone plot” in Figure 1.1. Although, the performance of electrochemical capacitors have advantages over the batteries such as a high power density, less weigh, non-toxic metal components and long life, but it is available for commercial products to have specific energy densities (5-10 Wh/kg) lower than lithium-ion batteries (35-170 Wh/kg) (Burke and Miller, 2011). The possible ways that could amend the energy density is enhancing the specific capacitance to meet the higher requirements such as portable electronics, hybrid electric vehicles, and large industrial equipments (Yu *et al.*, 2013).

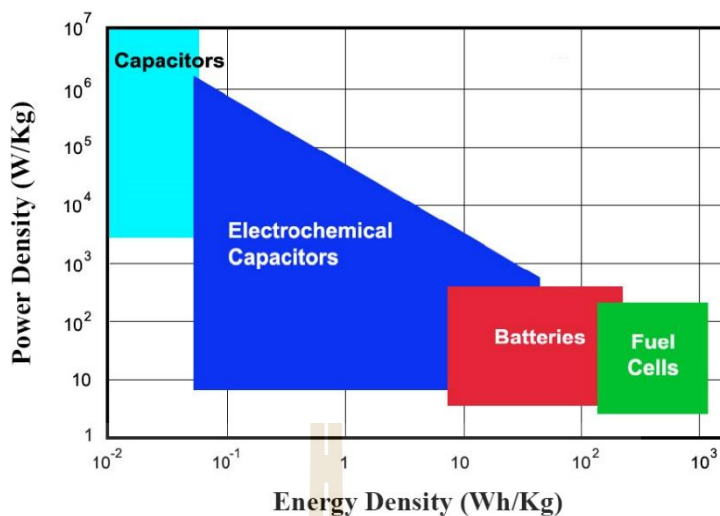


Figure 1.1 Ragone plot of various energy storage devices (Adapted from (Goodenough *et al.*, 2007)).

The development of new electrode materials is an essential step for the advancement of electrochemical capacitor. In general, the electrode materials can be divided into two categories on the basis of the charge storage mechanism: (1) electric double-layer capacitors (EDLCs) stored energy through the adsorption /desorption process such as carbon materials with very high surface area and (2) pseudocapacitors stored energy through the Faradic process such as oxide materials and conducting polymers. Mostly, these pseudocapacitors possess higher energy density due to the enhanced capacitance compared with EDLCs (Conway, 1999). A numerous reports have been explored using transition metal oxides in recent years. An excellent electrode material, hydrated RuO_x has high specific capacitance of 720 F/g and electrochemical stability due to a large specific area and high conductivity (Zheng and Jow, 1995). However, the restrictive price and toxicity of RuO₂ have limited practical uses (Lee *et al.*, 2012). Therefore, inexpensive nanostructured metal oxides were studied to be used as the electrode material for pseudocapacitors such as Fe₃O₄ (Wang *et al.*, 2006), SnO₂

(Prasad and Miura, 2004), Bi_2O_3 (Gujar *et al.*, 2006), Bi_2WO_6 (Nithya *et al.*, 2013), V_2O_5 (Lee and Goodenough, 1999), In_2O_3 (Prasad *et al.*, 2004), NiO (Nam *et al.*, 2002; Zhao *et al.*, 2013), Co_3O_4 (Gao *et al.*, 2010) and MnO_2 (Qu *et al.*, 2009). Therefore, the BiFeO_3 -based materials with their variable oxidation state have attracted considerable attention (Lokhande *et al.*, 2011). In recent years, it has been used as potential active electrode materials by the fabrication of various forms, such as thin-film (Lokhande *et al.*, 2007) and nanorod electrodes (Rana *et al.*, 2014) showed a high specific capacitance of 81 F/g and 450 F/g, respectively. However, the explanation of the electrochemical behavior of BiFeO_3 -based nanoparticles is still unclear and uncompleted. The factors such as morphology, electrolyte and conditions of measurements may influence to the electrochemical performances. As mentioned above, this research will be great important to explore and clearly understand the electrochemical properties of BiFeO_3 nanoparticle electrode and the effect of Co, Ni, and Cu doping, which should be also carried out to be used as the candidate for pseudocapacitors.

In this research, $\text{BiFe}_{1-x}\text{M}_x\text{O}_3$ (M = Co, Ni, and Cu) nanoparticles with different concentrations of the dopants ($x = 0.05, 0.1, 0.2, 0.3$) are synthesized with a simple solution method. The prepared nanoparticles are characterized by various techniques including, X-ray diffraction (XRD), scanning electron microscopy (SEM), transmission electron microscopy (TEM), X-ray absorption spectroscopy (XAS) and gas absorption technique. Magnetic properties at various temperatures of measurement of the nanoparticles are studied. Moreover, the electrochemical properties of the nanoparticles used as electrode materials were also studied.

1.2 Objectives of the dissertation

1.2.1 To synthesize the $\text{BiFe}_{1-x}\text{M}_x\text{O}_3$ ($\text{M} = \text{Co}, \text{Ni}$ and Cu) nanoparticles by simple solution method.

1.2.2 To characterize the microstructure and phase composition of the synthesized BiFeO_3 -based nanoparticles.

1.2.3 To study of the magnetic properties of the synthesized BiFeO_3 -based nanoparticles at various temperature of measurement.

1.2.4 To fabricate the BiFeO_3 -based electrode supercapacitors and study their electrochemical properties.

1.3 Limitation of the study

1.3.1 Synthesis of the $\text{BiFe}_{1-x}\text{M}_x\text{O}_3$ ($\text{M} = \text{Co}, \text{Ni}$ and Cu) nanoparticles with $x = 0, 0.05, 0.1, 0.2,$ and 0.3 .

1.3.2 Characterization of morphology and structure of the synthesized BiFeO_3 -based nanoparticles.

1.3.3 Investigation of magnetic properties of the synthesized nanoparticles at a temperature of 50 K to 350 K.

1.3.4 Fabrication of the $\text{BiFe}_{1-x}\text{M}_x\text{O}_3$ ($\text{M} = \text{Co}, \text{Ni},$ and Cu) electrodes.

1.3.5 Investigation of the electrochemical properties of the fabricated electrodes by Cyclic voltammetry (CV), Galvanostatic charge-discharge (GCD) and Electrochemical impedance spectroscopy (EIS).

1.4 Location of research

1.4.1 Advanced Materials Physics Laboratory (AMP), School of Physics, Institute of Science, Suranaree University of Technology (SUT), Nakhon Ratchasima, 30000 Thailand.

1.4.2 The Center for Scientific and Technological Equipment (SUT), Suranaree University of Technology (SUT), Nakhon Ratchasima, 30000 Thailand.

1.4.3 Department of Physics, Faculty of Science, Khon Kaen University, Khon Kaen, 40002 Thailand.

1.4.4 Synchrotron Light Research Institute (SLRI), 111 Surapat 3, Suranaree University of Technology, University Avenue, Muang District, Nakhon Ratchasima, Thailand, 30000.

1.5 Expected results

1.5.1 Skill and expertise for synthesis, fabrication, and characterization techniques of the $\text{BiFe}_{1-x}\text{M}_x\text{O}_3$ ($M = \text{Co}, \text{Ni}, \text{and Cu}$) nanoparticles with the improved properties for electrode material of electrochemical capacitors.

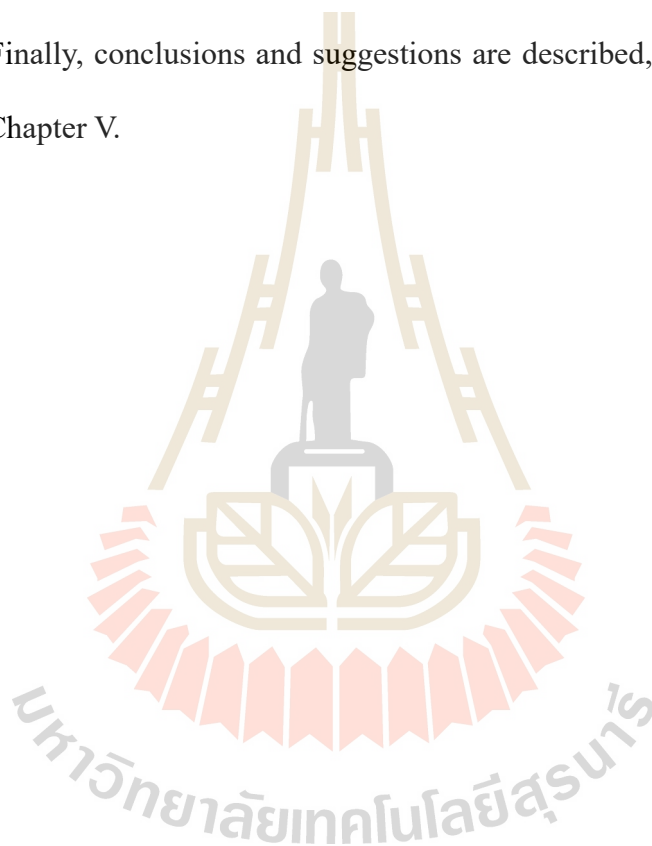
1.5.2 Understanding of the magnetic and electrochemical properties of the $\text{BiFe}_{1-x}\text{M}_x\text{O}_3$ ($M = \text{Co}, \text{Ni}, \text{and Cu}$) nanoparticles.

1.5.3 International publications (ISI).

1.6 Outline of thesis

This dissertation is divided into five chapters. The first chapter provides the introduction of the thesis. In the next chapter (chapter II), a brief review of information

concerning with background of BiFeO_3 , the theory approach concerning with magnetic and electrochemical properties are also detailed in this chapter. Chapter III presents chemical and regents and experimental method of the $\text{BiFe}_{1-x}\text{M}_x\text{O}_3$ nanoparticles and fabrication technique of the $\text{BiFe}_{1-x}\text{M}_x\text{O}_3$ electrodes. Moreover, the information of all measurements techniques used in this research are also summarized in this chapter. And then, the results obtained in this research and discussions of the results are given in Chapter IV. Finally, conclusions and suggestions are described, and future works are proposed in Chapter V.



CHAPTER II

LITERATURE REVIEWS

2.1 Fundamentals of BiFeO₃

2.1.1 Structure of BiFeO₃

Basic crystal structure is essential to explore the material system. The perovskite BiFeO₃ was first produced in the late 1950s. The room-temperature phase of BiFeO₃ is classed as rhombohedral belonging to the space group R3c (Moreau *et al.*, 1971). A perovskite-type unit cell with a rhombohedral structure has a lattice parameter of $a_{\text{rh}} = 3.965 \text{ \AA}$ and a rhombohedral angle of $\alpha = 89.3\text{-}89.4^\circ$ at room temperature with ferroelectric polarization along $[111]_{\text{pseudocubic}}$ (Catalan and Scott, 2009). Alternatively, the structure can be characterized in a hexagonal frame of reference by connecting two perovskite cubes along with their body diagonal, i.e., $[001]_{\text{hexagonal}} \parallel [111]_{\text{pseudocubic}}$. The hexagonal lattice parameters are $a_{\text{hex}} = 5.58 \text{ \AA}$ and $c_{\text{hex}} = 13.90 \text{ \AA}$. Two simple perovskite unit cells are shown to illustrate that successive oxygen octahedra along the polar $[111]$ axis rotate with opposite sense around $[111]$ as shown Figure 2.1. The red arrows on the Fe atoms indicate the orientation of the magnetic moments in the (111) plane (Lubk *et al.*, 2009).

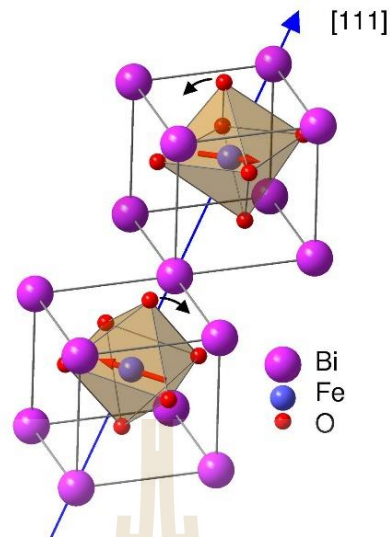


Figure 2.1 Schematic view of crystal structure of bulk BiFeO_3 (Adapted from (Lubk *et al.*, 2009)).

The Fe magnetic moments are coupled ferromagnetically within the pseudocubic (111) planes and antiferromagnetically between the near planes; this is called the G-type antiferromagnetic order. If the magnetic moments are oriented perpendicularly to the [111] direction, the symmetry also permits a canting of the antiferromagnetic sublattices resulting in a macroscopic magnetization called weak magnetism (Heeg *et al.*, 2006; Schwab *et al.*, 1997). According to a first-principles calculation, the spontaneous polarization of BiFeO_3 changes depending on whether the crystal structure is rhombohedral or tetragonal. The tetragonal structure of the BiFeO_3 (Space group: $P4mm$) possesses polarization of around $150 \mu\text{C}/\text{cm}^2$ along the [001] direction, and the rhombohedral structure (Space group: $R3c$) possesses polarization of around $100 \mu\text{C}/\text{cm}^2$ along the [111] direction without strain (Béa *et al.*, 2005; Zhu *et al.*, 2008). For BiFeO_3 , the rotation angle of the octahedra is $11\text{-}14^\circ$ around the polar [111] axis (Catalan and Scott, 2009), with the directly related Fe-O-Fe angle $154\text{-}156^\circ$.

The Fe-O-Fe angle is important because it controls both the magnetic exchange and orbital overlap between Fe and O, and as such it determines the magnetic ordering temperature and the conductivity.

2.1.2 Magnetism of BiFeO₃

The BiFeO₃ is a multiferroic materials which possesses a polarization (ferroelectric) ordering with a high Curie temperature T_c of 1103 K and a spin (antiferromagnetic) ordering of G type with a magnetic transition temperature T_N of 643 K (Kumar and Yadav, 2006). The multiferroics have known as material exhibiting ferromagnetic and ferroelectric properties at the same time, which have exhibited interesting physical as well as a possibility of practical applications for new memory device. In this section, this research will list magnetic properties of BiFeO₃ nanostructures that have been measured as following.

2.1.2.1 Magnetic symmetry and spin cycloid of BiFeO₃

Magnetism of BiFeO₃ can be attributed to both short- and long- range orderings. The local short-range magnetic ordering of BiFeO₃ is G-type antiferromagnet. One Fe⁺³ of spin is surrounded by six antiparallel spins on the neighbor of Fe⁺³ ion. Because the structural distortion, the arrangement of the neighboring spins is in fact not perfectly antiparallel. The canted spins induce a weak magnetic moment that couples with the ferroelectric polarization. Superimposed on this canting, however, is also a long-range superstructure consisting of an incommensurate spin cycloid of the antiferromagnetically ordered sublattices (Catalan and Scott, 2009). The cycloidal model of spin ordering in BiFeO₃ was first proposed by Sosnowska et al. (Sosnowska *et al.*, 1982), whose group has made a number of detailed studies via XRD, neutron scattering, Mossbauer measurements, etc. The cycloid has a very long repeat distance

of 64 nm (Lebeugle *et al.*, 2008). The magnetic easy plane (the plane within which the spins rotate) is defined by the propagation vector and the polarization vector (as shown in Figure 2.2). The canted antiferromagnetic spins (blue and green arrows) give rise to a net magnetic moment (purple arrows) that is spatially averaged out to zero due to the cycloidal rotation. The spins are contained within the plane defined by the polarization vector (red) and the cycloidal propagation vector (black). However, in recent years Zaleskii and co-workers (Bush *et al.*, 2003) have proposed that the simple cycloid is distorted at low temperatures. However, no published data from either group has indicated the phase-transition temperature where the spin reorientation transition should occur.

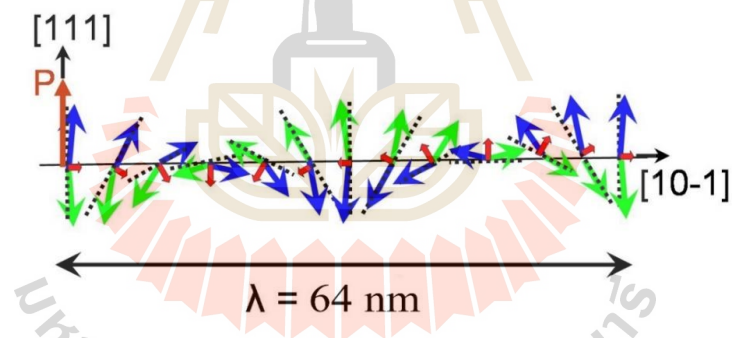


Figure 2.2 Scheme of the antiferromagnetic structure of BiFeO_3 , the magnetic moments describe a cycloid with a period of 64 nm (Adapted from (Lebeugle *et al.*, 2008).

2.1.2.2 Spin-glasslike behavior of BiFeO_3

The first evidence for spin-glass behavior in BiFeO_3 is first that there is a large difference between its field-cooled (FC) and zero-field-cooled (ZFC) magnetization below 240 K (Singh *et al.*, 2008; Singh *et al.*, 2008) as shown in Figure 2.3 (weaker FC effects were also reported by Pradhan *et al.* (Pradhan *et al.*, 2005) and

Nakamura *et al.* (Nakamura *et al.*, 1993)); second, there is a cusp at 50 K in the magnetic susceptibility; and third, the temperature of the cusp in magnetic ac susceptibility appears to be dependent upon the frequency of the magnetic field (Singh *et al.*, 2008).

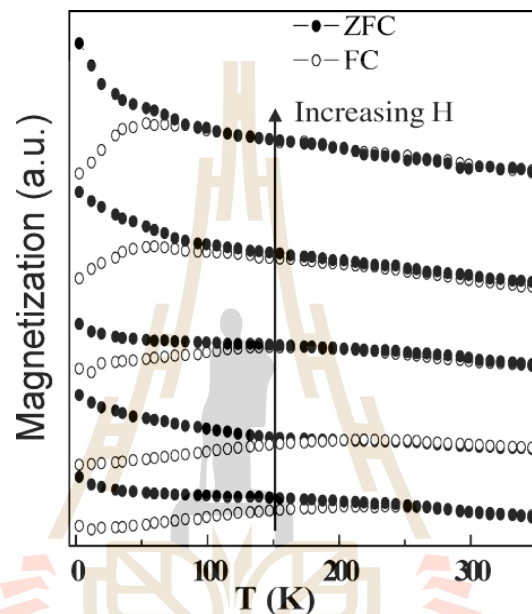


Figure 2.3 The much difference between Field-cooled (FC) and zero-field-cooled (ZFC) magnetization is consistent with a spin-glass state (Catalan and Scott, 2009).

2.1.2.3 Low-Temperature Ferromagnetism of BiFeO₃

As explained earlier, BiFeO₃ is antiferromagnetic at room temperature, with the weak local canting moment being completely cancelled by the averaging out effect of the cycloid. However, there are several reports including hysteresis measurements in single crystals suggesting that at very low temperatures, there could be a weakly ferromagnetic state (Lebeugle *et al.*, 2007). It is important to confirm whether or not this is intrinsic because, although the net magnetic moment is minuscule (10^{-6} μ_B per Fe), it would have important consequences regarding magnetic symmetry

and, thus, also whether or not the linear magnetic coupling is allowed. The existence of ferromagnetism at very low temperatures would also reflect an underlying competition between antiferromagnetic and ferromagnetic interactions, which, of course, would be consistent with the spin-glass state in the intermediate temperature range. On the other hand, the observation of ferromagnetic hysteresis at low temperatures is not universal and may be explained by even a very small concentration of impurities; Lebeugle *et al.* (Lebeugle *et al.*, 2007), for example, note that just 1 mol% of paramagnetic Fe^{3+} (probably due to the presence of $\text{Bi}_{25}\text{FeO}_{39}$) can account for all the low-temperature magnetic enhancement in their single crystals.

2.1.2.4 Size dependence of BiFeO_3 nanocrystals

There is a fast-growing body of research devoted to the manufacture and characterization of complex nanoscopic shapes other than thin films. These 3D nanostructures generally have their own distinctive size effects, and multiferroic BiFeO_3 is no exception. As more novel size-dependent or morphology-dependent properties of BFO nanostructures are being discovered, this implies that a certain “property” may be tuned to desired value in future industrial designs. For bulk BiFeO_3 , the magnetic hysteresis loop exhibits a typical antiferromagnetic curve with zero coercivity (Mazumder *et al.*, 2007). As the new century unfolds, the newly emerging nanotechnology on BiFeO_3 recommended a facile and inexpensive approach by controlling its dimensions down to 62 nm. For example, Park *et al.* reported their systematic studies on size-dependent magnetic properties of BiFeO_3 nanoparticles (Park *et al.*, 2007). The nanocrystals of BiFeO_3 show enhanced magnetization and superparamagnetism correlated with decreasing diameter as shown in Figure 2.4. They noted that the magnetic properties of BiFeO_3 nanoparticles with a mean size of 245 nm

experienced a remarkable similarity to that of the bulk sample which was not so highly significant. When the size of the system is less than 95 nm, the magnetic response can be initiated whereas the magnetic response of BFO nanoparticles increased rapidly in the range of 270-460% for sample below 62 nm. Superparamagnetism of 14 nm nanoparticles was also detected in their experiments. Combined with their Mössbauer study, it is believed that the increase of magnetization along with the decreasing particle size is primarily due to the contribution of uncompensated spins at the surface, strain anisotropies, and noncollinear magnetic ordering, leading to frustrated spin systems in addition to an increased suppression of the material's intrinsic spiral structure below a certain threshold value of particle size. Similar size-induced magnetism has also been reported for BiFeO₃ nanowires (Gao *et al.*, 2006) and nanopowders (Mazumder *et al.*, 2006). This is thought to be due to the large fraction of uncompensated spins from the surfaces of the nanocrystals, an effect that is well known from classic antiferromagnets such as NiO (Richardson *et al.*, 1991).

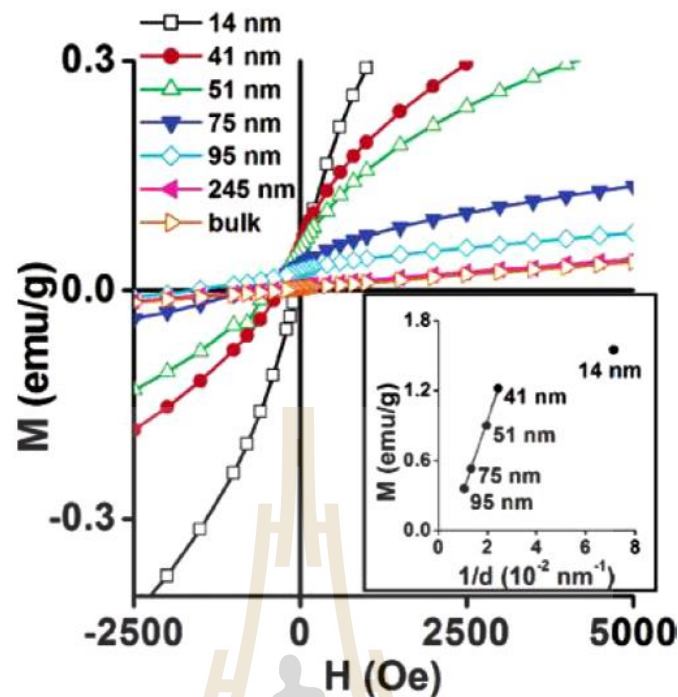


Figure 2.4 Ferromagnetic hysteresis due to uncompensated surface spins in BiFeO₃ nanocrystals (Park *et al.*, 2007).

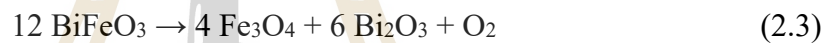
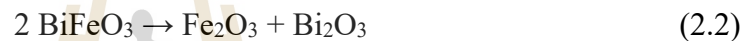
2.1.3 Phase decomposition and impurity for BiFeO₃

One major drawback in the research of BiFeO₃ bulk and thin films would be impurity and this also applies to the development of BiFeO₃ nanostructures. In practice, most studies have failed to synthesize single phase BiFeO₃ samples without generating secondary phase such as Bi₂₅FeO₃₉ and Bi₂Fe₄O₉. The initial solution was to let it react with excess Bi₂O₃ followed by leaching with diluted nitric acid to wash away the secondary oxides and residual Bi₂O₃ (Achenbach *et al.*, 1967). Scientists later declared that the protective atmosphere such as argon and nitrogen during heating process was of help to reduce the secondary phases (Singh *et al.*, 2006; Xie *et al.*, 2008). It has been argued that BiFeO₃ is metastable in air with respect to Bi₂Fe₄O₉ and Bi₂₅FeO₃₉ based

on thermodynamic factors (Selbach *et al.*, 2008). Hence, a decomposition process will be resulted as follows



On the other hand, Bi_2O_3 is widely known to evaporate easily when heated at high temperature. Thus, this will lead to the generation of iron-rich phases such as Fe_2O_3 or even Fe_3O_4 (Catalan and Scott, 2009; Lou *et al.*, 2007) as follows



Palai *et al.* (Palai *et al.*, 2008) reported the refined Bi_2O_3 - Fe_2O_3 phase diagram. These differential thermal analysis (DTA) data for BiFeO_3 and others for which the Bi/Fe ratio is varied with a view to determining the liquidus curves and the eutectic and peritectic horizontals, produce the phase diagram shown in Figure 2.5. The α , β , and γ phases are rhombohedral, orthorhombic, and cubic, respectively.

In this situation, the properties of the sample, especially the magnetic characteristics, will be strongly affected by these impurities. To minimize such problem, careful optimization of growth parameters including thermodynamic and kinetic conditions would be required. Meanwhile, upon this circumstance, reaction in hermetic systems or low temperature is evidently favorable in obtaining phase-pure perovskite samples.

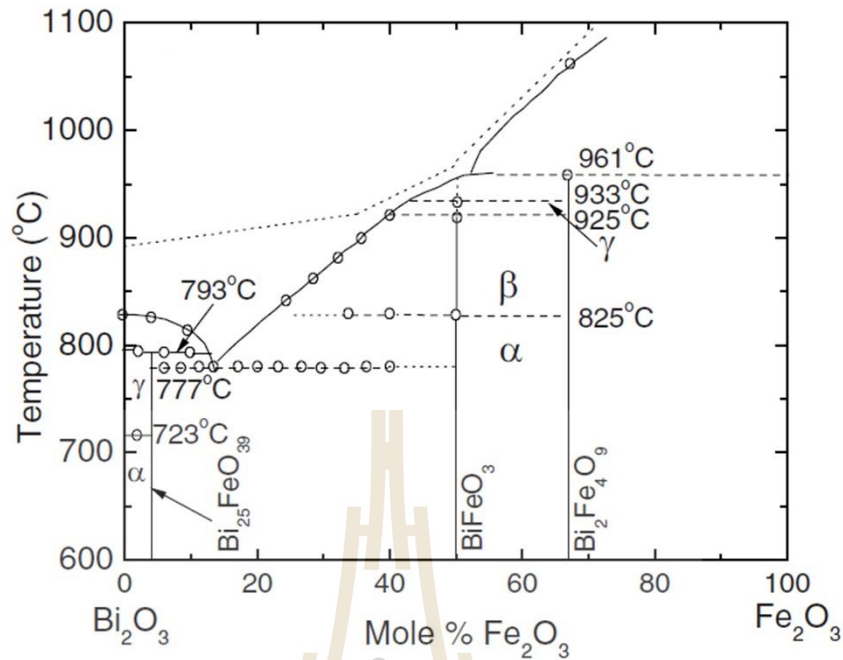


Figure 2.5 Compositional phase diagram of Bi₂O₃-Fe₂O₃ system (Palai *et al.*, 2008).

2.2 Study of Synthesis of BiFeO₃-based nanoparticle

Shami *et al.* (Shami *et al.*, 2011) synthesized BiFeO₃ powder by co-precipitation route. In the co-precipitation method, The analytical grade iron nitrate nonahydrate Fe(NO₃)₃·9H₂O and commercial grade bismuth oxide Bi₂O₃ (99.98% pure) were used as precursors. These were dissolved in nitric acid (HNO₃) and deionized water to form solutions of 0.4 M. For crystallization and phase formation, powder was calcined at different temperatures (400-600) °C for 1 h. The solution thus obtained was washed with deionized water till a pH of 7 was achieved and were dried in an electric oven at 100 °C. These pellets were further densified by cold iso-static pressing at 250 MPa and sintered at 500 °C for 2 h. All the heat treatments were carried out in the air. Phase formation and crystallite size of the BiFeO₃ powders were determined from the XRD analysis. The powder calcined at 400 °C contains a minor peak of Bi₂O₃, which

diminished at higher temperature. Further increase in calcination temperature up to 600 °C, improved the crystallinity of BiFeO₃ powders. The crystallite sizes of calcined powders were calculated using the Scherrer formula increased (31-93) nm with the increase in calcination temperature.

Kumar *et al.* (Kumar and Yadav, 2011) prepared BiFe_{1-x}Ni_xO₃ (with x = 0, 0.1) nanoparticles by the solgel method. Ferric nitrate Fe(NO₃)₃·9H₂O, bismuth nitrate Bi(NO₃)₃·5H₂O, nickel nitrate Ni(NO₃)₂·6H₂O were added into the solution of citric acid prepared in distilled water. Then, the solution was stirred with constant at 60-70 °C to avoid precipitation to obtain a homogeneous mixture. Thereafter ethylene glycol was added into the solution at a proportion of citric acid/ethylene glycol ratio of 60:40. The gel initially started to swell and filled the beaker. The resultant gel was dried at 100 °C in hot air oven for 12h. The obtained powders were calcined at 400 °C, leached in diluted HNO₃. Leaching was done to get a single phase.

Wang *et al.* (Wang *et al.*, 2013) synthesized BiFeO₃ nanoparticles through low-heating temperature solid-state precursor method. The resultant samples were leached with 20% HNO₃ to remove the unreacted Bi₂O₃ (~5-7% shown by our preliminary experiment) and then washed by deionized water for several times and dried at 80 °C for 3 h. BiFeO₃ powders were calcined from 450 to 600 °C. The particle morphology changes from an average length of 80-100 to 400-500 nm as the annealing temperature increases from 450 to 600 °C. With the increase of annealing temperature from 450 to 600 °C, the particle morphology changes from 80-100 nm spherical-like particles to 400-500 nm particles with plate and polyhedral like morphologies. This can be explained by the increase of temperature that leads to an enhanced diffusion of Bi ions,

which consequently accelerates the reaction process and improves the BiFeO₃ particles growth rate.

2.3 Study of magnetic and electrochemical properties of BiFeO₃

2.3.1 Study of magnetic properties of BiFeO₃

BiFeO₃ is one of several rare single-phase room temperature multiferroic materials and it has great potential for practical applications exhibiting ferroelectricity with high Curie temperature ($T_C \sim 1103$ K), and antiferromagnetic properties below $T_N \sim 643$ K (Simões *et al.*, 2007) (Catalan and Scott, 2009). The bulk form of BiFeO₃ ceramic has some disadvantages: (1) it is difficult to prepare pure single phase BiFeO₃, and (2) BiFeO₃-based materials have low electrical resistivity. The relatively high conductivity of BiFeO₃ is believed to be due to the degradation of Fe³⁺ species to Fe²⁺ species, which creates oxygen vacancies for charge compensation. This has prevented its practical applications as piezoelectric or magnetoelectric functional components (Simões *et al.*, 2007). The multiferroic nature of BiFeO₃ is due to stereochemical activity associated with the 6s² lone pair of Bi³⁺. It results in lowering of structural symmetry and hence ferroelectricity (Mazumder *et al.*, 2006). As shown in Table 2.1, much effort has been paid to improve the magnetization through cation substitution (A site and B site) in BiFeO₃ to get a sizable response to the application of magnetic field. For example, the enhancement in magnetic moment by the structural changes, suppression of spiral spin structure is observed when A site are partially substituted by rare-earth ions in Bi_{1-x}M_xFeO₃ (M = La, Dy, and Eu) induces a spontaneous magnetization (Lahmar *et al.*, 2009; Prashanthi *et al.*, 2010). Besides the A-site doping, many literatures are found which are based on B-site doping in BiFeO₃ to obtain a

collinear magnetic ordering. It was predicted that by substituting such as Mn, Ti, and Co ions for the B site in BiFeO₃,

Table 2.1 Lists of reports for magnetic properties of BiFeO₃ based nanoparticles.

Materials / preparation method	M _s (emu/g)	References
BiFeO ₃ / solid state	-	(Teague <i>et al.</i> , 1970)
Bi _{0.7} La _{0.3} FeO ₃ / solid state	0.02	(Zhang <i>et al.</i> , 2006)
Bi _{0.9} Gd _{0.1} FeO ₃ / sol-gel	8	(Lotey and Verma, 2012)
BiFeO ₃ / sol-gel	0.004	(Jia <i>et al.</i> , 2009)
Bi _{0.7} La _{0.3} FeO ₃ / solid state	0.15	(Rai <i>et al.</i> , 2011)
Bi _{0.8} Ba _{0.2} FeO ₃ / chemical route	0.35	(Das and Mandal, 2012)
BiFe _{0.75} Ni _{0.25} O ₃ / sol-gel	8.5	(Zhao <i>et al.</i> , 2013)

In study of Park *et al.* (Park *et al.*, 2007), single-crystalline BiFeO₃ nanoparticles synthesized by a facile sol-gel methodology. A magnetic response in BiFeO₃ can be initiated when the size of the system is less than about 95 nm. In small structures, the surface-to-volume ratio becomes very large with decreasing particle size, enhancing the tangible contribution to the particle's overall magnetization by uncompensated spins at the surface. For single-domain antiferromagnetic particles, the magnetization is expected to scale as $\sim 1/d$ (where d is the diameter of the particle), that is, as the surface to volume ratio. Magnetization as a function of temperature at an applied field strength of 200 Oe, after zero-field cooling (ZFC) and also with field cooling (FC) were studied as shown in Figure 2.6(a)-(b). Apparent sharp cusps observed

in the magnetization curves at 50 K are reproducible for bismuth ferrite samples with particle dimensions over 95 nm (e.g., 245 nm and bulk). A sharp cusp is observed for the 245 nm BiFeO₃ sample as well as for the bulk and may result from domain wall pinning effects as a result of local structural distortions. For BiFeO₃ nanoparticles possessing diameters of ≤ 95 nm, associated data curves exhibit a broad magnetization maximum around $T_{\max} = 85$ K, when T_{\max} represents a spin-glass-like freezing temperature.

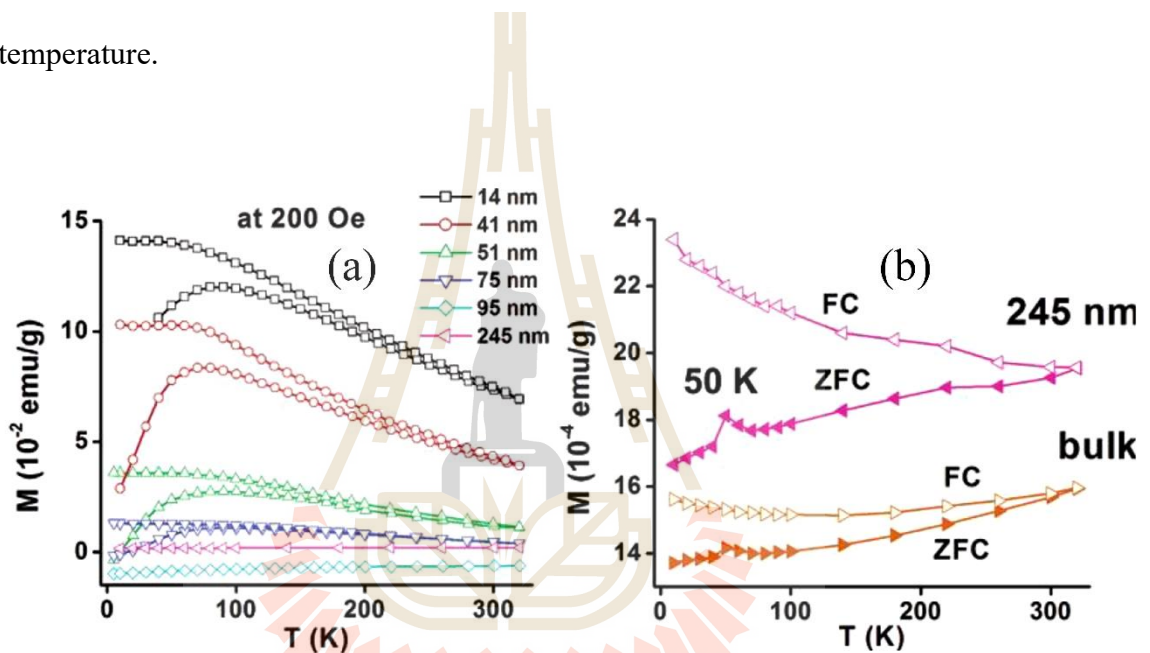


Figure 2.6 (a) Temperature dependence of the magnetization for BiFeO₃ nanoparticles of varying sizes, showing zero field cooling (ZFC) and field cooling (FC) curves. (b) Expanded plots of ZFC and FC curves for BiFeO₃ nanoparticles with diameters of 245 nm and the bulk (Park *et al.*, 2007).

Wang *et al.* (Wang *et al.*, 2013) synthesized BiFeO₃ nanoparticles through low-heating temperature solid-state precursor method. The BiFeO₃ powders were calcined from 450 to 600 °C. The particle morphology changes from an average length of 80-100 to 400-500 nm as the annealing temperature increases from 450 to 600 °C. A

vibrating sample magnetometer (VSM) was used to study the magnetic properties of the prepared samples. The magnetization curve measured at room temperature for BiFeO₃ powders synthesized from 450 to 600 °C. The magnetic hysteresis loop of the sample attained at 450-550 °C shows linear field dependence due to the fact that BiFeO₃ exhibits an inherent antiferromagnetic order of circular cycloid magnetic structure with a critical particle size of 62 nm. With the increase of reaction temperature to 600 °C, the M-H curves of the samples present a noteworthy hysteresis loop, and the saturation magnetization values increase with the temperature as shown in Figure 2.7(a). A partly enlarged curve of powders synthesized at 600 °C is shown in Figure 2.7(b). The curve shows weak ferromagnetism at room temperature with a remanent magnetization value (M_r) of approximately 3.3×10^{-5} emu/g and a coercive field value (H_c) of nearly 40 Oe.

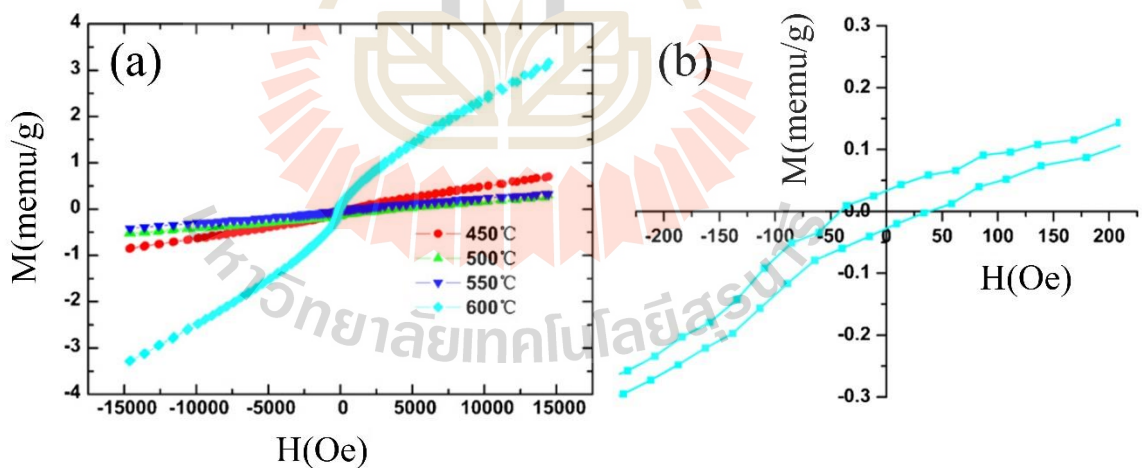


Figure 2.7 (a) VSM measurement of different BiFeO₃ nanoparticles synthesized from 450 to 600 °C and (b) the partially enlarged curve of BiFeO₃ powders synthesized at 600 °C (Wang *et al.*, 2013).

Li *et al.* (Li *et al.*, 2014) synthesized BiFeO_3 and $\text{BiFe}_{0.95}\text{Cu}_{0.05}\text{O}_3$ by the sol-gel method and studied the reasons for the enhancement of the magnetic properties. When Cu ions are doped into BiFeO_3 , the doublet peaks around 32° slightly shift toward lower angle direction. It also suggests that the doping Cu^{2+} has been completely incorporated into the BiFeO_3 structure. The crystalline structure and morphology of the samples were characterized by X-ray diffraction (XRD) scanning electron microscopy (SEM), respectively. It can be seen that the doping of Cu ions at B-sites does not affect the grain size and morphology. The samples show a uniformity of grain. The crystal grain of pure BiFeO_3 is nearly similar to that of the Cu-doped sample, and the average grain size of the two samples is about 0.8-1 μm . The magnetic properties of the samples were investigated at 300 K using a vibrating sample magnetometer (VSM). The M-H hysteresis loop of the BFC sample becomes very slim and close to a straight line. Both the values of the coercivity (H_c) and remanent magnetization (M_r) of Cu-doped BiFeO_3 are very small, which indicates that the BiFeO_3 material presents antiferromagnetic behavior. VSM data show that the magnetic behavior of the Cu-doped BiFeO_3 sample is similar to that of the pure BiFeO_3 sample. DSC measurements demonstrate that the substitution of Cu^{2+} ions at B-sites affects the magnetic order and decreases the Neel temperature of BiFeO_3 .

Battisha *et al.* (Battisha *et al.*, 2015) prepared $\text{BiFe}_{1-x}\text{Co}_x\text{O}_3$ ($x = 0, 0.03, 0.05$ and 0.1) powder by sol-gel technique. The average crystallite sizes of the samples calculated using Scherrer's formula were decreased by doping with Co ions to be equal to 42 and 18 nm for BiFeO_3 , and $\text{BiFe}_{0.95}\text{Co}_{0.05}\text{O}_3$, respectively. Saturation magnetization (M_s) at room temperature increases with the decrease in particle size and as a result of increasing the cobalt ion concentrations. The weak magnetic property of

BiFeO₃ nanoparticles should be attributed to the size-confinement effects of the BiFeO₃ nanostructures, which correlate with: a) the increased suppression of the known spiral spin structure (period length of 62 nm) with decreasing nanoparticle size and b) uncompensated spins and strain anisotropies at the surface. The enhancement of the ferromagnetism of the Co-doped BiFeO₃ could be attributed to the magnetic moment of Co²⁺ and the possible breakage of the space modulated spin cycloid period. In the BiFeO₃, there is an existed cycloid modulated period of magnetization of 62 nm which make BiFeO₃ showing no or weak ferromagnetization. Since the Co²⁺ ions have similar radius as that of Fe³⁺ ion (0.65 Å for Co²⁺ and 0.645 Å for Fe³⁺; six coordinations), a structural distortion can be expected. On the other hand, the bond angle of Fe³⁺-O-Co²⁺ is different with that of Fe³⁺-O-Fe³⁺, the magnetic moments of Fe³⁺ and Co²⁺ are different also, so the net magnetic moment is changed. The changes of both structure and net magnetic moment may change the canting of the antiferromagnetic arranged neighboring spins and break the spiral spin configuration and then enhance the magnetization.

Chakrabarti *et al.* (Chakrabarti *et al.*, 2015) investigated magnetic properties of BiFe_{1-x}Co_xO₃ (x = 0, 0.01, 0.03 and 0.05) nanoparticles. The average size of nanocube as obtained from particle size distribution of TEM images clearly reveals an increase in size from 13 nm for x = 0 to 85 nm for x = 0.05. M-H curves for all the samples reveal weak ferromagnetic behavior which is being enhanced with the increase of Co ions concentration. The substitution of Fe by Co disrupts cycloidal spin structure of BiFeO₃ and improves the ferromagnetic property. Enhancement of the saturation magnetization and coercivity by about 10 times in doped BiFeO₃ are due to changes in morphology. The temperature dependent M_s shows a decrease in M_s with the increase of

temperature. The variation of H_c also shows a similar trend as that of M_s increasing with the increase concentration of Co ions. A clear deviation between ZFC and FC curves has been noticed in all the samples. The broad maxima observed in both ZFC and FC magnetizations clearly show a deviation from the conventional spin glass system. The deviation between ZFC and FC increases with the decrease in temperature indicating a possibility of magnetic blocking on decreasing temperature.

Zhao *et al.* (Zhao *et al.*, 2013) synthesized $\text{BiFe}_{1-x}\text{Ni}_x\text{O}_3$ ($x = 0, 0.05, 0.10, 0.15, 0.20, \text{ and } 0.25$) nanoparticles by a sol gel process. Magnetic studies of the Ni-doped BiFeO_3 nanoparticles were ferromagnetic behavior at room temperature and increased with the increasing of Ni concentration. The enhanced magnetization was attributed to the suppression of the cycloidal spin structure by Ni substitution and the ferromagnetic exchange interaction between the neighboring Fe^{3+} and Ni^{3+} ions. The saturation magnetizations, coercive field and remanent magnetization are increasing with the decreasing of temperature. The ZFC curve for the samples decreases continuously with lowering of temperature whereas FC data increases with lowering of temperature. Such behavior has been identified to be cluster glass behavior. Superparamagnetism with blocking temperature of 10 K, 75 K, 125 K and 200 K for $x = 0.05, 0.15, 0.20, \text{ and } 0.25$ samples can be observed in the ZFC curves.

Vanga *et al.* (Vanga *et al.*, 2015) synthesized $\text{Bi}_{0.95}\text{Nd}_{0.05}\text{Fe}_{1-x}\text{Ni}_x\text{O}_3$ ($x = 0, 0.01, 0.03 \text{ and } 0.05$) samples by solgel method. For the X-ray diffraction measurement, there is slight shift in peak position is observed towards lower angle in the Ni co-doped samples due to the higher ionic radius of Ni (0.69 Å) compared to Fe (0.645 Å). The crystallite size decreases with increasing in concentration of Ni doping, the presence of Ni ion in Fe^{3+} site acts as an inhibitor and results in decreasing of crystallite size. The

inhibition is mainly due to the decrease in surface energy of BiFeO_3 with addition of dopant, while the bulk energy remains constant. In order to maintain the ratio between surface area to bulk volume the crystallite size decreases. An enhancement of magnetization is observed with increase in concentration of Ni doping in B-site. The saturation magnetization of $\text{Bi}_{0.95}\text{Nd}_{0.05}\text{Fe}_{0.99}\text{Ni}_{0.1}\text{O}_3$, $\text{Bi}_{0.95}\text{Nd}_{0.05}\text{Fe}_{0.97}\text{Ni}_{0.03}\text{O}_3$ and $\text{Bi}_{0.95}\text{Nd}_{0.05}\text{Fe}_{0.95}\text{Ni}_{0.05}\text{O}_3$ samples is 0.2, 0.68 and 1 emu/g respectively. Such an improved magnetization may be due to the following reasons. (1) The suppression of spin cycloid structure of BiFeO_3 as the particle size of the samples is less than 62 nm. (2) The decrease in crystallite size with the increase in Ni ion concentration gives rise to uncompensated spins at the surface which gives contribution to the overall magnetization. (3) The interaction between Ni and Fe ions can also improve the magnetization.

2.3.2 Study of electrochemical properties of BiFeO_3

The bismuth iron oxide in five crystal phase i.e. BiFeO_3 , $\text{Bi}_2\text{Fe}_4\text{O}_9$, $\text{Bi}_3\text{Fe}_5\text{O}_{12}$, $\text{Bi}_4\text{Fe}_2\text{O}_9$, and $\text{Bi}_{46}\text{Fe}_2\text{O}_{72}$ is well known with their variable oxidation state. That means this material may sustain the charges in its phase during the electrochemical charges. (Lokhande *et al.*, 2011). Therefore, the perovskite BiFeO_3 nanocrystalline electrode have attracted considerable attention, which is exploited as an efficient potential candidate by the fabrication of various forms for study of electrochemical properties.

Lokhande *et al.* (Lokhande *et al.*, 2007) studied the BiFeO_3 electrodes fabricated using electrodeposition method for electrochemical supercapacitors. The maximum specific capacitance of 81 F/g was obtained at 20 mV/s and the specific energy and specific power as 6.6832 J/g and 3.2958 W/g, respectively in an aqueous 1 M NaOH electrolyte. As shown in Figure 2.8(a), one pair of redox peak on this cyclic

voltammogram is seen, indicating the redox transitions of BiFeO_3 between different valence states. Since, the voltammetric responses on the positive sweeps are symmetric to their counterparts on the negative sweeps; this mixed oxide can be employed as an electrode material for electrochemical supercapacitor. The discharge profile as shown in Figure 2.8(b) that usually contains two parts; (1) a resistive component arising from the sudden voltage drop (linear portion parallel to y-axis) representing the voltage change due to the internal resistance. (2) Capacitive component (curved portion) is related to the voltage change due to change in energy within the capacitor.

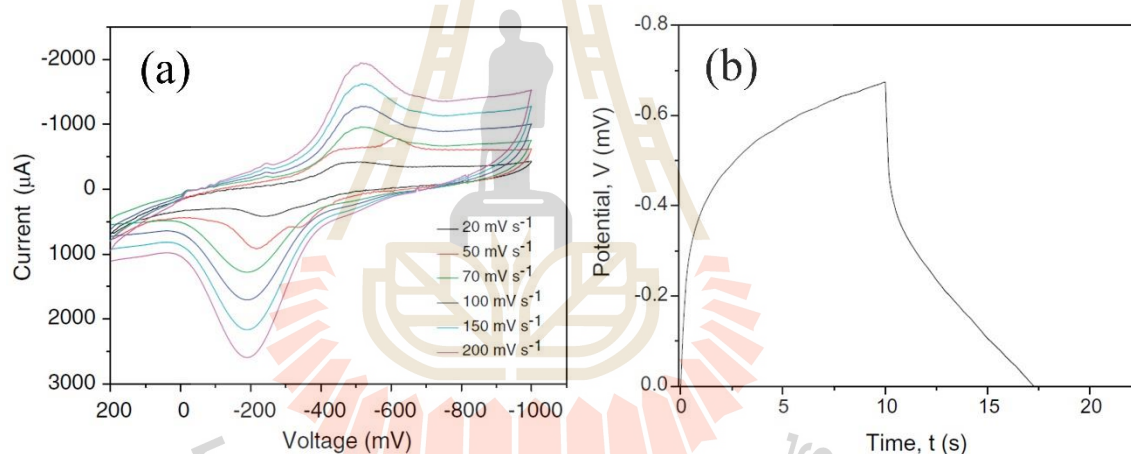


Figure 2.8 (a) The CV curves of BiFeO_3 electrodes at different scanning rates (b) The charge and discharge curve of BiFeO_3 electrode (Lokhande *et al.*, 2007).

Rana *et al.* (Rana *et al.*, 2014) developed BiFeO_3 in the form of nanorod on porous anodised alumina (AAO) templates using wet chemical technique. Cyclic voltammograms (CV) of different samples at a scan rate of 50 and 10mV/s in aqueous solution of 1M Na_2SO_4 are shown in Figure 2.9. High value of specific capacitance of 450 F/g has been calculated. This large value of specific capacitance can be attributed

to the nanostructure form of BiFeO₃ nanorod. Cyclic voltammograms of different samples are quite symmetrical with a mirror image of the current response from voltage, indicating ideal pseudo capacitive behavior and excellent reversibility in charging and discharging at a constant rate over the voltage range of -0.6 to +0.6V.

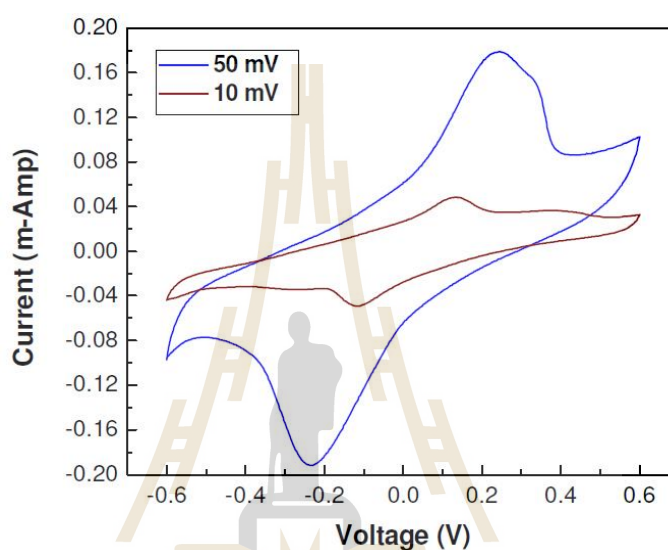


Figure 2.9 Cyclic voltammograms of BiFeO₃ nanorods on AAO at different scan rates (Rana *et al.*, 2014).

Jadhav *et al.* (Jadhav *et al.*, 2016) synthesized nanoflake bismuth ferrite thin film by electrodeposition technique. These films were then air annealed at 400 to 600 °C temperatures for 2 h. The cyclic voltammetry (CV) measurement was employed to explore the BFO electrodes for electrochemical supercapacitor application with NaOH electrolyte of different concentrations in a three-electrode system. It was found that the BiFeO₃ electrode material annealed at 600 °C exhibited maximum current density which could be attributed to the formation of complete ferrite structure. With the scan rate being increased from 10 to 1000 mV/s, the specific capacitance value of BiFeO₃

electrode was found to decrease from 101.63 F/g to 5.65 F/g, indicating that at lower scan rates, inner and outer sites were more active, and thus, full utilization of the electrode in NaOH electrolyte solution occurred. At higher scan rates, only outer sites could be more active than inner sites which were unable to participate in the redox reaction in the electrolyte solution. Galvanostatic charge-discharge (GCD) curves at various current densities in an electrochemical window from -0.8 V to 0.2 V showed a nontriangular symmetry and linear slopes, consolidating the good pseudocapacitive behavior. Using galvanostatic charge-discharge curve was found to be 72.2 F/g at 1 A/g in 2 M NaOH electrolyte. By charge-discharge tests at a current density of 5 A/g for 1500 cycles, the specific capacitance of the BFO electrode maintained 82.8 % of its initial value, indicating a good stability. The EIS measurement of the BiFeO₃ electrode at 600 °C was studied. The frequency response of capacitance reflects the amount of the surface area accessible to the electrolyte. The plot at the high-frequency side was parallel to the X-axis suggesting that the charge transfer resistance rates at high-frequency regions was faster than those at low frequency regions which could be due to an inherent property of ferrites.

2.4 Theoretical Approach

2.4.1 Magnetic properties of materials

Magnetism, the phenomenon by which materials assert an attractive or repulsive force or influence on other materials, has been known for thousands of years. The macroscopic magnetic properties of materials are a consequence of magnetic moments associated with individual electrons. Each electron in an atom has magnetic moments that originate from two sources. One is related to its orbital motion around the nucleus;

being a moving charge, an electron may be considered to be a small current loop, generating a very small magnetic field, and having a magnetic moment along its axis of rotation, as schematically illustrated in Figure 2.10(a). Each electron may also be thought of as spinning around an axis; the other magnetic moment originates from this electron spin, which is directed along the spin axis as shown in Figure 2.10(b).

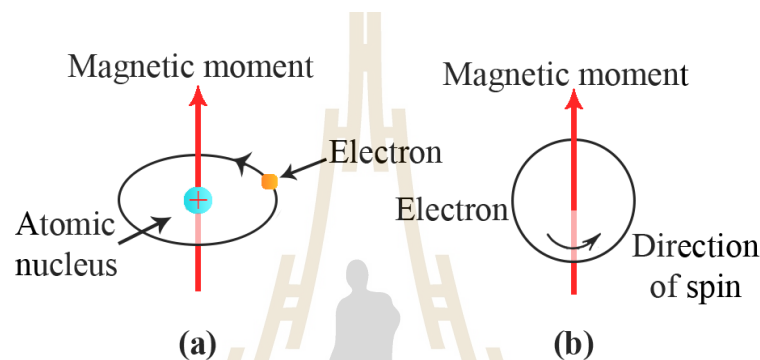


Figure 2.10 Demonstration of the magnetic moment associated with (a) an orbiting electron and (b) a spinning electron (Adapted from (Callister and Rethwisch, 2013).

Spin magnetic moments may be only in an “up” direction or in an antiparallel “down” direction. Thus each electron in an atom may be thought of as being a small magnet having permanent orbital and spin magnetic moments. The most fundamental magnetic moment is the Bohr magneton (μ_B), which is of magnitude $9.27 \times 10^{-24} \text{ A m}^2$. For each electron in an atom the spin magnetic moment is $\pm\mu_B$ (plus for spin up, minus for spin down). The spin moment of an electron with spin up will cancel that of one with spin down. The net magnetic moment, then, for an atom is just the sum of the magnetic moments of each of the constituent electrons, including both orbital and spin contributions, and taking into account moment cancellation. The magnetic field of one electron is cancelled by an opposite magnetic field produced by the other electron in

the pair. The unpaired electron in iron, cobalt and nickel atoms cannot cancel the electron magnetic fields, and thus these elements act like a very small magnet. The magnetic moments (μ) of atoms relate to the spins of electrons. The most common in the magnetic experiment is to apply a magnetic field (H) to a material and measure the magnetization (M) induced by the field. The magnetic field induction (B) in a sample is described by

$$B = H + 4\pi M \text{ [cgs]} \quad (4)$$

The susceptibility ($\chi = M / H$) and the permeability ($\mu = B / H$) are two quantities related to M and B , where the susceptibility is a measure of the increase in magnetic moment caused by H and the permeability represents the relative increase in flux caused by the presence of the magnetic material.

The arrangement of the magnetic moment can be used to classify type of magnetic behavior. The diamagnetism is present when the magnetic moments are paired and overall cancel each other ($\mu_{\text{net}} = 0$). Diamagnetism is a very weak form of magnetism that is nonpermanent and persists only while an external field is being applied. The magnitude of the induced magnetic moment is extremely small, and in a direction opposite to that of the applied field. The magnetic susceptibility is negative. Diamagnetism is found in all materials; but because it is so weak, it can be observed only when other types of magnetism are totally absent. This form of magnetism is of no practical importance. Diamagnetic substances, such as carbon, copper, water, and plastic.

The paramagnetic behavior is present in uncoupled magnetic moment material. Each atom possesses a permanent dipole moment by virtue of incomplete cancellation of electron spin and/or orbital magnetic moments. In the absence of an external magnetic field, the orientations of these atomic magnetic moments are random, such that a piece of material possesses no net macroscopic magnetization. In the presence of a field, the dipoles align with the external field. Both diamagnetic and paramagnetic materials are considered to be nonmagnetic because they exhibit magnetization only when in the presence of an external field. Paramagnetic substances, such as platinum, aluminum, and oxygen. The susceptibility (χ) is independent of temperature for diamagnetics, but that it varies inversely with the absolute temperature for paramagnetics as shown in equation:

$$\chi = \frac{C}{T} \quad (5)$$

This relation is called Curie's law, and C is the Curie constant per gram. T is the absolute temperature (Cullity and Graham, 2011). However, many paramagnetics do not obey this law. They obey instead the more general law called the Curie-Weiss law:

$$\chi = \frac{C}{T - \theta} \quad (6)$$

This adapted law comprises a term θ that is proposed for ferro-or antiferromagnetic materials, which incorporates the interaction between magnetic

moments, known as the temperature constant or weiss constant (θ). For any one substance, and equal to zero for those substances which obey Curie's law. When θ is non-zero this means that there is an interaction between neighbouring magnetic moments and the material is only paramagnetically ordered above the transition temperature. If θ is positive then the material undergoes a paramagnetic to ferromagnetic transition below the transition temperature and the value of θ relates to the transition temperature or simply the Curie temperature (T_c). Antiferromagnetic materials have a small positive susceptibility at all temperatures, but their susceptibilities in a peculiar way with temperature. The materials obey a Curie-Weiss law but with a negative value of θ and below the transition temperature. However, in practice the transition temperature between paramagnetic and antiferromagnetic phases arises at a positive temperature known as the Neel temperature (T_N).

Ferrimagnetism is observed in the material that the magnetic moment in the neighboring sublattices incomplete cancellation due to their different magnitudes. This happens when the populations consist of different materials or ions (such as Fe^{2+} and Fe^{3+}). The macroscopic magnetic characteristics of ferromagnets and ferrimagnets are similar; the distinction lies in the source of the net magnetic moments.

Anti-ferromagnetism is the magnetic behavior that magnetic moment coupling between adjacent atoms or ions occurs in materials. In one such group, this coupling results in an antiparallel alignment. The alignment of the spin moments of neighboring atoms or ions in exactly opposite directions ($\mu_{\text{net}} = 0$). The clue to antiferromagnetism is the behavior of susceptibility above Néel temperature (T_N). Above T_N , the susceptibility obeys the Curie-Weiss law for paramagnets but with a negative intercept indicating negative exchange interactions. Antiferromagnetic materials occur

commonly among transition metal compounds, especially oxides. Examples include hematite, metals such as chromium, alloys such as iron manganese (FeMn), and oxides such as nickel oxide (NiO).

The superparamagnetism is the magnetic behavior that occurs in small ferromagnetic or ferrimagnetic nanoparticles. In sufficiently small nanoparticles, magnetization can randomly flip direction under the influence of temperature. Their magnetic susceptibility is between that of ferromagnetic and paramagnetic materials. The superparamagnetism occurs in nanoparticles which are single-domain, i.e. composed of a single magnetic domain. This is possible when their diameter is below 3-50 nm, depending on the materials.

Ferromagnetism is permanent magnetic that the magnetic moments of the domains align along the direction of the applied magnetic field forming a large net magnetic moment. Permanent magnetic moments in ferromagnetic materials result from atomic magnetic moments due to electron spin-uncancelled electron spins as a consequence of the electron structure. There is also an orbital magnetic moment contribution that is small in comparison to the spin moment. Furthermore, in a ferromagnetic material, coupling interactions cause net spin magnetic moments of adjacent atoms to align with one another, even in the absence of an external field (Callister and Rethwisch, 2013). Certain metallic materials possess a permanent magnetic moment in the absence of an external field, and manifest very large and permanent magnetizations. Ferromagnetism substances, such as the transition metals iron (as BCC & ferrite), cobalt, nickel, and some of the rare earth metals such as gadolinium (Gd). Magnetic susceptibilities as high as 10^6 are possible for ferromagnetic materials. The maximum possible magnetization, or saturation magnetization (M_s), of

a ferromagnetic material represents the magnetization that results when all the magnetic dipoles in a solid piece are mutually aligned with the external field. The saturation magnetization is equal to the product of the net magnetic moment for each atom and the number of atoms present. For each of iron, cobalt, and nickel, the net magnetic moments per atom are 2.22, 1.72, and 0.60 Bohr magnetons, respectively.

To describe the magnetization change with applied field of material, the hysteresis loop is used. As an H field is applied, the domains change shape and size by the movement of domain boundaries. Schematic domain structures are represented at several points along the B-versus-H curve in Figure 2.11(a). Initially, the moments of the constituent domains are randomly oriented such that there is no net B (or M) field. As the external field is applied, the domains that are oriented in directions favorable to (or nearly aligned with) the applied field grow at the expense of those that are unfavorably oriented. This process continues with increasing field strength until the macroscopic specimen becomes a single domain, which is nearly aligned with the field. Saturation is achieved when this domain, by means of rotation, becomes oriented with the H field. From saturation, point S in Figure 2.11(b), as the H field is reduced by reversal of field direction, the curve does not retrace its original path. A hysteresis effect is produced in which the B field lags behind the applied H field, or decreases at a lower rate. At zero H field (point R on the curve), there exists a residual B field that is called the remanence. To reduce the B field within the specimen to zero (point C on Figure 2.11(b)), an H field of magnitude $-H_c$ must be applied in a direction opposite to that of the original field; H_c is called the coercivity. Upon continuation of the applied field in this reverse direction, as indicated in the Figure, saturation is ultimately achieved in the opposite sense, corresponding to point S'. A second reversal of the field to the point of

the initial saturation (point S) completes the symmetrical hysteresis loop and also yields both a negative remanence ($-B_r$) and a positive coercivity ($+H_c$) (Callister and Rethwisch, 2013).

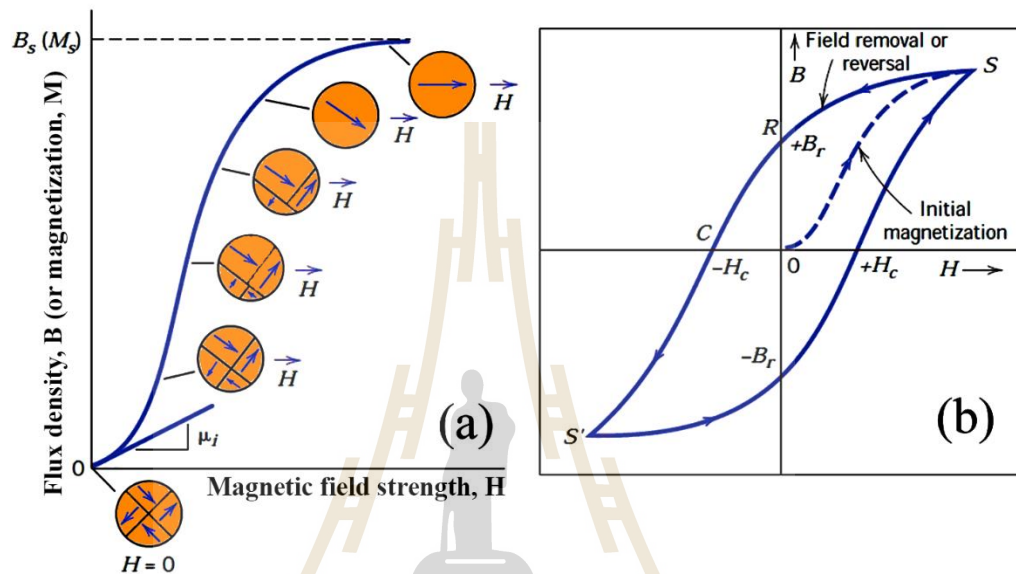


Figure 2.11 Hysteresis loop of a ferromagnetic behavior (Adapted from (Callister and Rethwisch, 2013).

2.4.2 Electrochemical properties of materials

2.4.2.1 The mechanisms of energy storage in electrochemical capacitor

Electrochemical capacitors are electrochemical energy storage devices.

In the past, all electrochemical capacitors were called “double-layer capacitors”. However, since some years it is known that double-layer capacitors together with pseudocapacitors are part of a new family of electrochemical capacitors called supercapacitors, also known as ultracapacitors. The structure of a supercapacitor is similar to that of a battery. It consists of two porous electrodes with a current collector on each electrode immersed in an electrolyte separated by a dielectric porous separator.

When a voltage potential is applied across the current collectors, the positive electrode attracts negative ions in the electrolyte, while the potential on the negative electrode attracts positive ions. The charge accumulated at both electrode surfaces generates energy when discharging as shown in Figure 2.12. The components made up of the supercapacitor including the electrodes, the separator, the current collector, as well as the electrolyte all are important factors affecting the overall performance of the device that must be considered in designing a high-performance supercapacitor device (Conway, 1999).

Moreover, the distribution of the two types of capacitance depends on the material and structure of the electrodes. Based upon current research and development, there are three types of electrochemical capacitors: electrochemical double-layer capacitors, pseudocapacitors, and hybrid capacitors. An overview of each one of these three classes of supercapacitors and their subclasses, distinguished by type of electrode material. A graphical taxonomy of the different classes and subclasses of supercapacitors is presented in Figure 2.13. There are two ways of supercapacitors storing energy in principal based on two types of capacitive behaviors: the electrical double layer (EDL) capacitance from the pure electrostatic charge accumulation at the electrode interface and the pseudo-capacitance due to fast and reversibility surface redox processes at characteristic potentials (Conway, 1999). The principle behind the electrochemical capacitor is demonstrated in Figure 2.14.

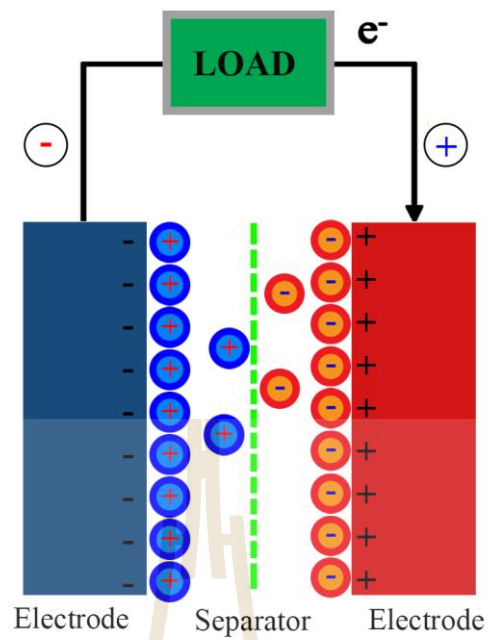


Figure 2.12 Schematic diagram of a supercapacitor device.

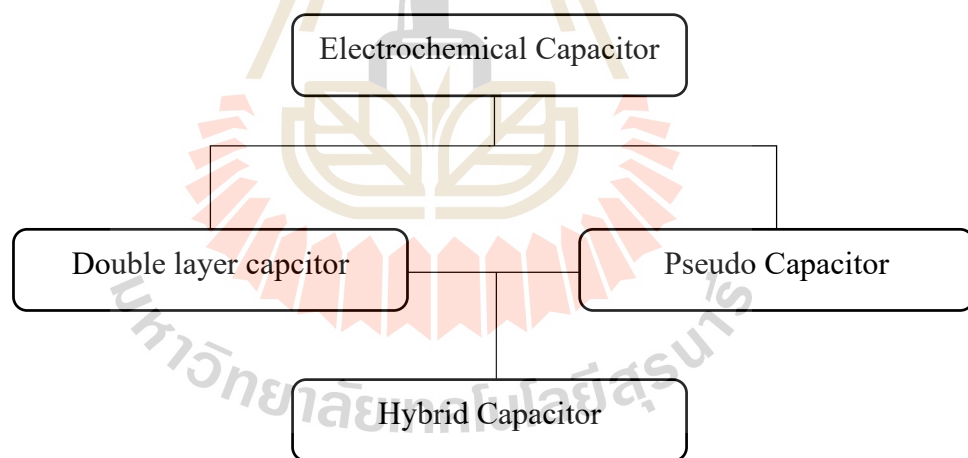


Figure 2.13 Flow-chart describing the different types of capacitors (Adapted from (Frackowiak and Beguin, 2001)).

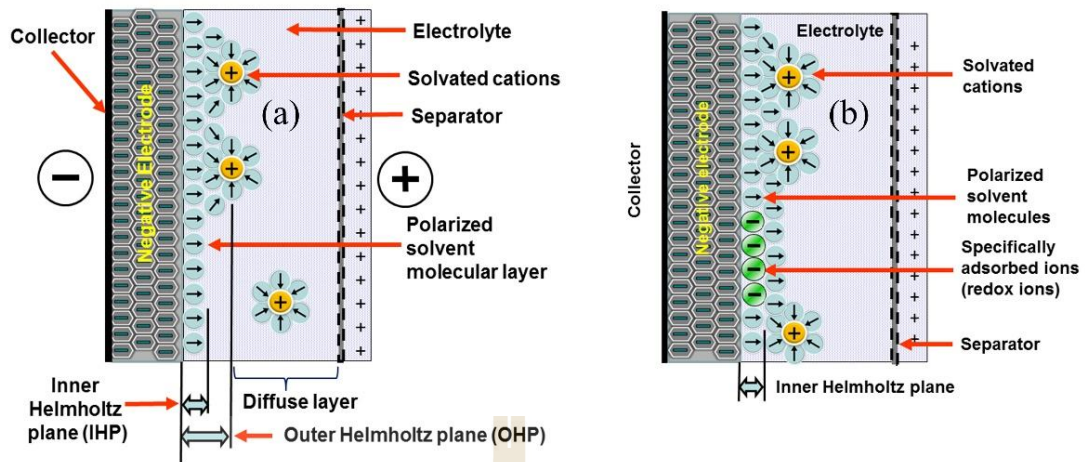


Figure 2.14 The principle charge storage mechanism of (a) EDLC (b) Pseudocapacitor (Adapted from <http://en.wikipedia.org/wiki/Supercapacitor>).

Conventional capacitors consist of two conducting electrodes separated by an insulating dielectric material. When a voltage is applied to a capacitor, opposite charges accumulate on the surfaces of each electrode. The charges are kept separately by the dielectric, thus they produce an electric field that allows the capacitor to store energy. Conventional capacitors store little energy due to the limited charge storage areas and geometric constraints of the separation distance between the two charged plates. The capacitance equation of conventional capacitor is as follows:

$$C = \frac{Q}{V} = \epsilon \frac{A}{d} \quad (7)$$

Where Q , V , ϵ , A , and d are charge (Coulombs), electric potential (Volts), the dielectric constant of dielectric, conductor surface area, and dielectric thickness, respectively. However, supercapacitors based on the EDLCs mechanism can store more energy because of the large interfacial area and the atomic range of charge separation

distances. The EDLCs utilize an electrochemical double-layer of charge to store energy, which store charge electrostatically, or non-Faradaically, and there is no transfer of charge between electrode and electrolyte. As voltage is applied, charge accumulates on the electrode surfaces. Following the natural attraction of unlike charges, ions in the electrolyte solution diffuse across the separator into the pores of the electrode of opposite charge as shown in Figure 2.14(a). The concept of the EDLCs was first described and modeled by von Helmholtz in the 19th century when he investigated the distribution of opposite charge at the interface of colloidal particles (Helmholtz, 1853). The Helmholtz double layer model states two layers of opposite charges formed at the electrode-electrolyte interface separated by an atomic distance. The model is similar to that of two-plate conventional capacitors. This simple Helmholtz EDLCs model was further modified by Gouy (Gouy, 1910) and Chapman (Chapman, 1913) on the consideration of a continuous distribution of the electrolyte ions (both cations and anions) in the electrolyte solution because of thermal motion, which is referred as a diffuse layer. Later, Stern (Stern, 1924) combined the Helmholtz model with the Gouy-Chapman model to explicitly recognize two regions of ion distribution - the inner region called the compact layer or stern layer and the diffuse layer. The inner Helmholtz plane (IHP) and outer Helmholtz plane (OHP) are used to distinguish the two types of adsorbed ions. The capacitance in the EDLCs (C_{dl}) can be treated as the combination of the capacitances from two regions, the differential capacitance of the Helmholtz layer (C_H) and the differential capacitance of the diffusion layer (C_{diff}) (Yu *et al.*, 2013). Thus, the overall double-layer differential capacitance (C_{dl}) can be expressed as

$$\frac{1}{C_{dl}} = \frac{1}{C_H} + \frac{1}{C_{diff}} \quad (8)$$

The maximum energy stored and power delivered for such a single cell supercapacitor is respectively given in equations (9) and (10):

$$E = \frac{1}{2} C_T V^2 \quad (9)$$

$$P = \frac{V^2}{4R_s} \quad (10)$$

where V is the cell voltage (in volts), C_T is the total capacitance of the cell (in farads) and R_s is the equivalent series resistance (ESR) (in ohms) of the electrochemical cell. Carbon electrode materials generally have higher surface area, lower cost, and more established fabrication techniques than other materials, such as conducting polymers and metal oxides (Conway, 1999) (Halper and Ellenbogen, 2006). Different forms of carbon materials that can be used to store charge in EDLC electrodes are activated carbons, carbon aerogels, and carbon nanotubes. Applying a voltage at the electrochemical capacitor terminals moves electrolyte ions to the opposite polarized electrode and forms a double-layer in which a single layer of solvent molecules acts as separator.

The main difference between the pseudo-capacitance and the EDL capacitance lies in that pseudo-capacitance is faradic in origin, involving fast and reversible redox reactions between the electrolyte and some electro-active species on the electrode surface (Conway, 1999). Pseudocapacitors store charge Faradaically through the transfer of charge between electrode and electrolyte as shown in Figure 2.14(b). This is accomplished through electrosorption, reduction-oxidation reactions, and intercalation

processes. The significance of pseudocapacitive materials is largely recognized by an enhanced capacitance relative to EDLC (10-100 times the capacitance), owing to the electron transfer reactions that occur during charging, which contrast the electrostatic process defined by a process where no Faradaic reactions take place. The amount of electric charge stored in a pseudocapacitance is linearly proportional to the applied voltage. The energy is stored via Faradaic process, the redox material particle and /or reaction sites are uniformly distributed in the electrode layer and both the oxidant (O_X) and the reductant (R_d) are insoluble in the electrolyte (Yu *et al.*, 2013), the redox process can be express as



where n is the overall electron transfer number involved in the reaction. The electrons enter the metal and the metal ions diffuse into the electrolyte for the forward reaction. According to the theory of electrochemical thermodynamics, the reversible electrode potential induced by the (11) reaction can be expressed as the Nernst form:

$$E = E_{O_X/R_d}^0 + \frac{RT}{nF} \ln \left(\frac{C_{O_X}}{C_{R_d}} \right) \quad (12)$$

where E_{O_X/R_d}^0 is the standard electrode potential (25 °C, 1.0 atm) of Reaction (11), C_{O_X} and C_{R_d} are the concentrations of O_X and reductant R_d within the entire electrode layer (mol./cm^3), E is the electrode potential (V), R is the universal gas constant ($8.314 \text{ J/K}\cdot\text{mol}$), and T is the temperature (K).

The ability of electrodes to accomplish pseudocapacitance effects by redox reactions, intercalation or electrosorption strongly depends on the chemical affinity of electrode materials to the ions adsorbed on the electrode surface as well as on the structure and dimension of the electrode pores. These Faradaic processes may allow pseudocapacitors to achieve greater capacitances and energy densities than EDLCs. Because of their high conductivity, metal oxides have also been explored as a possible electrode material for pseudocapacitors (Yu *et al.*, 2013). Transition-metal oxides have been known to exhibit high capacitance as shown in Table 2.2. Materials exhibiting redox behavior for use as electrodes in pseudocapacitors are transition-metal oxides (RuO₂, MnO₂, etc.) as well as conducting polymers (ECP) (polyaniline (PANI), polypyrrole (PPy), and poly (3, 4-ethylenedioxythiophene) and their derivatives). A good example of material giving pseudo-capacitive property is ruthenium oxide, which may be able to achieve higher energy and power densities than similar EDLCs and conducting polymer pseudocapacitors due to its intrinsic reversibility of various surface redox couples and high conductivity (Wen and Hu, 1992; Conway, 1999). Although RuO₂ exhibits excellent performances as a pure electrode material but it is unsuitable for widespread commercial use because of the high cost and toxicity of this material. Thus, a major area of research is the development of fabrication methods and composite materials to reduce the cost without reducing the performance. Pseudocapacitors are used as alternative pseudocapacitive materials that are inexpensive and easily synthesized by in situ oxidation or electropolymerization. However, the use of transition metals as electrodes is often limited by their poor conductivity and dense morphology of the oxide and region of electroactivity (Pang *et al.*, 2000). Moreover, these materials

typically suffer poor stability from mechanical stress of swelling and shrinking during doping and de-doping (Du *et al.*, 2009).

For hybrid Capacitors, hybrid capacitors attempt to exploit the relative advantages and mitigate the relative disadvantages of EDLCs and pseudocapacitors to realize better performance characteristics (Yu *et al.*, 2013). Utilizing both Faradaic and non-Faradaic processes to store charge, hybrid capacitors have achieved energy and power densities greater than EDLCs without the sacrifices in cycling stability and affordability that have limited the success of pseudocapacitors. Research has focused on three different types of hybrid capacitors, distinguished by their electrode configuration: composite, asymmetric, and battery-type respectively. The two most studied rechargeable, faradaic electrode components for hybrid capacitor applications are $\text{PbO}_2/\text{PbSO}_4$ and $\text{NiOOH}/\text{Ni}(\text{OH})_2$. The negative electrodes in these hybrid capacitors were fabricated using different carbon materials such as activated carbon, carbon nano-fibers and activated carbon cloth (Beliakov, 2002).

Table 2.2 Summary of the various metal oxide electrodes.

Electrode materials	Electrolytes	Specific capacitance (F/g)	References
RuO ₂ ·H ₂ O	0.5 M H ₂ SO ₄	650	(Kim and Kim, 2006)
RuO _x ·H ₂ O	0.1 M NaOH	1580	(Hu and Chen, 2004)
MnO ₂	0.5 M K ₂ SO ₄	261	(Yang <i>et al.</i> , 2007)
MnO ₂	0.1 M H ₂ SO ₄	678	(Pang <i>et al.</i> , 2000)
MnO ₂ /AC	0.65 M K ₂ SO ₄	29	(Brousse <i>et al.</i> , 2004)
Fe ₃ O ₄	1M Mn ₂ SO ₃	170	(Wang <i>et al.</i> , 2006)
SnO ₂	0.1 M Na ₂ SO ₄	285	(Prasad and Miura, 2004)
BiFeO ₃ thin film	1M NaOH	81	(Lokhande <i>et al.</i> , 2007)
BFO nanorods	1M Na ₂ SO ₄	450	(Rana <i>et al.</i> , 2014)
Bi ₂ O ₃	1 M NaOH	98	(Gujar <i>et al.</i> , 2006)
Bi ₂ WO ₆	1 M KOH	608	(Nithya <i>et al.</i> , 2013)
V ₂ O ₅	2 M KCl	350	(Lee and Goodenough, 1999)
In ₂ O ₃	0.1 M Na ₂ SO ₃	190	(Prasad <i>et al.</i> , 2004)
NiO	1 M KOH	138	(Zhao <i>et al.</i> , 2007)
NiO	1 M KOH	278	(Nam <i>et al.</i> , 2002)
Co ₃ O ₄	6.0M KOH	746	(Gao <i>et al.</i> , 2010)

2.4.2.2 Electrochemical cell configuration

In the electrochemical measurement, both of two-electrode and three electrode configurations were performed. Three-electrode system consists of a working electrode (WE), a counter electrode (CE), and a reference electrode (RE). WE is the electrode on which the reaction of interest is occurring. The potential is varied linearly with time. RE is the electrode which potential maintains a constant (non-polarizable). The connection with this electrode is due to a potential of a single electrode that cannot be measured directly. CE is an electrode used to close the current circuit in the electrochemical cell. In the configuration system, the current flows through WE and CE, while the voltage is measured between the WE and RE. Electrolyte is a solution that contains ions and act as charge carriers. This solution provides ions to the electrodes during oxidation and reduction. In the electrochemical cell, the ability to store charge depends on the accessibility of the ions to the surface-area, so ion size and pore size must be optimal. The energy density of cell can be limited by the electrolyte due to the cell voltage, and is strongly dependent on the electrolyte breakdown voltage, while the power density depends upon the cell's internal resistance (ESR) that is strongly dependent on electrolyte conductivity. There are two types of electrolyte used in ECs: organic and aqueous. Aqueous solution provides higher capacitance and power compared to the organic electrolytes due to their higher ionic concentration, better conductivity (up to 1 S/cm) and smaller ionic size. However, the drawback of aqueous electrolyte is low breakdown voltage (~1.23 V determined by the electrochemical breakdown of water) (Bockris and Reddy, 1970). Most of commercial ECs recently have preferred to use organic electrolytes that provide large window voltages in the range of 2.5-2.7 V, and thus enhance the energy density. However, the drawback of

organic electrolyte is greater resistance and this limits the cell power density. Electrolytes often used are listed in Table 2.3. In the study of electrochemical behaviour of the Bi_2WO_6 nanoparticles (Nithya *et al.*, 2013) investigated in various aqueous electrolytes, the redox behaviour and CV integrated current area of Bi_2WO_6 are high in KOH electrolyte compared with the LiOH and NaOH electrolyte. The current response in various electrolytes decreases in the order of 6 M KOH > 1 M KOH > 1 M NaOH > 1 M Na_2SO_4 . The improving for KOH due to its smaller hydration sphere radius, high ionic mobility and lower equivalent series resistance that leads to a higher capacitance (Nithya *et al.*, 2013). Moreover, the reported conductivity of K^+ ($73 \text{ cm}^2/\Omega \text{ mol}$) ions is greater than Na^+ ions ($50 \text{ cm}^2/\Omega \text{ mol}$) and Li^+ ions ($38 \text{ cm}^2/\Omega \text{ mol}$) at 25°C (Qu *et al.*, 2009). Therefore, 6 M KOH used as electrolyte for the electrochemical measurement in this work.

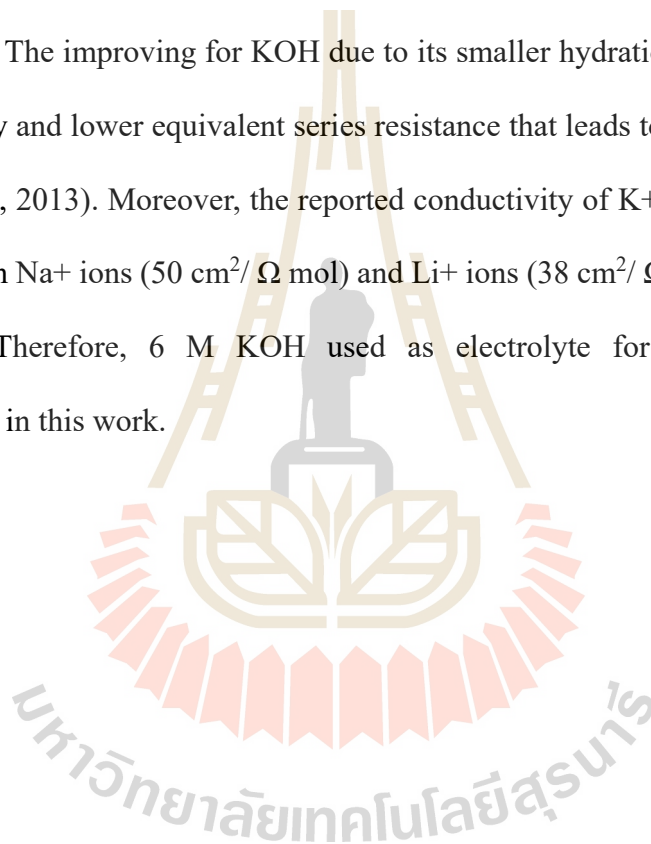


Table 2.3 Electrolytes that are used often (Inagaki, Konno *et al.* 2010).

Electrolytes	Ion size (nm)		Electrolytes	Ion size (nm)	
	Cation	Anion		Cation	Anion
Organic electrolytes			Inorganic electrolytes		
(C ₂ H ₅) ₄ N·BF ₄ (TEA ⁺ BF ₄ ⁻)	0.686	0.458	H ₂ SO ₄		0.533
(C ₂ H ₅) ₃ (CH ₃)N·BF ₄ (TEMA ⁺ BF ₄ ⁻)	0.654	0.458	KOH	0.26	0.533
(C ₂ H ₅) ₄ P·BF ₄ (TEP ⁺ BF ₄ ⁻)		0.458	Na ₂ SO ₄	0.36	
(C ₄ H ₉) ₄ N·BF ₄ (TBA ⁺ BF ₄ ⁻)	0.830	0.458	NaCl	0.36	0.508
(C ₆ H ₁₃) ₄ N·BF ₄ (THA ⁺ BF ₄ ⁻)	0.960	0.458	Li·PF ₆	0.152	0.474
(C ₂ H ₅) ₄ N·CF ₃ SO ₃	0.686	0.540	Li·ClO ₄	0.152	

Note: a is stokes diameter of hydrated ions, b is the diameter in PC, depending strongly on the solvent used.

CHAPTER III

EXPERIMENTAL PROCEDURE

Chapter III describes the experimental method of the research, which can be generally categorized into the following four main sections:

- (1) Sample preparation techniques: synthesis of $\text{BiFe}_{1-x}\text{M}_x\text{O}_3$ ($\text{M} = \text{Co}, \text{Ni}, \text{Cu}$) nanoparticles by simple solution method and fabrication of the $\text{BiFe}_{1-x}\text{M}_x\text{O}_3$ ($\text{M} = \text{Co}, \text{Ni}, \text{Cu}$) nanoparticle electrodes.
- (2) Material characterizations: X-ray diffraction (XRD), Scanning electron microscopy (SEM), Transmission electron microscopy (TEM), High-resolution transmission electron microscopy (HRTEM), X-ray absorption near edge structure (XANES) and Gas absorption technique.
- (3) Magnetic measurements: Vibrating sample magnetometer (VSM).
- (4) Electrochemical measurements: Cyclic voltammetry (CV), Galvanostatic charge-discharge (GCD) and Electrochemical impedance spectroscopy (EIS).

This chapter will give a brief introduction of these techniques and facilities, and the background theories of these method will also start one by one.

3.1 Sample preparation

3.1.1 Synthesis of $\text{BiFe}_{1-x}\text{M}_x\text{O}_3$ (M = Co, Ni, Cu) nanoparticles

In this study, $\text{BiFe}_{1-x}\text{M}_x\text{O}_3$ (M = Co, Ni, Cu) nanoparticles were synthesized by a simple solution method. In the first step, the precursor solution was prepared by dissolving 15 mmol each of Bismuth (III) nitrate pentahydrate [$\text{Bi}(\text{NO}_3)_3 \cdot 5\text{H}_2\text{O}$, 99.9%, Kento], iron (III) nitrate enneahydrate [$\text{Fe}(\text{NO}_3)_3 \cdot 9\text{H}_2\text{O}$, 99.9%, Kento] in ethylene glycol solution for 2 h. Then the metal sources i.e. Copper (II) nitrate hydrate [$\text{Cu}(\text{NO}_3)_2 \cdot x\text{H}_2\text{O}$, 99.99%, Sigma-aldrich], Nickel (II) nitrate hexahydrate [$\text{Ni}(\text{NO}_3)_2 \cdot 6\text{H}_2\text{O}$, 99.9%, Kento] and Cobalt (II) nitrate hexahydrate [$\text{Co}(\text{NO}_3)_2 \cdot 6\text{H}_2\text{O}$, 99.9%, Kento] were added to the solution. In each doping material system, four samples with different doping concentration of metal sources were introduced with molar concentration of 5, 10, 20, and 30 mol %. After that, the solution was mixed together under magnetic stirring for 3 h in order to obtain a homogeneous solution and then dried at 80 °C on a hotplate with stirring for 3 days. To achieve phase homogeneity, the dried powders were calcined in air at 600 °C for 3 h at a heating rate of 10 °C/min. Finally, the calcined powders were leached in 20 % diluted HNO_3 and deionized water seven to ten times and dried in an oven at 70 °C for 2 days. The materials used in this research are shown in Table 3.1.

Table 3.1 List of materials used as starting materials for $\text{BiFe}_{1-x}\text{M}_x\text{O}_3$ ($\text{M} = \text{Co}, \text{Ni}$ and Cu) nanoparticles preparation, quoting their source and purity.

Materials	Source	Purity
Bismuth(III) nitrate pentahydrate ($\text{Bi}(\text{NO}_3)_3 \cdot 5\text{H}_2\text{O}$)	Kento	99.9%
Iron(III) nitrate enneahydrate ($\text{Fe}(\text{NO}_3)_3 \cdot 9\text{H}_2\text{O}$)	Kento	99.9%
Copper(II) nitrate hydrate ($\text{Cu}(\text{NO}_3)_2 \cdot x\text{H}_2\text{O}$)	Sigma-aldrich	99.99%
Ni(II) nitrate hexahydrate ($\text{Ni}(\text{NO}_3)_2 \cdot 6\text{H}_2\text{O}$)	Kento	99.9%
Co(II) nitrate hexahydrate ($\text{Co}(\text{NO}_3)_2 \cdot 6\text{H}_2\text{O}$)	Kento	99.9%
Ethylene glycol	Carlo erba reagents	

3.1.2 Fabrication of the $\text{BiFe}_{1-x}\text{M}_x\text{O}_3$ ($\text{M} = \text{Co}, \text{Ni}, \text{Cu}$) nanoparticle electrodes

The working electrodes were prepared by mixing the $\text{BiFe}_{1-x}\text{M}_x\text{O}_3$ ($\text{M} = \text{Co}, \text{Ni}$ and Cu) nanoparticles, acetylene black as conductive carbon and a polyvinylidene difluoride (PVDF) as binders (weight ratio of 80:10:10) using n-methyl-2 pyrrolidone (NMP) as a solvent to form a slurry. The slurry was coated on to a nickel foam current collector. Then, the electrode was dried at 70°C in a vacuum oven for 12 h and pressed at 20 MPa, respectively. Each working electrode contained about 3 mg of electroactive material and the area of coating was about 1 cm^2 . The electrochemical measurement was employed to explore the electrodes for electrochemical supercapacitor application in 6 M KOH aqueous electrolyte. The process of the electrode fabrication and the electrochemical measurement is presented as follows:

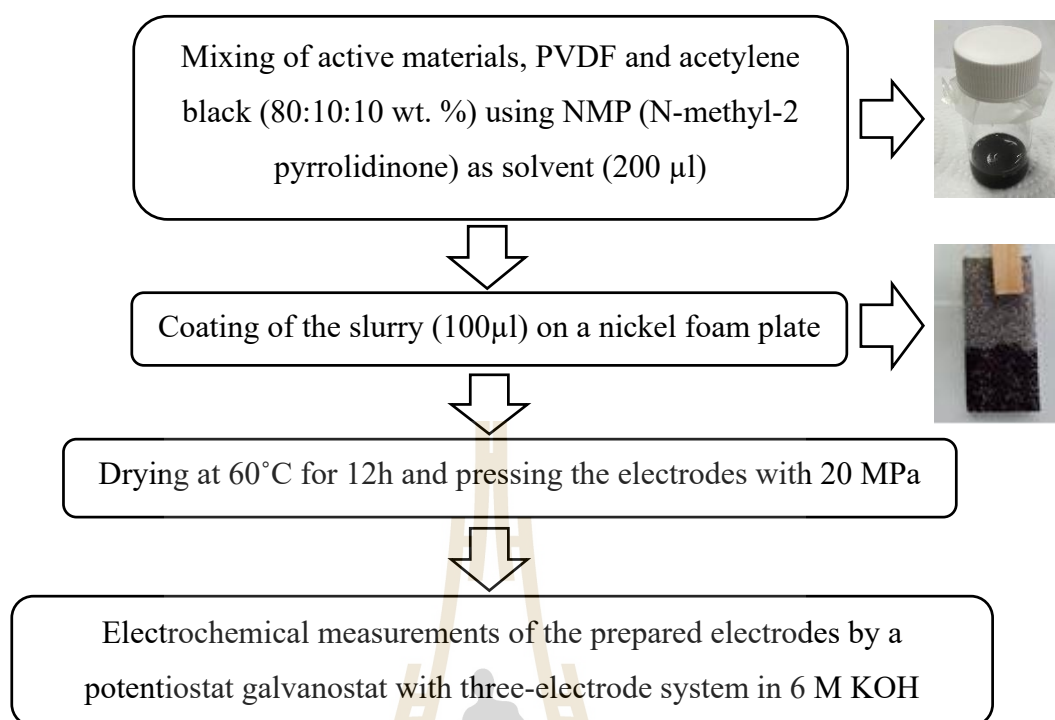


Figure 3.1 Schematic diagram of fabrication of the electrode and measuring electrochemical parameters.

The flowchart diagram showing the overview of the experimental procedure performed in this work is illustrated in Figure 3.2

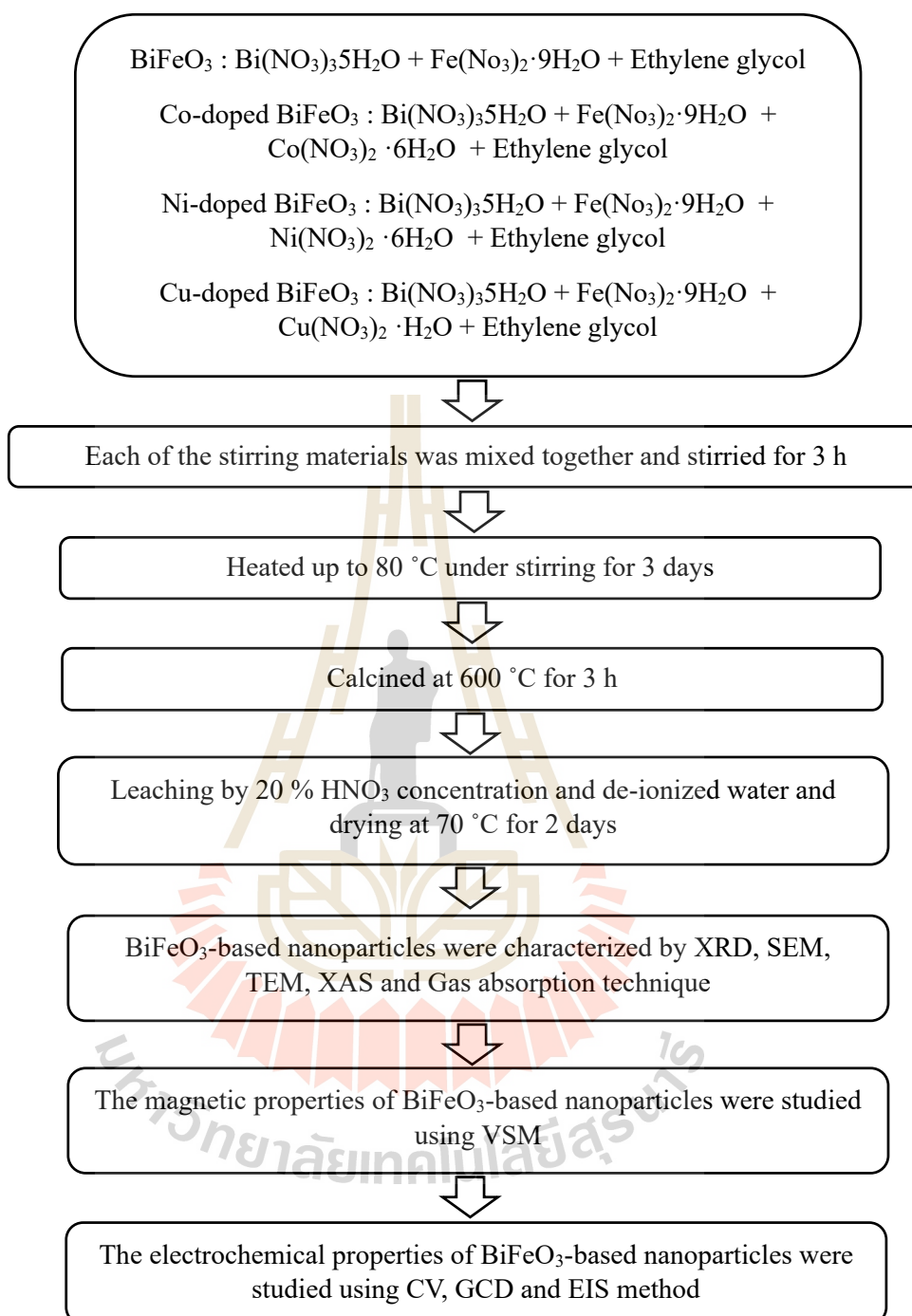


Figure 3.2 Diagram showing preparation and characterization of BiFe_{1-x}M_xO₃ (M = Co, Ni, and Cu) nanoparticles.

3.2 Material characterization

In this research, the phase composition and microstructure of the $\text{BiFe}_{1-x}\text{M}_x\text{O}_3$ ($\text{M} = \text{Co}, \text{Ni}, \text{Cu}$) nanoparticles were characterized by XRD, SEM and TEM techniques. The surface area and pore size distribution of the nanoparticles was investigated by Gas absorption techniques. The valence state of all samples were characterized by using XANES. Magnetic properties are evaluated by VSM and electrochemical properties are studied on a potentiostat galvanostat (PGSTAT302N) via CV, GCD and EIS techniques. The several characterization techniques were used and brief concepts are given as follows:

3.2.1 X-ray diffraction (XRD)

X-ray diffraction (XRD) is the most effective methods originally used for determining the crystal structure of materials (Leng, 2009). Diffraction methods can identify chemical compounds from their crystalline structure, not from their compositions of chemical elements. Traditionally, the XRD instrument is called an X-ray diffractometer. The basic function of a diffractometer is to detect X-ray diffraction from materials and to record the diffraction intensity as a function of the diffraction angle (2θ). X-ray beams incident on a crystalline solid will be diffracted by the crystallographic planes as illustrated in Figure 3.3. The constructive and destructive interferences occur if a phase difference is $n\lambda$ (in phase) and $n\lambda/2$ (out of phase). Two in-phase incident waves, beam 1 and beam 2, are deflected by two crystal planes (A and B). The deflected waves will not be in phase except when the following relationship (Bragg equation) is satisfied.

$$2d\sin\theta = n\lambda \quad (3.1)$$

Where d is the spacing between the parallel crystal planes, θ is the angle of incident beam, λ is the wavelength of the incident X-ray beam and n is an integer. In order to keep these beams in phase, their path difference ($SQ + QT = 2d \sin \theta$) has to equal one or multiple X-ray wavelengths ($n\lambda$). The diffractometer records changes of diffraction intensity with 2θ . A number of intensity peaks located at different 2θ provide a ‘fingerprint’ for a crystalline solid. Identification of crystalline substance and crystalline phases in a specimen is achieved by comparing the specimen diffraction spectrum with spectra of known crystalline substances.

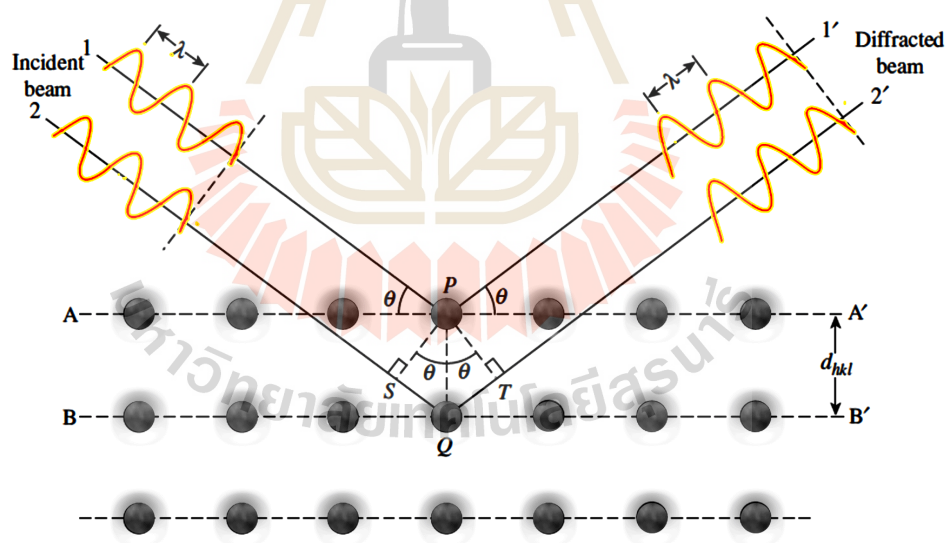


Figure 3.3 Bragg diffraction by crystal planes (Adapted from (Leng, 2009)).

In this thesis, the phase and structure analysis of the synthesized nanoparticles was carried out by X-ray diffraction (XRD; D2 Advance Bruker) with Cu K_{α} at $\lambda = 0.15406$ nm as shown in Figure 3.4. The XRD pattern were recorded in the 2θ of 15° -

80° with the time step of 0.5 and the step size of 0.02. The crystalline phase identification was carried out by comparison with the Joint Committee on Powder Diffraction Standards (JCPDS) diffraction files. The Rietveld refinement technique with TOPAS software was used to investigate the crystal structure. The crystallite size of the nanocrystalline samples was measured from the line broadening analysis of the diffraction peak at an angle 2-theta of 22.39° by using the Debye-Scherer equation (Patterson, 1939):

$$D = \frac{k\lambda}{\beta \cos\theta} \quad (3.2)$$

where D is the crystallite size (nm), k is the spherical shape factor (0.9), λ is the X-ray wavelength, θ is the diffraction angle, and β is the full width at half maximum (FWHM) intensity.



Figure 3.4 X-ray diffractometer (XRD; Bruker D2, Germany, SUT).

3.2.2 Scanning electron microscopy (SEM)

Scanning electron microscopy (SEM) is a technique used to examine microscopic structure by scanning the surface of materials (Leng, 2009). The SEM technique utilizes electron beams to scan the surface of a sample specimen (Ni, 2013), as shown in Figure 3.5. The specimen is irradiated by a focused electron beam and the signals create useful images describing the surface morphology of the specimen. The SEM operates under a vacuum, and electrons produced by a field emission source are accelerated in a field gradient. The beam passes through electromagnetic lenses, focusing onto the specimen. As a result of this bombardment different types of electrons are emitted from the specimen. These signal electrons emitted from the specimen are collected by a detector and amplified. The most common signals used for imaging are secondary electrons, backscattered electrons, and characteristic X-rays. In normal conditions, the secondary electrons created from inelastic surface scattering can reach the detector in greater numbers, depending on incidence angle, and generate topographic information. A detector catches the secondary electrons and an image of the sample surface is constructed by comparing the intensity of these secondary electrons to the scanning primary electron beam. Finally the image is displayed on a screen. Samples must be electronically conductive to prevent charging effects that can blur image quality at higher resolutions. To avoid this, some insulating samples are gold sputtered to provide a nanometer-thick conductive surface layer. In the study of supercapacitors, SEM can provide important information about the material surface morphologies for investigations of physical modifications or treatments effects on material phases and morphologies (Yu *et al.*, 2013) (Frackowiak, 2007). In this work, the morphologies of

samples were obtained using scanning electron microscope (SEM, JSM-7800F), as shown in Figure 3.6.

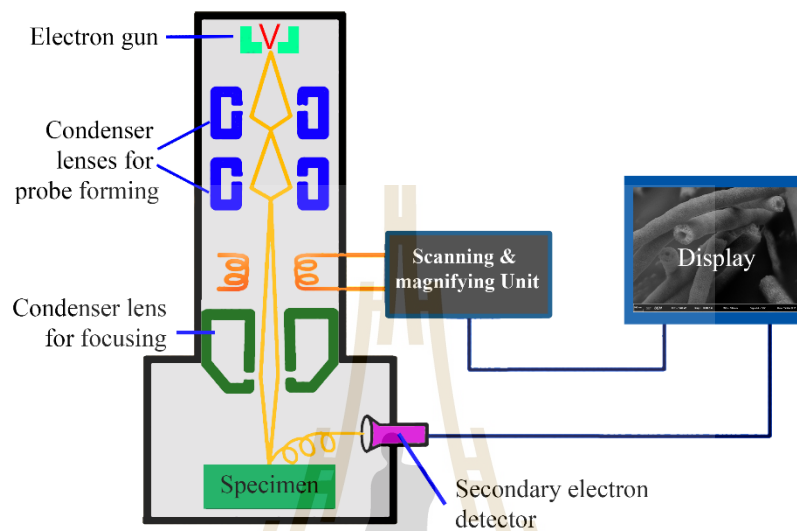


Figure 3.5 Diagram of major components of SEM (Adapted from (Ni, 2013)).



Figure 3.6 Scanning electron microscope (SEM, JSM-7800F, SUT).

3.2.3 Transmission electron microscopy (TEM)

Transmission electron microscopy (TEM) is an electron microscopy technique used to examine observed morphology, particle size distribution and phase composition (Williams and Carter, 1996). Similar to SEM, TEM also utilizes a highly focused electron beam. However, TEM imaging requires a very thin specimen to achieve good image quality. This means that sample preparation is extremely important. A sample layer must be thin enough to allow electrons to pass through. An electron gun emits high energy beams that can penetrate several microns into a solid. The electrons can penetrate through a thin specimen. An image is formed from the interaction of the electrons transmitted through the specimen; the image is magnified and focused onto an imaging device, such as a fluorescent screen, on a layer of photographic film, or to be detected by a sensor such as a CCD camera.

In this work, all prepared samples was dispersed in ethanol and then dripped and dried on a copper grid and then measured under a 200 keV by using FEI TEM (TECNAI G²20, FEI, USA), as shown in Figure 3.7. The Bright field TEM images, high-resolution (HRTEM) TEM images and corresponding selected areas of electron diffraction (SAED) patterns of the samples were also recorded in this work.



Figure 3.7 Transmission Electron Microscopes (FEI TEM, TECNAI G220, SUT).

3.2.4 X-ray absorption near-edge spectroscopy (XANES)

X-ray Absorption Spectroscopy (XAS) is a powerful technique for the structural study of material. This technique based on the measurement of transitions from core electronic states of the metal to the excited electronic states and the continuum (Yano and Yachandra, 2009). The XAS can be divided into 2 regions consist of X-ray absorption near-edge structure (XANES) and extended X-ray absorption fine structure (EXAFS) which studies the fine structure in the absorption at energies greater than the threshold for electron release. These two methods give complementary structural information, the XANES spectra report the electronic structure and the symmetry of the metal site, and the EXAFS reports numbers, types, and distances to ligands and neighboring atoms from the absorbing element. The sudden increases in absorption are called absorption edges, and correspond to the energy required to eject a core electron into the excited

electronic states. XAS measures the energy dependence of the X-ray absorption coefficient $\mu(E)$ at and above the absorption edge of a selected element. The $\mu(E)$ can be measured two ways. First way is transmission mode, which is the simplest type of XAS measurement. In a transmission experiment, the intensity of the X-ray beam is measured before and after a sample and the absorption coefficient $\mu(E)$ calculated using the equation 3.3. The intensity of the X-ray beam is typically measured using ionisation detectors. Second way is Fluorescence mode. In a fluorescence experiment, the absorbance of the sample is measured by monitoring the intensity of the X-ray fluorescence produced when higher-shell electrons relax into the hole left by the photoelectron. The $\mu(E)$ is calculated using the equation 3.4 (Lee *et al.*, 1981).

$$\mu(E)x = -\ln(I/I_0) \quad (3.3)$$

$$\mu(E) = C(F/I_0) \quad (3.4)$$

where I_0 is the X-ray intensity hitting, I is the intensity transmitted, $\mu(E)$ is absorption coefficient, and x is the thickness of the sample, F is the intensity of the fluorescence X-rays, C is approximately constant. An x-ray is absorbed by an atom when the energy of the X-ray is transferred to a core-level electron (K, L, or M shell) which is ejected from the atom. The absorption discontinuity is known as the K-edge, when the photoelectron originates from a 1s core level, and an L-edge when the ionization is from a 2s or 2p electron. X-ray absorption near-edge structure (XANES) spectra provide detailed information about the oxidation state and coordination environment of the metal atoms. The K-edge absorption edge energy increases with

increasing oxidation state. In general, the rising edge position shifts when the effective number of positive charges.

In this work, to characterize the oxidation state of Co, Ni, Cu and Fe, X-ray absorption near edge spectra (XANES) of Co, Ni, and Cu *K*-edge spectra were collected in the fluorescence and Fe *K*-edge spectra were collected in the transmission modes at the SUT-NANOTEC-SLRI XAS Beamline (BL 5.2) (electron energy, 1.2 GeV; bending magnet; beam current, 80-150 mA; $(1.1-1.7) \times 10^{11}$ photon/s) at the Synchrotron Light Research Institute (SLRI), Nakhon Ratchasima, Thailand. Finally, the normalized XANES data were processed and analyzed using ATHENA software which included an IFEFFIT package (Newville, 2001; Ravel and Newville, 2005).

3.2.5 Gas adsorption techniques

In N₂ adsorption analysis, a sample is exposed to N₂ gas of different pressures at a given temperature (usually at -196 °C, the liquid-nitrogen temperature). Increment of pressure results in increased amount of N₂ molecules adsorbed on the surface of the sample. The pressure at which adsorption equilibrium is established is measured and the universal gas law is applied to determine the quantity of N₂ gas adsorbed. Thus, an adsorption isotherm is obtained. If the pressure is systematically decreased to induce desorption of the adsorbed N₂ molecules, a desorption isotherm is obtained. Analysis of the adsorption and desorption isotherms in combination with some physical models yields information about the pore structure of the sample such as surface area, pore volume, pore size and surface nature. The adsorption isotherm can have different shape which is based on the adsorbent, adsorbate and the adsorbent adsorbate interaction. According to IUPAC adsorption isotherm is classified into six types.

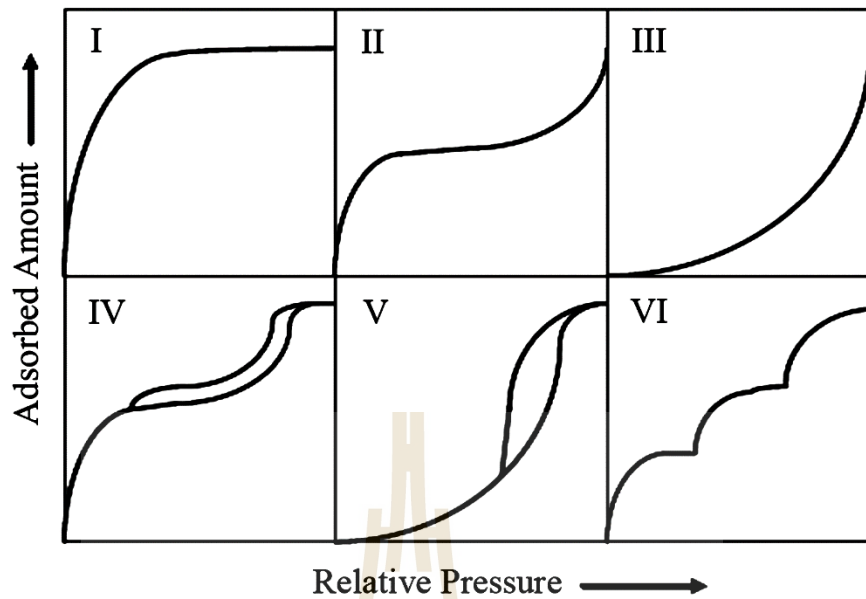


Figure 3.8 The IUPAC classification of adsorption isotherms (Adapted from Donohue and Aranovich, 1998).

Generally, pores in materials are classified into three groups according to pore size distributions namely, micropores (pore size < 2 nm), mesopores (2-50 nm), and macropores (> 50 nm). Type I is the typical isotherm of micro-porous (< 2 nm) materials having relatively small external surface area. Type II or anti s-shaped adsorption isotherm is the normal forms for macroporous (> 50 nm) and non porous adsorbents. Type III is characteristic of non-porous with low adsorbate-adsorbent interaction. A hysteresis loop feature in type IV related to the capillary condensation of the adsorbate in the mesopores (2-50 nm) materials. Type V isotherm is related to weak adsorbateadsorbent interaction at low P/P_0 , while the number of pore in the system is limited at middle and high relative pressure. Finally, type VI isotherm is characteristic of nonporous adsorbents with homogeneous surface.

The Brunauer Emmett Teller (BET) is a characterization technique to observe the specific surface area of materials. The principle measurement of the BET method is based on the physical adsorption of gas on the surface of sample and by calculating the amount of adsorbate gas corresponding to a monomolecular layer on the surface (Brunauer *et al.*, 1938). For BET method, the phenomenon of adsorption can be expressed with the following equation.

$$\frac{1}{W\left[\left(\frac{P_0}{P}\right)-1\right]} = \frac{1}{W_m C} + \frac{C-1}{W_m C} \left(\frac{P}{P_0}\right) \quad (3.5)$$

where W is the volume of gas adsorbed at standard temperature and STP pressure (273.15 K and 1.103×10^5 Pa) (ml). W_m is the volume of gas adsorbed at STP to produce an apparent monolayer on the sample surface (ml). P_0 is saturated pressure of adsorbate gas (Pa). P is partial vapour pressure of adsorbate gas in equilibrium with the surface at 77.4 K. C is dimensionless constant. By decreasing in relative pressure, desorption nitrogen was observed. The specific surface area can be calculated by

$$a_{\text{BET}} = \frac{W_m \sigma N_A}{m V_0} \quad (3.6)$$

where W_m arise from the slop and the intercept of plot between the relative pressure and $1/W[(P/P_0) - 1]$, σ is the area of the surface occupied by individual gas molecules, N_A is the Avogadro number, m is the sample mass and V_0 is the molar volume of gas ($22414 \text{ cm}^3/\text{molar}$ at atmospheric pressure).

The Barrett-Joyner-Halenda (BJH) method is a procedure for calculating pore size distributions from experimental isotherms using the Kelvin model of pore filling. It applies only to the mesopore and small macropore size range (Barrett *et al.*, 1951). For the adsorption isotherm depending on the shape of mesopore, Kelvin equation represents the relationship between mesopore size and critical condensation pressure. The Kelvin equation is used to calculate pore size distribution from desorption isotherm. Core radius (r) can be calculated by the Kelvin equation as follows:

$$\ln \frac{P}{P_0} = - \frac{2\gamma V_L}{RT r} \quad (3.7)$$

where γ is surface tension, V_L is molar volume of liquid adsorptive, R is gas constant and T is absolute temperature. If γ and V_L of nitrogen at liquid nitrogen temperature (77 K) are applied, the following equation can be obtained.

$$r = 0.953 / \ln (P_0 / P) \quad (3.8)$$

In this work, the specific surface area (S_p) and porosity of the nanoparticles were measured by using the N_2 adsorption technique. Using computer interfaced BEL SORP-miniII instruments, all samples were thoroughly degassed at 80 °C for 18 h. Specific surface area was calculated by using the BET method. The pore size distributions were obtained from the analysis of the adsorption branch of the isotherm by the BJH method.

3.2.6 Magnetic measurements

Vibrating sample magnetometer (VSM) is the instrument that measures the magnetic behavior of magnetic materials (Foner, 1959; Kirupakar and Vishwanath,

2016). The vibrating sample magnetometer operates on the principle that when a sample material is placed in a uniform magnetic field as shown in Figure 3.9. If the sample is magnetic, this constant magnetic field will magnetize the sample by aligning the magnetic domains, or the individual magnetic spins, with the field. As the sample is moved up and down. The magnetic field around the sample (magnetic stray field) is changing as a function of time and can be sensed by a set of pick-up coils. The alternating magnetic field will cause an electric current in the pick-up coils according to Faraday's Law of induction, which informs that a changing magnetic field will produce an electric field. This current will be proportional to the magnetization of the sample. The greater the magnetization, the greater the induced current. The induction current is amplified by a transimpedance amplifier and lock-in amplifier. The various components are hooked up to a computer interface. Using controlling and monitoring software, the system can tell us how much the sample is magnetized and how its magnetization depends on the strength of the constant magnetic field. The output is a hysteresis curve, which shows the relationship between the induced magnetic flux density and the magnetizing force and gives important information about the magnetic saturation, the remanence, the coercivity and the level of residual magnetism left in the material.

In this work, the magnetic measurements were performed using the vibrating sample magnetometer (VSM) option in the Quantum Design Versalab instrument. A powder of sample was weighed and transferred into a small sample holder, and the magnetization were collected in a magnetic field range of ± 30 kOe at various temperatures (50, 100, 150, 200, 250, 300, and 350 K). The parameters like saturation magnetization (M_s), remanent magnetization (M_r) and coercivity field (H_c) were

obtained from the magnetization curve. The zero field-cooled and field-cooled (ZFC-FC) magnetizations were also studied in this work. The ZFC spectra were typically obtained by cooling in zero magnetic fields from a high temperature to a low temperature (350 to 50 K). The magnetization was measured at step wise increasing temperatures in a small field (500 Oe). The FC magnetization curve is obtained by measuring at stepwise decreasing temperatures in the same small applied field at each temperature.

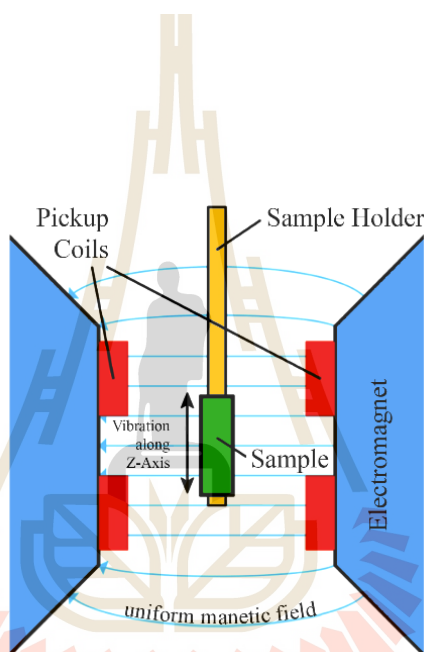


Figure 3.9 Schematic diagram of the vibrating sample magnetometer (VSM) (Adapted from McElfresh, 1994)

3.3 Electrochemical measurements

Electrochemical behaviors of the prepared $\text{BiFe}_{1-x}\text{M}_x\text{O}_3$ ($M = \text{Co}, \text{Ni}$ and Cu) electrodes were studied on a autolab potentiostat galvanostat (PGSTAT 302N). The electrochemical method was used to evaluate the electrochemical performance via cyclic voltammetry (CV), electrochemical impedance spectroscopy (EIS), and galvanostatic charge-discharge (GCD) techniques. To characterize an electrochemical

cell, three-electrode configurations was performed. Figure 3.10 gives a schematic view of a cell connected to an electrochemical workstation. The three-electrode system consists of the active materials, a platinum wire (Pt) and silver/silver chloride (Ag/AgCl) electrodes used as working, counter, and reference electrodes, respectively. Basically, the current flows through the CE and the WE, and the voltage is measured (or controlled) between RE and WE.

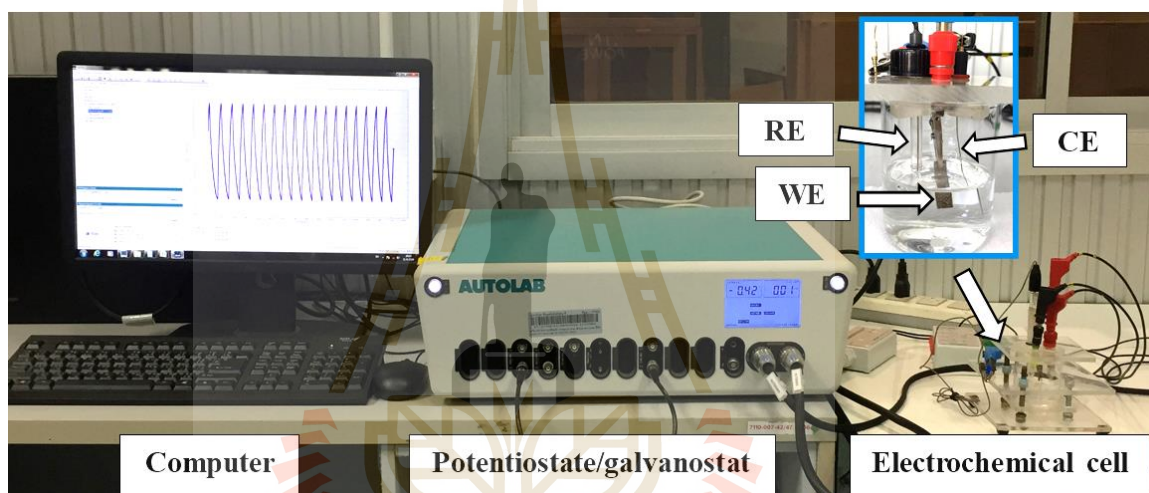


Figure 3.10 Experimental set up of electrochemical measurements consist of personal computer, potentiostat/galvanostat and electrochemical cell.

Nova is the electrochemistry software from Metrohm Autolab. This application is used to control all compatible instruments and accessories as well as to analyze results of the measurements. The view of the Nava software (version 1.10) is shown in Figure 3.11.

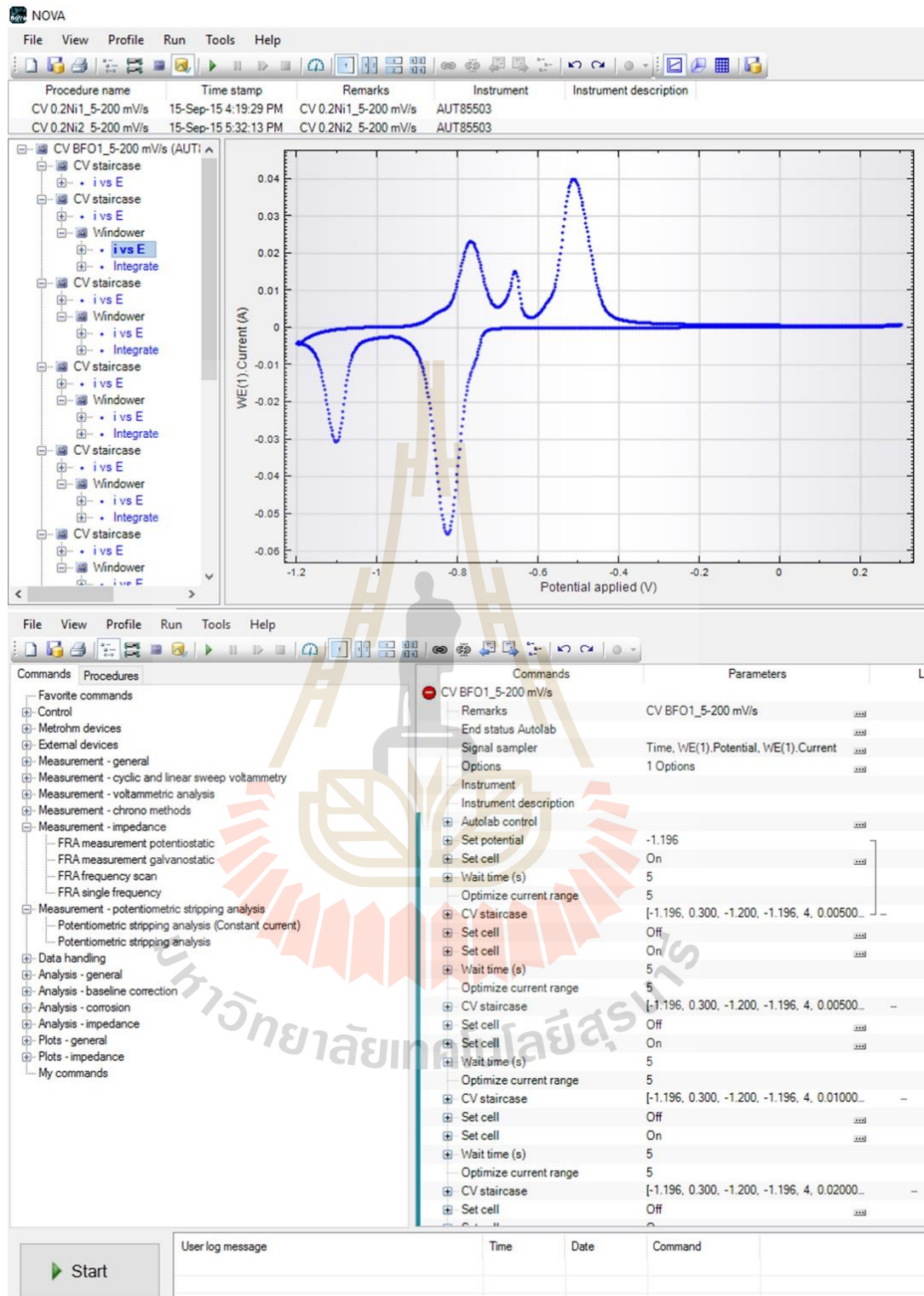


Figure 3.11 View of measurement and set up of the Nova 1.10 software.

3.3.1 Cyclic voltammetry

Cyclic Voltammetry (CV) is a preferred technique for initial screening of materials for electrochemical capacitor applications. The major advantage comes from the ability of this technique to provide detailed information about the capacitance and its voltage dependence, power characteristics, and the reversibility of the electrochemical reaction (Zheng, 2003). The principle of this technique is to apply a linear voltage ramp to an electrode between two voltage limits and to measure the resulting current. During scanning of the electrode potential (difference between working electrode and reference electrode), the current passing between the working electrode and the counter electrode can be recorded. The current passing through the working electrode is then plotted as a function of electrode potential to yield a CV with a typical example plot shown in Figure 3.12. This plot is known as voltammogram, which shows three different schematic voltammograms of ideal capacitor, resistive capacitor, and faradaic capacitor. An ideal capacitor display a rectangular shape due to the capacitance (C) would keep constant at a scan rate. When the resistances present, the rounding of the voltammogram corners was observed. However, most EDLC devices suffer due to internal resistance; hence they display distorted voltammograms with irregular peaks. Prominent peaks that can occur within narrow voltage windows are usually evidence of pseudo-capacitive behavior (Conway *et al.*, 1997). The redox peak will present with the cell that store energy via redox reaction (electron transfer). For sample with different oxidation states, the voltammogram with multiple peaks will be observed.

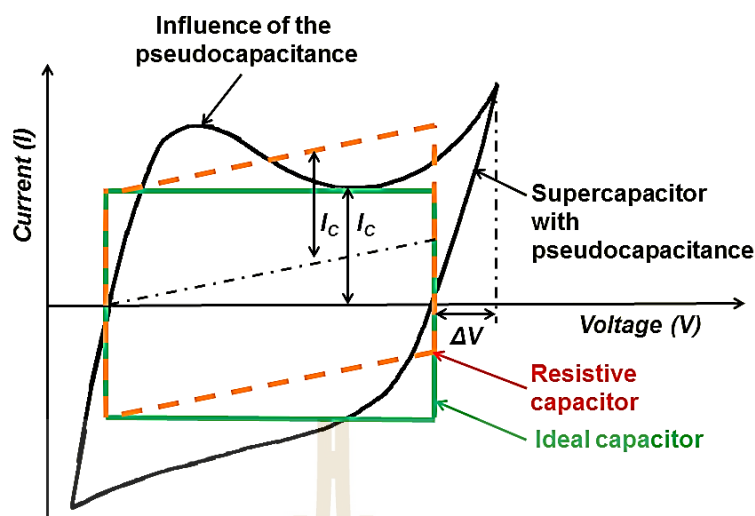


Figure 3.12 Cyclic voltammogram of three different electrochemical capacitors: ideal, resistive, faradaic capacitors (Adapted from <https://en.wikipedia.org/wiki/Pseudocapacitance>).

Reversibility is the important parameter in all electrochemical systems. Cyclic voltammetry can also provide an indication of the degree of reversibility of an electrochemical reaction. By looking at the voltammograms we can see whether the reaction is reversible or not. There are three types of the electron transfer process including reversible, irreversible and quasi-reversible. In a reversible system, the electrode process is defined as electrochemically reversible when the rate of the electron transfer is higher than the rate of the mass transport. The electron transfers with rapidly rate in both forward and reverse scan. The current ratio between the reverse peaks (cathodic peaks, $I_{p,c}$) and the forward peaks (anodic peaks, $I_{p,a}$) is constant and equal to 1.0 and proportional to the concentrations of the active species. The peak current (i_p) at room temperature is given by the Randles-Sevcik equation (Brownson and Banks, 2014; Nithya *et al.*, 2013):

$$i_p^{\text{rev}} = 2.687 \times 10^{-5} n^{3/2} ACD^{1/2} v^{1/2} \quad (3.9)$$

where n , A , C , D , and v are the number of electron transferred/molecule, the electrode surface area (cm^2), the concentration (mol/cm^3), the diffusion coefficient (cm^2/s), and the potential scan rate (V/s), respectively. The anodic ($E_{p,a}$) and cathodic peak potentials ($E_{p,c}$) are independent of the scan rate. The separation between the potentials of the forward and reverse peaks (called peak-to-peak separation), ΔE_p , at room temperature, at all scan rates is equal to

$$\Delta E = E_{p,a} - E_{p,c} = \frac{0.059}{n} V \quad (3.10)$$

In an irreversible process, the electron transfer is lower than that of the mass transport and the rate electron transfer in the reverse scan is very slow. The peak current and the peak potential, respectively are given by

$$i_p^{\text{irrev}} = 0.4958 n F A C D^{1/2} \left(\frac{\alpha n_a F}{RT} \right)^{1/2} v^{1/2} \quad (3.11)$$

$$E_p = E^0 - \frac{RT}{\alpha n_a F} \left[0.78 - \ln \frac{K^0}{D^{1/2}} + \ln \left(\frac{\alpha n_a F v}{RT} \right)^{1/2} \right] \quad (3.12)$$

where α and n_a are the transfer coefficient and the number of electrons involved in the charge transfer step, respectively, F is faradays constant ($96,500 \text{ C}/\text{mol}$), α is transfer coefficient, R is gas constant ($8.3145 \text{ J}/\text{mol K}$) and T is temperature (K). In irreversible process, the cathodic and anodic peak potentials are dependent of the scan

rate. A quasi-reversible process is not uncommon that in electron transfer processes one observes that at low scan rates the process behaves reversibly, whereas at high scan rates the process behaves irreversibly (such behaviour is more easily seen for processes that are not complicated by coupled reactions). Processes occurring in the transition zone between reversible and irreversible behaviour are called quasireversible. A quasireversible process occurs when the rate of the electron transfer is of the same order of magnitude as the mass transport. The voltammograms of a quasi-reversible system exhibit a larger separation in peak potentials compared to a reversible system.

In cyclic voltammetry, the enclosed area of the CV curve can be used to estimate the electrochemical specific capacitance (C_{CV}) using the following equation (Yan *et al.*, 2012):

$$C_{CV} = \frac{1}{vm\Delta V} \int IdV \quad (3.13)$$

where I is the response current density discharge current (A/cm^2), $\int IdV$ is the area of the CV curve, v is the potential scan rate (mV/s), m is the mass of the electroactive materials in the electrodes (g/cm^2), and ΔV is the potential window (V). According to this equation, the specific capacitance of materials decreases with increasing of scan rate due to short time at high scan rate caused large internal resistance and hardly penetrated of electrolyte ions into inner pores during charge (Yuan *et al.*, 2008). Moreover, the variations of specific capacitance value are also depend on the number of active sites that are actively participated in the redox reactions. The number of active sites (N) is given by the relation (Nithya *et al.*, 2013; Ranjusha *et al.*, 2012):

$$N = \frac{C \times M \times \Delta V}{F} \quad (3.14)$$

where C is the specific capacitance (F/g), M is the molecular weight (g/mol), V is the potential window (V), F is the Faraday's constant (96,500 C/mol).

In this work, the cyclic voltammetry measurement was performed at a potential window in the range of -1.2 V to 0.3 V and different scan rates of 5, 10, 20, 40, 60, 80, and 100 mV/s were applied in 6M KOH at room temperature.

3.3.2 Galvanostatic charge-discharge

The charging-discharging (GCD) technique is electrochemical analysis to determine the kinetics and mechanism of electrode reactions. Moreover, this technique is also one of the most reliable approaches to determine specific capacitance, energy density, power density, and cycle life of a supercapacitor (Yu *et al.*, 2013). GCD measurements are performed by applying a constant cell current, during which the cell voltage is recorded as a function of charging or discharging time. In this work, the GCD curves at different current densities of 1, 2, 5, 10, 15, and 20A/g were tested to investigate the capacitance performances of the electrodes. The discharge behavior of the electrode was found to be asymmetrical and non-linear, the specific capacitance was calculated using the following equation (Nithya *et al.*, 2013):

$$C_{GCD} = \frac{2E}{m(\Delta V)^2} \quad (3.15)$$

where C_{GCD} is the specific capacitance (F/g), E is the energy density, m is The total mass of the active material, ΔV is the discharge potential window. The important

performance indicators for evaluating an electrochemical supercapacitor such as specific energy density (W/kg), specific power density (W/kg) were calculated using following equations (Nithya *et al.*, 2013):

$$E = \frac{I \int V(t) dt}{m} \quad (3.16)$$

$$P = \frac{E}{t} \quad (3.17)$$

where $\int V(t)dt$ is the integral area of the discharge curve, I is the current density, M is the active material and t is the discharge time. Moreover, because of long term cycling stability is important for practical applications for supercapacitors. Therefore, endurance of the electrodes was tested up to 500 charge-discharge cycles at a current density of 10 A/g.

3.3.3 Electrochemical impedance spectroscopy (EIS)

Electrochemical impedance spectroscopy (EIS) is an helpful experimental tool to characterize frequency response of a cell electrode for studying the electrochemical reaction occurs at the electrode/electrolyte interface (Bard *et al.*, 1980). The measurement proceeds by applying sinusoidal potential of small amplitude to the cell electrodes and measured the resulting current response to obtain the impedance of the system (Taberna *et al.*, 2006). The apply sinusoidal potential and the responding current ($\Delta I(\omega)$) are given as

$$\Delta I(\omega) = \Delta I e^{j(\omega t + \phi)} \quad (3.18)$$

where I is the current amplitude. $\omega = 2\pi f$ is the angular frequency, and Φ is phase shift between current response and the potential. The electrochemical impedance $Z(\omega)$ is defined as

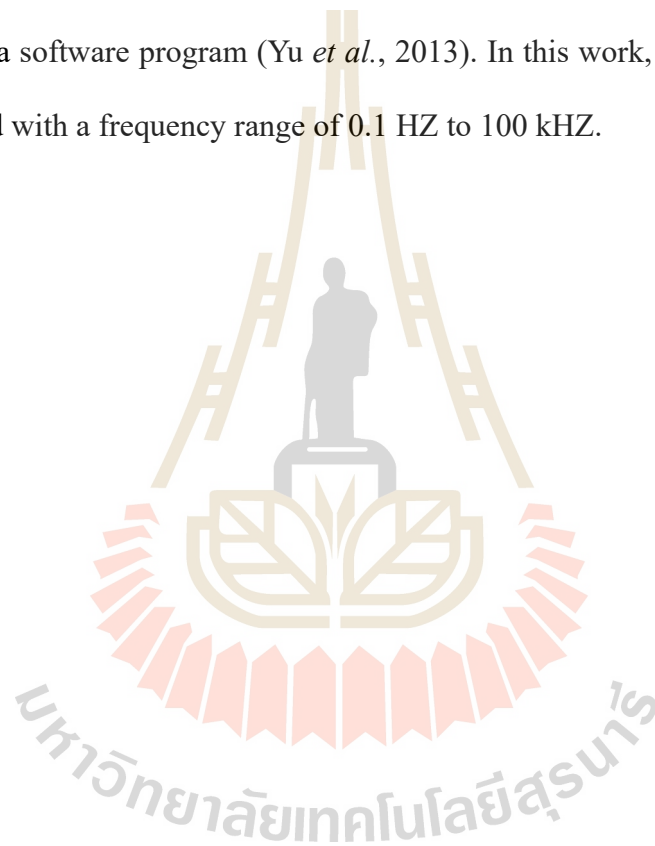
$$Z(\omega) = \frac{\Delta V}{\Delta I} = |Z(\omega)|e^{-j\phi} = Z' + jZ'' \quad (3.19)$$

where Z' and Z'' are the real part and the imaginary part of the impedance, respectively defined as

$$Z'^2 + Z''^2 = |Z(\omega)|^2 \quad (3.20)$$

The impedance responses recorded by the EIS instrument are normally shown as Nyquist plots that illustrate the relationship between imaginary part impedance ($-Z''$) and real part impedance (Z') based on the equivalent circuit having the components of solution resistance (R_s), charge-transfer resistance (R_{ct}), constant phase element (CPE) and Warburg impedance (W). The intercept in the Z' axis at a high frequency refers to R_s which stands for ohmic resistance of the electrolyte, internal resistance of the electrode material and contact resistance at the electrode/current collector interface (Nithya *et al.*, 2013). The semicircle diameter at high frequency region corresponds to charge transfer resistance (R_{ct}) in which caused by faradic reaction. The slope of the linear curve at low frequency is called the Warburg resistance (W) and was used to describe the frequency dependent of ion diffusion into the bulk of the electrode surface. For not ideal cell or cell with lack of surface homogeneity, the constant phase element (CPE or Q) is used. The parameter “ N ” obtained from CPE is used to observed the

quality of the electrode material ($N = 1, 0$ and $0.5 < n < 1$) indicates the ideal capacitors, the insulators, and the moderate capacitor behavior, respectively. To observe these parameters, analysis of EIS data can be used by modeling or fitting of impedance spectra with an equivalent circuit (EC). Depending on the shape of the EIS spectrum, the EC model is usually composed of resistors (R), inductors (L), and capacitors (C) connected in series or in parallel. After an EC is designed, it can be used to fit the EIS spectra with a software program (Yu *et al.*, 2013). In this work, the EIS measurement was collected with a frequency range of 0.1 Hz to 100 kHz.



CHAPTER IV

RESULTS AND DISCUSSION

Chapter IV demonstrates the experimental results and their discussions. It is divided into three different groups of prepared samples: Co-doped BiFeO₃, Ni-doped BiFeO₃ and Cu-doped BiFeO₃ nanoparticles, respectively. For each group of study, the crystal structure and phase composition of the synthesized nanoparticles can be determined by using X-ray diffraction (XRD) results. The morphology of the nanoparticles are investigated by scanning electron microscope (SEM) and transmission electron microscope (TEM). The electronic structure of the nanoparticles was investigated by X-ray absorption spectroscopy (XAS). The specific surface area and pore distribution was evaluated by Brunauer-Emmett-Teller (BET) method and Barrett-Joyner-Halenda (BJH) method, respectively. The results of the magnetic properties at different temperature of measurement are demonstrated. The effects of doping concentrations on structural and magnetic properties is discussed. The influence of particle size on magnetic properties of the nanoparticles is certainly interpreted. The electrochemical behaviors of different electrode materials (Co-doped BiFeO₃, Ni-doped BiFeO₃ and Cu-doped BiFeO₃ nanoparticles) were studied by cyclic voltammetry (CV), galvanostatic charge-discharge, and electrochemical impedance spectroscopy (EIS) method. The effects of doping concentration on the electrochemical properties is also discussed.

4.1 Co-doped BiFeO₃ nanoparticles

4.1.1 Structural and morphology characterization

4.1.1.1 X-ray diffraction (XRD) analysis of the Co-doped BiFeO₃ nanoparticles

Figure 4.1 shows the XRD patterns of the BiFe_{1-x}Co_xO₃ (x = 0, 0.05, 0.1, 0.2, and 0.3) nanoparticles calcined at 600 °C for 3h in air atmosphere. The main diffraction peaks of all the samples at $2\theta = 22.4^\circ, 31.7^\circ, 32.1^\circ, 38.9^\circ, 39.5^\circ, 45.7^\circ, 51.3^\circ, 51.7^\circ, 56.4^\circ, 57.0^\circ, 57.2^\circ, 66.3^\circ, 67.1^\circ, 70.6^\circ, 71.3^\circ, 71.7^\circ, 75.6^\circ, 76.1^\circ$ correspond to the crystallite planes of (012), (104), (110), (006), (202), (024), (116), (122), (018), (214), (300), (208), (220), (313), (036), (312), (128), and (134), respectively for a rhombohedral structure of the main phase BiFeO₃ with the space group R3c (JCPDS No.86-1518). In all the samples small impurity peaks are presented which correspond to the orthorhombic structures of Bi₂Fe₄O₉ (in x = 0.05 and x = 0.1 samples) with the space group Pbam (JCPDS No.72-1832), the cubic structure of CoFe₂O₄ (in x = 0.2 and x = 0.3 samples) with the space group Fd3m (JCPDS No.02-1045) and the cubic structure of Co₃O₄ (in x = 0.2 and x = 0.3 samples) with the space group Fd3m (JCPDS No.80-1537). A shift in the peak position was observed towards the lower angles in the Co-doped samples. These changes confirm the substitution of the Fe site with Co ions and it is evident that the Co ions have been effectively incorporated into the crystal structure of BiFeO₃ (Battisha *et al.*, 2015; Khan *et al.*, 2015; Chakrabarti *et al.*, 2015).

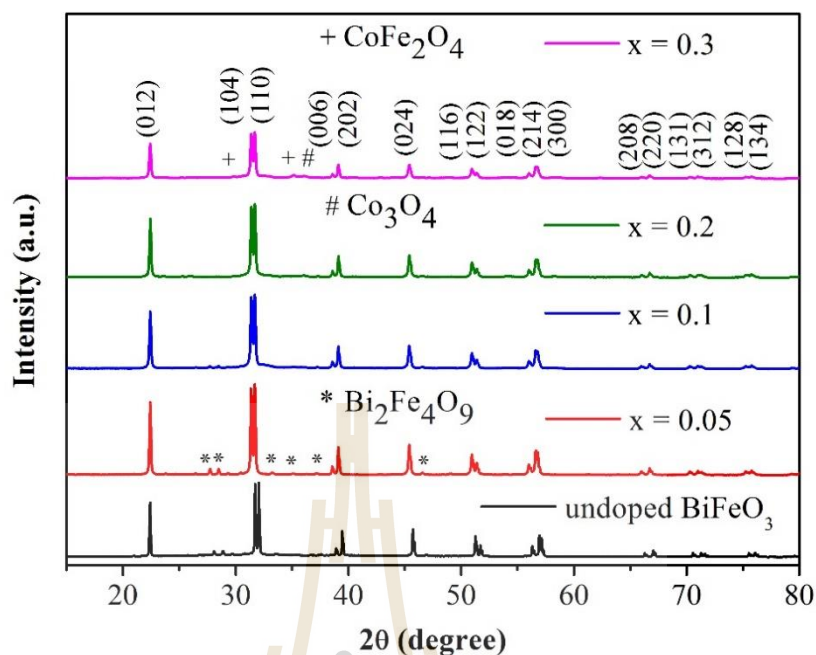


Figure 4.1 XRD patterns of $\text{BiFe}_{1-x}\text{Co}_x\text{O}_3$ ($x = 0, 0.05, 0.1, 0.2, \text{ and } 0.3$) nanoparticles.

The crystallite size of the $\text{BiFe}_{1-x}\text{Co}_x\text{O}_3$ ($x = 0, 0.05, 0.1, 0.2, \text{ and } 0.3$) nanoparticles is calculated by the Scherrer equation using (012) the peak shown in Table 4.1. The variations in the crystallite size of the nanoparticles does not linearly depend on the Co doping concentration. The crystallite sizes of the $\text{BiFe}_{1-x}\text{Co}_x\text{O}_3$ ($x = 0, 0.05, 0.1, 0.2, \text{ and } 0.3$) samples are 88.8, 64.9, 57.8, 58.7, and 54.5 nm, respectively, which decrease with the increases in Co doping concentrations, except for $x = 0.2$ sample with slightly decreasing. Figure 4.2-4.4 shows the Rietveld refinement using TOPAS software used to estimate the crystal structure profiles of the $\text{BiFe}_{1-x}\text{Co}_x\text{O}_3$ with $x = 0, 0.05, 0.1, 0.2, \text{ and } 0.3$ nanoparticles. The lattice parameters (a and c), unit cell volume (V), crystal density (ρ), phase composition (%) of BiFeO_3 , $\text{Bi}_2\text{Fe}_4\text{O}_9$, CoFe_2O_4 and Co_3O_4 , residuals of the weighted pattern (R_{wp}) and pattern (R_p) and goodness of fit (GOF) were calculated as shown in Table 4.1. The reliability of fitting such as R_{wp} , R_p ,

and GOF is confirmed. The R_{wp} , and R_p values of fitting less than 10 % and the GOF values about 2-3 indicating acceptable matched between experimental and theoretical XRD pattern for all samples based on rhombohedral unit cell (R3c) of BiFeO_3 . The lattice parameters a and c , and unit cell volume (V) of Co-doped BiFeO_3 samples are smaller than undoped BiFeO_3 . The a -parameter of undoping sample (5.5793 nm) is higher than Co-doped BiFeO_3 (5.5746-5.5754 nm). Especially, the decrease in c -parameter from 13.8743 nm for $x = 0$ to 13.8532 nm for $x = 0.2$. This reduction may occur due to Co^{3+} (0.54 Å) with a small ionic radius substitutes the Fe^{3+} (0.645 Å), which agree with reports (Chakrabarti *et al.*, 2015; Khan *et al.*, 2015). The quantitative analysis shows that the $\text{Bi}_2\text{Fe}_4\text{O}_9$ phase composition of $\text{BiFe}_{1-x}\text{Co}_x\text{O}_3$ in $x = 0$ to 0.1 samples decreased from 20.9 to 4.2 %, the CoFe_2O_4 phase composition in $x = 0.2$ and 0.3 samples increased from 4.5 to 18.1 %, respectively, and the Co_3O_4 phase composition in $x = 0.2$ and 0.3 samples increased from 8.1 to 14.3 %, respectively. This is the evidence of that the higher Co doping helped to prevent the formation of the $\text{Bi}_2\text{Fe}_4\text{O}_9$ phase and the development of the spinel phase of CoFe_2O_4 and Co_3O_4 .

Table 4.1 List of Crystallite size (D), lattice parameters (a, c), unit cell volume (V), crystal density (ρ), phase composition of BiFeO₃, Bi₂Fe₄O₉, CoFe₂O₄ and Co₃O₄, residuals of the weighted pattern (R_{wp}), pattern (R_p), and goodness of fit (GOF) of BiFe_{1-x}Co_xO₃ with x = 0, 0.05, 0.1, 0.2, and 0.3 nanoparticles.

Parameters	x = 0	x = 0.05	x = 0.1	x = 0.2	x = 0.3
D (nm)	88.8	64.9	57.8	58.7	54.5
a (Å)	5.5793	5.5747	5.5754	5.5746	5.5748
c (Å)	13.8743	13.8566	13.8556	13.8532	13.8540
V (Å) ³	374.0372	372.9290	373.0022	372.8312	372.804
ρ (g/cm ³)	8.333	8.362	8.364	8.376	8.383
BiFeO ₃ (%)	79.12	91.22	95.78	87.33	67.23
Bi ₂ Fe ₄ O ₉ (%)	20.88	8.78	4.22	-	-
CoFe ₂ O ₄ (%)	-	-	-	4.52	18.05
Co ₃ O ₄ (%)	-	-	-	8.14	14.28
R_{wp} (%)	7.68	7.58	8.27	7.99	6.25
R_p (%)	5.98	5.91	6.42	6.19	5.01
GOF	2.70	2.53	3.01	2.89	2.30

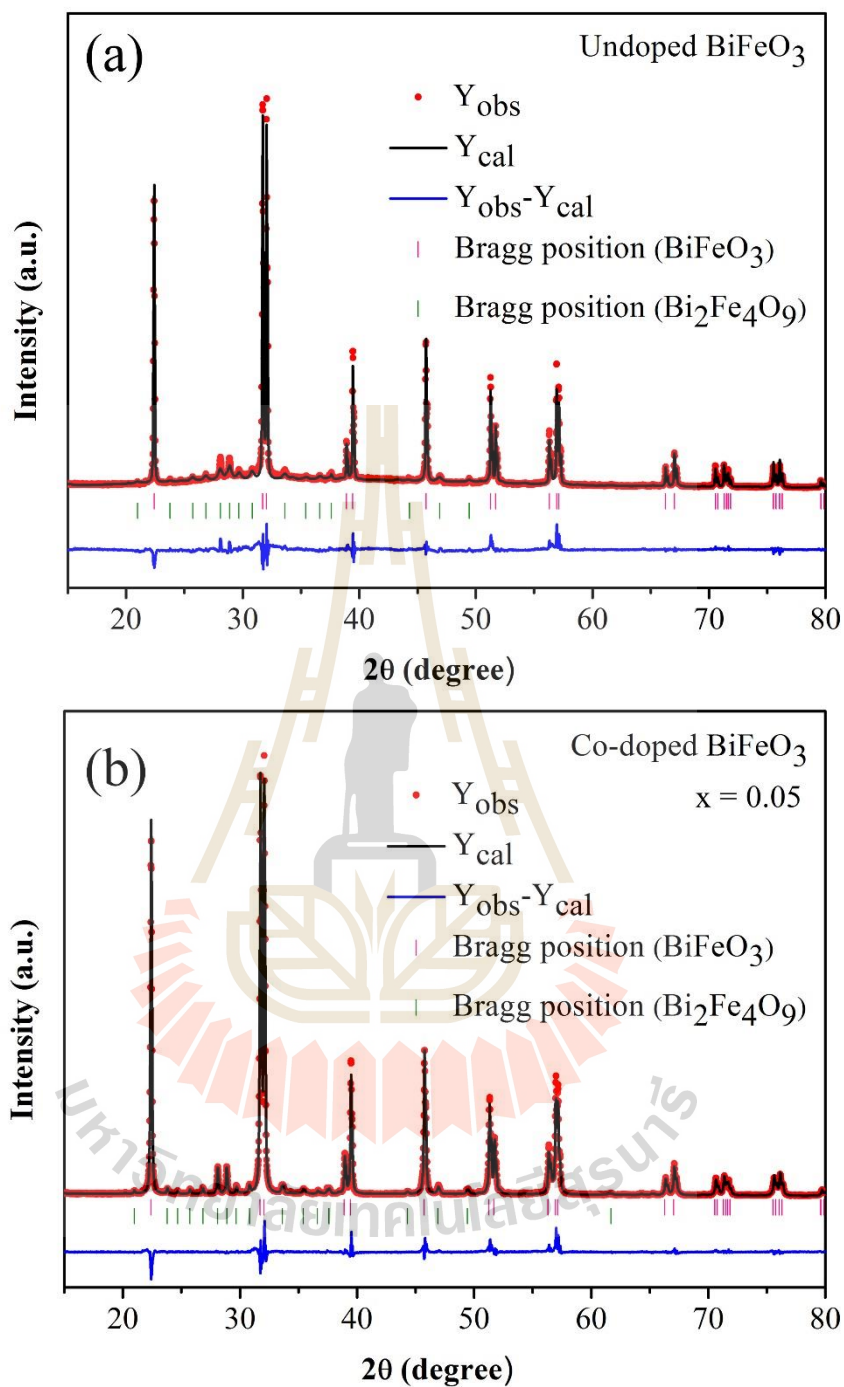


Figure 4.2 Rietveld refinement of XRD data for (a) BiFeO_3 (b) Co-doped BiFeO_3 ($x = 0.05$) nanoparticles.

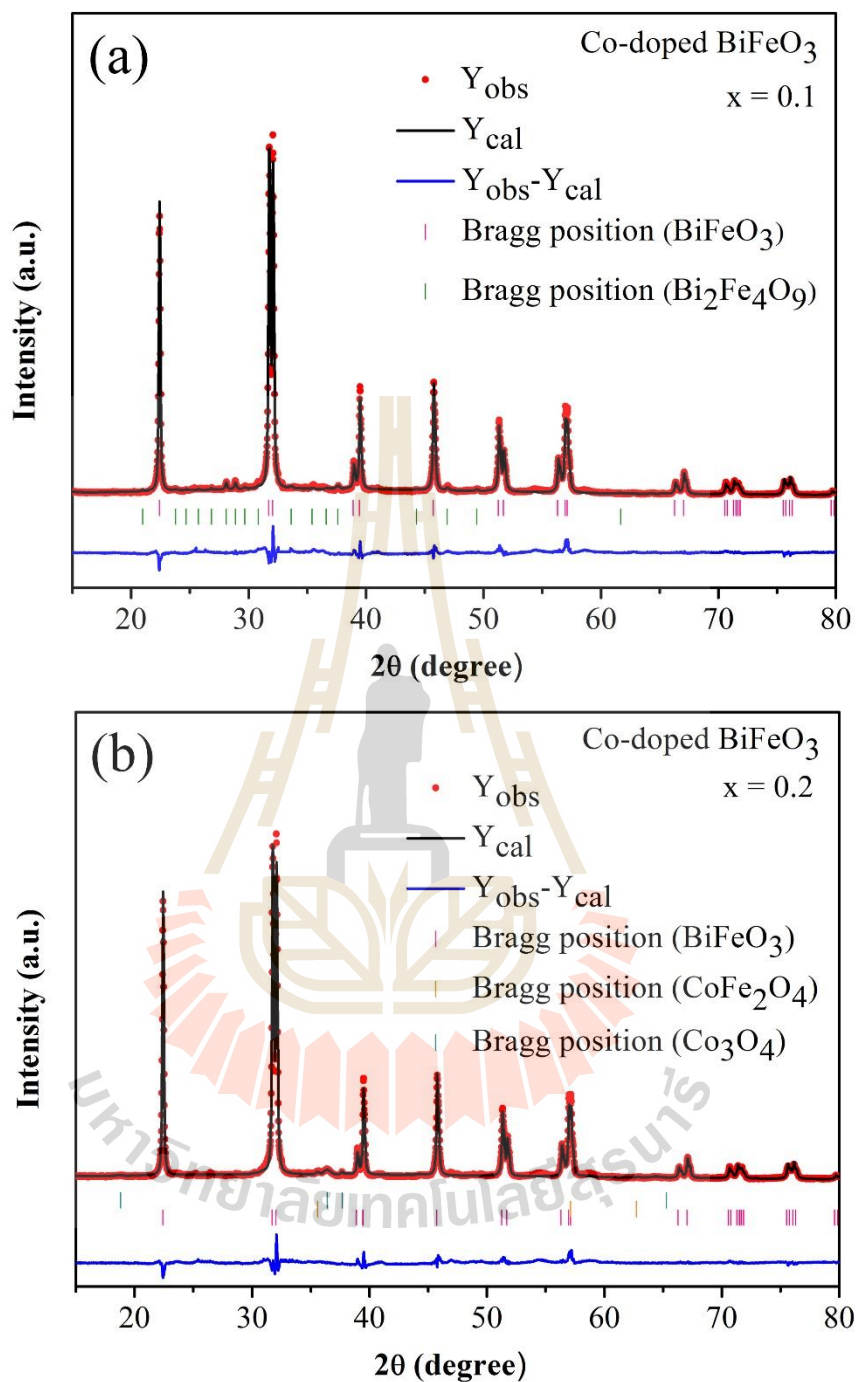


Figure 4.3 Rietveld refinement of XRD data for Co-doped BiFeO₃ nanoparticles: (a) x = 0.1 (b) x = 0.2.

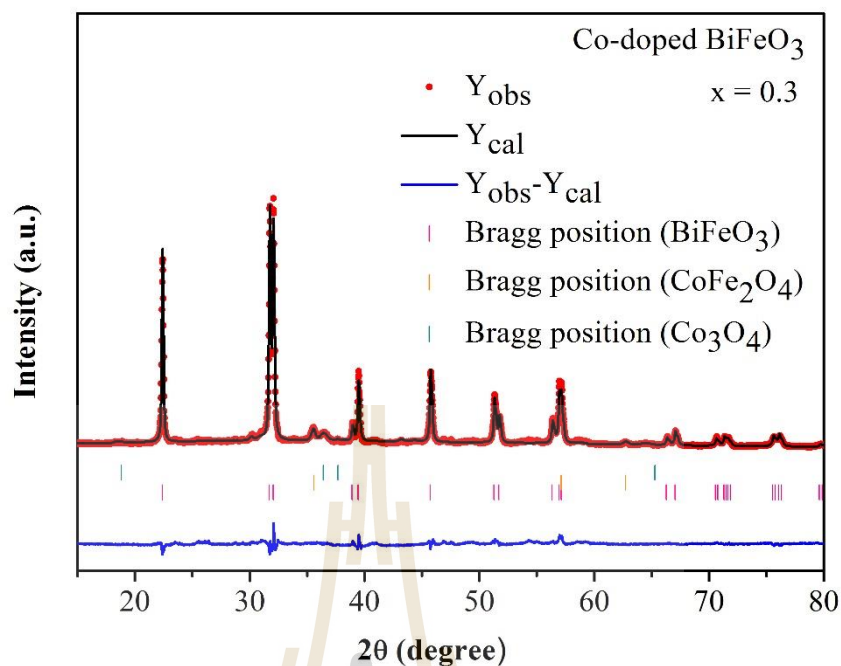


Figure 4.4 Rietveld refinement of XRD data for Co-doped BiFeO_3 ($x = 0.3$) nanoparticles.

4.1.1.2 Morphology of the Co-doped BiFeO_3 nanoparticles by SEM and TEM

The morphology of the nanoparticles was analyzed by scanning electron microscope (SEM) as shown in Figure 4.5. The undoped sample shows the sizes of the nanoparticles to be about 100-200 nm, while the Co-doped samples show decreases in the sizes of nanoparticles of about 50-150 nm. This indicates that Co doping causes decreases in the size of the nanoparticles. The mean particle size from the SEM image is in good agreement with the crystallite size calculated by using Scherrer's formula.

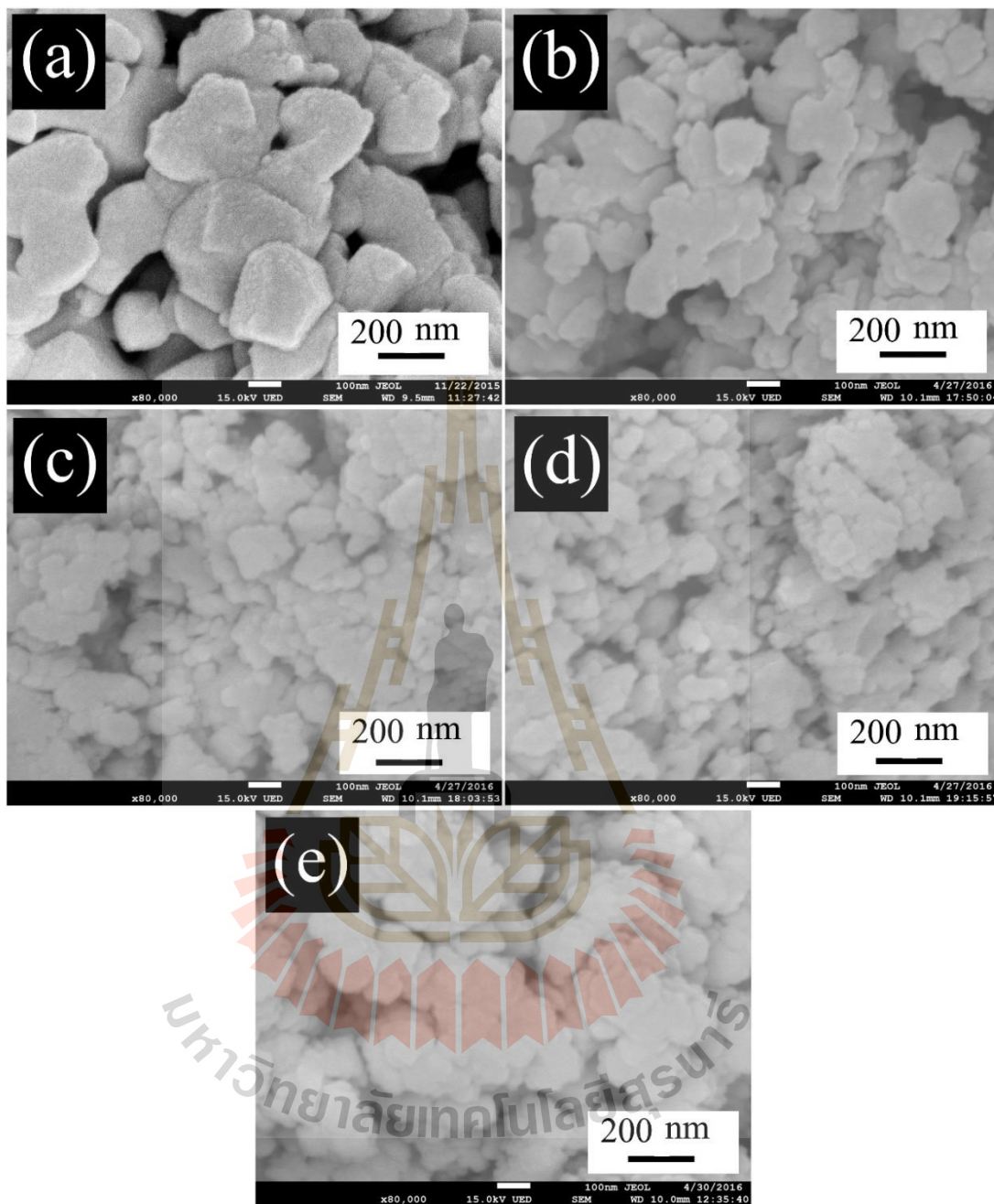
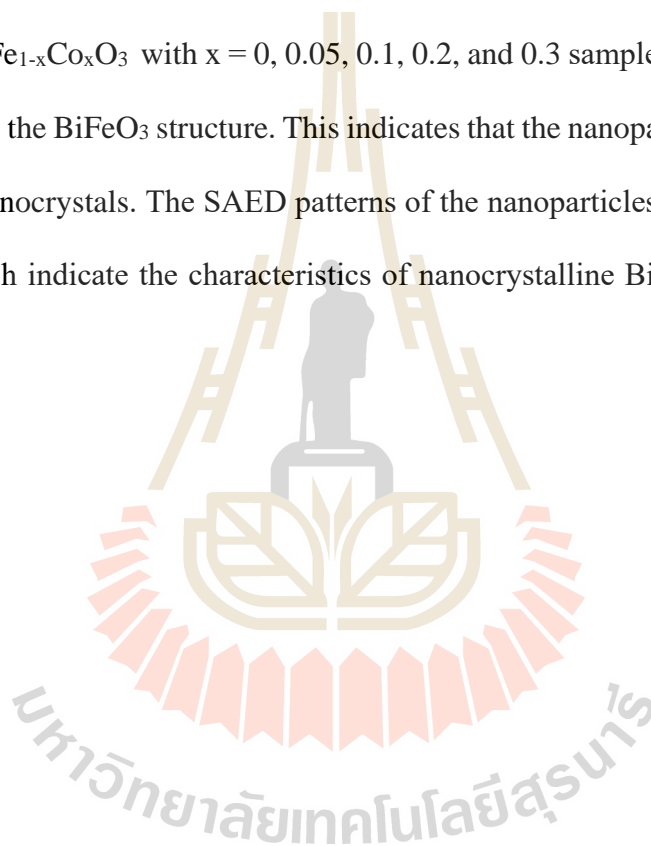


Figure 4.5 SEM images of $\text{BiFe}_{1-x}\text{Co}_x\text{O}_3$ nanoparticles: (a) $x = 0$, (b) $x = 0.05$, (c) $x = 0.1$, (d) $x = 0.2$, and (e) $x = 0.3$.

The morphology and structure of Co-doped BiFeO_3 nanoparticles was investigated by transmission electron microscopy (TEM). Bright field TEM images,

high-resolution (HRTEM) TEM images and corresponding selected areas of electron diffraction (SAED) patterns are shown in Figure 4.6. The TEM bright field images show that the particles sizes obtained were about 50-200 nm. This correspond to the XRD and SEM results. To better investigate the crystal structure, HRTEM was performed, which shows the lattice fringes of the (104), (012), (110), (110), and (110) planes with interplanar spacing of approximately 0.281, 0.395, 0.279, 0.279, and 0.279 nm of the $\text{BiFe}_{1-x}\text{Co}_x\text{O}_3$ with $x = 0, 0.05, 0.1, 0.2,$ and 0.3 samples, respectively, which correspond to the BiFeO_3 structure. This indicates that the nanoparticles are surrounded by BiFeO_3 nanocrystals. The SAED patterns of the nanoparticles show spotty and ring patterns which indicate the characteristics of nanocrystalline BiFeO_3 (JCPDS No.86-1518).



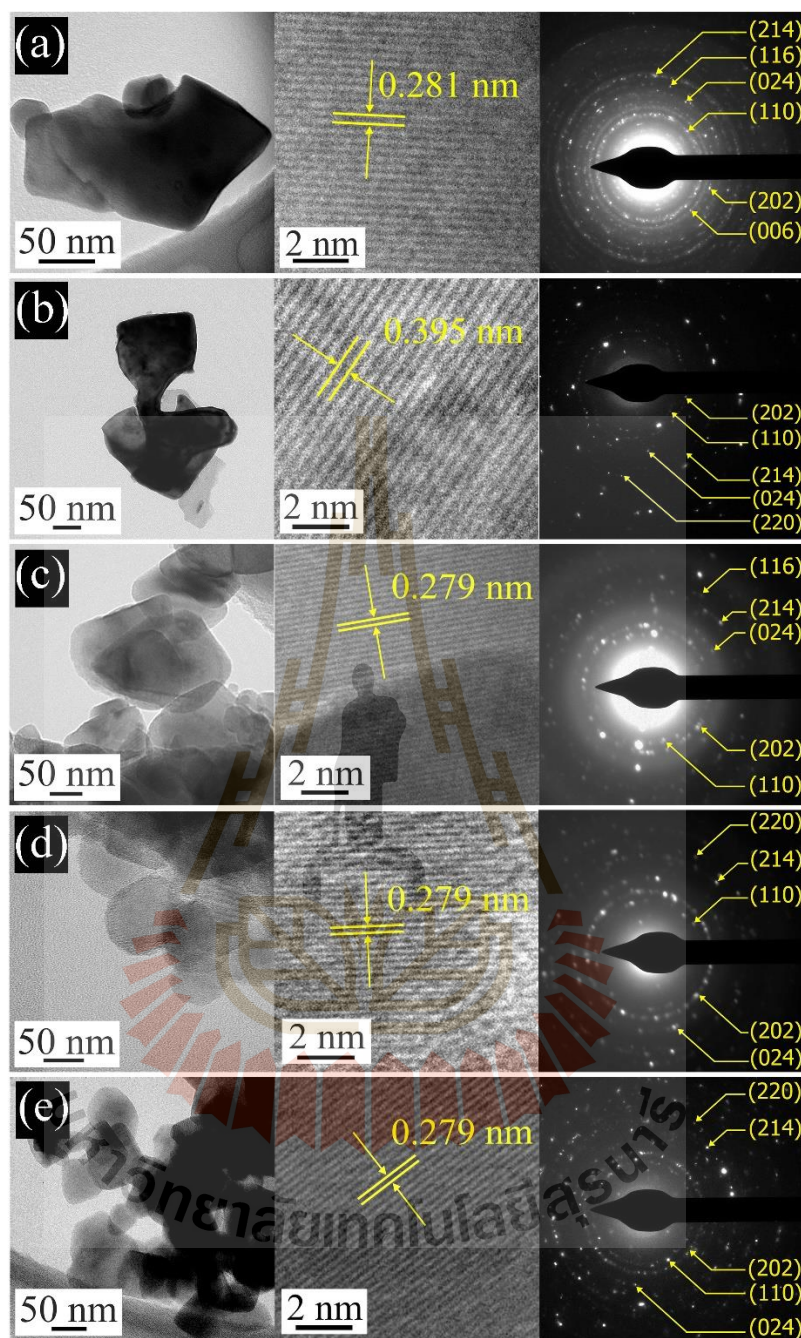
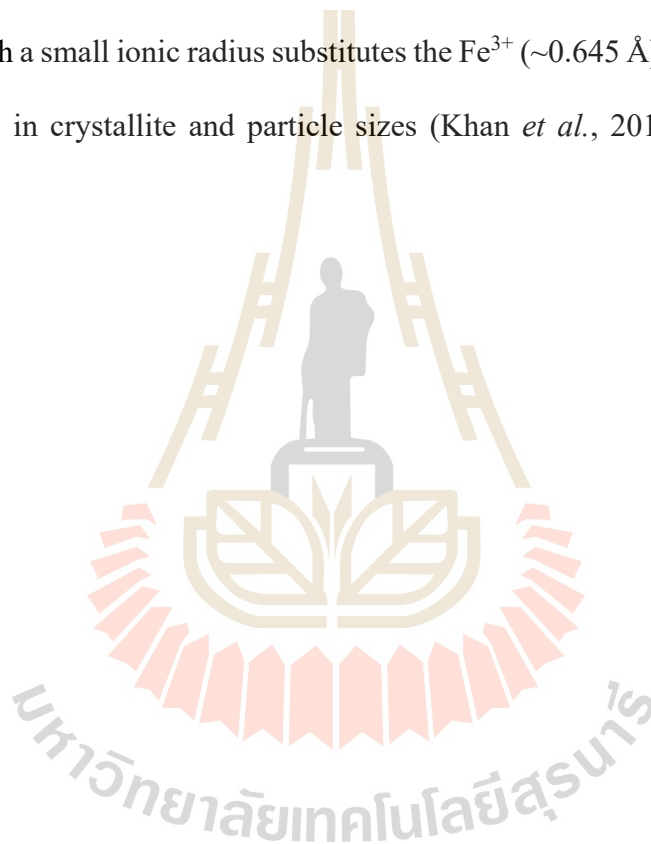


Figure 4.6 Bright field TEM images (left), high-resolution (HRTEM) TEM images (middle) and corresponding selected areas electron diffraction (SAED) patterns (right) of $\text{BiFe}_{1-x}\text{Co}_x\text{O}_3$ nanoparticles: (a) $x = 0$, (b) $x = 0.05$, (c) $x = 0.1$, (d) $x = 0.2$, and (e) $x = 0.3$.

4.1.1.3 X-ray absorption spectroscopy study of the Co-doped BiFeO₃ nanoparticles

X-ray absorption near-edge structure (XANES) spectra at the Fe and Co *K*-edge were measured at the room temperature to study the valence state of Fe and Co ions in the structure of the Co-doped BiFeO₃ samples. Figure 4.7 shows normalized Bi *M*₅-edges and Fe *K*-edges XANES spectra of all samples. The Bi *M*₅-edge XANES spectra of BiFe_{1-x}Co_xO₃ nanoparticles can be seen with $x = 0, 0.05, 0.1, 0.2,$ and 0.3 as compared with those of the standard materials with Bi oxidation states are shown in Figure 4.7(a). The oxidation states of Bi in all samples are shown along with the standard samples of Bi₂O₃ for Bi³⁺. It was found that the position of the absorption edge at Bi *M*₅-edge is similar to Bi₂O₃ which is typical for Bi in the oxidation state of +3. Figure 4.7(b) shows the XANES spectra at the Fe *K*-edge of all the samples, which match that of Fe₂O₃, indicating that the oxidation state of Fe is 3+. Figure 4.8 shows normalized Co *K*-edges XANES spectra of all samples. The Co *K*-edge XANES spectra of the BiFe_{1-x}Co_xO₃ nanoparticles can be seen with $x = 0.05, 0.1, 0.2,$ and 0.3 as compared with those of the standard materials with different Co oxidation states. The position of the edge energies for all samples is higher than that for the CoO (Co²⁺) standard samples. The absorption edge at the Co *K*-edge of all the samples match with Co₃O₄ (Mixing of Co²⁺ and Co³⁺) standard samples. The edge energies of Bi *M*₅-edge, Fe *K*-edge and Co *K*-edge of BiFe_{1-x}Co_xO₃ ($x = 0.05, 0.1, 0.2,$ and 0.3) samples are shown in Table 4.2-4.4. The edge energies of Bi *M*₅-edge and Fe *K*-edge of BiFe_{1-x}Cu_xO₃ ($x = 0.05, 0.1, 0.2,$ and 0.3) samples are close to the Bi₂O₃ and Fe₂O₃ standard. The edge energies of Co *K*-edge of BiFe_{1-x}Co_xO₃ ($x = 0.05, 0.1, 0.2,$ and 0.3) samples are 7721.30, 7721.38, 7721.46 and 7721.66 eV, respectively, are found to show a slight increase and

to be very close to the Co_3O_4 (7721.89 eV) standard. Clearly, the oxidation states of Co are between 2+ and 3+. The XANES analysis provides strong evidence that mixing of Co^{+2} (~ 0.65 Å) and Co^{3+} (~ 0.545 Å) is substituting the Fe^{3+} (~ 0.645 Å) site. The tendency of Co^{3+} seems to slightly increase. Furthermore, the XANES analysis provides strong evidence that mixing of Co^{2+} (0.65 Å) and Co^{3+} (0.545 Å) substitutes the Fe^{3+} (~ 0.645 Å) site. Moreover, this provides strong evidence that the presence of Co^{+3} (0.545 Å) with a small ionic radius substitutes the Fe^{3+} (~ 0.645 Å) site which may cause the decreases in crystallite and particle sizes (Khan *et al.*, 2015; Chakrabarti *et al.*, 2015).



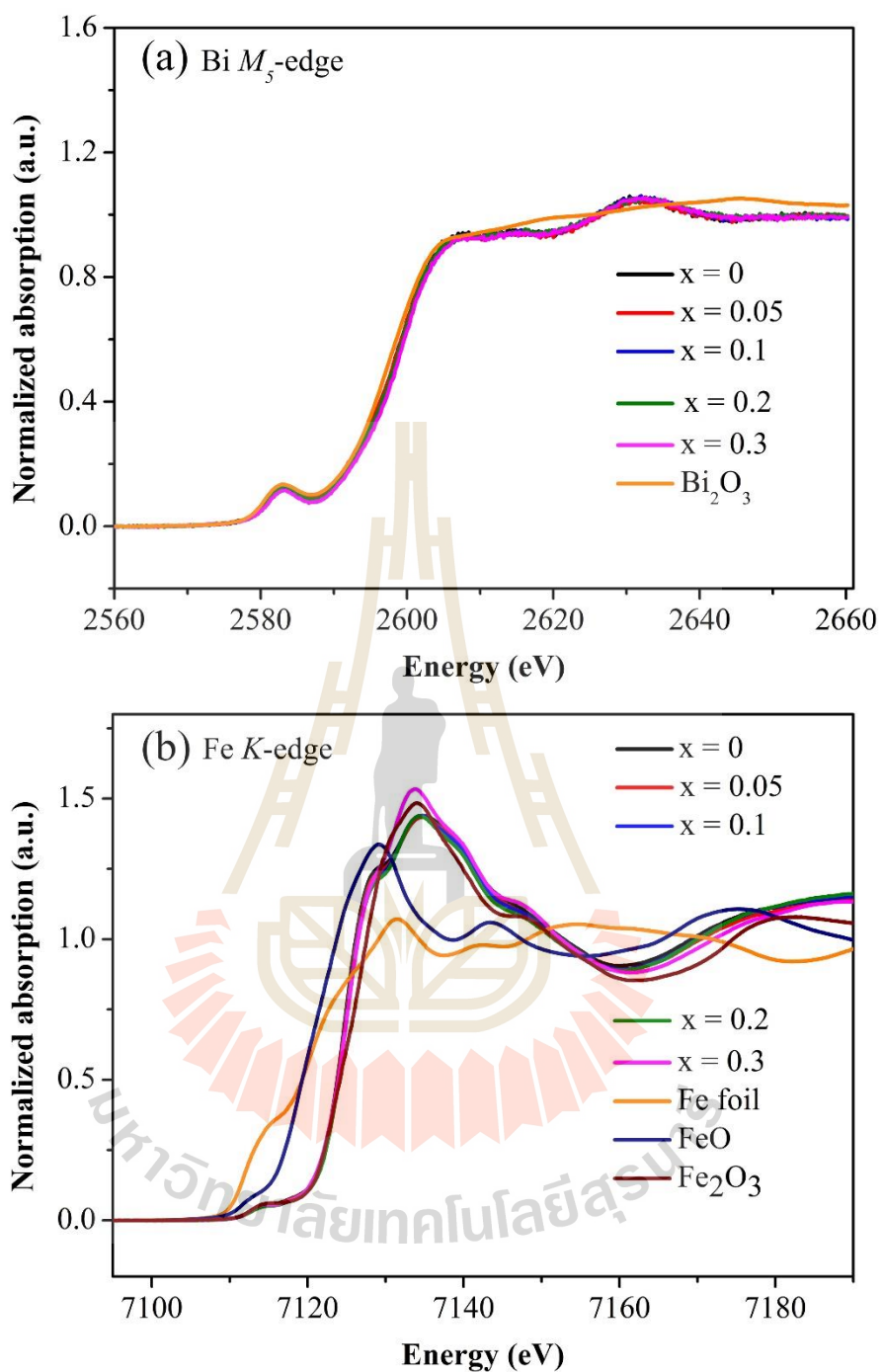


Figure 4.7 XANES spectra of $\text{BiFe}_{1-x}\text{Co}_x\text{O}_3$ ($x = 0, 0.05, 0.1, 0.2,$ and 0.3) nanoparticles: (a) Bi M_5 -edge and (b) Fe K -edge.

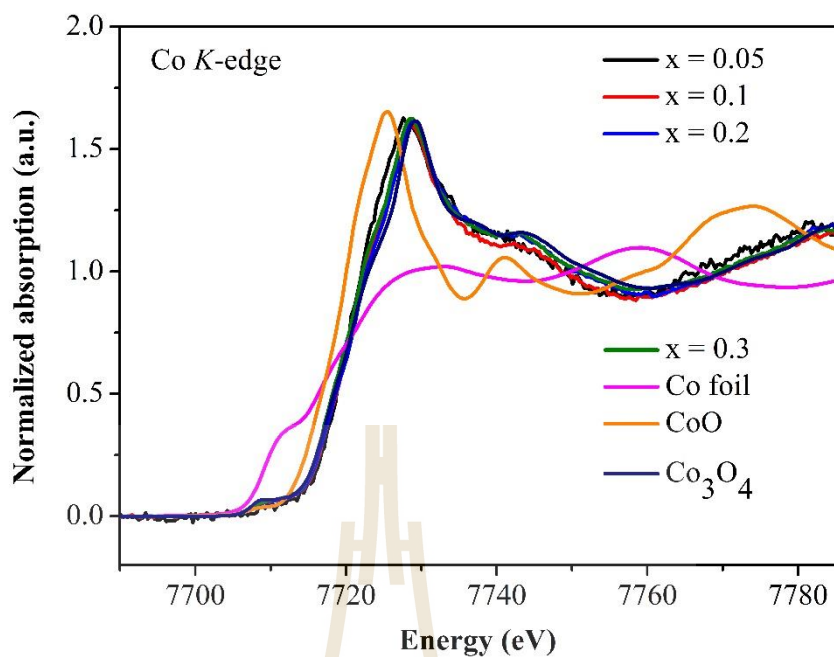


Figure 4.8 XANES spectra at Co K-edge of $\text{BiFe}_{1-x}\text{Co}_x\text{O}_3$ ($x = 0, 0.05, 0.1, 0.2,$ and 0.3) nanoparticles.

Table 4.2 Absorption edges and oxidation states at Bi M_5 -edge of all Co-doped BiFeO_3 samples along with the standard samples.

Samples/standard	Absorption edge at	Edge shift at	Oxidation state
	Bi (eV)	Bi (eV)	
Bi_2O_3	2597.25	0	+3
BiFeO_3	2598.63	1.38	+3
$\text{BiFe}_{0.95}\text{Co}_{0.05}\text{O}_3$	2598.73	1.48	+3
$\text{BiFe}_{0.9}\text{Co}_{0.1}\text{O}_3$	2599.29	2.04	+3
$\text{BiFe}_{0.8}\text{Co}_{0.2}\text{O}_3$	2598.99	1.74	+3
$\text{BiFe}_{0.7}\text{Co}_{0.3}\text{O}_3$	2599.15	1.90	+3

Table 4.3 Absorption edges and oxidation states at Fe *K*-edge of all Co-doped BiFeO₃ samples along with the standard samples.

Samples/standard	Absorption edge at Fe (eV)	Edge shift at Fe (eV)	Oxidation state
Fe foil	7112	13.64	0
FeO	7120.87	4.77	+2
Fe ₂ O ₃	7125.64	0	+3
BiFeO ₃	7124.62	1.02	+3
BiFe _{0.95} Co _{0.05} O ₃	7124.77	0.87	+3
BiFe _{0.9} Co _{0.1} O ₃	7124.86	0.78	+3
BiFe _{0.8} Co _{0.2} O ₃	7124.87	0.77	+3
BiFe _{0.7} Co _{0.3} O ₃	7125.07	0.57	+3

Table 4.4 Absorption edges and oxidation states at Co *K*-edge of all Co-doped BiFeO₃ samples along with the standard samples.

Samples/standard	Absorption edge at Co (eV)	Edge shift at Co (eV)	Oxidation state
CoO	7718.24	0	+2
Co ₃ O ₄	7721.89	3.65	+2,+3
BiFe _{0.95} Co _{0.05} O ₃	7721.30	3.06	+2,+3
BiFe _{0.9} Co _{0.1} O ₃	7721.38	3.14	+2,+3
BiFe _{0.8} Co _{0.2} O ₃	7721.46	3.22	+2,+3
BiFe _{0.7} Co _{0.3} O ₃	7721.66	3.42	+2,+3

4.1.1.4 Characterization of surface area and pore size distribution of the Co-doped BiFeO₃ nanoparticles by BET method and BJH method

The N₂ adsorption-desorption isotherms and pore size distributions obtained by the BET and BJH plot, respectively of the BiFe_{1-x}Co_xO₃ nanoparticles are shown in Figure 4.9. Generally, the pores of the materials are classified into three groups according to pore size distributions namely, micropores (pore size < 2 nm), mesopores (2-50 nm), and macropores (> 50 nm). Figure 4.9(a) shows hysteresis loop features of N₂ adsorption-desorption isotherms, which indicate characteristic of non-porous with weak interaction between sample surface and adsorbate in all samples. The presence of micropores and mesopores in particles is shown by the BJH curve in Figure 4.9(b). The specific surface area (S_{BET}), the mean pore diameter (D_{MP}), the total pore volume (V_{TP}), meso pore diameter (D_{BJH}) and the particle size (D_{BET}) of BiFe_{1-x}Co_xO₃ ($x = 0, 0.05, 0.1, 0.2, \text{ and } 0.3$) nanoparticles are shown in Table 4.5. The S_{BET} and total V_{TP} of Co doping concentrations for $x = 0$ to $x = 0.3$ samples increase from 3.64 to 9.81 m²/g and 0.0254 to 0.1199 cm³/g, respectively. Conversely, the particle size of $x = 0$ to $x = 0.3$ samples decreases from 197.8 to 73.0 nm, respectively. The D_{MP} of undoped samples (25.55 nm) is lower than that of Co-doped samples (48.89 to 56.55 nm). This may be related to capacitance and capacity retention, which will be discussed in Section 4.1.3. All the samples with higher concentrations of Co dopant showed a decrease in particle size which shows a tendency to increase their specific surface areas, and total pore volume as calculated and cited in Table 4.5. By comparison, the average particle size calculated by BET is larger than the crystallite size calculated by XRD for all samples as shown in Figure 4.10. The

differences in the results occur from aggregates and agglomerates of crystals, which indicate that the particles include several crystallites (Gaber *et al.*, 2014).

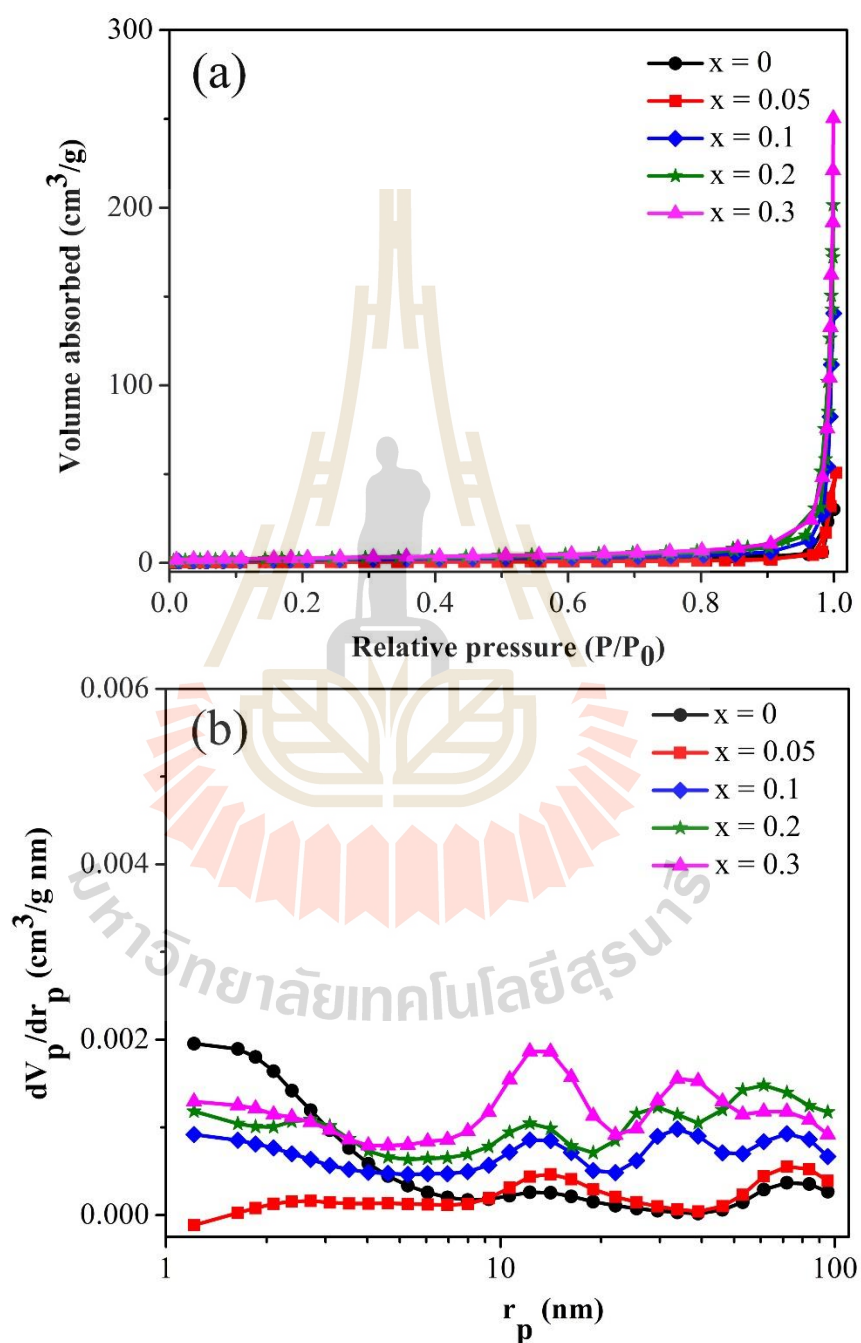


Figure 4.9 N₂ adsorption-desorption isotherms (a) and pore-size distribution (b) of the $\text{BiFe}_{1-x}\text{Co}_x\text{O}_3$ nanoparticles.

Table 4.5 Specific surface area (S_{BET}), mean pore diameter (D_{MP}), total pore volume (V_{TP}), meso pore diameter (D_{BJH}), particle size (D_{BET}) of $\text{BiFe}_{1-x}\text{Co}_x\text{O}_3$ ($x = 0, 0.05, 0.1, 0.2,$ and 0.3) nanoparticles.

Samples	S_{BET} (m^2/g)	D_{MP} (nm)	V_{TP} (cm^3/g)	D_{BJH} (nm)	D_{BET} (nm)
BiFeO_3	3.64	25.55	0.0254	3.28	197.81
$\text{Bi}_{0.95}\text{Co}_{0.05}\text{O}_3$	5.05	54.30	0.0336	24.48	142.09
$\text{Bi}_{0.9}\text{Co}_{0.1}\text{O}_3$	5.96	53.19	0.0792	29.50	120.36
$\text{Bi}_{0.8}\text{Co}_{0.2}\text{O}_3$	8.17	56.55	0.1156	33.04	87.68
$\text{Bi}_{0.7}\text{Co}_{0.3}\text{O}_3$	9.81	48.89	0.1199	41.06	72.96

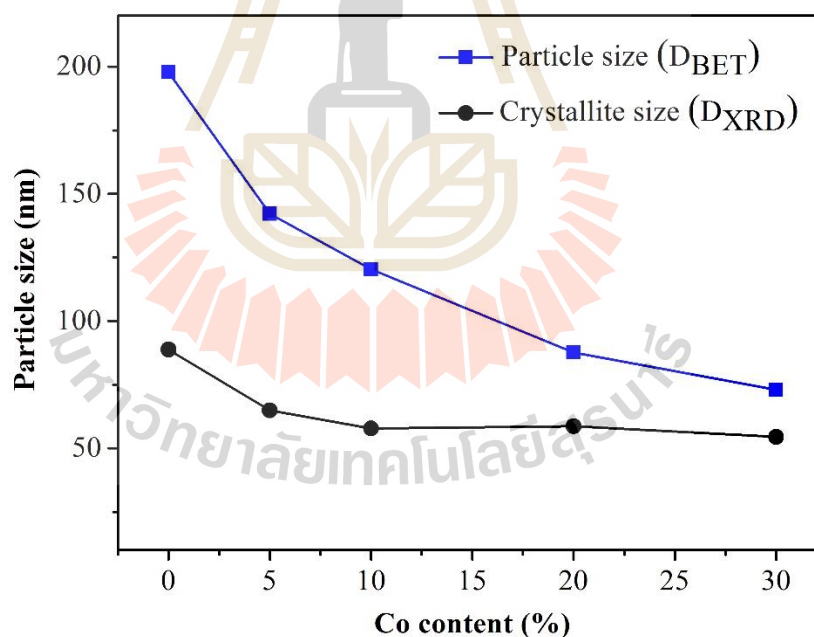


Figure 4.10 Variations of crystallite size calculated by XRD and particle size calculated from BET of $\text{BiFe}_{1-x}\text{Co}_x\text{O}_3$ nanoparticles as a function of Co content (%).

4.1.2 Magnetic properties of the Co-doped BiFeO₃ nanoparticles

Figure 4.11(a)-4.11(e) shows the magnetic hysteresis (M-H) curves of the BiFe_{1-x}Co_xO₃ (x = 0, 0.05, 0.1, 0.2, and 0.3) nanoparticles at 50, 100, 200, 300 and 350 K of temperature. Clearly, the saturation magnetization (M_s) increases linearly with increasing Co doping concentrations at all temperatures. The magnetization of BiFeO₃ slightly increases from 0.207 to 0.223 emu/g with increases in temperature from 50 to 350 K, respectively as shown in Table 4.6-4.7. Conversely, the magnetization of the BiFe_{1-x}Co_xO₃ (x = 0.05, 0.1, 0.2, and 0.3) samples slightly increases with the decreases of temperature from 300 to 50 K, except at 200 K which shows the highest level of magnetization at 1.43, 2.36, 2.78, and 9.24 for x = 0.05, 0.1, 0.2, and 0.3, respectively.

The secondary phase of Bi₂Fe₄O₉ in the x = 0 to x = 0.1 samples does not influence the increases of the M_s because it exhibits an antiferromagnetic nature with a very low M_s, as reported previously (Wang *et al.*, 2009; Rao *et al.*, 2016; Lin *et al.*, 2015). In this study, the magnetization of the BiFe_{1-x}Co_xO₃ (x = 0.05, 0.1, 0.2 and 0.3) samples at room temperature was 1.08, 2.15, 2.48, and 8.25 emu/g. By comparison, M_s of 10% Co-doped BiFeO₃ (2.15 emu/g) of this research is lower than 10% Co-doped BiFeO₃ (4.2-5.78 emu/g) in other reports (Montes *et al.*, 2010; Battisha *et al.*, 2015). The observed increases in magnetization may arise from three reasons: (1) From the M-H curves at temperatures of 50-350 K, The undoped BiFeO₃ shows weak ferromagnetic behavior, while all Co doping samples exhibit the ferromagnetic behavior with the increasing M_s due to increasing of the magnetic source content. (2) The magnetization is mainly dependent on the Co content which provides strong evidence of the effects of the sizes of the BiFeO₃ nanoparticles. It is known that particles on the nanoscale exhibit significantly different properties from bulk BiFeO₃ (Zhang *et al.*, 2005). Improved

magnetization may be due to suppression of the spin cycloid structure of the particle size when it is less than 62 nm which causes the intrinsic spiral spin structure to be incompletely suppressed and the decreases in crystallite size with increases of Co content results in an increase in surface-volume ratio and the contribution of uncompensated spin at the surface to the total magnetic moment of the particle increases. (3) the high M_s of CoFe_2O_4 nanoparticles (2.0 to 58.30 emu/g) (Kim *et al.*, 2003) and Co_3O_4 nanoparticles (60.76 to 71.09 emu/g) (Gopinath *et al.*, 2016) were measured at room temperature. Thus, the increases in the secondary phase of the CoFe_2O_4 and Co_3O_4 nanoparticles in the $\text{BiFe}_{1-x}\text{Co}_x\text{O}_3$ ($x = 0.2$ to $x = 0.3$) samples may cause an increase in saturation magnetization.

The hysteresis loops of all samples indicated improving ferromagnetism by Co doping influenced by variations in the coercivity (H_c) between 52.85 to 17970.57 Oe. The H_c values increase with decreases of temperature for all samples. At low temperature (50 K), the $\text{BiFe}_{0.9}\text{Co}_{0.1}\text{O}_3$ sample shows the highest H_c value of 17970.57 Oe. The H_c of all samples increases with measurements at low temperature which may occur for two reasons: (1) an increase in H_c is the alignment of the magnetic moment in the direction of the external magnetic field and (2) thermal fluctuations of nanoparticles decrease with the decreases in the temperature (Khan *et al.*, 2015). At higher temperatures (300 K), BiFeO_3 shows the lowest H_c value of 52.85 Oe. The variations of H_c correspond to decreasing of the crystallite size in the multi-domain region. The particle size dependence on coercivity can be expressed by the equation (Cullity and Graham, 2011):

$$H_c = a + \frac{b}{D} \quad (4.1)$$

Where a and b are constants and D is the particle size. The coercivity may decrease with the increase in particle size above a critical size. Thus, the increasing of H_c of Co-doped BiFeO_3 samples from $x = 0$ to $x = 0.1$ is due to the decrease in the crystallite size of BiFeO_3 . Especially, in the $x = 0.2$ and $x = 0.3$ samples, the crystallite size varies slightly, which is related to slight decreases in the H_c values. This conforms to the crystallite-size and the temperature-dependent behavior of BiFeO_3 nanoparticle (Park *et al.*, 2007). Furthermore, the H_c of the $x = 0.2$ and $x = 0.3$ samples are lower than the $x = 0$ to $x = 0.1$ samples which may due to the presence and variations in the small H_c values of CoFe_2O_4 (No to 193 Oe) (Kim *et al.*, 2003) and Co_3O_4 (49.32 to 56.90 Oe) nanoparticles (Gopinath *et al.*, 2016). Thus, the presence of the CoFe_2O_4 and Co_3O_4 secondary phases influence H_c in the $\text{BiFe}_{1-x}\text{Co}_x\text{O}_3$ ($x = 0.2$ to $x = 0.3$) samples. Clearly, this is evidence that the size effects of BiFeO_3 and the presence of CoFe_2O_4 and Co_3O_4 are strongly influenced by the H_c values. Moreover, the remanent magnetization (M_r) increases due to increase of the Co content, decrease in the crystallite size of BiFeO_3 and decrease in temperature.

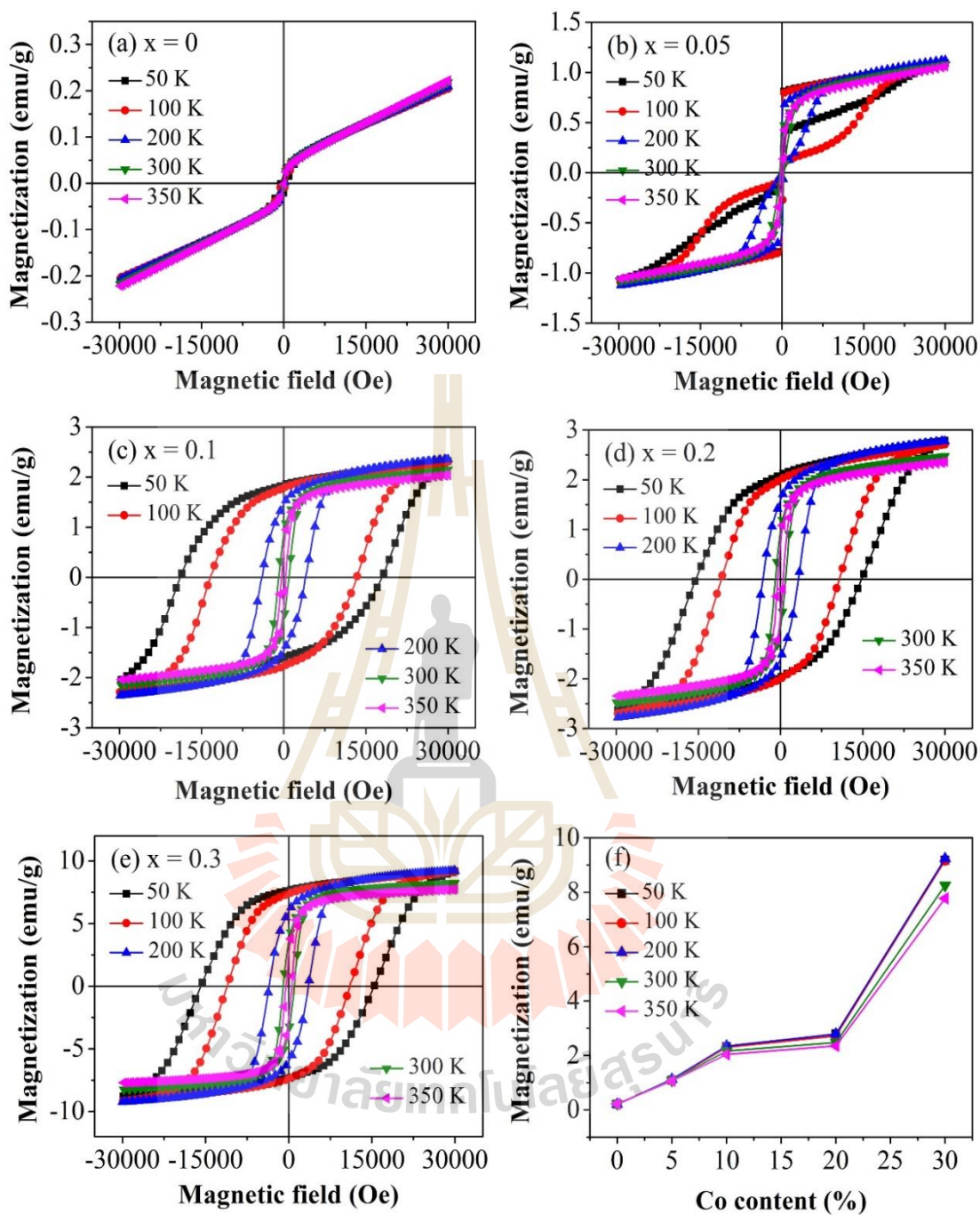


Figure 4.11 Magnetization hysteresis loops at different temperature of $\text{BiFe}_{1-x}\text{Co}_x\text{O}_3$ nanoparticles: (a) $x = 0$, (b) $x = 0.05$, (c) $x = 0.1$, (d) $x = 0.2$, and (e) $x = 0.3$. (f) Variations in saturation magnetization as a function of Co content (%).

Table 4.6 Coercivity (H_c), saturation magnetization (M_s) and remanent magnetization (M_r) values of $\text{BiFe}_{1-x}\text{Co}_x\text{O}_3$ ($x = 0, 0.05, 0.1, \text{ and } 0.2$) samples at different temperatures.

Sample	T (K)	H_c (Oe)	M_s (emu/g)	M_r (emu/g)
x = 0	50	524.35	0.207	0.019
	100	342.73	0.210	0.017
	200	108.14	0.206	0.010
	300	52.85	0.219	0.005
	350	30.59	0.223	0.004
x = 0.05	50	256.15	1.088	0.569
	100	363.71	1.087	0.611
	200	382.86	1.127	0.480
	300	400.74	1.080	0.348
	350	180.74	1.063	0.189
x = 0.1	50	17970.57	2.323	1.845
	100	13352.09	2.303	1.788
	200	3923.34	2.348	1.461
	300	949.65	2.165	0.857
	350	335.87	2.039	0.580
x = 0.2	50	14779.74	2.789	2.126
	100	10695.73	2.717	2.013
	200	3263.01	2.786	1.595
	300	910.82	2.480	0.969
	350	525.91	2.352	0.731

Table 4.7 Coercivity (H_c), saturation magnetization (M_s) and remanent magnetization (M_r) values of $\text{BiFe}_{1-x}\text{Co}_x\text{O}_3$ ($x = 0.3$) samples at different temperatures.

Sample	T (K)	H_c (Oe)	M_s (emu/g)	M_r (emu/g)
x = 0.3	50	15400.33	9.179	7.765
	100	11029.97	9.167	7.392
	200	3560.41	9.236	5.983
	300	1003.20	8.250	3.563
	350	571.12	7.775	2.511

Figure 4.12-4.14 shows temperature dependent of the magnetization for the undoped BiFeO_3 and $\text{BiFe}_{1-x}\text{Co}_x\text{O}_3$ ($x = 0.05, 0.1, 0.2$ and 0.3) nanoparticles, showing the ZFC (zero field cooling) and FC (field cooling) curves, under 50 K to 350 K with an applied field set at 500 Oe. The FC curves of the Co-doped BiFeO_3 samples increase in magnetization with a lowering of temperature from 350 to 50 K. This may be attributed to the development of the incommensurate sinusoidal spin structure (Naik and Mahendiran, 2009) and indicates that the Co-doped BiFeO_3 samples have typical ferromagnetic properties. The decreases in the magnetization of the ZFC curves with from a lowering of temperature broad maximum magnetization ~ 250 to 50K for $x = 0$ samples and Co-doped BiFeO_3 samples is decrease with a lowering of temperature from 350 to 50 K is evidence of the antiferromagnetic exchange interaction of the spins (Kumar and Yadav, 2011). The feature of the ZFC curves of $x = 0$ sample shows a prominent and broad magnetization maximum around $T_{\max} \sim 250$ K, which can be attributed to the magnetic blocking mechanism. However, the decrease in the magnetization of the ZFC curves for $x = 0.05, 0.1, 0.2$, and 0.3 samples did not show

any form of broad maximum magnetization. The splitting of ZFC and FC magnetizations at low temperature also reveals spin-glass transition in BiFeO₃ (Singh *et al.*, 2008). The ZFC and FC curves of $x = 0$ samples exhibit an irreversible thermomagnetization process below 287 K that is there exist an obvious difference between the ZFC curve and FC curve, which increases with decreasing the temperature as shown in Figure 4.12(a). The Co doped BiFeO₃ ($x = 0.05, 0.1, 0.2$ and 0.3) samples show increases in the difference between the ZFC and FC magnetization curves which are greater than 350 K as shown in Figure 4.12(b)-Figure 4.14. This result conform to other reports of BiFeO₃, which show a magnetic transition below 650 K, indicating that the sample becomes ferromagnetic at the Neel temperature when the particle size is reduced (Vijayanand *et al.*, 2009). The divergence between FC and ZFC magnetization curves of the Co doped BiFeO₃ samples more than 350 K is similar to that found for other ferro- and ferrimagnetic materials (Joy and Date, 2000). Moreover, a splitting between FC and ZFC magnetization curves can attributed to an inhomogeneous mixture of AFM and FM (Siwach *et al.*, 2007). The evidence for spin-glass behavior in BiFeO₃ that there is a cusp at 50 K (Catalan and Scott, 2009). The cusp (at about 50 K) in all samples with the particle size less than 89 nm could not be observed. This result conforms to reports for the presence of the cusp at about 50 K that can be observed for BiFeO₃ nanoparticles with particle size larger than 95 nm (Park *et al.*, 2007) and when the applied magnetic field is larger than 2 KOe (Huang *et al.*, 2013).

The para/antiferromagnetic characteristics and the magnetic susceptibility can be explained by the Curie-Weiss law quite well in a high temperature range (Yin *et al.*, 2009). The temperature dependence of the inverse magnetic susceptibility, $1/\chi$, and the

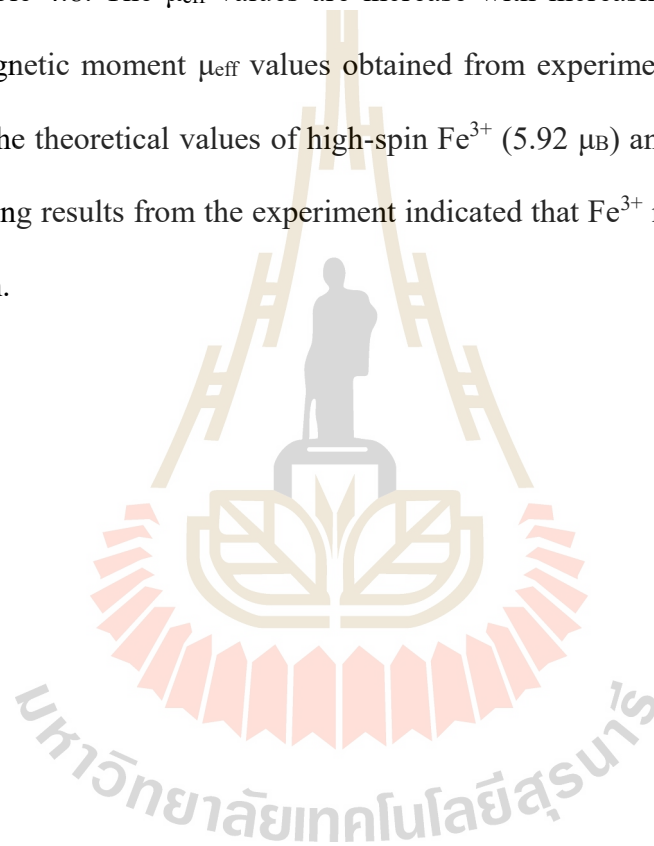
fitting curves are shown in the inset of Figure 4.12-4.14. The experimental data is fitted according to the Curie-Weiss law:

$$\chi = \frac{C}{T - \theta} \quad (4.2)$$

Where χ is susceptibility, θ is the Curie-Weiss temperature and C defines the Curie constant. In this equation, Weiss temperature (θ) can either be positive, negative or zero. When $\theta = 0$ then the Curie-Weiss law equates to Curie's law. If θ is positive then there is ferromagnetic interaction; if θ is negative then there is antiferromagnetic interaction. The Curie constant (C) are 35.73, 60.55, 175.12, 243.59, and 804.61 emu K/g Oe for $x = 0, 0.1, 0.2,$ and 0.3 samples, respectively, which increase with increasing of Co doping concentration. The Curie-Weiss temperature (θ) value obtained from the Curie-Weiss fit of undoped-BiFeO₃ at $T = 50-130$ K and $T = 250-350$ K is -1641.04 K and -1605.18 K, respectively. This negative values of the θ indicated the antiferromagnetic characteristics of undoped-BiFeO₃ with weak FM and without FM component. Conversely, the Curie-Weiss law fitting result provides a positive Curie-Weiss temperature of $74.61, 42.85, 19.24$ and 23.33 K for Co-doped BiFeO₃ with $x = 0.05, 0.1, 0.2$ and 0.3 , respectively, which is probably due to the strong canted AFM ordering with a manifest FM component. In the theory, a Fe³⁺ ion at an octahedrally coordinated site suggests a High-spin (HS) configuration ($s = 5/2$) or Low-spin (LS) configuration ($s = 1/2$). The calculated magnetic moments of high-spin Fe³⁺ and low-spin Fe³⁺ are $5.92 \mu_B$ and $1.73 \mu_B$, respectively (Griffith, 1961). By fitting with Curie-Weiss law, the theoretical effective moment can compute from Curie constant by using the equation (Kittel, 1986):

$$\mu_{\text{eff}} = 2.84 \sqrt{(T - \theta)} = 2.84 \sqrt{C} \quad (4.3)$$

The effective magnetic moment (μ_{eff}) values from experiment of the un-doped BiFeO₃ and Co-doped BiFeO₃ samples with $x = 0.05, 0.1, 0.2,$ and $0.3,$ respectively are shown in Table 4.8. The μ_{eff} values are increase with increasing of Co doping. The effective magnetic moment μ_{eff} values obtained from experiment for all samples are higher than the theoretical values of high-spin Fe³⁺ (5.92 μ_B) and low-spin Fe³⁺ (1.73 μ_B). This fitting results from the experiment indicated that Fe³⁺ must be in a high spin configuration.



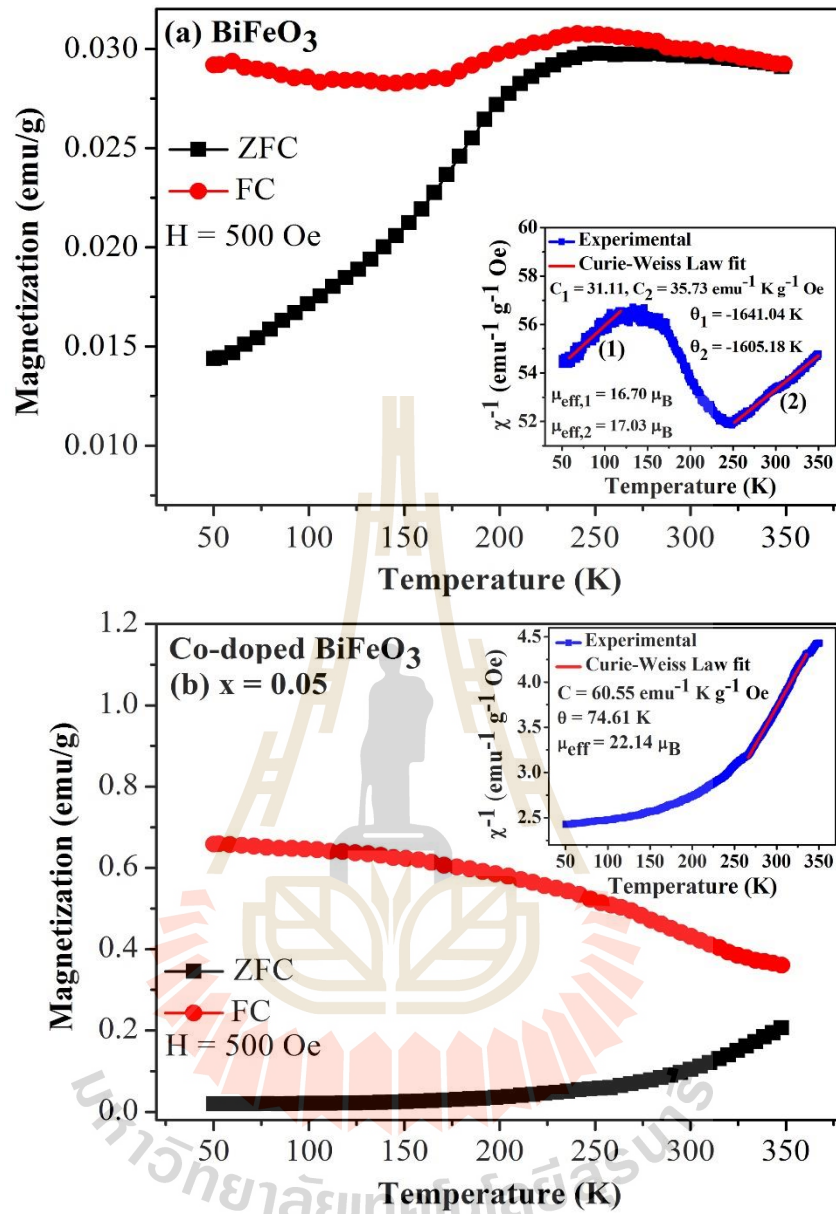


Figure 4.12 ZFC/FC curves and fitting the data to the Curie-Weiss law (inset) for (a) BiFeO₃ and (b) BiFe_{0.95}Co_{0.05}O₃ nanoparticles.

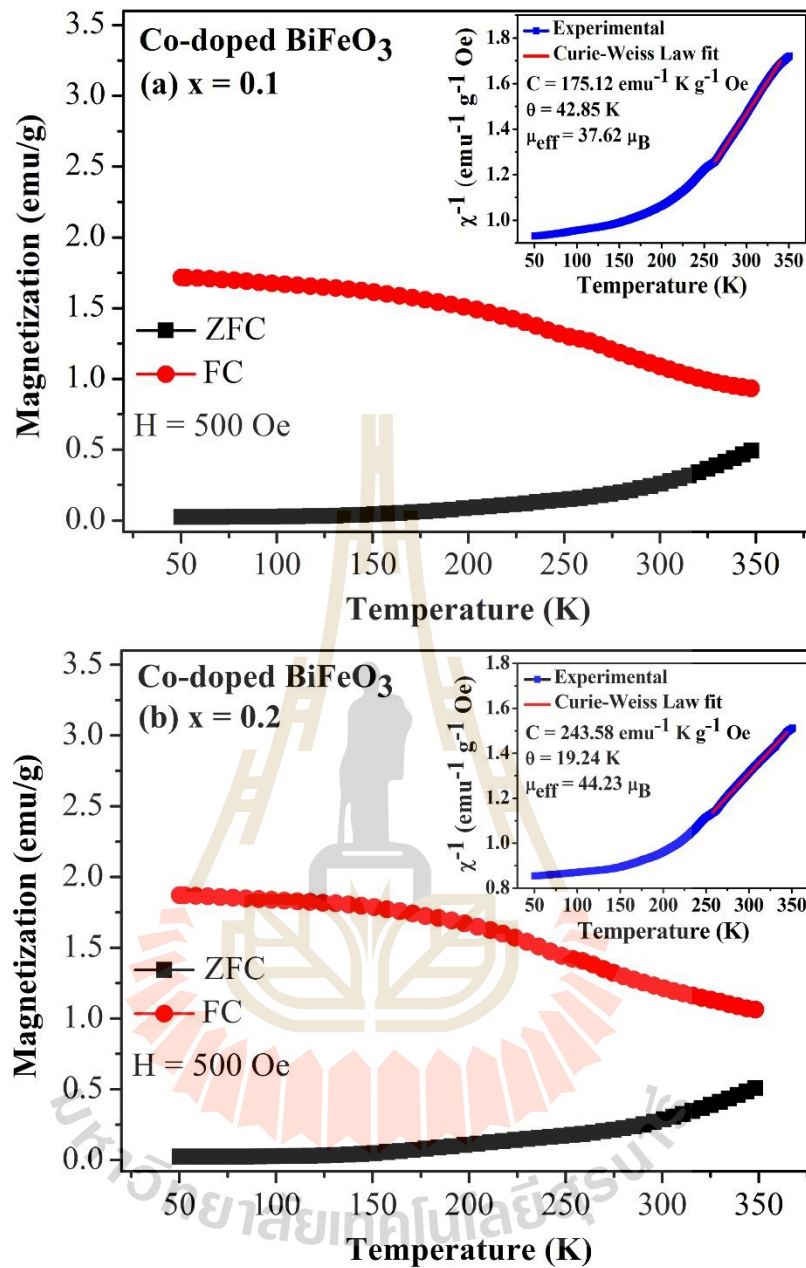


Figure 4.13 ZFC/FC curves and fitting the data to the Curie-Weiss law (inset) for (a) BiFe_{0.9}Co_{0.1}O₃ and (b) BiFe_{0.8}Co_{0.2}O₃ nanoparticles.

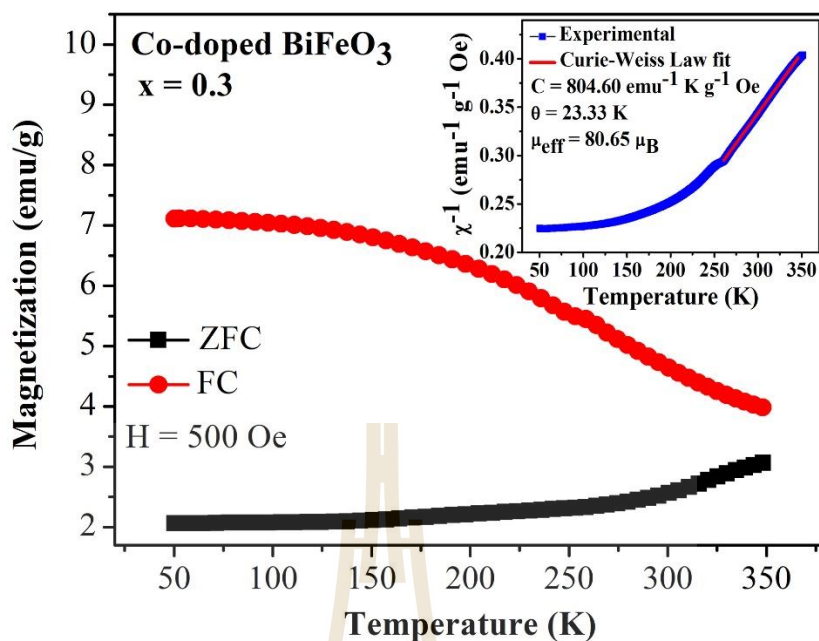


Figure 4.14 ZFC/FC curves and fitting the data to the Curie-Weiss law (inset) for $\text{BiFe}_{0.7}\text{Co}_{0.3}\text{O}_3$ nanoparticles.

Table 4.8 Effective magnetic moment (μ_{eff}), Curie-Weiss temperature (θ) obtained from Curie-Weiss's law fitting results for Co-doped BiFeO_3 .

Doping level	μ_{eff} (μ_{B})	θ (K)
$x = 0$	16.70 ^a , 17.03 ^b	-1641.04 ^a , -1605.18 ^b
$x = 0.05$	22.14	74.61
$x = 0.1$	37.62	42.85
$x = 0.2$	44.23	19.24
$x = 0.3$	80.65	23.33

a is fitting at $T = 50\text{-}130$ K, **b** is fitting at $T = 250\text{-}350$ K

4.1.3 Electrochemical properties of Co-doped BiFeO₃ nanoparticles

4.1.3.1 Cyclic voltammetry measurement

The cyclic voltammetry (CV) curves of the BiFe_{1-x}Co_xO₃ nanoparticles recorded between -1.2 V to 0.3 V at different potential scan rates of 5 to 100 mV/s are presented in Figure 4.15(a)-4.15(e). All samples exhibited a pseudocapacitive behavior. Well-defined redox peaks were observed for all the samples, indicating that the redox transitions of the nanoparticles are similar to the redox properties of bismuth oxide and Fe₂O₃ in hydroxide electrolyte (KOH, NaOH) in various works, which can be attributed to the reversible reaction of bismuth (III) to bismuth metal (Vivier *et al.*, 2001) and which correspond to the conversion between Fe²⁺ and Fe³⁺ (Hang *et al.*, 2005; Wang *et al.*, 2014), respectively. The anodic peak could be assigned to the oxidation process of Fe²⁺/Fe³⁺ (~ -0.78 V) and Bi_{metal}/Bi³⁺ (~ -0.65 V and -0.51 V), while the cathodic peak relate to the reduction process of Bi³⁺/Bi_{metal} (~ -0.82 V) and Fe³⁺/Fe²⁺ (~ -1.10 V), respectively. The current response of all electrodes was enhanced when the scan rates were increased. The height of the peak current varied and a progressive shift in the peaks to higher potentials was observed with increasing scan rates from 5 to 100 mV/s. This is attributed to the presence of inner active sites, which completely inhibit the redox transitions at higher scan rates of CV, probably owing to the diffusion effect of protons within the electrodes (Kötz and Carlen, 2000). The specific capacitances calculated for different as synthesized samples at different scan rates from the equation 3.13. The calculated specific capacitances vs scan rates are plotted in Figure 4.15(f). The specific capacitances of all the samples decrease with increasing scan rates. At slow scan rates, the ions would have enough time to arrive the electrode surface leading to the full utilization of the material. All the electrodes exhibited the highest specific

capacitance at a scan rate of 5 mV/s. The maximum specific capacitance of 397.28 F/g at a scan rate of 5 mV/s was obtained for the pure BiFeO₃ sample. The specific capacitance of the nanoparticles depends linearly on Co doping concentrations with continuous decreases. The specific capacitance of the nanoparticles decreases from the undoped samples (397.28-183.67 F/g) to BiFe_{0.7}Co_{0.3}O₃ samples (216.16-48.61 F/g) at 5-100 mV/s for CV measurements, respectively. In general, increases in the specific surface area in electrochemical capacitors is a likely reason for the increase in the specific capacitance, especially in carbon materials. On the contrary, the specific capacitance of these BiFe_{1-x}Co_xO₃ nanoparticles decreases. However, specific capacitance does not only depend on surface area, but also on other factors, such as the pore size distribution and pore volume (Long *et al.*, 2001; Reddy and Reddy, 2003; Khajonrit *et al.*, 2016). All the samples have distributions of different mesopores sizes of pores as shown in Figure 4.9, indicating that they have a porous structure, which is specific to supercapacitor materials (Long *et al.*, 2001; Reddy and Reddy, 2003). A mean pore diameter of the BiFeO₃ samples showed small mesopore sizes about 3.28 nm. This may provide more active sites for chemical reactions (Dubal *et al.*, 2013). The decreases in the specific capacitance of the BiFe_{1-x}Co_xO₃ samples with increases in Co doping can possibly be attributed to all samples enriched with mesopores, which were decrease in size with increases of Co doping from 24.48, 29.50, 33.04, and 41.06 nm for 5, 10, 20, and 30% Co doping samples, respectively. The high specific capacitances (468.2 F/g) of Co₃O₄ at 10 mV/s 6 M KOH (Xu *et al.*, 2014) and the increase of Co₃O₄ phase composition (8.1 to 14.3 %) with Co content with x = 0.2 to x = 0.3 may not help in improving capacity retention and specific capacitance. But the decreases in the capacity retention and the specific capacitance in the x = 0.2 to x = 0.3 samples may be

due to increases in the phase composition (4.5 to 18.1 %) of CoFe_2O_4 and the specific capacitances of 195 F/g at 1 mV/s 1 M KOH (Sankar *et al.*, 2015), which were lower than those of the BiFeO_3 nanoparticles (397.3 F/g) at the scan rate of 5 mV/s in 6M KOH solution.

The number of active sites of the electrodes were calculated using equation 3.14. The calculated number of active sites involved in the redox reaction at different scan rates corresponding to 5-100 mV/s are 1.93-0.89, 1.65-0.75, 1.62-0.68, 1.32-0.41, and 1.05-0.24 for $x = 0, 0.05, 0.1, 0.2,$ and 0.3 samples, respectively as shown in Table 4.9-4.10. The number of redox sites participating at lower scan rates is higher compared with the higher scan rates. At slow scan rates, the ions would have enough time to arrive the electrode surface leading to the full utilization of the material. At higher scan rates, the ions would not have enough time to utilize the material and hence the surface adsorption process only takes place (Selvan *et al.*, 2008; Nithya *et al.*, 2013). According to the equation 3.15, the calculated diffusion co-efficient for 6 M KOH electrolyte at different scan rates corresponding to 5-100 mV/s are $2.61-1.38 \times 10^{-16}$, $1.64-0.76 \times 10^{-16}$, $2.01-0.73 \times 10^{-16}$, $1.43-0.13 \times 10^{-16}$, and $0.88-0.03 \times 10^{-16}$ cm^2/s in $x = 0, 0.05, 0.1, 0.2,$ and 0.3 samples, respectively as shown in Table 4.9-4.10. The value of diffusion co-efficient depends mainly on the peak current since the other parameters in the equation such as the number of electrons transferred during the redox reaction, concentration and scan rate. The diffusion co-efficient at lower scan rates is higher compared with the higher scan rates. Moreover, since the peak current of BiFeO_3 sample is higher than Co-doped BiFeO_3 samples, the value of diffusion co-efficient of BiFeO_3 is found to be higher than Co-doped BiFeO_3 samples. The decreasing of number of active sites and diffusion co-efficient correspond to decreasing specific capacitances

with increasing of Co doping concentrations. Moreover, the tendency of edge shift slightly increase above Bi^{3+} position with increasing of Co doping with $x = 0, 0.05, 0.1, 0.2,$ and 0.3 samples, which is 1.38, 1.46, 2.04, 1.74, and 1.90 respectively. This may be inactive and did not participate in the redox reaction of the conversion between $\text{Bi}^{(0)}$ and Bi^{3+} , which may lead to the reduction of height of the peak current and deterioration of specific capacitances.



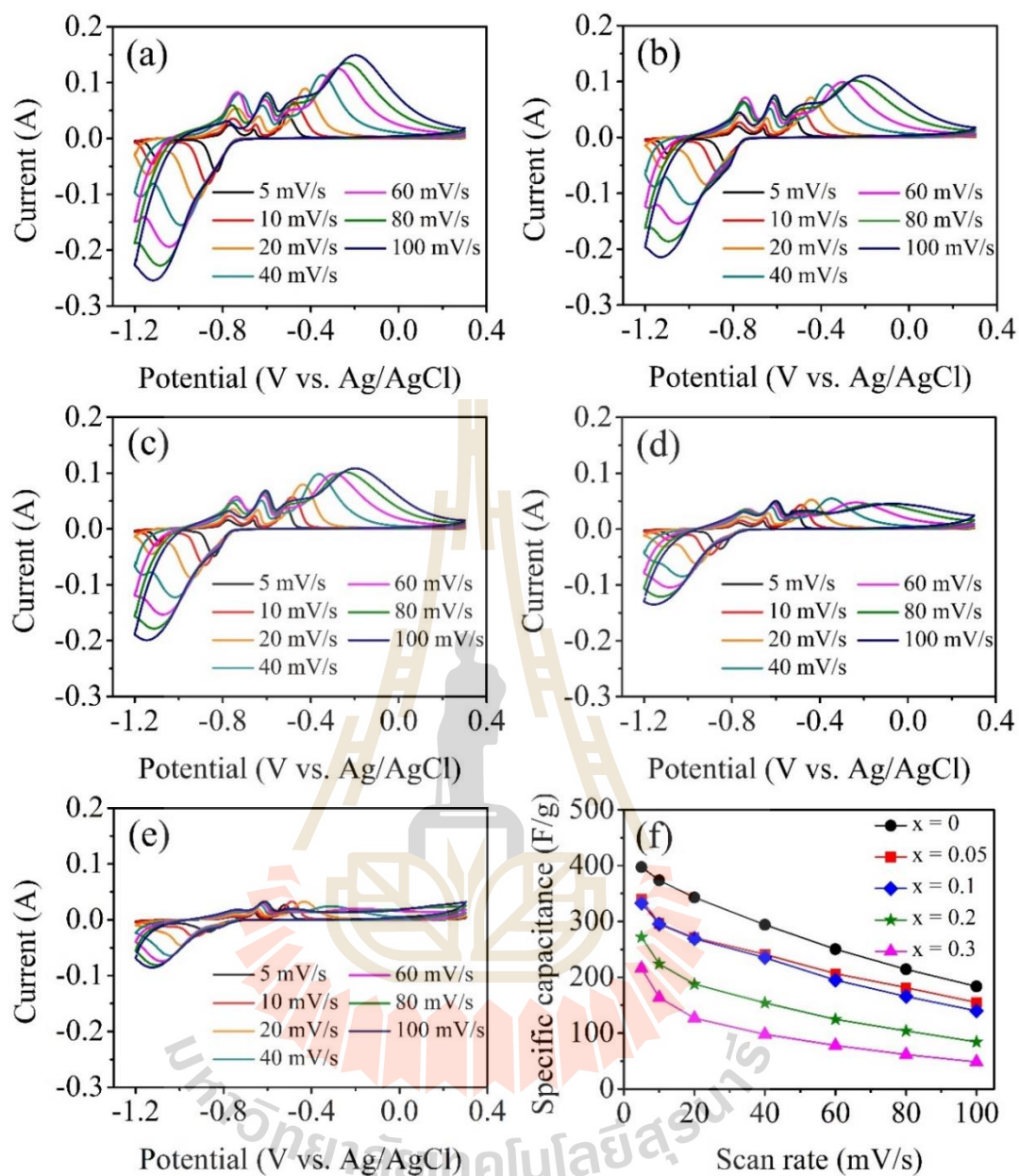


Figure 4.15 CV curves of the BiFe_{1-x}Co_xO₃ nanoparticles: (a) $x = 0$, (b) $x = 0.05$, (c) $x = 0.1$, (d) $x = 0.2$, and (e) $x = 0.3$. (f) Specific capacitance vs scan rate.

Table 4.9 Specific capacitances, number of active sites (N) and diffusion coefficients (D) of $\text{BiFe}_{1-x}\text{Co}_x\text{O}_3$ ($x = 0, 0.05, \text{ and } 0.1$) samples at various scan rates.

Sample	Scan rate (mV/s)	Specific capacitance (F/g)	Number of active site	Diffusion coefficient (cm^2/s) $\times 10^{-16}$
$x = 0$	5	397.28	1.93	2.61
	10	373.65	1.82	2.48
	20	342.79	1.67	2.34
	40	294.02	1.43	2.00
	60	250.26	1.22	1.63
	80	214.23	1.04	1.42
	100	183.67	0.89	1.38
$x = 0.05$	5	339.69	1.65	1.64
	10	296.41	1.44	1.63
	20	270.95	1.32	1.59
	40	241.04	1.17	1.39
	60	206.61	1.00	1.01
	80	181.58	0.88	0.80
	100	155.05	0.75	0.76
$x = 0.1$	5	332.69	1.62	2.01
	10	295.37	1.44	2.00
	20	269.23	1.31	1.96
	40	235.07	1.14	1.51

Table 4.10 Specific capacitances, number of active sites (N), and diffusion coefficients (D) of $\text{BiFe}_{1-x}\text{Co}_x\text{O}_3$ ($x = 0.1, 0.2,$ and 0.3) samples at various scan rates.

Sample	Scan rate (mV/s)	Specific capacitance (F/g)	Number of active site	Diffusion coefficient (cm^2/s) $\times 10^{-16}$
x = 0.1	60	194.90	0.95	1.01
	80	165.83	0.81	0.80
	100	139.93	0.68	0.73
x = 0.2	5	271.93	1.32	1.43
	10	223.93	1.09	1.17
	20	187.79	0.91	0.86
	40	154.17	0.75	0.47
	60	124.89	0.61	0.24
	80	104.17	0.51	0.16
	100	84.23	0.41	0.13
	x = 0.3	5	216.16	1.05
10		163.77	0.80	0.67
20		126.97	0.62	0.33
40		97.96	0.48	0.09
60		78.01	0.38	0.04
80		61.55	0.30	0.03
100		48.61	0.24	0.03

4.1.3.2 Galvanostatic charge-discharge measurements

Galvanostatic charge-discharge measurements were conducted for the electrodes at current densities from 1 to 20 A/g which are shown in Figure 4.16(a)-4.16(e). The specific potential window of -1.2 and 0.3 V is adopted to avoid the hydrogen and oxygen evolution reaction. All samples show the nonlinear form of curves which exhibit the pseudocapacitive behavior of the nanoparticles. The discharge curve consists of a steep voltage (IR) drop due to internal resistance and a capacitive component (curved portion) related to the voltage change due to changes in energy within the capacitor (Fusalba *et al.*, 1999). This IR drop is a common phenomenon occurring in transition metal oxides (Nithya *et al.*, 2013; Yuan *et al.*, 2009). All samples show that current density increases with decreases of the discharge time. The maximum specific capacitance of 232.24 F/g at 1A/g current density was obtained from the undoped samples (Khajonrit *et al.*, 2016). The specific capacitances calculated for different as synthesized samples at different current density from the equation 3.15. The charge-discharge curves, demonstrate the relationship between specific capacitance and current density in Figure 4.16(f). The specific capacitance at all current densities also continuously decreases from $x = 0.05$ to $x = 0.3$, which may be due to the fact that the surface of the electrode is inaccessible at high charge-discharge rates (Lokhande *et al.*, 2007), increasing in ionic resistivity and decreasing in charge diffusion deeper into the inner active sites (Nithya *et al.*, 2013; Senthilkumar *et al.*, 2013). At a current density of 1A/g, all the electrodes exhibited the highest specific capacitance. This indicated that a low current density should be suitable for practical applications for the electrodes. The specific capacitance of the nanoparticles decreases from undoped samples (232.24-88.03 F/g) to BiFe_{0.7}Co_{0.3}O₃ samples (130.17-13.75 F/g) at 1-20A/g, respectively.

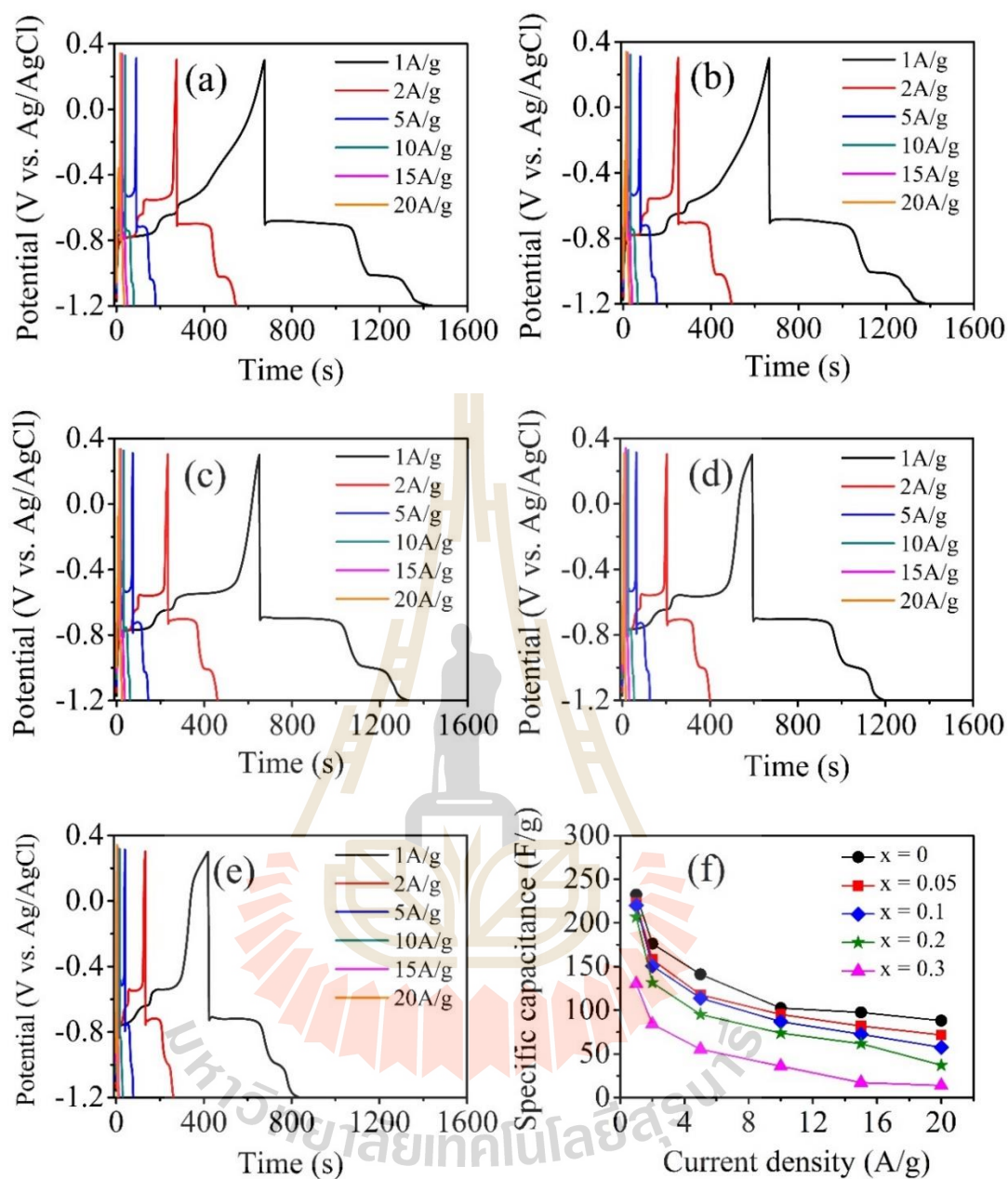


Figure 4.16 Galvanostatic charge-discharge curves of the BiFe_{1-x}Co_xO₃ nanoparticles: (a) $x = 0$, (b) $x = 0.05$, (c) $x = 0.1$, (d) $x = 0.2$, and (e) $x = 0.3$. (f) Specific capacitance vs current density.

Performance with energy density and power density in a Ragone plot of the BiFeO₃ and Co-doped BiFeO₃ electrodes were calculated based on the galvanostatic charge-discharge as shown in Figure 4.17. The energy density are decreased with increasing of Co doping concentration and increasing of current density, while the power density are increased with increasing of current density as shown in Table 4.11-4.12. Among different electrodes, BiFeO₃ electrodes shows highest energy density (72.71 Wh/Kg) at current density of 1 A/g. At the current density of 1 A/g, the power density are increase with Co doping concentration for x = 0 to x = 0.2 samples. The highest power density was observed in Co-doped BiFeO₃ (x = 0.05) electrodes (6197.18 W/Kg) at current densities of 20 A/g.

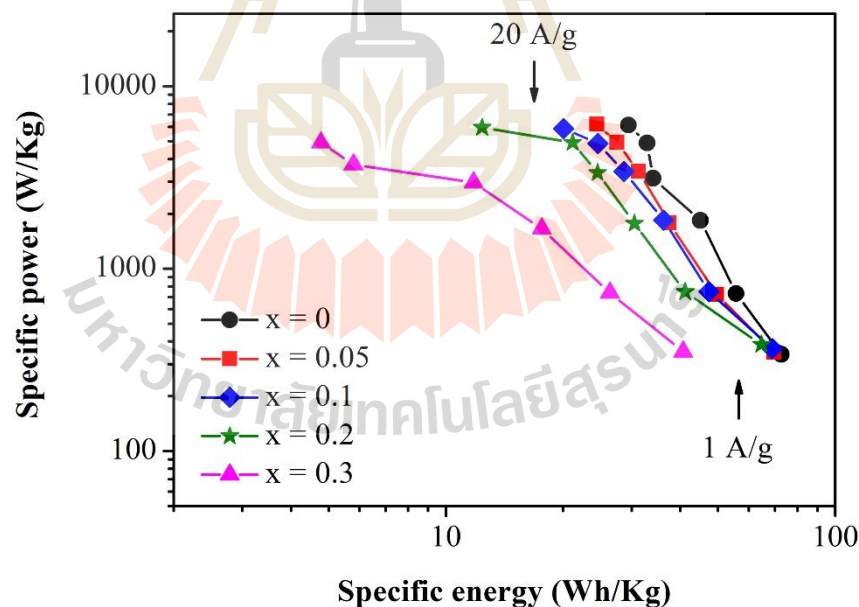


Figure 4.17 Ragone plot showing energy densities and power densities relationship of BiFeO₃ and Co-doped BiFeO₃ electrodes.

Table 4.11 Specific capacitance, energy densities, and power densities of $\text{BiFe}_{1-x}\text{Co}_x\text{O}_3$ ($x = 0, 0.05$, and 0.1) samples at various current densities.

Sample	Current density (A/g)	Specific capacitance (F/g)	Energy density (Wh/Kg)	Power density (W/Kg)
x = 0	1	232.24	72.71	339.48
	2	176.20	55.67	731.64
	5	141.03	45.05	1838.66
	10	102.48	34.04	3133.76
	15	97.54	32.88	4890.50
	20	88.03	29.44	6127.17
x = 0.05	1	222.68	69.69	347.58
	2	157.92	49.60	724.09
	5	117.58	37.49	1785.05
	10	95.12	31.22	3416.41
	15	81.88	27.54	4932.84
	20	71.61	24.44	6197.18
x = 0.1	1	220.08	68.94	364.61
	2	150.75	47.40	748.75
	5	113.75	36.28	1847.24
	10	86.83	28.67	3405.94
	15	72.45	24.58	4862.64
	20	57.37	20.06	5869.92

Table 4.12 Specific capacitance, energy densities, and power densities of $\text{BiFe}_{1-x}\text{Co}_x\text{O}_3$ ($x = 0.2$ and 0.3) sample at various current densities.

Sample	Current density (A/g)	Specific capacitance (F/g)	Energy density (Wh/Kg)	Power density (W/Kg)
x = 0.2	1	206.63	64.64	384.14
	2	131.53	41.17	746.70
	5	95.06	30.51	1771.77
	10	73.79	24.53	3357.41
	15	61.73	21.17	4916.13
	20	36.98	12.39	5946.67
	x = 0.3	1	130.17	40.71
2		84.08	26.39	736.59
5		55.35	17.64	1657.96
10		35.89	11.78	2965.03
15		17.16	5.79	3723.21
20		13.75	4.78	4914.29

Long term cycling stability is important for practical applications for supercapacitors. Endurance of the electrodes was tested up to 500 charge-discharge cycles at a current density of 10 A/g which is shown in Figure 4.18. The capacity retentions of the Co-doped BiFeO_3 samples with $x = 0, 0.1, 0.20,$ and 0.30 were 58.59, 50.40, 28.78, and 25.01 %, respectively, after 500 cycles. Capacity retention can be improved by 5 % Co doping. The $\text{BiFe}_{0.95}\text{Co}_{0.05}\text{O}_3$ electrodes showed higher capacity retention than the BiFeO_3 electrodes. The capacity retention of the $\text{BiFe}_{0.95}\text{Co}_{0.05}\text{O}_3$

electrodes (61.70 %) in this work was lower than that of the $\text{BiFe}_{0.95}\text{Cu}_{0.05}\text{O}_3$ electrodes (77.13 %) (Khajonrit *et al.*, 2016). It decreased to 82 % after 20 cycles and increased to 91 % after 60 cycles, and then slightly decreased to 22% after 500 cycles. The increase in capacity retention of 91% after 60 cycles in this electrode may be due to the additional cycles needed to fully activate the sample (Wei *et al.*, 2010; Vivier *et al.*, 2001).

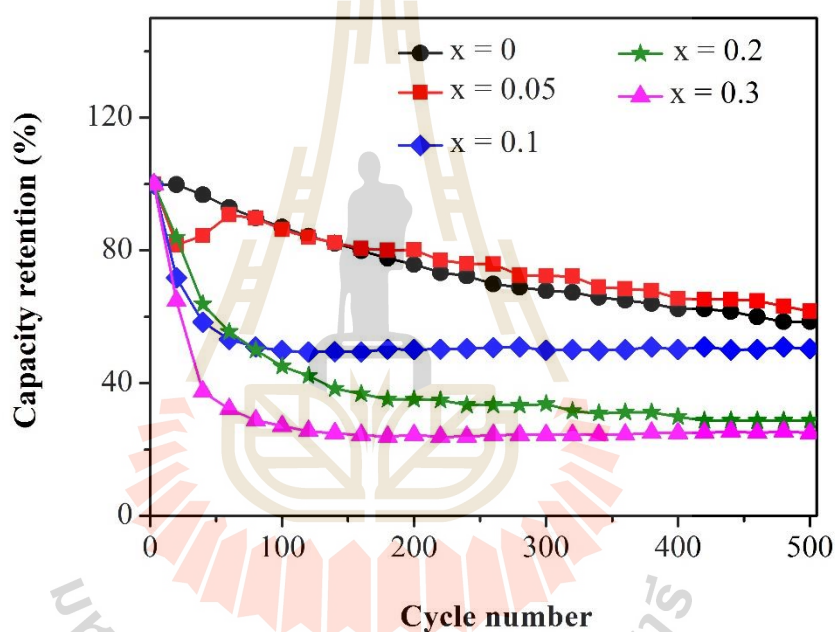


Figure 4.18 Capacity retention (%) of the $\text{BiFe}_{1-x}\text{Co}_x\text{O}_3$ electrodes after 500 cycles at 10A/g current density.

4.1.3.3 Electrochemical impedance spectroscopy (EIS) measurements.

EIS is a very important tool to investigate electrochemical behavior of electrode materials. Figure 4.19 shows Nyquist plots of the nanoparticle electrodes, which consist of the real part (Z') vs an imaginary part (Z'') based on the equivalent circuit having the components of solution resistance (R_s), charge-transfer resistance

(R_{ct}), constant phase element (CPE), and Warburg impedance (W) as shown in Figure 4.20. The intercept in the Z' axis at a high frequency refers to R_s which stands for ohmic resistance of the electrolyte, internal resistance of the electrode material, and contact resistance at the electrode/current collector interface (Nithya *et al.*, 2013). The semicircle diameter at high frequency region corresponds to R_{ct} in which caused by faradic reaction. The small R_{ct} values indicate that all the electrodes providing the charge transfer performance at the electrode/electrolyte interface are facile (Nithya *et al.*, 2013). The slope of the linear curve at low frequency is called the W and was used to describe the frequency dependent of ion diffusion into the bulk of the electrode surface. For not ideal cell or cell with lack of surface homogeneity, the CPE or Q is used. The parameter “N” obtained from CPE is used to observed the quality of the electrode material ($N = 1, 0$, and $0.5 < n < 1$) indicates the ideal capacitors the insulators, and the moderate capacitor behavior, respectively (Yu *et al.*, 2013). In this work, the EIS measurement was collected with a frequency range of 0.1 HZ to 100 KHz. The small values of R_s of the $\text{BiFe}_{1-x}\text{Co}_x\text{O}_3$ ($x = 0, 0.05, 0.1, 0.2$, and 0.3) electrodes are 0.24, 0.27, 0.27, 0.28, and 0.28 Ω , respectively, which suggest that all electrodes provide good electrical conductivity of the electrolyte. The semi-circle at high frequency corresponds to R_{ct} . The R_{ct} of the $\text{BiFe}_{1-x}\text{Co}_x\text{O}_3$ ($x = 0, 0.05, 0.1, 0.2$, and 0.3) electrodes are 0.13, 0.07, 0.08, 0.08, and 0.06 Ω , respectively. The N of the electrodes are in range of 0.747-0.956. This indicated that the electrodes imply the moderate capacitor close to ideal capacitor behavior.

Generally, the high capacitance can be attributed to the high surface area and enhanced electrical conductivity of the electrodes (Guan *et al.*, 2013). But in this work, variations in the specific capacitances and capacity retention of the Co-doped BiFeO_3

electrodes are not attributed to slight increases of surface area and slight differences in the R_{ct} , CPE, W , and R_s values. The straight lines close to 90° are parallel to the imaginary axis at low frequencies which indicate a good capacitive behavior and a low diffusion resistance of the ions in the structure of the electrodes (Guan *et al.*, 2013; Yang *et al.*, 2012; Wang *et al.*, 2011). The more vertical the curve, the more closely the supercapacitor performs as an ideal capacitor. Interestingly, increases in Co doping concentrations with $x = 0$ to $x = 0.3$ correspond to the curves which move away from the vertical line. Thus, the vertical curve of the BiFeO_3 electrodes close to 90° provides a greater capacitance with low diffusion resistance of ions in the structure of the electrodes than for the Co-doped BiFeO_3 samples. This leads to decreases in the specific capacitance in $\text{BiFe}_{1-x}\text{Co}_x\text{O}_3$ with $x = 0$ to $x = 0.3$ samples.

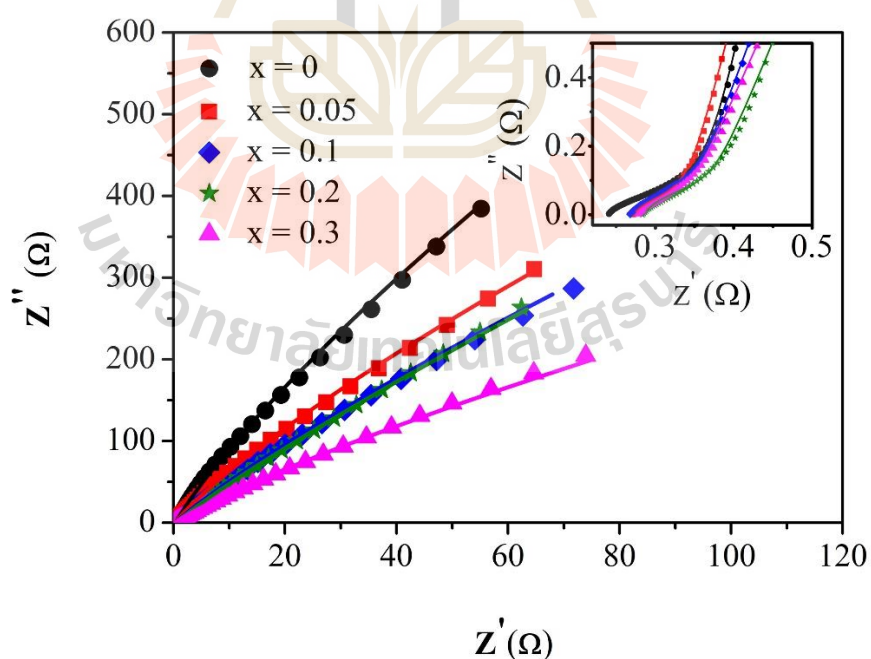


Figure 4.19 Nyquist plots of the $\text{BiFe}_{1-x}\text{Co}_x\text{O}_3$ ($x = 0, 0.05, 0.1, 0.2,$ and 0.3) electrodes.

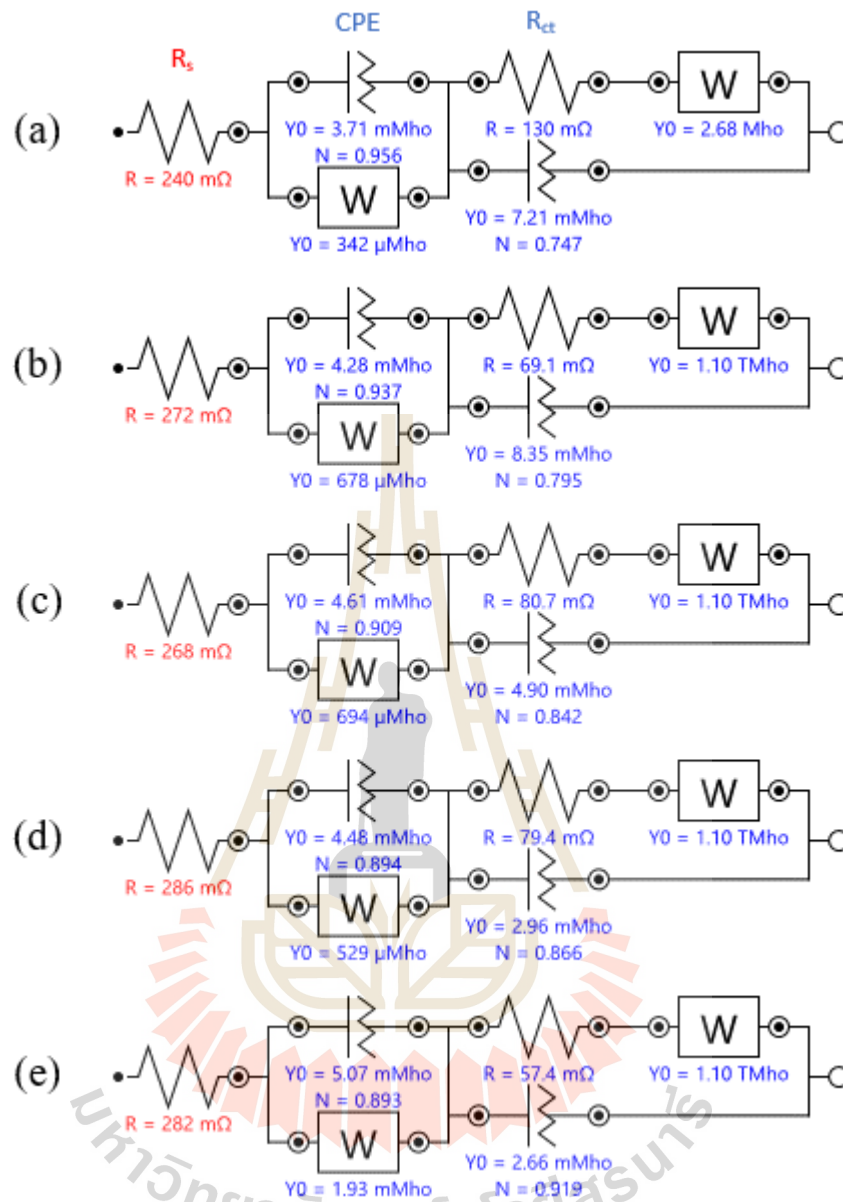


Figure 4.20 Equivalent circuit of the BiFe_{1-x}Co_xO₃ electrodes: (a) $x = 0$, (b) $x = 0.05$, (c) $x = 0.1$, (d) $x = 0.2$, and (e) $x = 0.3$.

4.2 Ni-doped BiFeO₃ nanoparticles

4.2.1 Structural and morphology characterization

4.2.1.1 X-ray diffraction (XRD) analysis of the Ni-doped BiFeO₃ nanoparticles

The XRD patterns of the BiFe_{1-x}Ni_xO₃ ($x = 0, 0.05, 0.1, 0.2,$ and 0.3) nanoparticles calcined at 600 °C for 3 h are shown in Figure 4.21. It can be seen that all the samples are found in the main phase of BiFeO₃ revealing the rhombohedral structure with the space group R3c with the space group R3c (JCPDS No.86-1518). Small impurity peaks of Bi₂Fe₄O₉ (in $x = 0, x = 0.05,$ and $x = 0.1$ samples) with the space group Pbam (JCPDS No.72-1832) and NiFe₂O₄ (in $x = 0.2$ and $x = 0.3$ samples) with the space group R3c (JCPDS No.86-2267) were observed.

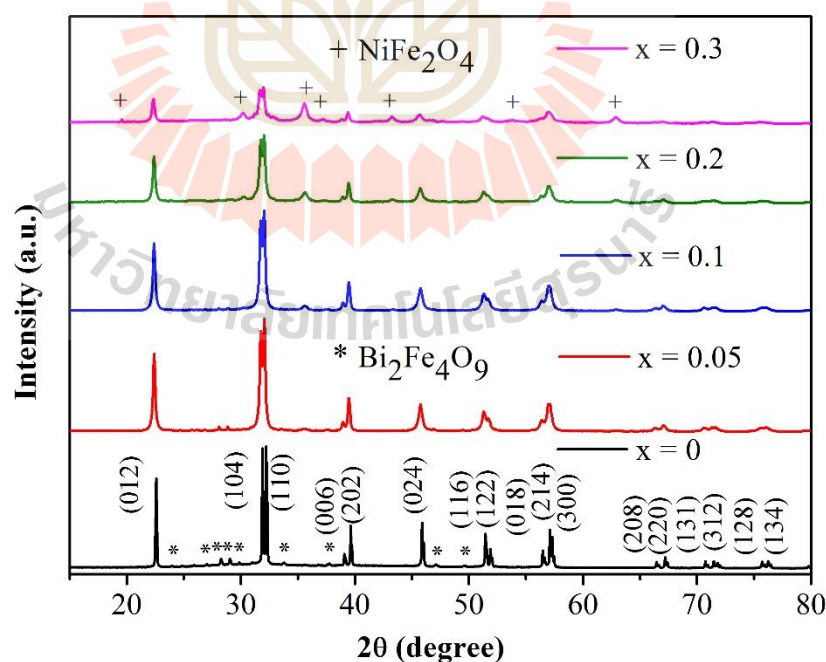


Figure 4.21 XRD patterns of BiFe_{1-x}Ni_xO₃ ($x = 0, 0.05, 0.1, 0.2,$ and 0.3) nanoparticles.

The development of the spinel phase of NiFe_2O_4 helped to prevent the formation of the $\text{Bi}_2\text{Fe}_4\text{O}_9$ phase. A shift in the peak position was observed slight towards the lower angles in the Ni-doped samples. These changes confirm the substitution of the Fe^{3+} ($\sim 0.645 \text{ \AA}$) site with ionic radius of Ni^{2+} (0.69 \AA) (Vanga *et al.*, 2015). The crystallite size of BiFeO_3 is calculated by the Scherrer equation using (012) the peak shown in Table 4.13. The crystallite sizes of 88.8, 40.9, 36.9, 36.2, and 41.1 nm decrease with increasing Ni doping concentrations of $x = 0, 0.05, 0.1, 0.2,$ and $0.3,$ respectively. Figure 4.22-4.24 shows the Rietveld refinement using TOPAS software used to estimate the crystal structure profiles of the $\text{BiFe}_{1-x}\text{Ni}_x\text{O}_3$ ($x = 0, 0.05, 0.1, 0.2,$ and 0.3) nanoparticles. The crystallite size (D), lattice parameters (a and c), unit cell volume (V), crystal density (ρ), phase composition (%) of BiFeO_3 , $\text{Bi}_2\text{Fe}_4\text{O}_9$, and NiFe_2O_4 , residuals of the weighted pattern (R_{wp}) and pattern (R_p), and goodness of fit (GOF) calculated from Rietveld refinement using TOPAS software are shown in Table 12. The reliability of fitting such as R_{wp} , R_p , and GOF is confirmed. The R_{wp} , and R_p values of fitting less than 10 % and the GOF values $\sim 2-3$ indicating acceptable matched between experimental and theoretical XRD pattern for all samples based on rhombohedral unit cell (R3c) of BiFeO_3 . The c -parameter decreases from 13.8743 nm for $x = 0$ to 13.8652 nm for $x = 0.1$. Especially, the increase in a parameter from 5.5793 nm for $x = 0$ to 5.5816 nm for $x = 0.3$, which related with the increasing of Ni doping concentration. These confirm that the Fe^{3+} ($\sim 0.645 \text{ \AA}$) site is substituted with higher ionic radius of Ni^{2+} (0.69 \AA). The crystallite size decreases with increase in concentration of Ni doping, the presence of Ni ion in Fe^{3+} site acts as an inhibitor and results in decrease of crystallite size (Ianculescu *et al.*, 2010; Vanga *et al.*, 2015). The inhibition is mainly due to the decrease in surface energy of BiFeO_3 with addition of dopant, while the bulk

energy remains constant. In order to maintain the ratio between surface area to bulk volume the crystallite size decreases (Castro *et al.*, 2003; Vanga *et al.*, 2015). The quantitative analysis shows that the NiFe_2O_4 phase composition of $\text{BiFe}_{1-x}\text{Ni}_x\text{O}_3$ ($x = 0.05, 0.1, 0.2, \text{ and } 0.3$) samples are 5.4, 14.8, 35.5, and 66.4 %, respectively, and the $\text{Bi}_2\text{Fe}_4\text{O}_9$ phase composition in $x = 0, 0.05, \text{ and } 0.1$ samples are 20.9, 5.1, 4.8 %, respectively.

Table 4.13 List of crystallite sizes (D), lattice parameters (a, c), unit cell volume (V), crystal density (ρ), phase composition of BiFeO_3 , $\text{Bi}_2\text{Fe}_4\text{O}_9$, and NiFe_2O_4 , residuals of the weighted pattern (R_{wp}), pattern (R_{p}), and goodness of fit (GOF) of $\text{BiFe}_{1-x}\text{Ni}_x\text{O}_3$ ($x = 0, 0.05, 0.1, 0.2, \text{ and } 0.3$) nanoparticles.

Parameters	x = 0	x = 0.05	x = 0.1	x = 0.2	x = 0.3
D (nm)	88.8	40.9	36.9	36.2	34.1
a (Å)	5.5793	5.5800	5.5802	5.5811	5.5816
c (Å)	13.8743	13.8659	13.8652	13.8688	13.8743
V (Å) ³	374.0372	373.8975	373.8936	374.1176	374.3944
ρ (g/cm ³)	8.333	8.340	8.343	8.348	8.349
BiFeO_3 (%)	79.12	89.87	80.44	64.47	33.56
$\text{Bi}_2\text{Fe}_4\text{O}_9$ (%)	20.88	5.11	4.77	-	-
NiFe_2O_4 (%)	-	5.42	14.79	35.53	66.44
R_{wp} (%)	7.68	8.48	7.50	8.62	8.06
R_{p} (%)	5.98	6.76	5.89	6.76	6.19
GOF	2.70	2.99	2.75	3.09	3.18

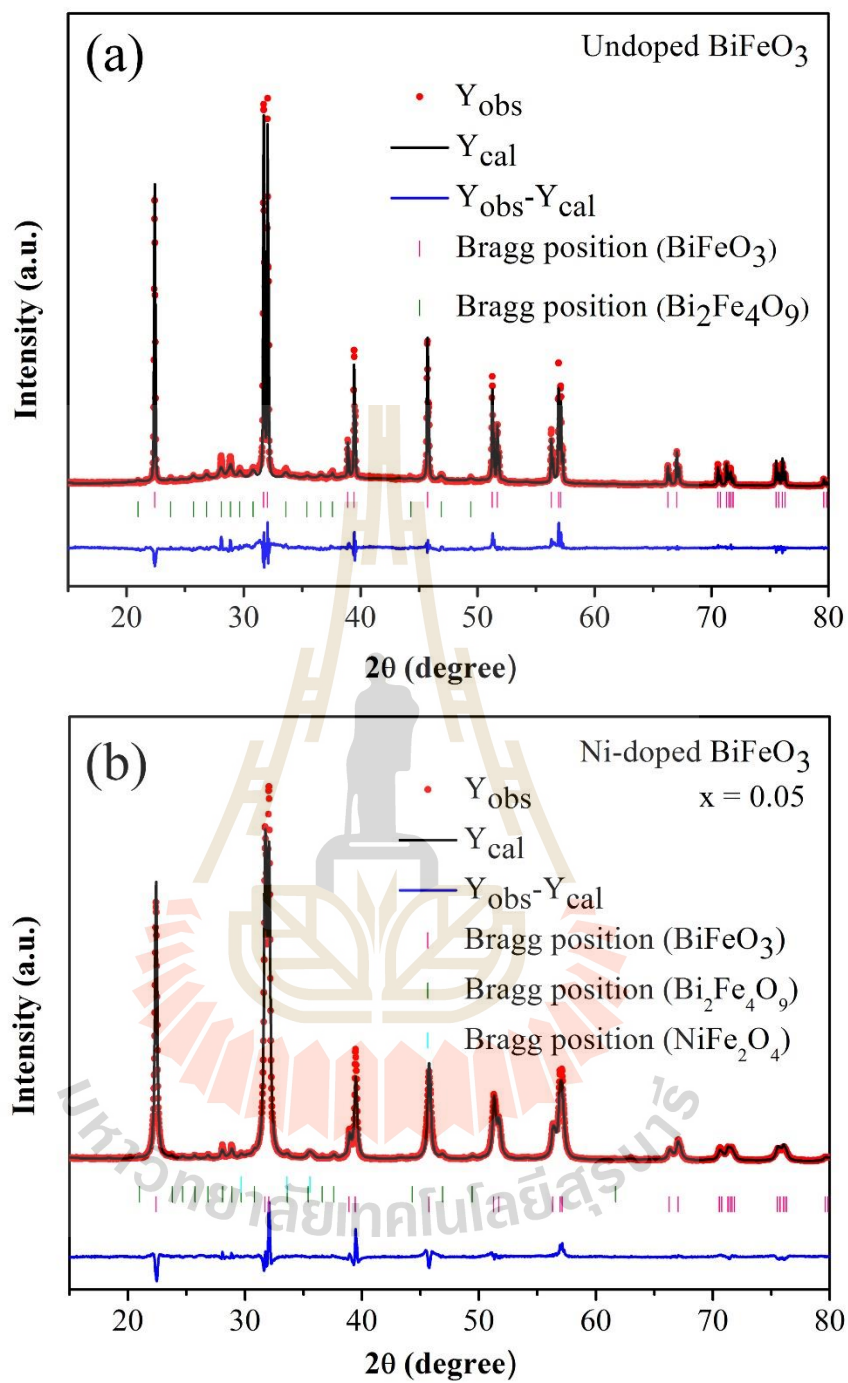


Figure 4.22 Rietveld refinement of XRD data for (a) BiFeO_3 (b) Ni-doped BiFeO_3 ($x = 0.05$) nanoparticle.

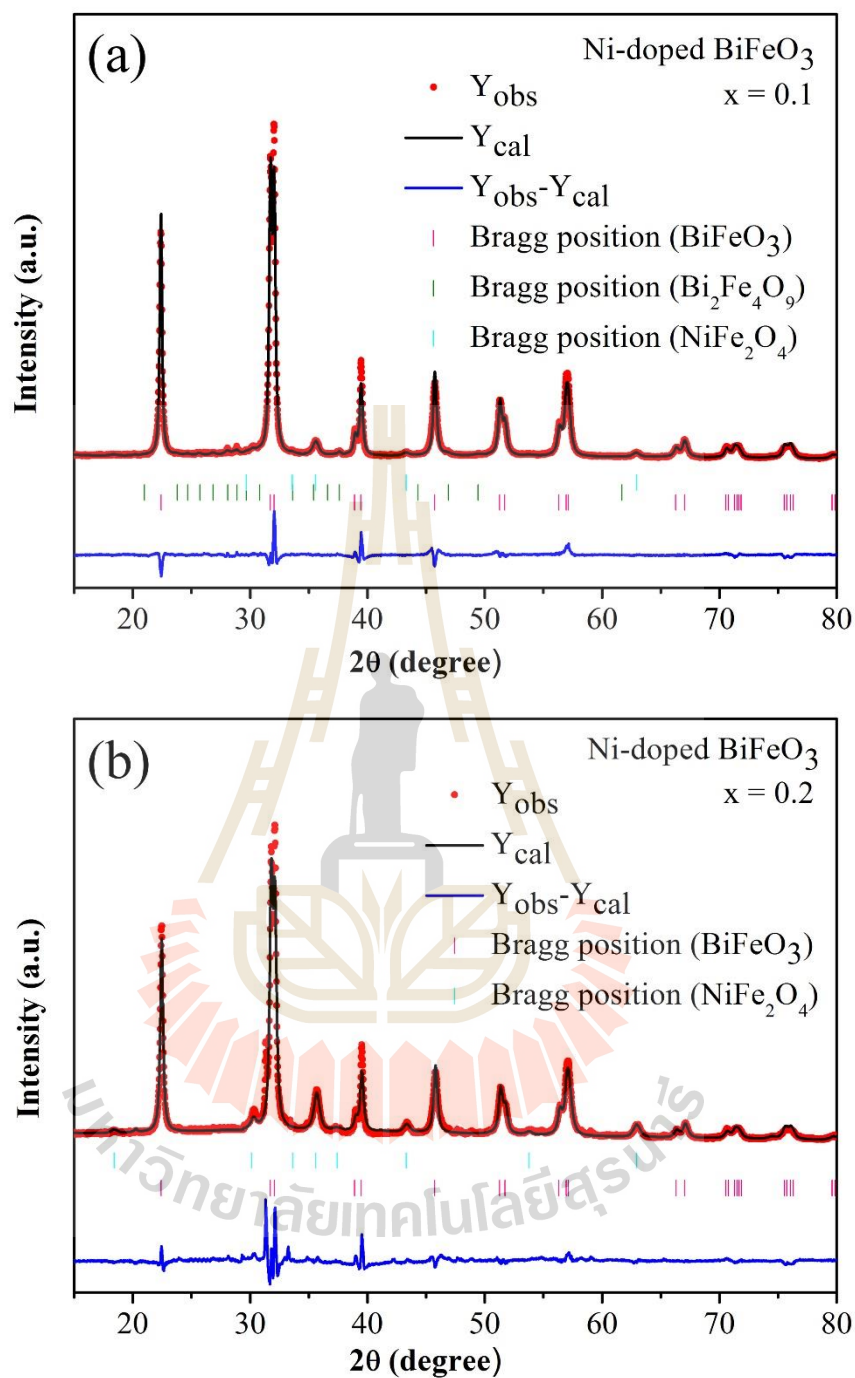


Figure 4.23 Rietveld refinement of XRD data for Ni-doped BiFeO_3 nanoparticle: (a) $x = 0.1$ (b) $x = 0.2$.

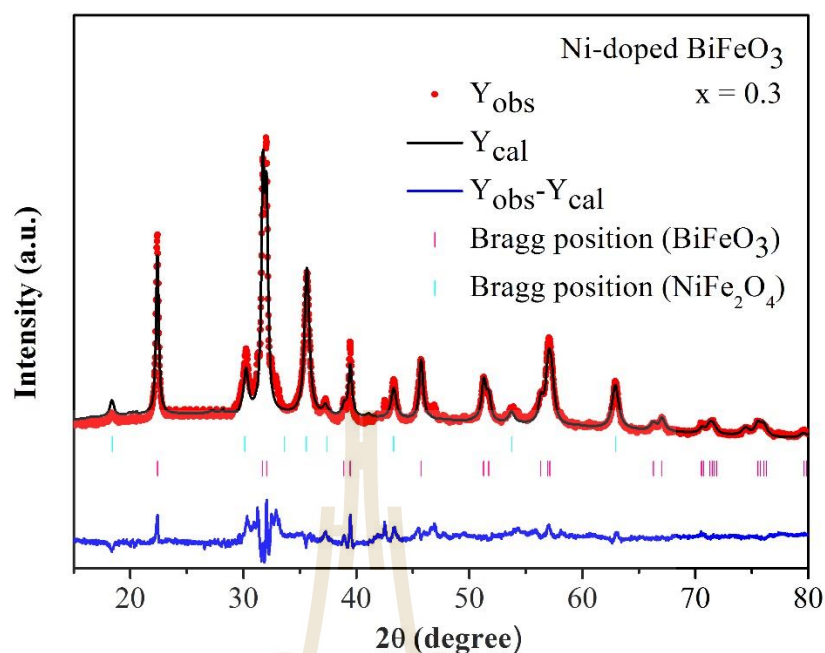


Figure 4.24 Rietveld refinement of XRD data for Ni-doped BiFeO_3 ($x = 0.3$) nanoparticle.

4.2.1.2 Morphology of the Ni-doped BiFeO_3 nanoparticles by SEM and TEM.

Figure 4.25 shows the SEM images revealing the particle sizes of the $\text{BiFe}_{1-x}\text{Ni}_x\text{O}_3$ nanoparticles. The undoped sample shows the nanoparticles sizes to be about 100-200 nm, while the Ni-doped samples show decreasing sizes of nanoparticles of about 50-100 nm. This indicates that Ni doping causes decreasing sizes of the nanoparticles. The mean particle size from the SEM image is in good agreement with the crystallite size measured by using Scherrer's formula.

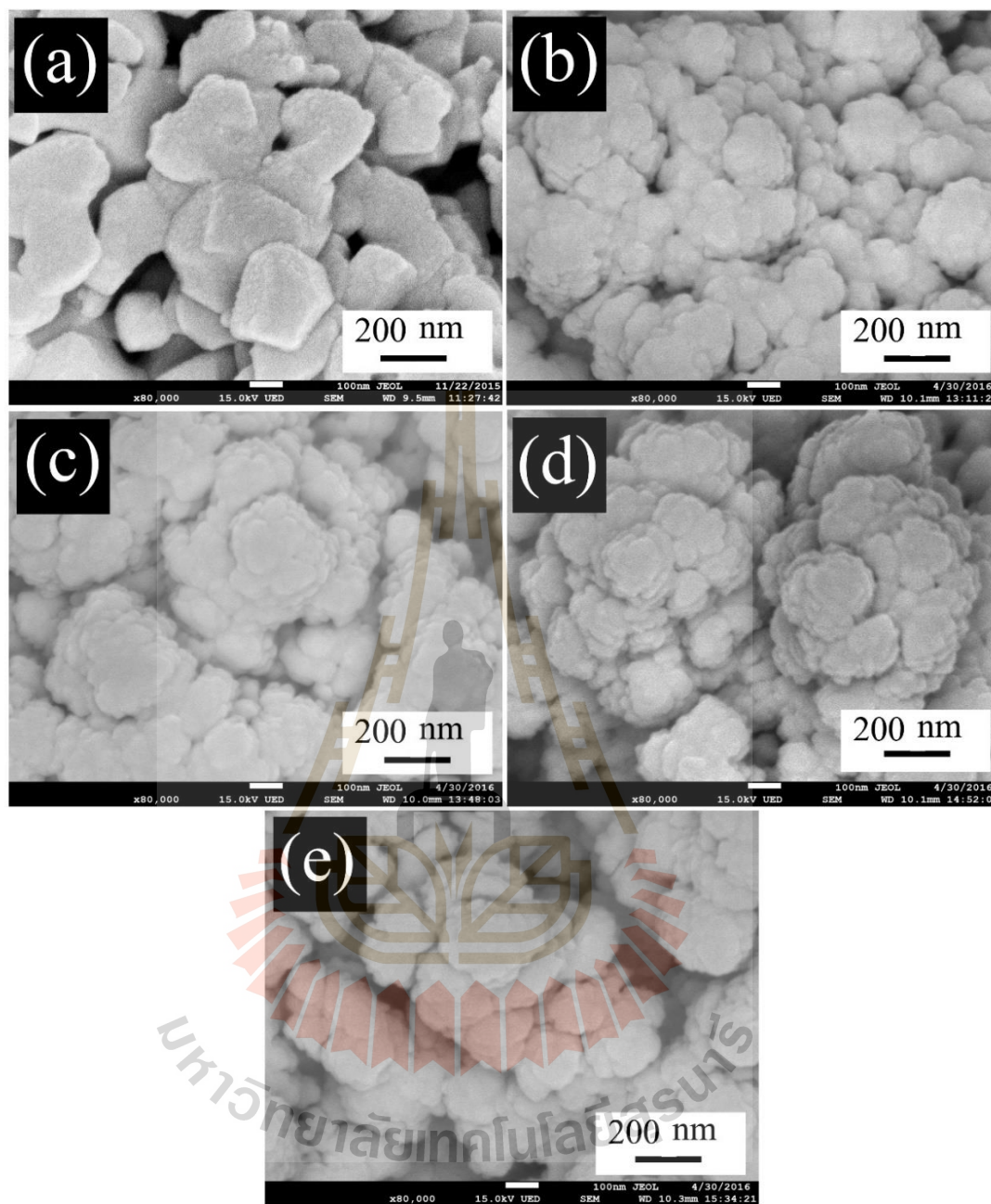
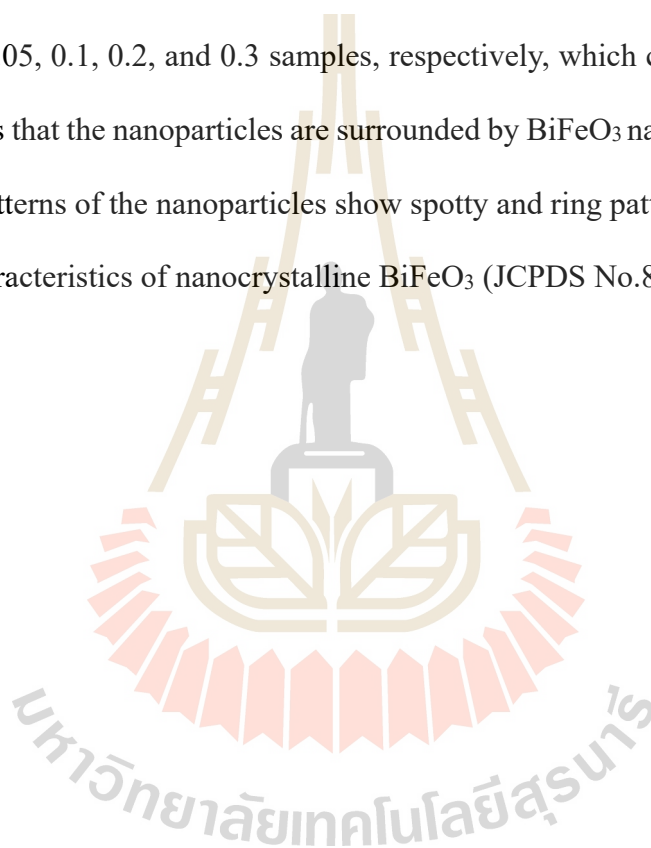


Figure 4.25 SEM images of $\text{BiFe}_{1-x}\text{Ni}_x\text{O}_3$ nanoparticles: (a) $x = 0$, (b) $x = 0.05$, (c) $x = 0.1$, (d) $x = 0.2$, and (e) $x = 0.3$.

The morphology and structure of the BiFeO_3 and Ni-doped BiFeO_3 nanoparticles were investigated by TEM. Bright field TEM images, high-resolution

(HRTEM) images and corresponding selected areas of electron diffraction (SAED) patterns are shown in Figure 4.26. The TEM bright field images show that the particles sizes obtained were about 30-200 nm. This is in agreement with the XRD and SEM results. To better investigate the crystal structure, HRTEM was performed, which shows the lattice fringes of the (104), (202), (104), (012), and (104) planes with interplanar spacing of approximately 0.281, 0.227, 0.281, 0.395, and 0.281 nm of the $\text{BiFe}_{1-x}\text{Ni}_x\text{O}_3$ with $x = 0, 0.05, 0.1, 0.2,$ and 0.3 samples, respectively, which correspond to BiFeO_3 . This indicates that the nanoparticles are surrounded by BiFeO_3 nanocrystals. Moreover, the SAED patterns of the nanoparticles show spotty and ring patterns. The spotty rings show the characteristics of nanocrystalline BiFeO_3 (JCPDS No.86-1518).



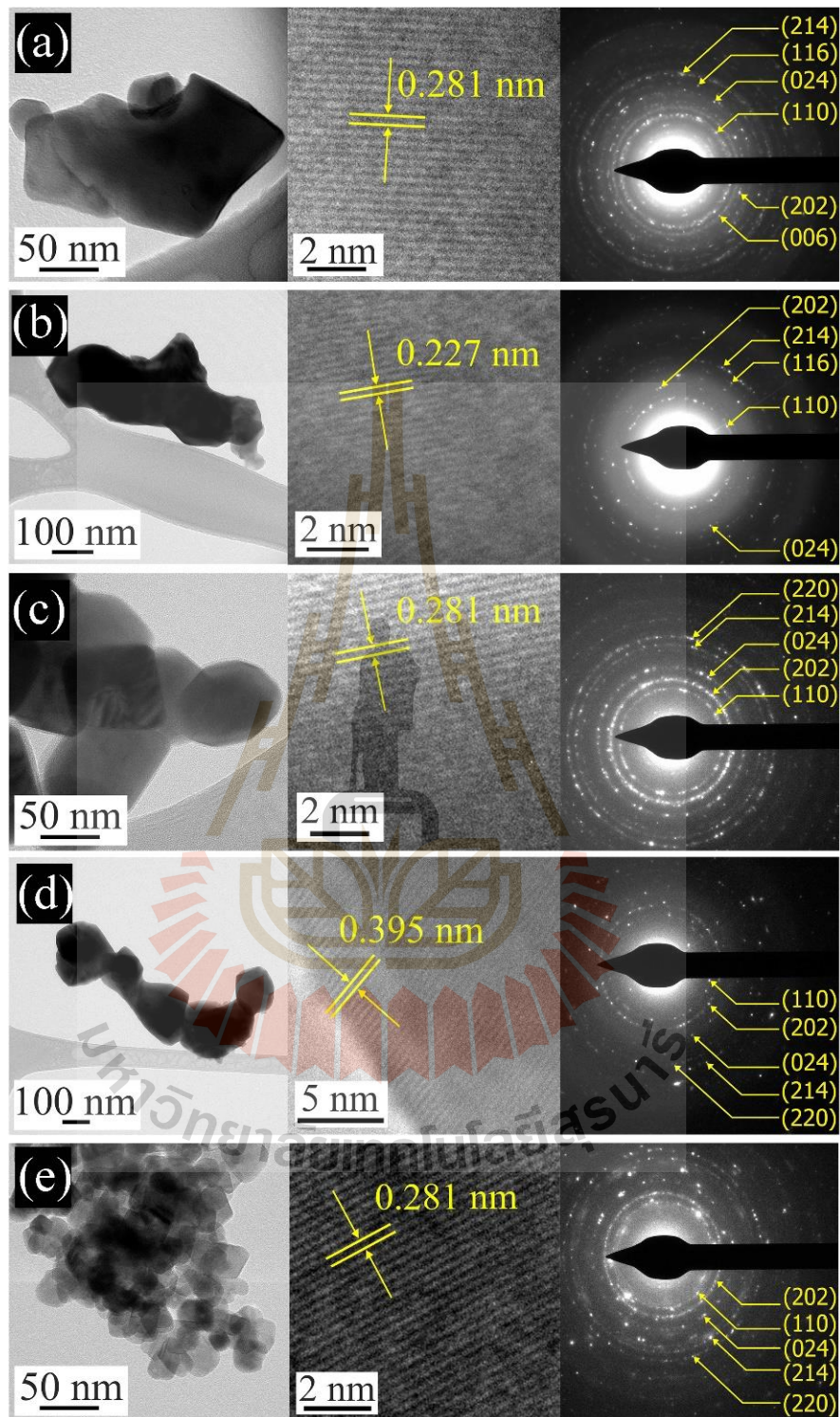


Figure 4.26 Bright field TEM images (left), HRTEM images (middle), and SAED patterns (right) of $\text{BiFe}_{1-x}\text{Ni}_x\text{O}_3$ nanoparticles: (a) $x = 0$, (b) $x = 0.05$, (c) $x = 0.1$, (d) $x = 0.2$, and (e) $x = 0.3$.

4.2.1.3 X-ray absorption spectroscopy study of the Ni-doped BiFeO₃ nanoparticles.

The normalized XANES spectra of Bi *M*₅-edges, Fe *K*-edges and Ni *K*-edge XANES spectra of all samples are shown in Figure 4.27-4.28. The edge energies of Bi *M*₅-edge, Fe *K*-edge, and Ni *K*-edge of BiFe_{1-x}Ni_xO₃ (x = 0.05, 0.1, 0.2, and 0.3) samples are shown in Table 4.14-4.16. The edge energies of Bi *M*₅-edge, Fe *K*-edge, and Ni *K*-edge of BiFe_{1-x}Ni_xO₃ (x = 0.05, 0.1, 0.2, and 0.3) samples are close to the Bi₂O₃, Fe₂O₃, and NiO standard, respectively. The Bi *M*₅-edge XANES spectra of BiFe_{1-x}Ni_xO₃ nanoparticles can be seen with x = 0, 0.05, 0.1, 0.2, and 0.3 as compared with those of the standard materials with Bi oxidation states are shown in Figure 4.27(a). The oxidation states of Bi in all samples are show along with the standard samples of Bi₂O₃ for Bi³⁺. It was found that the position of the absorption edge at Bi *M*₅-edge is similar to Bi₂O₃ which is typical for Bi in the oxidation state of +3. Figure 4.27(b) shows the XANES spectra at the Fe *K*-edge of all the samples, which match that of Fe₂O₃, indicating that the oxidation state of Fe is 3+. The Ni *K*-edge XANES spectra of BiFe_{1-x}Ni_xO₃ nanoparticles can be seen with x = 0.05, 0.1, 0.2, and 0.3 as compared with those of the standard materials with different Ni oxidation states are shown in Figure 4.8. The absorption edge at the Ni *K*-edge of all the samples match those of Ni⁺² of NiO standard samples and the oxidation state of the Ni ion conforms with that of the starting materials (Ni⁺²). Clearly, the XANES analysis provides strong evidence that Ni⁺² of large ionic radius is substituting the Fe³⁺ site.

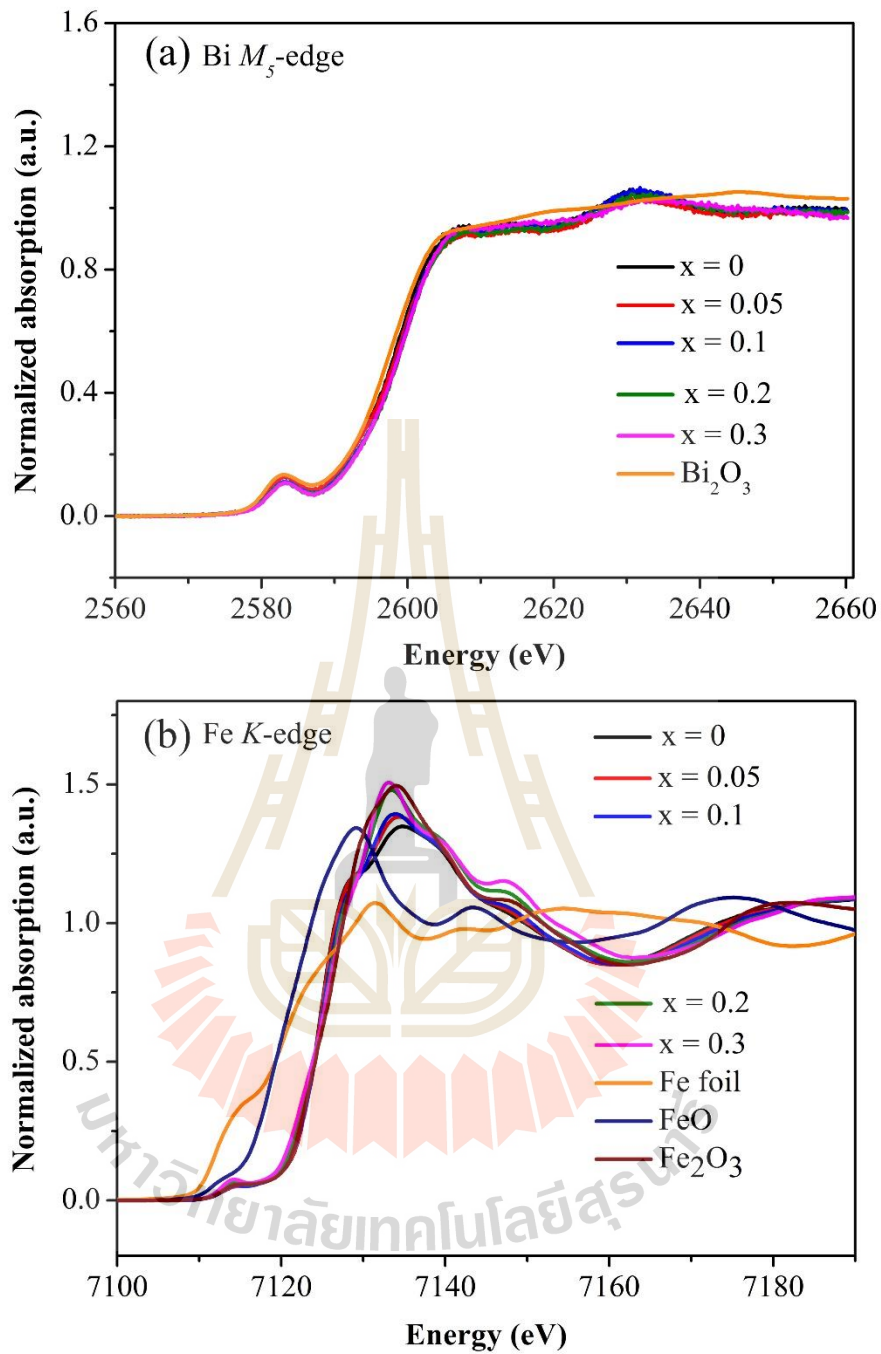


Figure 4.27 XANES spectra of $\text{BiFe}_{1-x}\text{Ni}_x\text{O}_3$ ($x = 0, 0.05, 0.1, 0.2,$ and 0.3) nanoparticles: (a) Bi M_5 -edge and (b) Fe K -edge.

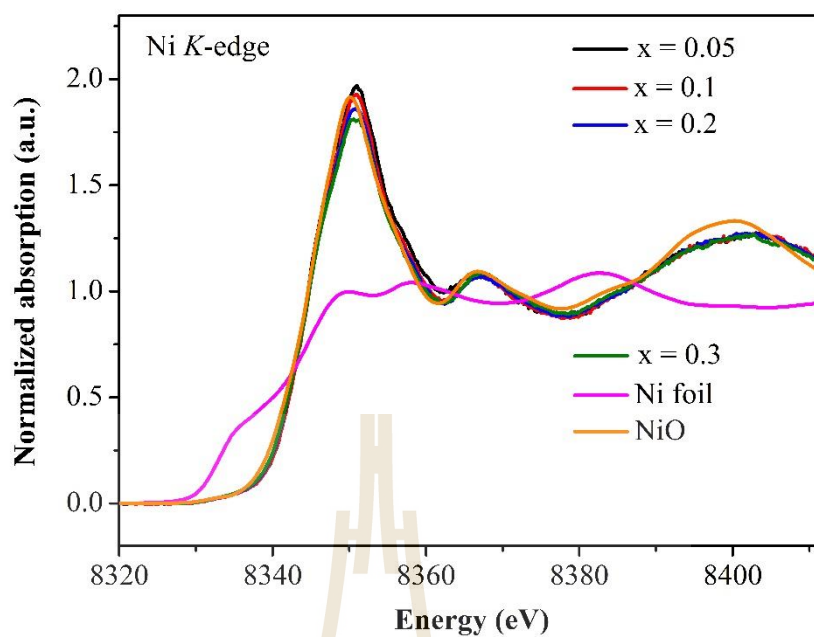


Figure 4.28 XANES spectra at Ni *K*-edge of $\text{BiFe}_{1-x}\text{Ni}_x\text{O}_3$ ($x = 0, 0.05, 0.1, 0.2,$ and 0.3) nanoparticles.

Table 4.14 Absorption edges and oxidation states at Bi *M₅*-edge of all Ni-doped BiFeO_3 samples along with the standard samples.

Samples/standard	Absorption edge at	Edge shift at	Oxidation state
	Bi (eV)	Bi (eV)	
Bi_2O_3	2597.25	0	+3
BiFeO_3	2598.63	1.38	+3
$\text{BiFe}_{0.95}\text{Ni}_{0.05}\text{O}_3$	2598.76	1.51	+3
$\text{BiFe}_{0.9}\text{Ni}_{0.1}\text{O}_3$	2598.65	1.40	+3
$\text{BiFe}_{0.8}\text{Ni}_{0.2}\text{O}_3$	2599.39	2.14	+3
$\text{BiFe}_{0.7}\text{Ni}_{0.3}\text{O}_3$	2599.51	2.26	+3

Table 4.15 Absorption edges and oxidation states at Fe *K*-edge of all Ni-doped BiFeO₃ samples along with the standard samples.

Samples/standard	Absorption edge at Fe (eV)	Edge shift at Fe (eV)	Oxidation state
Fe foil	7112	13.64	0
FeO	7120.87	4.77	+2
Fe ₂ O ₃	7125.64	0	+3
BiFeO ₃	7124.62	1.02	+3
BiFe _{0.95} Ni _{0.05} O ₃	7124.45	1.19	+3
BiFe _{0.9} Ni _{0.1} O ₃	7124.46	1.18	+3
BiFe _{0.8} Ni _{0.2} O ₃	7124.28	1.36	+3
BiFe _{0.7} Ni _{0.3} O ₃	7124.08	1.56	+3

Table 4.16 Absorption edges and oxidation states at Ni *K*-edge of all Co-doped BiFeO₃ samples along with the standard samples.

Samples/standard	Absorption edge at Ni (eV)	Edge shift at Ni (eV)	Oxidation state
Ni foil	8332.82	11.29	0
NiO	8344.11	0	+2
BiFe _{0.95} Ni _{0.05} O ₃	8344.99	0.88	+2
BiFe _{0.9} Ni _{0.1} O ₃	8344.94	0.83	+2
BiFe _{0.8} Ni _{0.2} O ₃	8344.44	0.33	+2
BiFe _{0.7} Ni _{0.3} O ₃	8344.26	0.15	+2

4.2.1.4 Characterization of surface area and pore size distribution of the Ni-doped BiFeO₃ nanoparticles by BET method and BJH method

The N₂ adsorption-desorption isotherms and pore size distributions obtained by the BJH plot of BiFe_{1-x}Ni_xO₃ nanoparticles with x = 0, 0.05, 0.1, 0.2, and 0.3 are shown in Figure 4.29. Figure 4.29(a) shows features of N₂ adsorption-desorption isotherms. The hysteresis loop features of all samples are characteristic of non-porous with low adsorbate-sample surface interaction. The presences of micropores and mesopores in particles are shown by the BJH curve (Figure 4.29 (b)). This may be related to capacitance and capacity retention, which will be discussed in Section 4.2.3. Table 4.17 shows the specific surface area (S_{BET}), the mean pore diameter (D_{MP}), the total pore volume (V_{TP}), and the particle size (D_{BET}) of BiFe_{1-x}Ni_xO₃ (x = 0, 0.05, 0.1, 0.2, and 0.3) nanoparticles. In general, the decrease in the size of BiFeO₃ nanoparticles is related to an increase in surface area (Park *et al.*, 2007). In this research, the decreases in the crystallite size led to a sharp increase in the surface area from 3.64 m²/g of the BiFeO₃ sample to 21.6 m²/g in the BiFe_{0.7}Ni_{0.3}O₃ sample. The particle size decreases from 197.8 nm for un-doped samples to 32.9 nm for 30 % Ni-doped samples were calculated by using the gas absorption technique. A comparison of the average crystallite size calculated by XRD and the average particle size estimated by BET showed that the average particle size calculated by BET is larger than the crystallite size calculated by XRD in all samples except for the BiFe_{0.95}Ni_{0.05}O₃ sample as shown in Figure 4.30. The difference in the results occurs from aggregates and/or agglomerates of crystals, which indicates that the particles include several crystallites (Gaber *et al.*, 2014).

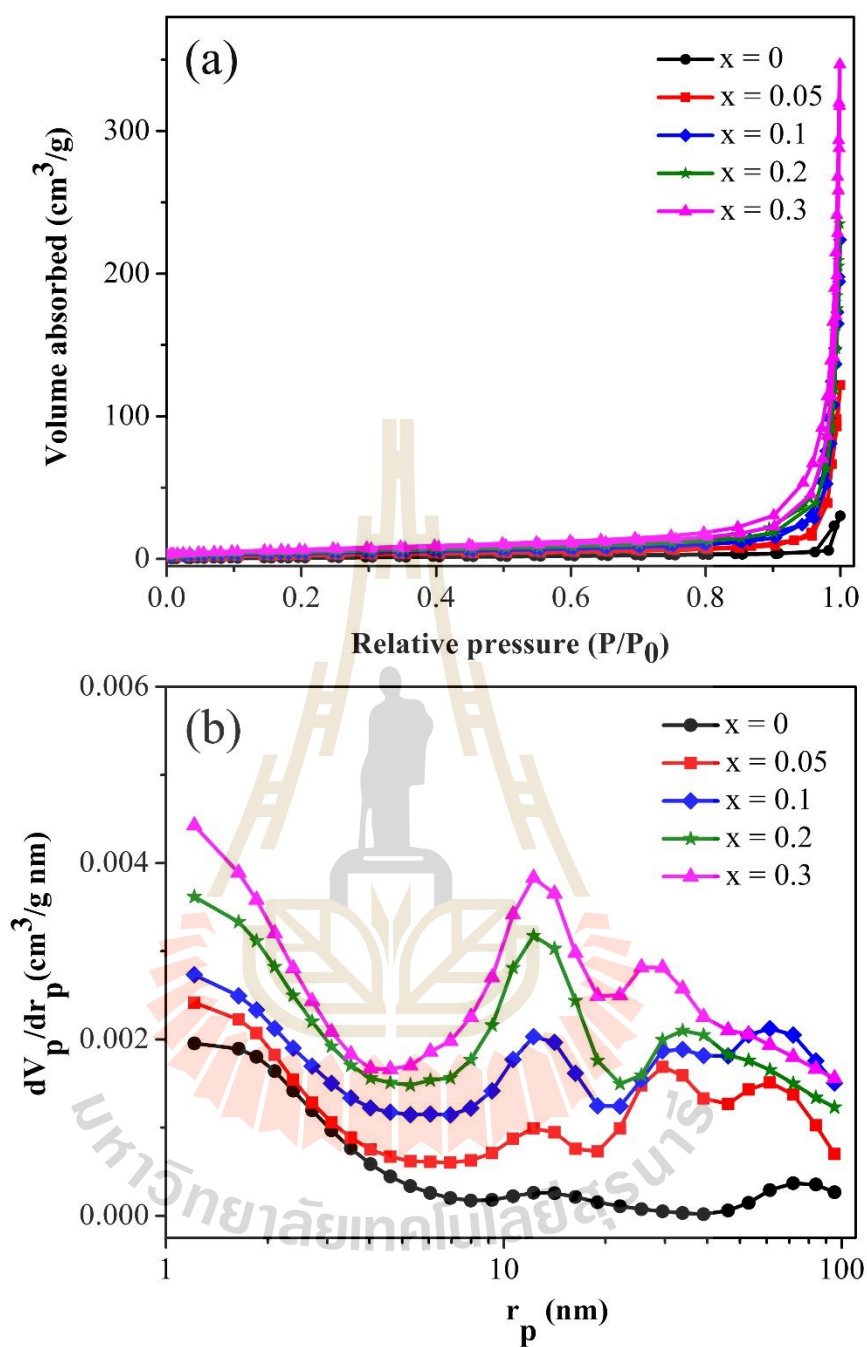


Figure 4.29 N_2 adsorption-desorption isotherms (a) and pore-size distribution (b) of the $\text{BiFe}_{1-x}\text{Ni}_x\text{O}_3$ nanoparticles.

Table 4.17 Specific surface area (S_{BET}), mean pore diameter (D_{MP}), total pore volume (V_{TP}), particle size (D_{BET}) of $\text{BiFe}_{1-x}\text{Ni}_x\text{O}_3$ ($x = 0, 0.05, 0.1, 0.2, \text{ and } 0.3$) nanoparticles.

Samples	S_{BET} (m^2/g)	D_{MP} (nm)	V_{TP} (cm^3/g)	D_{BJH} (nm)	D_{BET} (nm)
BiFeO_3	3.64	25.55	0.0254	3.28	197.81
$\text{Bi}_{0.95}\text{Ni}_{0.05}\text{O}_3$	9.47	49.63	0.1175	2.42	75.99
$\text{Bi}_{0.9}\text{Ni}_{0.1}\text{O}_3$	14.01	49.91	0.1748	24.48	51.33
$\text{Bi}_{0.8}\text{Ni}_{0.2}\text{O}_3$	17.65	39.07	0.1724	24.48	40.72
$\text{Bi}_{0.7}\text{Ni}_{0.3}\text{O}_3$	21.85	39.52	0.2159	24.48	32.89

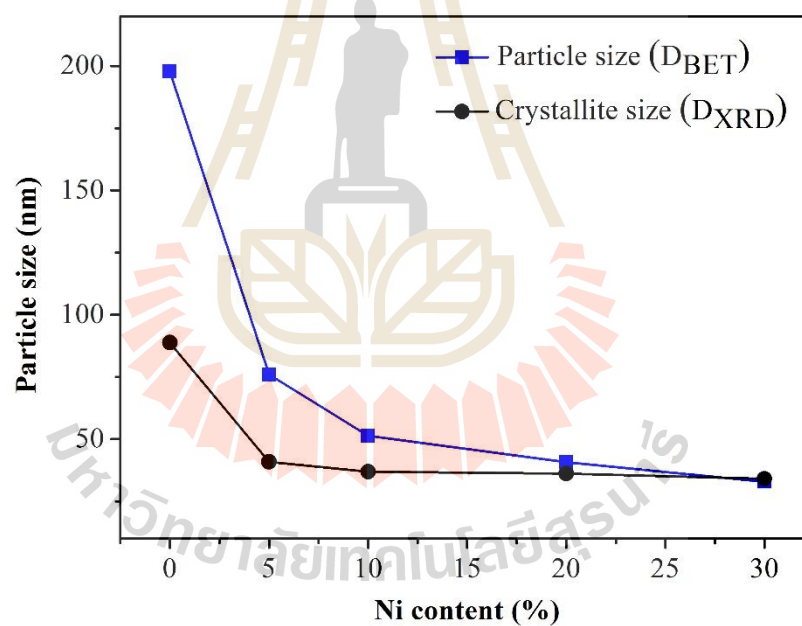


Figure 4.30 Variations of crystallite size calculated by XRD and particle size calculated from BET of $\text{BiFe}_{1-x}\text{Ni}_x\text{O}_3$ nanoparticles as a function of Ni content (%).

4.2.2 Magnetic properties of the Ni-doped BiFeO₃ nanoparticles

The magnetic hysteresis (M-H) loops of the BiFe_{1-x}Ni_xO₃ ($x = 0, 0.05, 0.1, 0.2,$ and 0.3) nanoparticles at 50, 100, 200, 300, and 350 K of temperature are shown in Figure 4.31(a)-4.31(e). Figure 4.31(f) shows the saturation magnetization (M_s) increases linearly with increasing Ni doping concentrations at all temperatures. Interestingly, the magnetization of BiFeO₃ decreases with decreasing temperature. Conversely, the magnetizations of BiFe_{1-x}Ni_xO₃ ($x = 0.05, 0.1, 0.2,$ and 0.3) samples increases with decreasing temperature from 350 to 50 K. The BiFe_{0.7}Ni_{0.3}O₃ sample at a low temperature (50 K) shows the highest magnetization of 22.12 emu/g. The secondary phase of Bi₂Fe₄O₉ in the $x = 0$ to $x = 0.1$ samples does not influence the increases of the M_s because it exhibits an antiferromagnetic nature with a very low M_s , as reported previously (Wang *et al.*, 2009; Rao *et al.*, 2015; Lin *et al.*, 2015). By comparison, the magnetization of the BiFe_{1-x}Ni_xO₃ ($x = 0.05, 0.1, 0.2,$ and 0.3) samples in this study at room temperature were 0.51, 6.43, 12.20, and 19.12 emu/g and at 50 K of temperature were 2.87, 7.45, 14.12, and 22.12 emu/g, respectively. These results were found to be higher than those reported in the literature, which were 5 % and 25% Ni-doped BiFeO₃ at 50 K of temperature (1.29 and 8.04 emu/g) (Zhao *et al.*, 2013), 10 % Ni-doped BiFeO₃ at room temperature (~3.04 emu/g) (Kumar and Yadav, 2011), and 5% Ni-doped BiFeO₃ at room temperature (~1.4 emu/g) (Wang and Qi, 2012). The observed increases in the magnetization may arise for three reasons: (1) the magnetization is increasing linearly with increasing of the magnetic source (Ni) content. (2) The magnetization is mainly dependent on the Ni content which provides strong evidence of the effects of the sizes of the BiFeO₃ nanoparticles. It is known that particles on the nanoscale exhibit significantly different properties from bulk BiFeO₃

(Zhang *et al.*, 2005). Improving magnetization may be due to suppression of the spin cycloid structure of the particle size when it is less than 62 nm which causes the intrinsic spiral spin structure to be incompletely suppressed and the decreases in crystallite size with increases of Ni content results in an increase in surface-volume ratio and the contribution of uncompensated spin at the surface to the total magnetic moment of the particle increases. (3) The high M_s of NiFe_2O_4 nanoparticles are between 32.1 to 49.1 emu/g measured at 300 to 80 K of temperature, respectively (George *et al.*, 2006). So, the increases of the secondary phase of the NiFe_2O_4 nanoparticles in the $\text{BiFe}_{1-x}\text{Ni}_x\text{O}_3$ ($x = 0.05$ to 0.3) samples may cause an increase in saturation magnetization with a decrease in grain size (Morr and Haneda, 1981; Chinnasamy *et al.*, 2001; George *et al.*, 2006).

All the samples show the hysteresis loops are field dependent on magnetization measurements indicating weak ferromagnetism with the coercivity (H_c) between 5.51 to 524.34 Oe. The H_c value shows increases with decreases of temperature in all samples. At low temperature (50 K), the BiFeO_3 sample shows the highest H_c value of 524.35 Oe. The H_c of all samples increases with low measurements of temperature which may occur for two reasons: (1) an increase in H_c is the alignment of the magnetic moment in the direction of the external magnetic field and (2) thermal fluctuations of nanoparticles decrease with decreases in the temperature (Khan *et al.*, 2015). At higher temperatures (350 K), $\text{BiFe}_{0.8}\text{Ni}_{0.2}\text{O}_3$ shows the lowest H_c value of 5.51 Oe. The variations of H_c correspond to the crystallite size, which is in the multi-domain region. The particle size dependence on coercivity can be expressed by the equation 4.1. Thus, the coercivity may decrease with an increase in particle size above a critical size. The H_c of BiFeO_3 and $\text{BiFe}_{0.95}\text{Ni}_{0.05}\text{O}_3$ samples decrease due to a increase in the crystallite

size of BiFeO₃ and an increase in temperature. This conform to the crystallite-size and the temperature-dependent behavior of BiFeO₃ (Park *et al.*, 2007). The phase composition of NiFe₂O₄ may influence H_c in the BiFe_{1-x}Ni_xO₃ (x = 0.05 to x = 0.3) samples. The H_c values of NiFe₂O₄ nanoparticles are between 50 Oe at 300 K and 263 Oe at 80 K (George *et al.*, 2006). The NiFe₂O₄ has a critical size of 13 to 15nm corresponding to the formation of single domain particles (George *et al.*, 2006). In this research, the crystallite sizes of the NiFe₂O₄ nanoparticles were 42.7, 20.9, 32.1, and 26.1 nm of BiFe_{1-x}Ni_xO₃ (x = 0.05, 0.1, 0.2, and 0.3, respectively) samples. The variations in the H_c values of BiFe_{1-x}Ni_xO₃ (from x = 0.1 to x = 0.3) samples at 150 to 350 K are related to the variations in the crystallite sizes of the NiFe₂O₄ nanoparticles, especially the decreases of H_c in the BiFe_{0.8}Ni_{0.2}O₃ samples. The remanent magnetization (M_r) increases with increases of the Ni content due to decreases in the crystallite size of BiFeO₃ at all temperatures, except in x = 0.2 sample at 300 and 350 K, which may be due to the increases of the crystallite size of the NiFe₂O₄ nanoparticles. Clearly, this is evidence that the size effects of BiFeO₃ and NiFe₂O₄ are strongly influenced by the H_c and M_r values of the BiFe_{1-x}Ni_xO₃ nanoparticles.

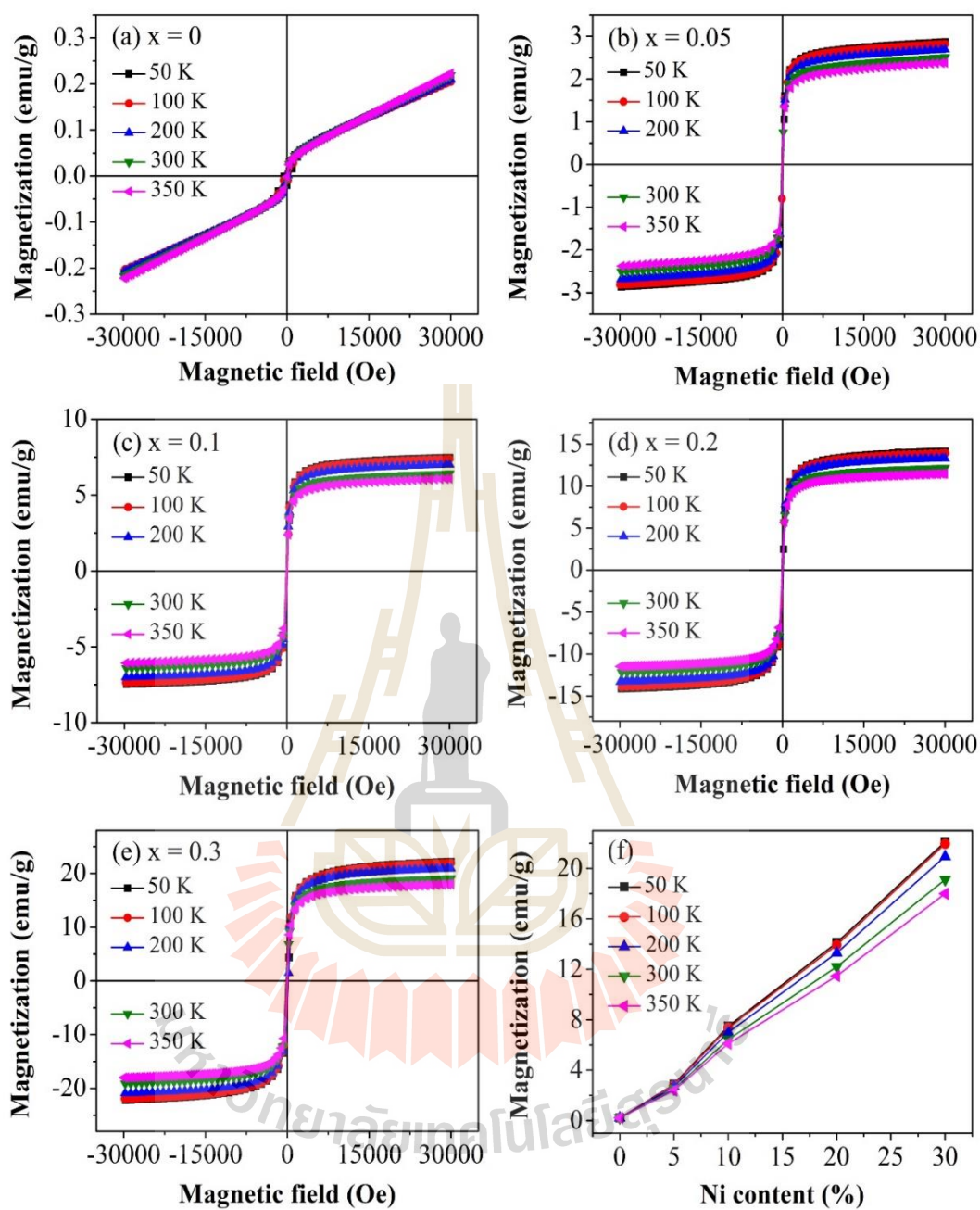


Figure 4.31 Magnetization hysteresis loops at different temperature of $\text{BiFe}_{1-x}\text{Ni}_x\text{O}_3$ nanoparticles: (a) $x = 0$, (b) $x = 0.05$, (c) $x = 0.1$, (d) $x = 0.2$, and (e) $x = 0.3$. (f) Variations in saturation magnetization as a function of Ni content (%).

Table 4.18 Coercivity (H_c), saturation magnetization (M_s) and remanant magnetization (M_r) values of $\text{BiFe}_{1-x}\text{Ni}_x\text{O}_3$ ($x = 0, 0.05, 0.1, \text{ and } 0.2$) samples at different temperatures.

Sample	T (K)	H_c (Oe)	M_s (emu/g)	M_r (emu/g)
x = 0	50	524.35	0.207	0.019
	100	342.73	0.210	0.017
	200	108.14	0.206	0.010
	300	52.85	0.219	0.005
	350	30.59	0.223	0.004
x = 0.05	50	90.56	2.869	0.505
	100	46.00	2.815	0.269
	200	30.21	2.692	0.184
	300	13.07	2.512	0.063
	350	10.68	2.383	0.053
x = 0.1	50	68.42	7.482	0.805
	100	59.75	7.365	0.796
	200	40.12	7.005	0.576
	300	31.79	6.432	0.461
	350	25.81	6.105	0.265
x = 0.2	50	96.68	14.116	2.315
	100	43.83	13.933	1.231
	200	25.44	13.298	0.746
	300	5.58	12.199	0.224
	350	5.51	11.470	0.150

Table 4.19 Coercivity (H_c), saturation magnetization (M_s) and remanant magnetization (M_r) values of $\text{BiFe}_{1-x}\text{Ni}_x\text{O}_3$ ($x = 0.3$) samples at different temperatures.

Sample	T (K)	H_c (Oe)	M_s (emu/g)	M_r (emu/g)
x = 0.3	50	166.74	22.118	4.442
	100	108.50	21.950	3.171
	200	40.67	20.939	1.605
	300	23.39	19.121	0.646
	350	10.31	17.995	0.411

The ZFC (zero field cooling) and FC (field cooling) magnetization curves of the $\text{BiFe}_{1-x}\text{Ni}_x\text{O}_3$ ($x = 0, 0.05, 0.1, 0.2,$ and 0.3) samples are shown in Figure 4.32-4.34, which measured 50 K to 350 K in the applied field 500 Oe. The FC curves of the Ni-doped BiFeO_3 samples increases in magnetization with a lowering of temperature from 350 to 50 K. This may be attributed to the development of the incommensurate sinusoidal spin structure (Naik and Mahendiran, 2009). The decreases in the magnetization of the ZFC curves with a lowering of temperature for $x = 0$ samples and Ni-doped BiFeO_3 samples suggest a antiferromagnetic property (Kumar and Yadav, 2011). Temperature broad maximum magnetization of un-doped BiFeO_3 and $\text{BiFe}_{1-x}\text{Ni}_x\text{O}_3$ ($x = 0.05, 0.1, 0.2,$ and 0.3) samples are ~ 250 K and $\sim 148, 154, 185,$ and 210 K, respectively. The feature of the ZFC curves of all samples show a prominent and broad magnetization maximum, which can be attributed to the magnetic blocking mechanism. However, the blocking temperatures (T_B) of the Ni-doped BiFeO_3 nanoparticles are increased with increasing of Ni doping. The splitting of ZFC and FC magnetizations at low temperature also reveals spin-glass transition in BiFeO_3 (Singh *et al.*, 2008). The

deviation between ZFC and FC of all sample increases with decreases in temperature. The ZFC and FC curves of $x = 0, 0.05, 0.1, 0.2,$ and 0.3 samples exhibit an irreversible thermomagnetization process below $\sim 287, 239, 264, 333,$ and 310 K, respectively. The temperature dependence of the inverse magnetic susceptibility, $1/\chi$, and the fitting curves are shown in the inset of Figure 4.32-4.34. The experimental is fitted data according to the Curie-Weiss law. The Curie constant (C) are $35.73, 699.12, 1911.38, 4459.63,$ and 7000.50 emu K/g Oe for $x = 0, 0.05, 0.1, 0.2,$ and 0.3 samples, respectively, which increase with increasing of Ni doping concentration. The Curie-Weiss temperature (θ) value obtained from the Curie-Weiss fit of undoped-BiFeO₃ at $T = 50-130$ K and $T = 250-350$ K and Ni-doped BiFeO₃ at $T = 250-350$ K are shown in Table 4.18. This negative values of the θ of all samples indicated the antiferromagnetic characteristics with weak FM and without FM component. By fitting with Curie-Weiss law, the theoretical effective moment can compute from Curie constant (C). The effective magnetic moment (μ_{eff}) values from experiment of the un-doped BiFeO₃ and Ni-doped BiFeO₃ samples with $x = 0.05, 0.1, 0.2,$ and 0.3 are shown in Table 4.20. The μ_{eff} values are increase with increasing of Ni doping. The μ_{eff} values obtained from experiment for all samples are higher than the theoretical values of high-spin Fe³⁺ ($5.92 \mu_B$) and low-spin Fe³⁺ ($1.73 \mu_B$). This fitting results from the experiment indicated that Fe³⁺ must be in a high spin configuration.

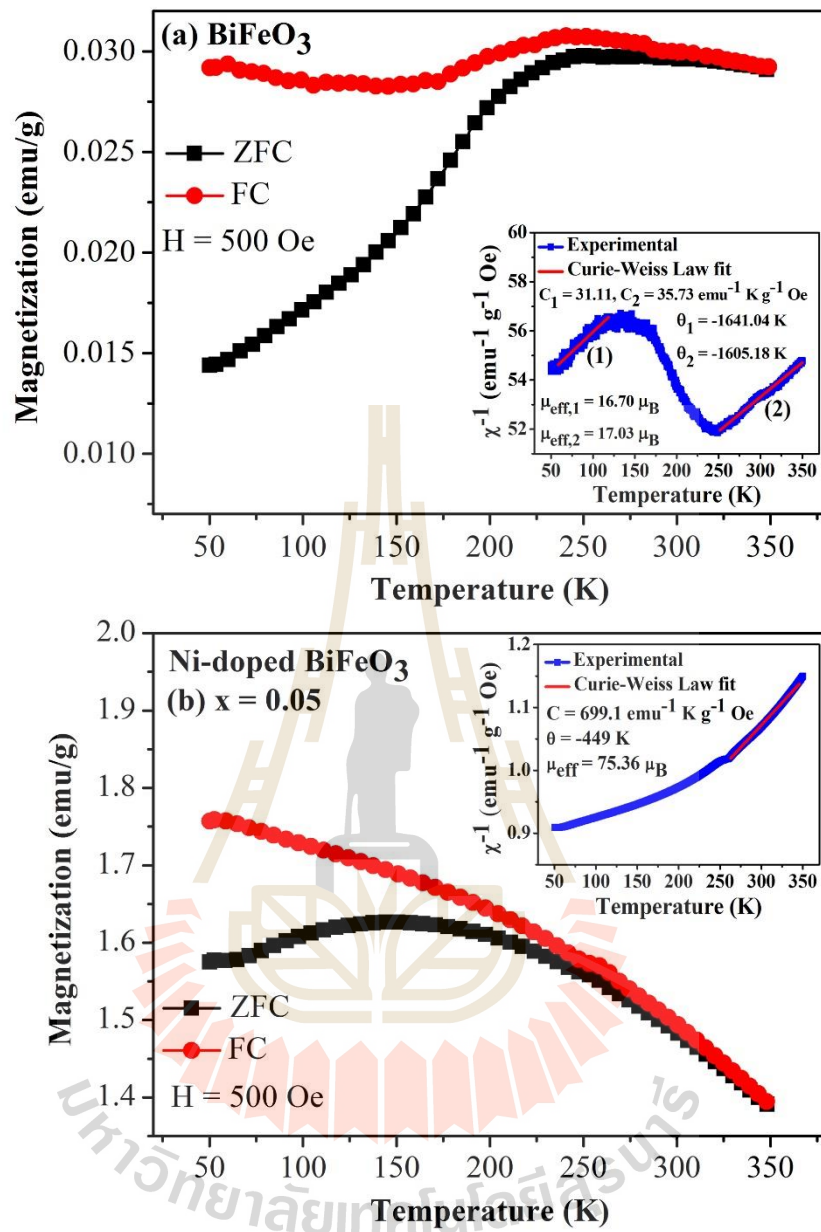


Figure 4.32 ZFC/FC curves and fitting the data to the Curie-Weiss law (inset) for (a) BiFeO₃ and (b) BiFe_{0.95}Ni_{0.05}O₃ nanoparticles.

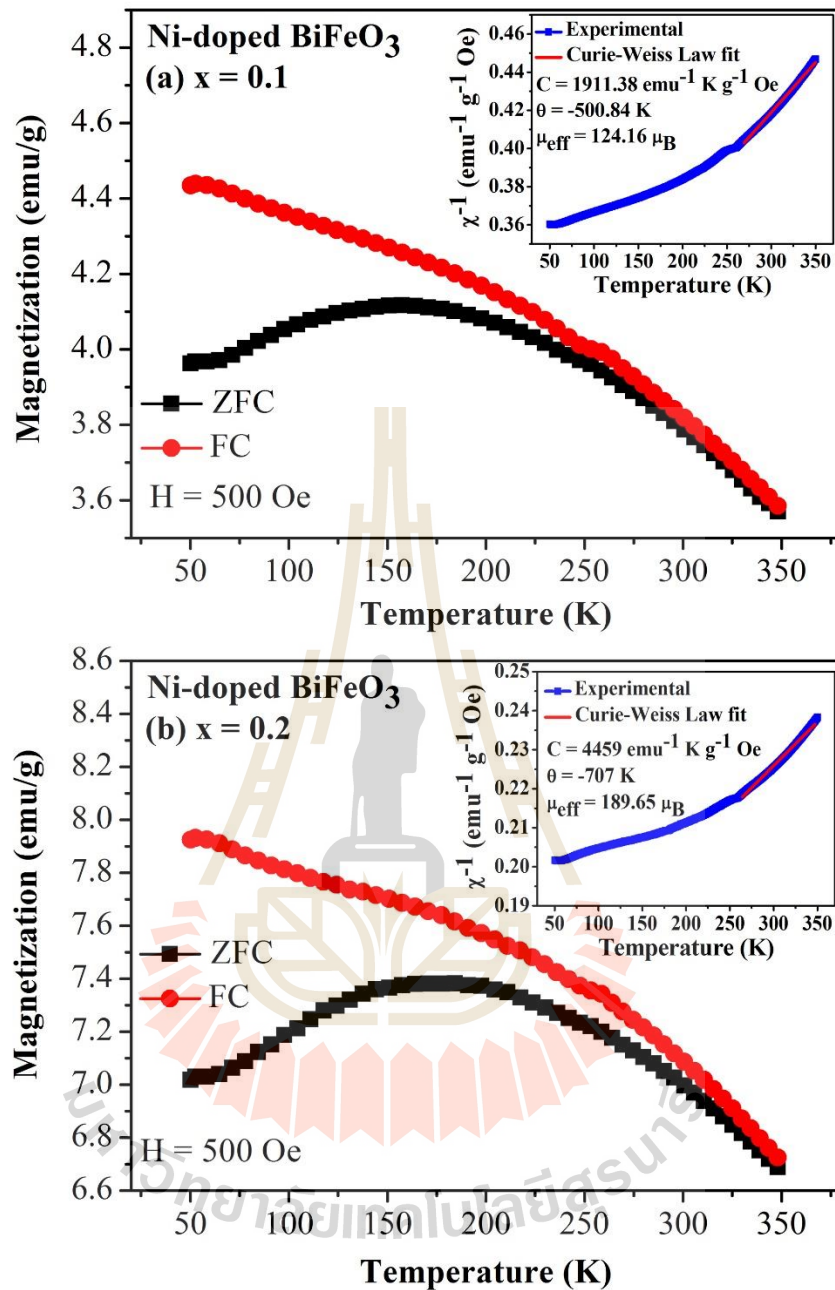


Figure 4.33 ZFC/FC curves and fitting the data to the Curie-Weiss law (inset) for (a) BiFe_{0.9}Ni_{0.1}O₃ and (b) BiFe_{0.8}Ni_{0.2}O₃ nanoparticles.

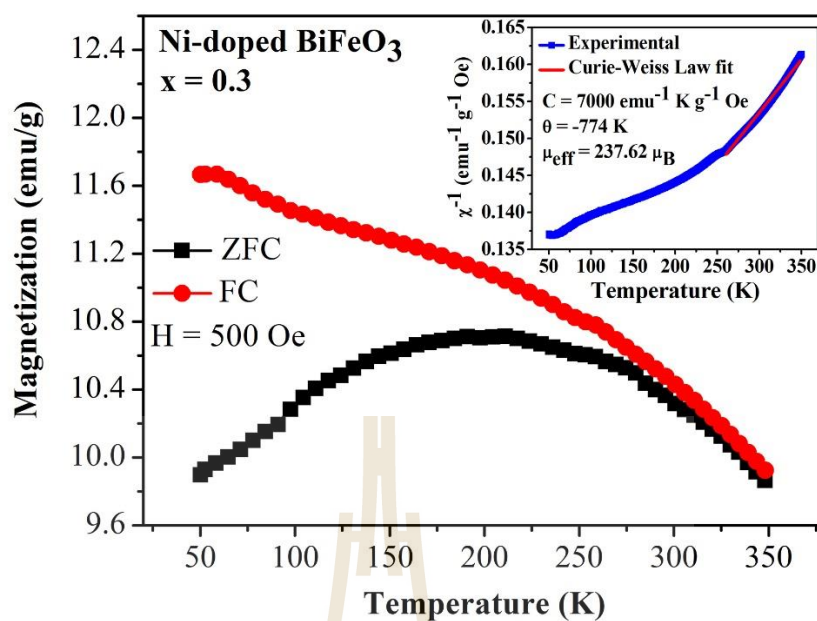


Figure 4.34 ZFC/FC curves and fitting the data to the Curie-Weiss law (inset) for $\text{BiFe}_{0.7}\text{Ni}_{0.3}\text{O}_3$ nanoparticles.

Table 4.20 Effective magnetic moment (μ_{eff}), Curie-Weiss temperature (θ) obtained from Curie-Weiss law fitting results for Ni-doped BiFeO_3 .

Doping level	μ_{eff} (μ_B)	θ (K)
$x = 0$	16.70 ^a , 17.03 ^b	-1641.04 ^a , -1605.18 ^b
$x = 0.05$	75.36	-449.62
$x = 0.1$	124.16	-500.84
$x = 0.2$	189.65	-707.43
$x = 0.3$	237.62	-774.53

a is fitting at $T = 50\text{-}130$ K, **b** is fitting at $T = 250\text{-}350$ K

4.2.3 Electrochemical properties of Ni-doped BiFeO₃ nanoparticles

4.2.3.1 Cyclic voltammetry measurement

The cyclic voltammetry (CV), galvanostatic charge-discharge (GVD), and electrochemical impedance spectroscopy (EIS) analyses were used to evaluate the electrochemical performance of the BiFe_{1-x}Ni_xO₃ ($x = 0, 0.05, 0.1, 0.2, \text{ and } 0.3$) electrodes. All these electrochemical measurements were conducted in 6 M KOH solution using a three-electrode system. The CV measurements were performed between -1.2 to 0.3 V at different potential scan rates of 5 to 100 mV/s. Figure 4.35(a)-4.35(e) show the CV curves of the BiFe_{1-x}Ni_xO₃ nanoparticles. The samples exhibited a pseudocapacitive behavior. Redox peaks were observed for all the samples, indicating the redox transitions of the nanoparticles between different valence states. The current response of all electrodes was enhanced when the scan rates were increased. The height of the peak current varied and a progressive shift in the peaks to higher potentials was observed with increasing scan rates from 5 to 100 mV/s. The specific capacitances calculated for different as synthesized samples at different scan rates from the equation 3.13. The calculated specific capacitances vs scan rates were plotted in Figure 4.35(f). The specific capacitances of all the samples decrease with increasing scan rates. This is attributed to the presence of inner active sites, which completely inhibit the redox transitions at higher scan rates of CV, probably owing to the diffusion effect of protons within the electrodes (Kötz and Carlen, 2000). At slow scan rates, the ions would have enough time to arrive the electrode surface leading to the full utilization of the material. All the electrodes exhibited the highest specific capacitance at a scan rate of 5 mV/s. The maximum specific capacitance of 397.3 F/g at a scan rate of 5 mV/s was obtained for the pure BiFeO₃ sample. The specific capacitance of the nanoparticles depends

linearly on Ni doping concentrations with continuously decreases. The specific capacitance of these $\text{BiFe}_{1-x}\text{Ni}_x\text{O}_3$ nanoparticles decreases from 397.28-183.67 F/g in the undoped BiFeO_3 sample to 194.34-123.95 F/g in the $\text{BiFe}_{0.7}\text{Ni}_{0.3}\text{O}_3$ sample (at 5-100 mV/s for CV measurement).

The number of active sites of the electrodes were calculated using equation 3.14. The calculated number of active sites involved in the redox reaction at different scan rates corresponding to 5-100 mV/s are 1.93-0.89, 1.76-0.71, 1.57-0.72, 1.44-0.85, and 0.94-0.60 in $x = 0, 0.05, 0.1, 0.2,$ and 0.3 samples, respectively as shown in Table 4.21-4.22. The number of redox sites participating at lower scan rates is higher compared with the higher scan rates. At slow scan rates, the ions would have enough time to arrive the electrode surface leading to the full utilization of the material. At higher scan rates, the ions would not have enough time to utilize the material and hence the surface adsorption process only takes place (Selvan *et al.*, 2008; Nithya *et al.*, 2013). According to the equation 3.9, the calculated diffusion co-efficient for 6 M KOH electrolyte at different scan rates corresponding to 5-100 mV/s are $2.61-1.38 \times 10^{-16}$, $1.53-0.66 \times 10^{-16}$, $1.43-0.47 \times 10^{-16}$, $1.46-0.09 \times 10^{-16}$, and $1.15-0.02 \times 10^{-16}$ cm^2/s in $x = 0, 0.05, 0.1, 0.2,$ and 0.3 samples, respectively. The value of diffusion co-efficient depends mainly on the peak current since the other parameters in the equation such as the number of electrons transferred during the redox reaction, concentration and scan rate. The diffusion co-efficient at lower scan rates is higher compared with the higher scan rates. Moreover, since the peak current of BiFeO_3 sample is higher than Ni-doped BiFeO_3 samples, the value of diffusion co-efficient is found to be higher than Ni-doped BiFeO_3 samples. The decreasing of diffusion co-efficient and number of active sites correspond to decreasing of specific capacitance with higher Ni doping concentration. The edge

shift above Bi^{3+} position is 1.38, 1.51, 1.40, 2.14, and 2.26 for $x = 0, 0.05, 0.1, 0.2,$ and 0.3 samples, respectively, which slightly increase with increasing of Ni doping, except $x = 0.1$. This increase of Ni doping may cause inactive and did not participate in the redox reaction of conversion between Bi^0 and Bi^{3+} , which may lead to the reduction of height of the peak current and deterioration of specific capacitances.



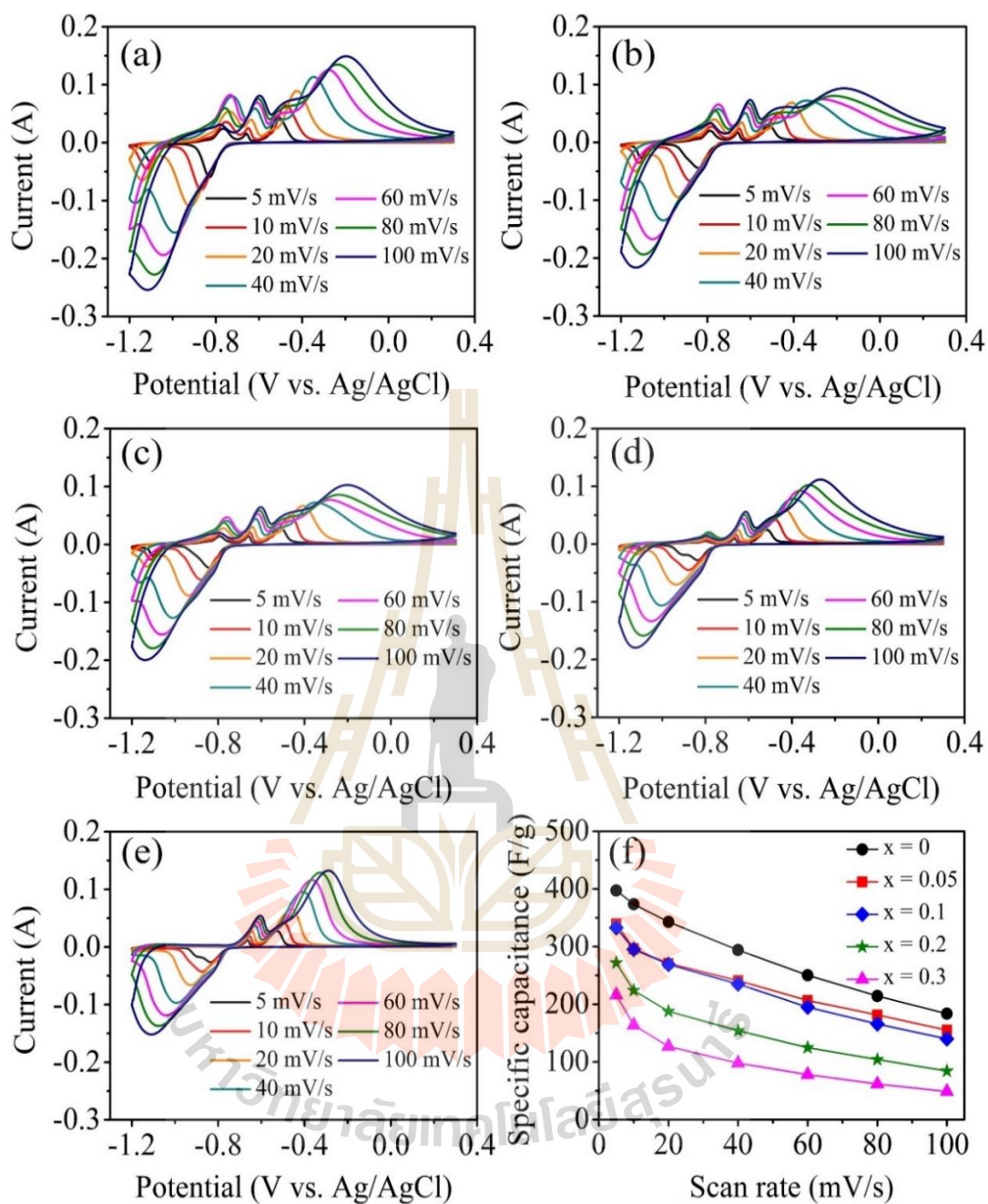


Figure 4.35 CV curves of the BiFe_{1-x}Ni_xO₃ nanoparticles: (a) $x = 0$, (b) $x = 0.05$, (c) $x = 0.1$, (d) $x = 0.2$, and (e) $x = 0.3$. (f) Specific capacitance vs scan rate.

Table 4.21 Specific capacitances, number of active sites (N) and diffusion coefficients (D) of $\text{BiFe}_{1-x}\text{Ni}_x\text{O}_3$ ($x = 0, 0.05, \text{ and } 0.1$) samples at various scan rates.

Sample	Scan rate (mV/s)	Specific capacitance (F/g)	Number of active site	Diffusion coefficient (cm^2/s) $\times 10^{-16}$
x = 0	5	397.28	1.93	2.61
	10	373.65	1.82	2.48
	20	342.79	1.67	2.34
	40	294.02	1.43	2.00
	60	250.26	1.22	1.63
	80	214.23	1.04	1.42
	100	183.67	0.89	1.38
x = 0.05	5	361.48	1.76	1.53
	10	303.16	1.47	1.38
	20	269.19	1.31	1.02
	40	234.24	1.14	0.82
	60	199.53	0.97	0.62
	80	169.65	0.82	0.57
	100	145.34	0.71	0.66
x = 0.1	5	323.25	1.57	1.43
	10	286.12	1.39	1.27
	20	260.90	1.27	0.84
	40	231.97	1.13	0.71
	60	191.33	0.93	0.50

Table 4.22 Specific capacitances, numbers of active site (N) and diffusion coefficients of $\text{BiFe}_{1-x}\text{Ni}_x\text{O}_3$ ($x = 0.1, 0.2,$ and 0.3) samples at various scan rates.

Sample	Scan rate (mV/s)	Specific capacitance (F/g)	Number of active site	Diffusion coefficient (cm^2/s) $\times 10^{-16}$
x = 0.1	80	171.69	0.83	0.44
	100	147.08	0.72	0.47
x = 0.2	5	296.56	1.44	1.46
	10	274.83	1.34	1.11
	20	256.00	1.24	0.80
	40	236.20	1.15	0.37
	60	216.26	1.05	0.19
	80	196.58	0.96	0.12
	100	175.34	0.85	0.09
x = 0.3	5	194.34	0.94	1.15
	10	184.76	0.90	0.88
	20	172.98	0.84	0.44
	40	159.84	0.78	0.12
	60	148.77	0.72	0.05
	80	137.50	0.67	0.03
	100	123.95	0.60	0.02

4.2.3.2 Galvanostatic charge-discharge measurements.

The galvanostatic charge-discharge behavior of the electrodes at current densities from 1 to 20 A/g are shown in Figure 4.36(a)-4.36(e). The nonlinear curves confirm the pseudocapacitive behavior of the material. The discharge curve of the electrodes consists of two parts: a steep voltage (IR) drop due to internal resistance and a capacitive component (curved portion) related to the voltage change due to changes in energy within the capacitor (Fusalba *et al.*, 1999). This (IR) drop is a common phenomenon occurring in transition metal oxides (Nithya *et al.*, 2013; Yuan *et al.*, 2009). The galvanostatic charge-discharge curves measured in all samples show that current density increases with decreases of the discharge time. The maximum specific capacitance of 232.24 F/g at 1A/g current density was obtained from the undoped sample. The specific capacitances calculated for different as synthesized samples at different current density from the equation 3.15. The specific capacitance at all current densities also continuously decreased from $x = 0.05$ to $x = 0.3$ as shown in Figure 4.36(f). This decrease in the capacitance is due to the fact that the surface of the electrode is inaccessible at high charge-discharge rates (Lokhande *et al.*, 2007), increasing in ionic resistivity and decreasing in charge diffusion deeper into the inner active sites (Nithya *et al.*, 2013; Senthilkumar *et al.*, 2013). Therefore, the specific capacitance of the electrodes at a low current density should be suitable for practical applications. At a current density of 1 A/g, all the electrodes exhibited the highest specific capacitance. In general, increases in the specific surface area in electrochemical capacitors is a likely reason for the increase in the specific capacitance, especially in carbon materials. On the contrary, the specific capacitance of these $\text{BiFe}_{1-x}\text{Ni}_x\text{O}_3$ nanoparticles decreases from 232.24-88.09 F/g in the undoped sample to 89.62-9.38

F/g in the $\text{BiFe}_{0.7}\text{Ni}_{0.3}\text{O}_3$ samples (at 1-20 A/g for GCD measurement) with increases in the specific surface area. However, specific capacitance does not only depend on surface area, but also on other factors, such as the pore size distribution (Long *et al.*, 2001; Reddy and Reddy, 2003; Khajonrit *et al.*, 2016). All the samples have distributions of different mesopores sizes of pores as shown in Figure 4.29, indicating that they have a porous structure, which is specific to supercapacitor materials (Long *et al.*, 2001; Reddy and Reddy, 2003). The decreases in the specific capacitance of the $\text{BiFe}_{1-x}\text{Ni}_x\text{O}_3$ samples with increases in Ni doping can possibly be attributed to all samples enriched with mesopores show a mean pore diameter of the BiFeO_3 and 5% Ni doping samples showed small mesopore sizes (~ 3.28 and 2.42 nm, respectively) which were smaller than the 10, 20, and 30% Ni doping samples (~ 24.48 nm). This may provide more active sites for chemical reactions (Dubal *et al.*, 2013). Moreover, increases in the NiFe_2O_4 phase composition may influence the specific capacitance due to the fact that the specific capacitance of NiFe_2O_4 nanoparticles (42.8 F/g) (Yang *et al.*, 2013) is lower than that of BiFeO_3 nanoparticles (397.28 F/g) at the same scan rate of 5 mV/s in 6 M KOH solution (Khajonrit *et al.*, 2016). This indicates that the increases in the phase composition of NiFe_2O_4 (5.4 to 66.4 %) may lead to decreases in the specific capacitances of the $\text{BiFe}_{1-x}\text{Ni}_x\text{O}_3$ ($x = 0.05$ to 0.3) samples.

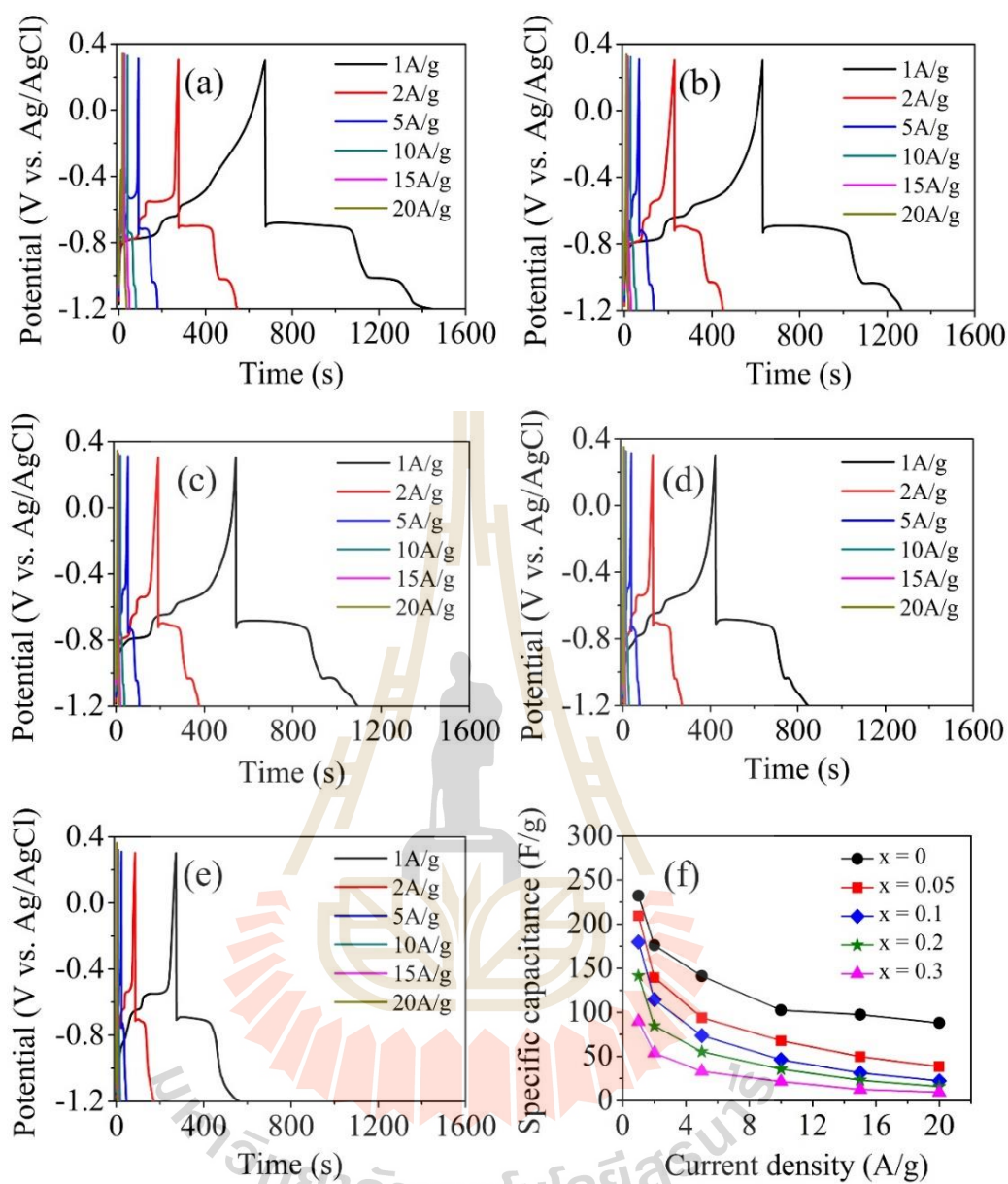


Figure 4.36 Galvanostatic charge-discharge curves of the BiFe_{1-x}Ni_xO₃ nanoparticles:

(a) $x = 0$, (b) $x = 0.05$, (c) $x = 0.1$, (d) $x = 0.2$, and (e) $x = 0.3$. (f) Specific capacitance vs current density.

Table 4.23 Specific capacitances, energy densities, and power densities of $\text{BiFe}_{1-x}\text{Ni}_x\text{O}_3$ ($x = 0, 0.05$, and 0.1) samples at various current densities.

Sample	Current density (A/g)	Specific capacitance (F/g)	Energy density (Wh/Kg)	Power density (W/Kg)
x = 0	1	232.24	72.71	339.48
	2	176.20	55.67	731.64
	5	141.03	45.05	1838.66
	10	102.48	34.04	3133.76
	15	97.54	32.88	4890.50
	20	88.03	29.44	6127.17
x = 0.05	1	209.35	65.71	371.12
	2	139.53	43.88	711.21
	5	93.91	30.06	1651.91
	10	67.81	22.42	3022.47
	15	49.71	16.58	4061.22
	20	38.44	12.94	5065.22
x = 0.1	1	179.81	56.55	368.32
	2	114.44	36.01	701.79
	5	73.65	23.26	1616.80
	10	46.34	15.08	2919.35
	15	31.37	10.46	3921.88
	20	22.20	7.67	4524.59

Table 4.24 Specific capacitances, energy densities, and power densities of $\text{BiFe}_{1-x}\text{Ni}_x\text{O}_3$ ($x = 0.2$ and 0.3) sample at various current densities.

Sample	Current density (A/g)	Specific capacitance (F/g)	Energy density (Wh/Kg)	Power density (W/Kg)
x = 0.2	1	141.36	44.38	376.75
	2	84.71	26.64	718.89
	5	55.38	17.79	1698.94
	10	35.46	11.69	3007.14
	15	23.01	7.71	4141.79
	20	15.64	5.44	4780.49
x = 0.3	1	89.62	28.12	349.13
	2	53.74	16.88	709.81
	5	33.09	10.54	1679.20
	10	21.46	7.06	2988.24
	15	12.49	4.25	4135.14
	20	9.38	3.33	5000.00

Figure 4.37 shown with energy density and power density of the BiFeO_3 and Ni-doped BiFeO_3 electrodes were calculated based on the galvanostatic charge-discharge. The energy density are decrease with increasing of Ni doping concentration and increasing of current density, while the power density are increase with increasing of current density as shown in Table 4.23-4.24. Among different electrodes, BiFeO_3 electrodes shows highest energy density (72.71 Wh/Kg) at current density of 1 A/g. The

highest power density was observed in BiFeO₃ electrode (6127.17 W/Kg) at current densities of 20 A/g.

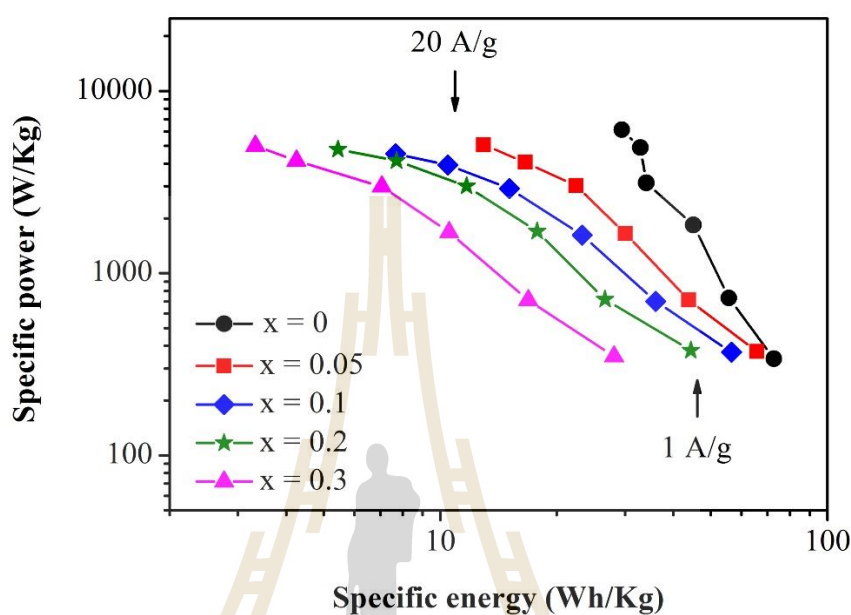


Figure 4.37 Ragone plot showing energy densities and power densities relationship of BiFeO₃ and Ni-doped BiFeO₃ electrodes.

The cycling performance of the BiFe_{1-x}Ni_xO₃ ($x = 0.05, 0.1, 0.2,$ and 0.3) electrodes at 10 A/g current density are shown in Figure 4.38. The life cycle (stability) of the electrodes is important for practical applications. The capacity retentions of the Ni-doped BiFeO₃ samples with $x = 0, 0.1, 0.20,$ and 0.30 were 58.59, 42.29, 38.19, and 34.94 %, respectively, after 500 cycles. Capacity retention can be improved by Ni content. BiFe_{0.95}Ni_{0.05}O₃ showed the highest of the capacity retention about 82.16 %. It increased to 102 % after 80 cycles, and then slightly decreased to 82 % after 500 cycles. The capacity retention of over 100 % in this electrode was due to the additional cycles

needed to fully activate the sample (Wei *et al.*, 2010; Vivier *et al.*, 2001), which may be due to the small mesopore size of about 2.4 nm.

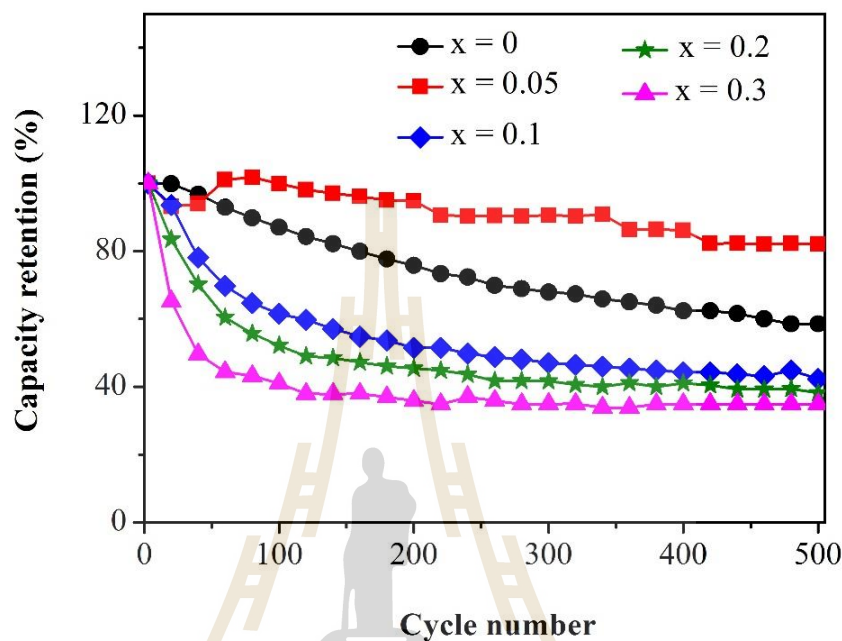


Figure 4.38 Capacity retention (%) of the $\text{BiFe}_{1-x}\text{Ni}_x\text{O}_3$ electrodes after 500 cycles at 10 A/g current density.

4.2.3.3 Electrochemical impedance spectroscopy (EIS) measurements.

Figure 4.39 shows Nyquist plots of the $\text{BiFe}_{1-x}\text{Ni}_x\text{O}_3$ ($x = 0, 0.05, 0.1, 0.2,$ and 0.3) electrodes. The small values of R_s of the $\text{BiFe}_{1-x}\text{Ni}_x\text{O}_3$ ($x = 0, 0.05, 0.1, 0.2,$ and 0.3) electrodes are 0.24, 0.26, 0.25, 0.25, and 0.24 Ω , respectively, which suggests that all electrodes provide good electrical conductivity of the electrolyte. The semi-circle at high frequency corresponds to R_{ct} . The small values of R_{ct} of the $\text{BiFe}_{1-x}\text{Ni}_x\text{O}_3$ ($x = 0, 0.05, 0.1, 0.2,$ and 0.3) electrodes are 0.13, 0.07, 0.08, 0.10, and 0.09 Ω , respectively, which indicates that all the electrodes providing the charge transfer performance at the electrode/electrolyte interface are facile (Nithya *et al.*, 2013). The

N of the electrodes are in range of 0.747-0.956. This indicated that the electrodes imply the moderate capacitor close to ideal capacitor behavior. Generally, the high capacitance can be attributed to the high surface area and enhanced electrical conductivity of the electrodes (Guan *et al.*, 2013). But in this work, variations in the specific capacitances and capacity retention of the Ni-doped BiFeO₃ electrodes are not attributed to slight increases of surface area and slight differences in the R_{ct} , CPE, W, and R_s values. The curves move away from the vertical line corresponding to increases in Ni doping concentrations. Interestingly, the straight lines close to 90° are parallel to the imaginary axis at low frequencies indicate a pure capacitive behavior and low diffusion resistance of ions in the structure of the electrode. The more vertical the curve the more closely the supercapacitor performs as an ideal capacitor (Guan *et al.*, 2013; Yang *et al.*, 2012; Wang *et al.*, 2011). This corresponds to the high specific capacitances in the BiFeO₃ electrodes which provide a more perfect capacitance than the Ni-doped BiFeO₃ samples.

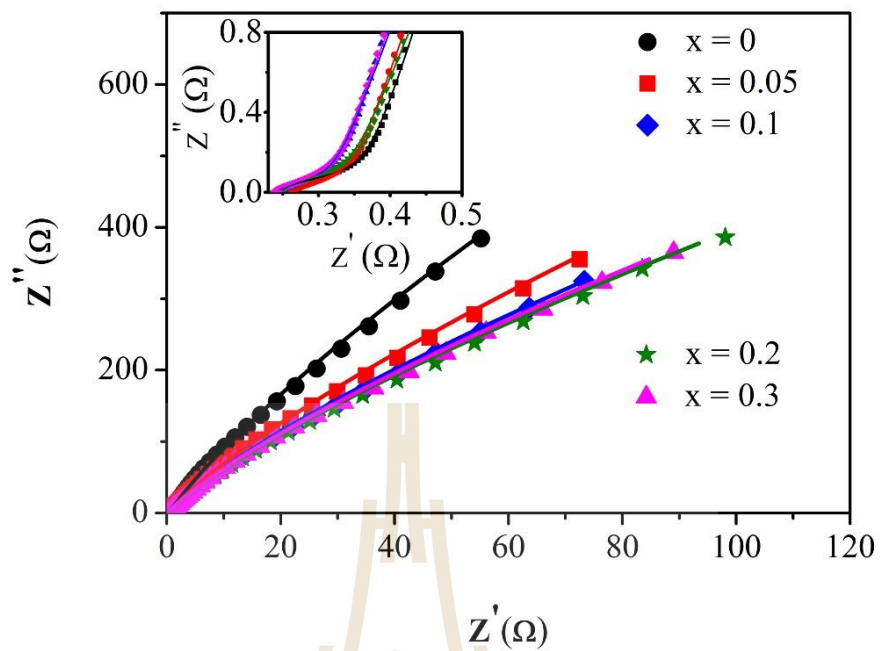


Figure 4.39 Nyquist plots of the BiFe_{1-x}Ni_xO₃ ($x = 0, 0.05, 0.1, 0.2,$ and 0.3) electrodes.

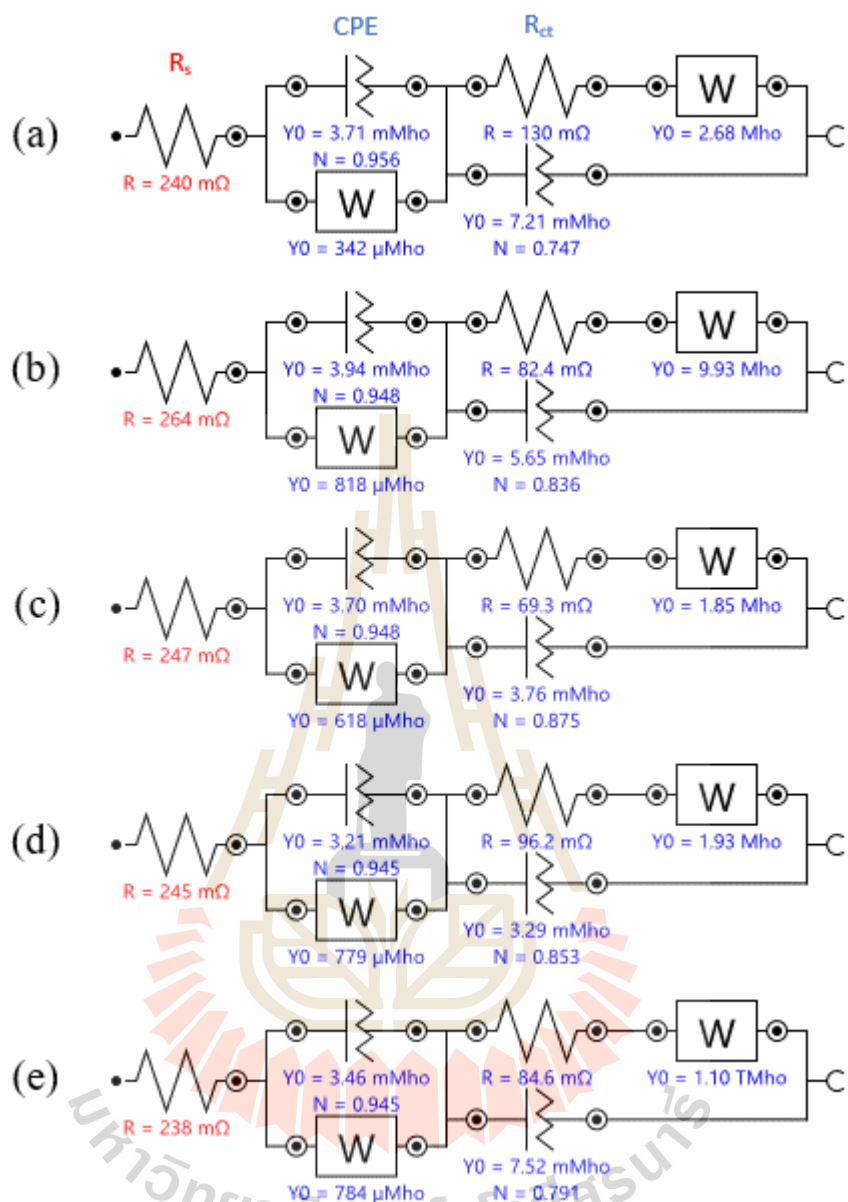


Figure 4.40 Equivalent circuit of the BiFe_{1-x}Ni_xO₃ electrodes: (a) $x = 0$, (b) $x = 0.05$, (c) $x = 0.1$, (d) $x = 0.2$, and (e) $x = 0.3$.

4.3 Cu-doped BiFeO₃ nanoparticles

4.3.1 Structural and morphology characterization

4.3.1.1 X-ray diffraction (XRD) analysis of the Cu-doped BiFeO₃ nanoparticles

The XRD patterns of the crystalline powders of BiFe_{1-x}Cu_xO₃ ($x = 0, 0.05, 0.1, 0.2,$ and 0.3) calcined at 600 °C for 3 h are shown in Figure 4.41. All the samples show the XRD patterns of the main phases of BiFeO₃ revealing the rhombohedral structure with the space group R3c (JCPDS No.86-1518) and Bi₂Fe₄O₉ as the impurity phase with the space group Pbam (JCPDS No.72-1832). By comparing the intensity of impurity peaks, all of the Cu-doped samples have higher intensities of impurity peaks than undoped sample. The crystallite sizes of 88.8, 75.2, 70.4, 66.6, and 66.4 nm of the nanoparticles calculated using the Debye-Scherrer equation decrease with increasing Cu doping concentration $x = 0, 0.05, 0.1, 0.2,$ and $0.3,$ respectively shown in Table 4.25. The variations in the crystallite size of the nanoparticles does not linearly depend on the Co doping concentration. This reduction may occur due to Cu³⁺ (0.54 Å) with a small ionic radius substitutes the Fe³⁺ (0.645 Å). The data reveals that the presence of Cu ions in BiFeO₃ system prevents the growth of crystal grains. To prevent particle growth, the motion of grain boundaries must be impeded. When the moving boundaries attached to the ferric interstitials are substituted by Cu ions they offer a retarding force on the boundaries (Agrawal *et al.*, 2014). If the retarding force generated is more than the driving force for grain growth, the particles cannot grow any longer. Figure 4.42-4.44 shows the Rietveld refinement using TOPAS software used to estimate the crystal structure profiles of the BiFe_{1-x}Cu_xO₃ ($x = 0, 0.05, 0.1, 0.2,$ and 0.3) nanoparticles. The variation in the crystallite size of the nanoparticles does not linearly

depend on Cu doping concentration. The crystallite size (D), lattice parameters (a and c), unit cell volume (V), crystal density (ρ), phase composition (%) of BiFeO_3 and $\text{Bi}_2\text{Fe}_4\text{O}_9$, residuals of the weighted pattern (R_{wp}) and pattern (R_p), and goodness of fit (GOF) calculated from Rietveld refinement using TOPAS software are shown in Table 4.25. The reliability of fitting such as R_{wp} , R_p , and GOF is confirmed. The R_{wp} , and R_p values of fitting less than 10 %, and the GOF values ~2-3 indicating acceptable matched between experimental and theoretical XRD pattern for all samples based on rhombohedral unit cell (R3c) of BiFeO_3 . The lattice parameters a and c, and unit cell volume (V) of Co-doped BiFeO_3 samples are smaller than undoped BiFeO_3 . The a-parameter decreases from 5.5793 nm for $x = 0$ to 5.5783 nm for $x = 0.05$. Especially, the decrease in c-parameter from 13.8743 nm for $x = 0$ to 13.8708 nm for $x = 0.3$, which related to the increasing of Cu doping concentration and decreasing of crystallize size. These confirm that the Fe^{3+} (~0.645 Å) site is substituted with lower ionic radius of Cu^{3+} (0.54 Å). The quantitative analysis shows that the $\text{Bi}_2\text{Fe}_4\text{O}_9$ phase compositions decrease from 37.45 to 34.24 % for $\text{BiFe}_{1-x}\text{Cu}_x\text{O}_3$ with $x = 0.05$ to 0.3 samples, respectively.

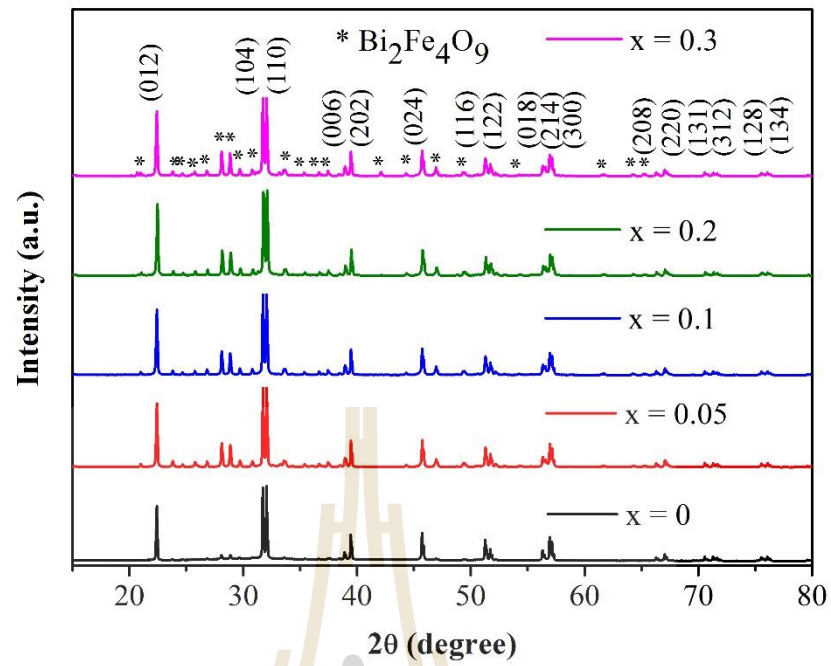


Figure 4.41 XRD patterns of BiFe_{1-x}Cu_xO₃ (x = 0, 0.05, 0.1, 0.2, and 0.3) nanoparticles.

Table 4.25 List of crystallite sizes (D), lattice parameters (a, c), unit cell volume (V), crystal density (ρ), phase composition of BiFeO_3 and $\text{Bi}_2\text{Fe}_4\text{O}_9$, residuals of the weighted pattern (R_{wp}), pattern (R_p), and goodness of fit (GOF) of $\text{BiFe}_{1-x}\text{Cu}_x\text{O}_3$ ($x = 0, 0.05, 0.1, 0.2, \text{ and } 0.3$) nanoparticles.

Parameters	x = 0	x = 0.05	x = 0.1	x = 0.2	x = 0.3
D (nm)	88.8	75.2	70.4	66.6	66.4
a (Å)	5.5793	5.5783	5.5788	5.5791	5.5789
c (Å)	13.8743	13.8714	13.8712	13.8710	13.8708
V (Å) ³	374.0372	373.8119	373.8814	373.9106	373.8858
ρ (g/cm ³)	8.333	8.348	8.357	8.377	8.398
BiFeO_3 (%)	79.12	62.53	66.39	66.58	65.76
$\text{Bi}_2\text{Fe}_4\text{O}_9$ (%)	20.88	37.45	33.61	33.42	34.24
R_{wp} (%)	7.68	8.65	7.64	7.24	8.25
R_p (%)	5.98	6.61	5.80	5.39	6.17
GOF	2.70	2.86	2.59	2.49	2.89

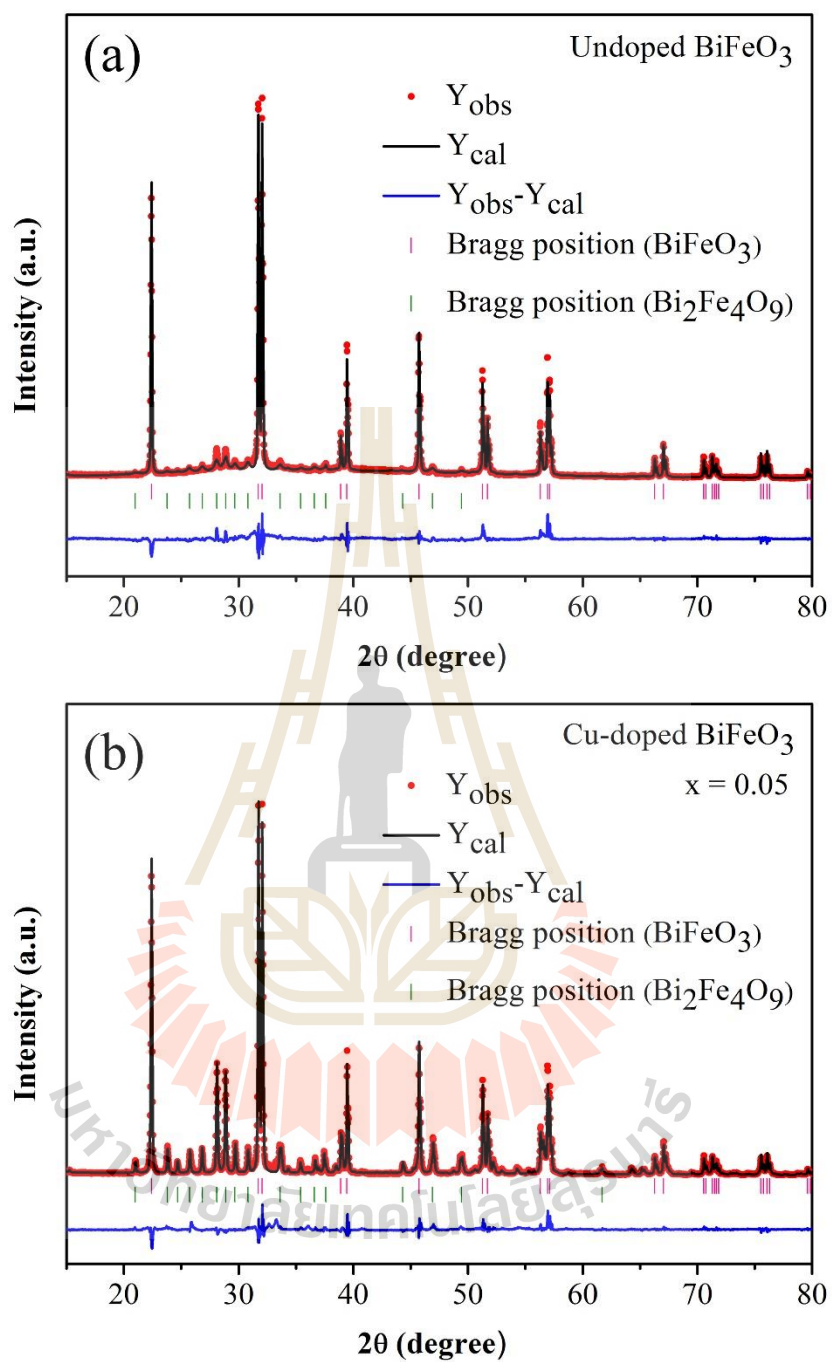


Figure 4.42 Rietveld refinement of XRD data for (a) BiFeO_3 (b) Cu-doped BiFeO_3 ($x = 0.05$) nanoparticles.

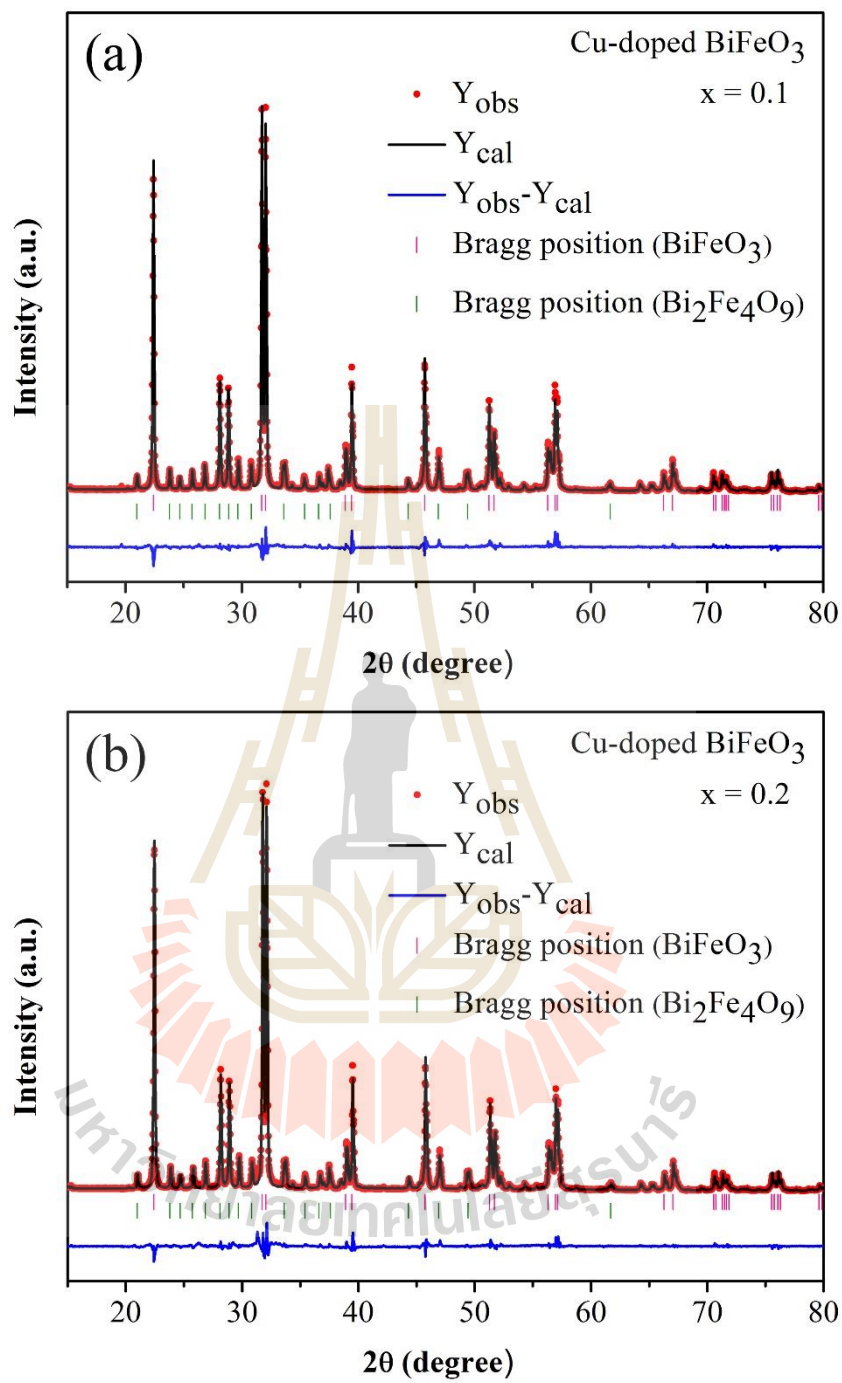


Figure 4.43 Rietveld refinement of XRD data for Cu-doped BiFeO_3 nanoparticles (a) $x = 0.1$ (b) $x = 0.2$.

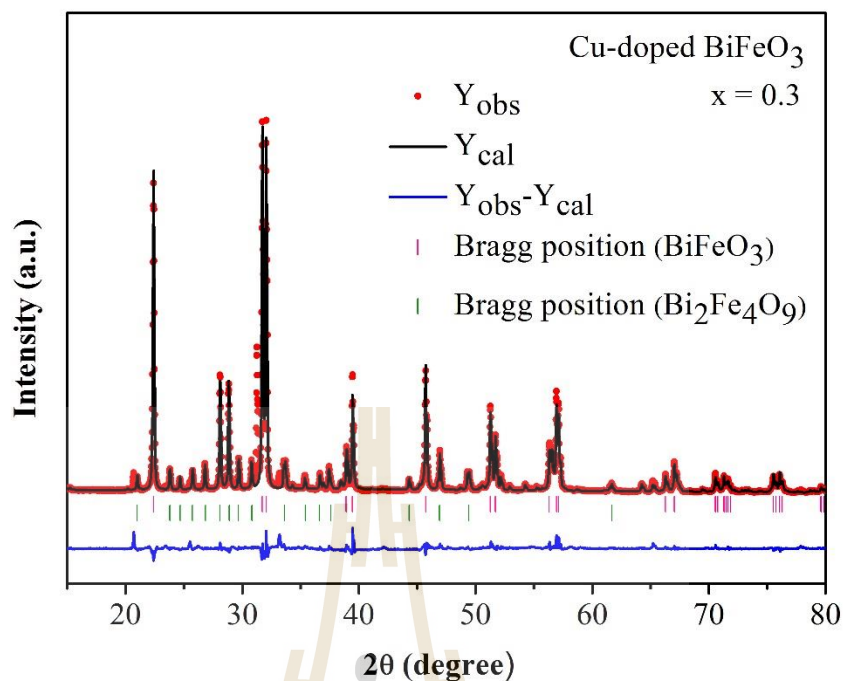


Figure 4.44 Rietveld refinement of XRD data for Cu-doped BiFeO_3 ($x = 0.3$) nanoparticles.

4.3.1.2 Morphology of the Cu-doped BiFeO_3 nanoparticles by SEM and TEM

Figure 4.45 shows the SEM images revealing the particle sizes of the $\text{BiFe}_{1-x}\text{Cu}_x\text{O}_3$ nanoparticles. The undoped sample shows the nanoparticles sizes to be about 100-200 nm, while the Cu-doped samples show decreasing sizes of nanoparticles of about 50-100 nm. This indicates that Cu doping causes decreasing sizes of the nanoparticles. The mean particle size from the SEM image is in good agreement with the crystallite size measured by using Scherrer's formula.

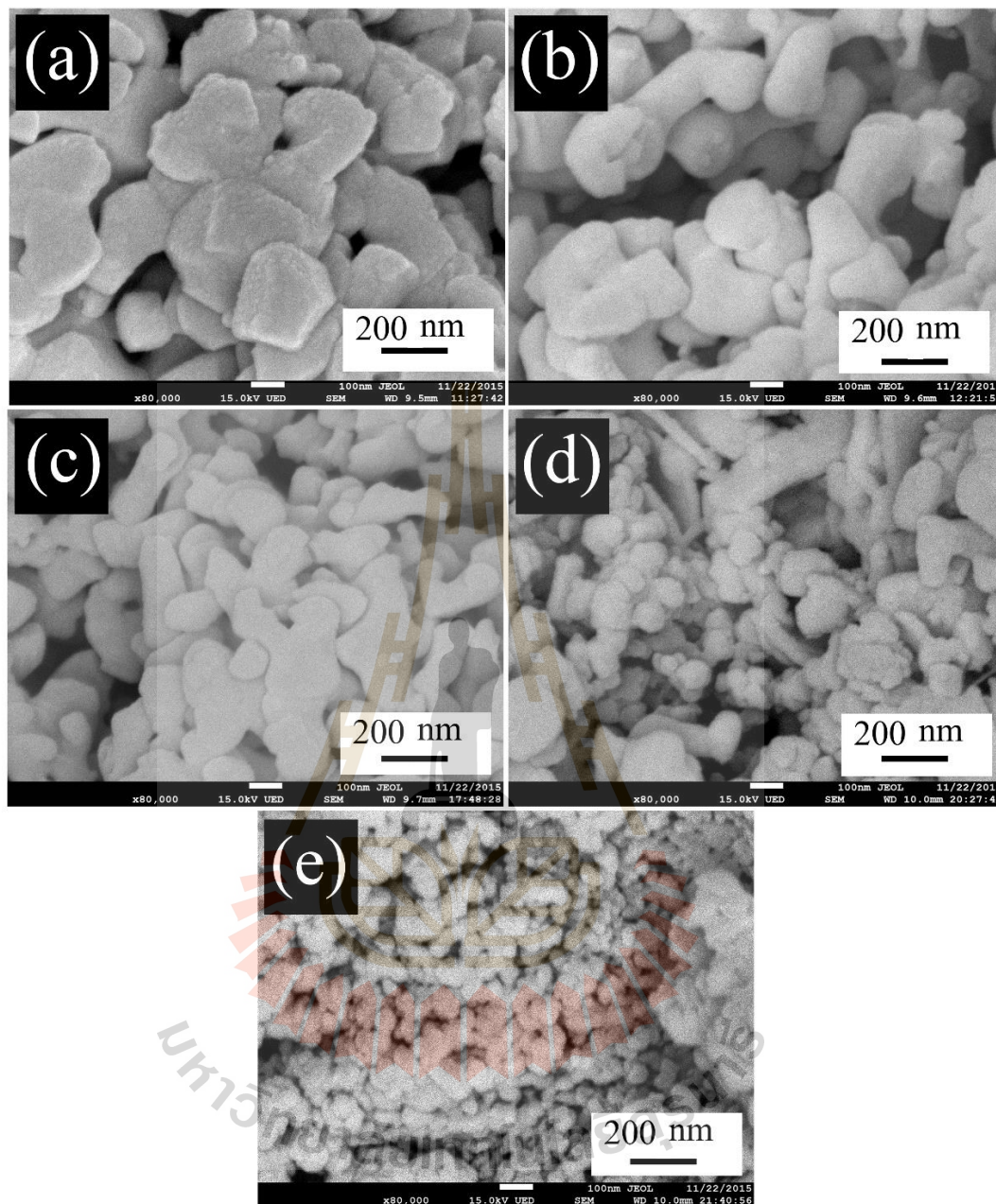
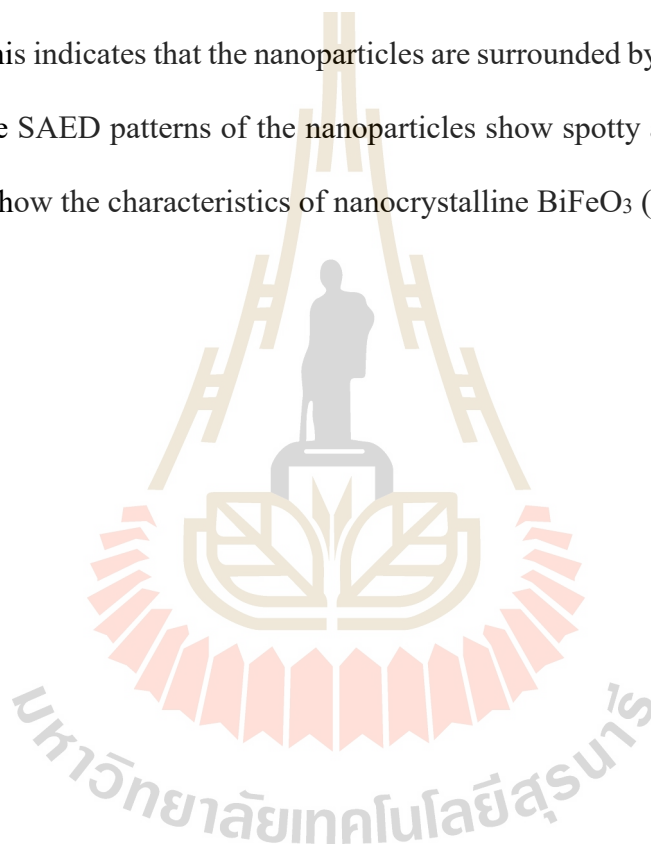


Figure 4.45 SEM images of $\text{BiFe}_{1-x}\text{Cu}_x\text{O}_3$ nanoparticles: (a) $x = 0$, (b) $x = 0.05$, (c) $x = 0.1$, (d) $x = 0.2$, and (e) $x = 0.3$.

The morphology and structure of the BiFeO_3 and Cu-doped BiFeO_3 nanoparticles were investigated by TEM. Bright field TEM images, high-resolution (HRTEM) TEM images, and corresponding selected areas of electron diffraction

(SAED) patterns are shown in Figure 4.46. The TEM bright field images show that the particles sizes obtained were about 30-200 nm. This is in agreement with the XRD and SEM results. To better investigate the crystal structure, HRTEM was performed, which shows the lattice fringes of the (104), (202), (104), (012), and (104) planes with interplanar spacing of approximately 0.281, 0.227, 0.281, 0.395, and 0.281 nm of the $\text{BiFe}_{1-x}\text{Ni}_x\text{O}_3$ with $x = 0, 0.05, 0.1, 0.2,$ and 0.3 samples, respectively, which correspond to BiFeO_3 . This indicates that the nanoparticles are surrounded by BiFeO_3 nanocrystals. Moreover, the SAED patterns of the nanoparticles show spotty and ring patterns. The spotty rings show the characteristics of nanocrystalline BiFeO_3 (JCPDS No.86-1518).



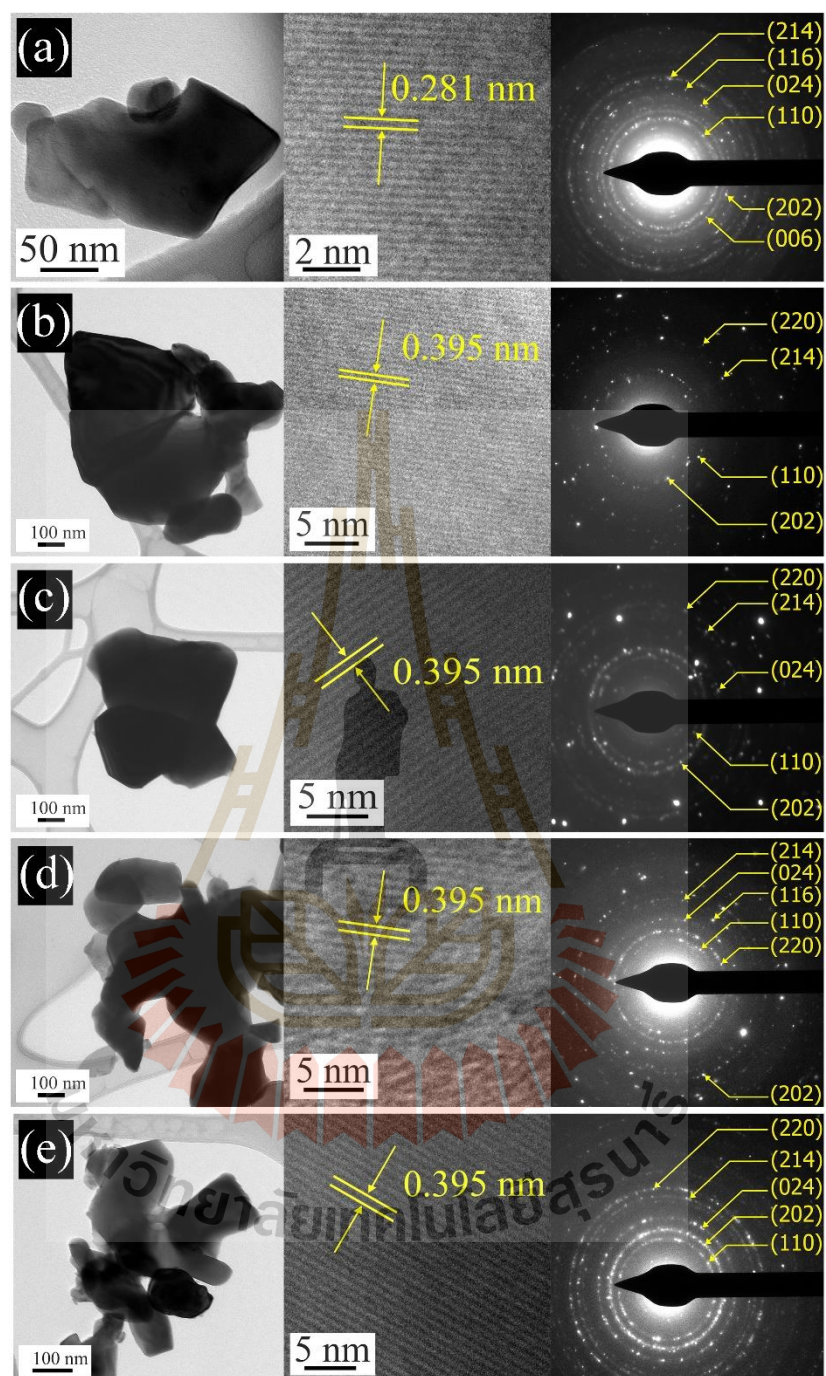


Figure 4.46 Bright field TEM images (left), high-resolution (HRTEM) TEM images (middle), and corresponding selected areas electron diffraction (SAED) patterns (right) of $\text{BiFe}_{1-x}\text{Cu}_x\text{O}_3$ nanoparticles: (a) $x = 0$, (b) $x = 0.05$, (c) $x = 0.1$, (d) $x = 0.2$, and (e) $x = 0.3$.

4.3.1.3 X-ray absorption spectroscopy study of the Cu-doped BiFeO₃ nanoparticles

Figure 4.47-4.48 shows normalized Bi *M*₅-edges and Fe *K*-edges XANES spectra of all samples. The Bi *M*₅-edge XANES spectra of the BiFe_{1-x}Cu_xO₃ nanoparticles can be seen with $x = 0, 0.05, 0.1, 0.2,$ and 0.3 as compared with those of the standard materials with Bi oxidation states is shown in Figure 4.47(a). The oxidation states of Bi in all samples are shown along with the standard samples of Bi₂O₃ for Bi³⁺. It was found that the position of the absorption edge at Bi *M*₅-edge is similar to Bi₂O₃ which is typical for Bi in the oxidation state of +3. Figure 4.47(b) shows the XANES spectra at the Fe *K*-edge of all the samples, which match that of Fe₂O₃, indicating that the oxidation state of Fe is 3+. The Cu *K*-edge XANES spectra of BiFe_{1-x}Cu_xO₃ nanoparticles as compared with those of the standard materials with different Cu oxidation states are shown in Figure 4.48. The absorption edge at the Cu *K*-edge of all the samples does not match those of the Cu⁺¹ and Cu⁺² standard samples and the oxidation state of the Cu ion differs from that of the starting materials (Cu⁺²). The edge energies of Bi *M*₅-edge, Fe *K*-edge, and Cu *K*-edge of the BiFe_{1-x}Cu_xO₃ samples are shown in Table 4.26-4.28. The edge energies of Bi *M*₅-edge and Fe *K*-edge of BiFe_{1-x}Cu_xO₃ ($x = 0.05, 0.1, 0.2,$ and 0.3) samples are close to the Bi₂O₃ and Fe₂O₃ standard, respectively. The edge energies of Cu *K*-edge of BiFe_{1-x}Cu_xO₃ ($x = 0.05, 0.1, 0.2,$ and 0.3) samples are 8983.93, 8983.68, 8983.16, and 8983.08 eV, respectively, are higher than the CuO (8983.01 eV) standard. Clearly, the oxidation state of Cu is not 2+ and could be 3+. The XANES feature of the Cu-doped BiFeO₃ is similar to that of the Fe *K*-edge of the BiFeO₃ parent structure. This suggests that Cu ions likely occupy the Fe site in the BiFeO₃ structure. Furthermore, the XANES analysis provided strong

evidence that Cu^{+3} ($\sim 0.54 \text{ \AA}$) of small ionic radius substituting the Fe^{3+} ($\sim 0.645 \text{ \AA}$) site causes the decrease in particle size.

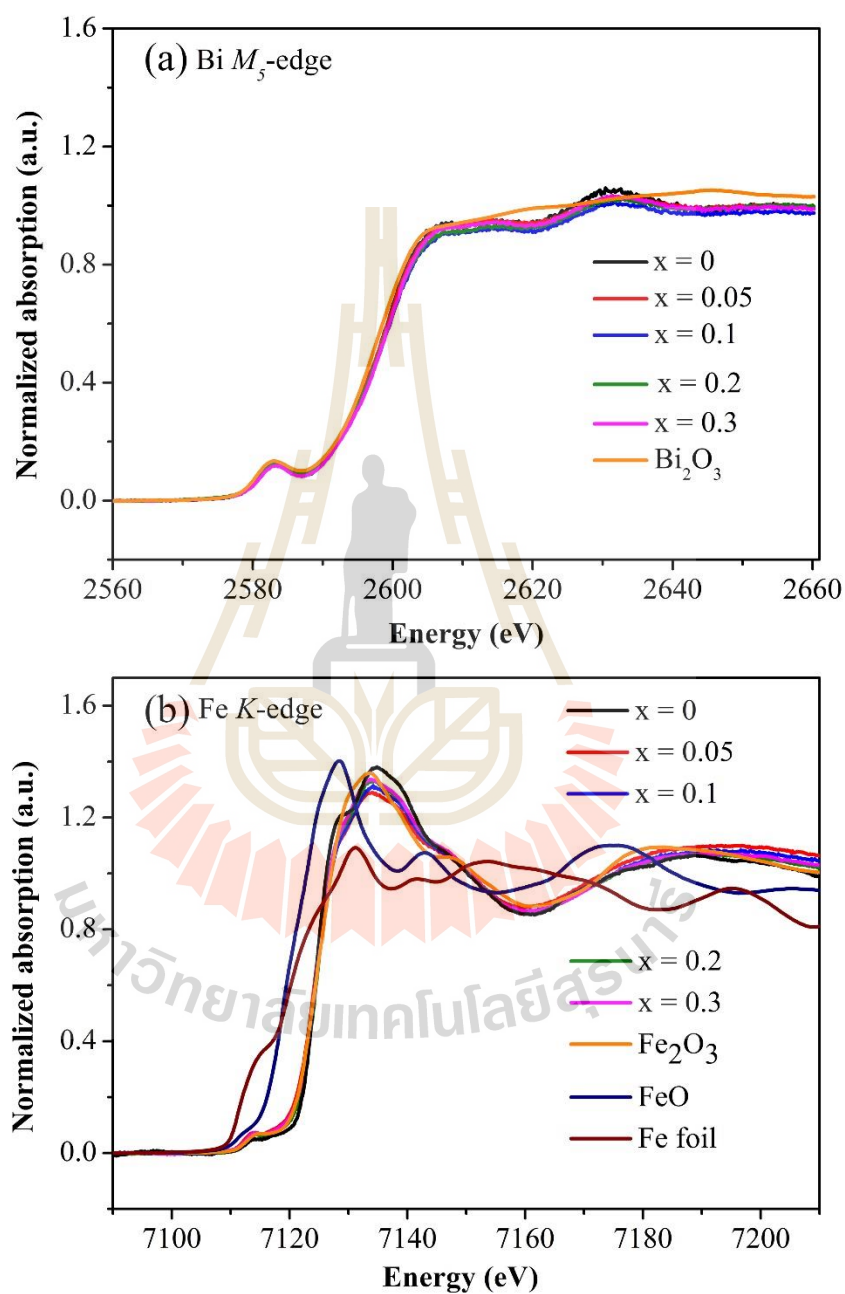


Figure 4.47 XANES spectra of $\text{BiFe}_{1-x}\text{Cu}_x\text{O}_3$ ($x = 0, 0.05, 0.1, 0.2,$ and 0.3) nanoparticles: (a) Bi M_5 -edge and (b) Fe K -edge.

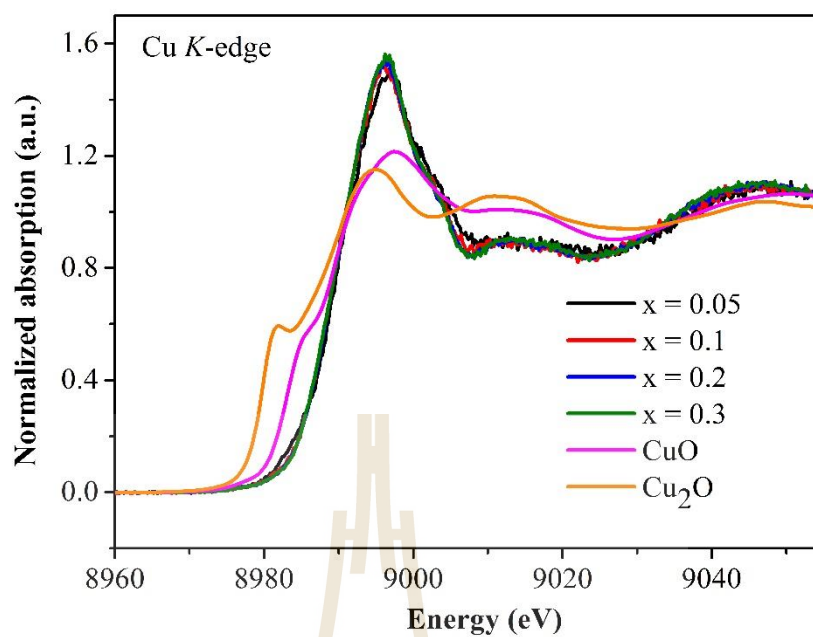


Figure 4.48 XANES spectra at Cu *K*-edge of $\text{BiFe}_{1-x}\text{Cu}_x\text{O}_3$ ($x = 0, 0.05, 0.1, 0.2,$ and 0.3) nanoparticles.

Table 4.26 Absorption edges and oxidation states at Bi M_5 -edge of all Cu-doped BiFeO_3 samples along with the standard samples.

Samples/standard	Absorption edge at Bi (eV)	Edge shift at Bi (eV)	Oxidation state
Bi_2O_3	2597.25	0	+3
BiFeO_3	2598.63	1.38	+3
$\text{BiFe}_{0.95}\text{Cu}_{0.05}\text{O}_3$	2598.25	1.00	+3
$\text{BiFe}_{0.9}\text{Cu}_{0.1}\text{O}_3$	2598.65	1.40	+3
$\text{BiFe}_{0.8}\text{Cu}_{0.2}\text{O}_3$	2598.67	1.42	+3
$\text{BiFe}_{0.7}\text{Cu}_{0.3}\text{O}_3$	2598.77	1.52	+3

Table 4.27 Absorption edges and oxidation states at Fe *K*-edge of all Cu-doped BiFeO₃ samples along with the standard samples.

Samples/standard	Absorption edge at Fe (eV)	Edge shift at Fe (eV)	Oxidation state
FeO	7120.87	4.77	+2
Fe ₂ O ₃	7125.64	0	+3
BiFeO ₃	7124.62	1.02	+3
BiFe _{0.95} Cu _{0.05} O ₃	7124.33	1.31	+3
BiFe _{0.9} Cu _{0.1} O ₃	7124.39	1.25	+3
BiFe _{0.8} Cu _{0.2} O ₃	7124.51	1.13	+3
BiFe _{0.7} Cu _{0.3} O ₃	7124.71	0.93	+3

Table 4.28 Absorption edges and oxidation states at Cu *K*-edge of all Cu-doped BiFeO₃ samples along with the standard samples.

Samples/standard	Absorption edge at Cu (eV)	Edge shift at Cu (eV)	Oxidation state
Cu foil	8978.61	4.4	0
Cu ₂ O	8979.89	3.12	+1
CuO	8983.01	0	+2
BiFe _{0.95} Cu _{0.05} O ₃	8988.93	5.92	+3
BiFe _{0.9} Cu _{0.1} O ₃	8988.68	5.67	+3
BiFe _{0.8} Cu _{0.2} O ₃	8989.16	6.15	+3
BiFe _{0.7} Cu _{0.3} O ₃	8989.08	6.07	+3

4.3.1.4 Characterization of surface area and pore size distribution of the Cu-doped BiFeO₃ nanoparticles by BET method and BJH method

The N₂ adsorption-desorption isotherms and pore size distributions (BJH plot) of BiFe_{1-x}Cu_xO₃ nanoparticles with x = 0, 0.05, 0.1, 0.2, and 0.3 are shown in Figure 4.49. Figure 4.49(a) shows features of N₂ adsorption-desorption isotherms. The hysteresis loop features of all samples indicate characteristic of non-porous with low adsorbate-sample surface interaction. The presence of micropores and mesopores in particles is shown by the BJH curve (Figure 4.49 (b)). The BiFe_{1-x}Cu_xO₃ samples with x = 0, 0.05, 0.1, 0.2, and 0.3 have specific surface areas of 3.6, 3.9, 4.7, 4.8, and 6.8 m²/g, respectively. In general, the decrease in the size of BiFeO₃ nanoparticles is related to an increase in surface area (Park *et al.*, 2007). In this research, we confirm that all the samples with higher concentrations of Cu dopant showed a decrease in particle size which shows a tendency of increasing their specific surface area as calculated and cited in Table 4.27. The observed pores may simplify the improvement in the electrolyte contact area, which will increase the concentration of ions in the electrode material (Zhang *et al.*, 2010). This may lead to the higher capacitance and better capacity retention in the BiFe_{0.95}Cu_{0.05}O₃ sample, which will be discussed in section 4.3.3. All the samples with higher concentrations of Cu dopant showed a decrease in particle size which shows a tendency to increase their specific surface area, and total pore volume as calculated and cited in Table 4.29. By comparison, the average particle size calculated by BET is larger than the crystallite size calculated by XRD for all samples as shown in Figure 4.50. The differences in the results occur from aggregates and agglomerates of crystals, which indicate that the particles include several crystallites (Gaber *et al.*, 2014).

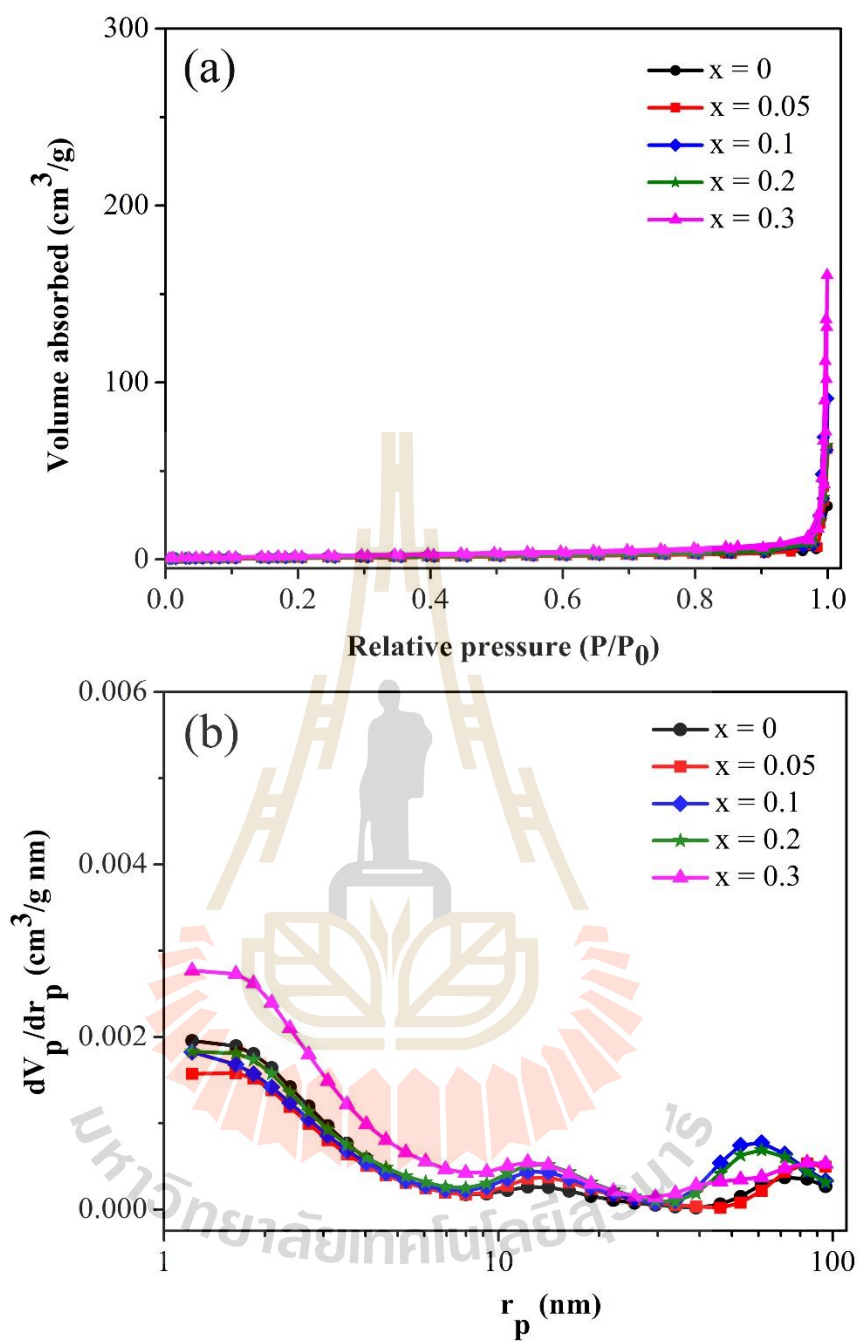


Figure 4.49 N_2 adsorption-desorption isotherms (a) and pore-size distribution (b) of the $\text{BiFe}_{1-x}\text{Cu}_x\text{O}_3$ nanoparticles.

Table 4.29 Specific surface area (S_{BET}), mean pore diameter (D_{MP}), total pore volume (V_{TP}), meso pore diameter (D_{BJH}), particle size (D_{BET}) of $\text{BiFe}_{1-x}\text{Cu}_x\text{O}_3$ ($x = 0, 0.05, 0.1, 0.2,$ and 0.3) nanoparticles.

Samples	S_{BET} (m^2/g)	D_{MP} (nm)	V_{TP} (cm^3/g)	D_{BJH} (nm)	D_{BET} (nm)
BiFeO_3	3.64	25.55	0.0254	3.28	197.81
$\text{Bi}_{0.95}\text{Cu}_{0.05}\text{O}_3$	3.94	33.15	0.0302	2.42	182.43
$\text{Bi}_{0.9}\text{Cu}_{0.1}\text{O}_3$	4.73	35.64	0.0420	4.21	151.79
$\text{Bi}_{0.8}\text{Cu}_{0.2}\text{O}_3$	4.81	37.26	0.0449	4.82	148.91
$\text{Bi}_{0.7}\text{Cu}_{0.3}\text{O}_3$	6.82	36.14	0.0448	5.43	104.76

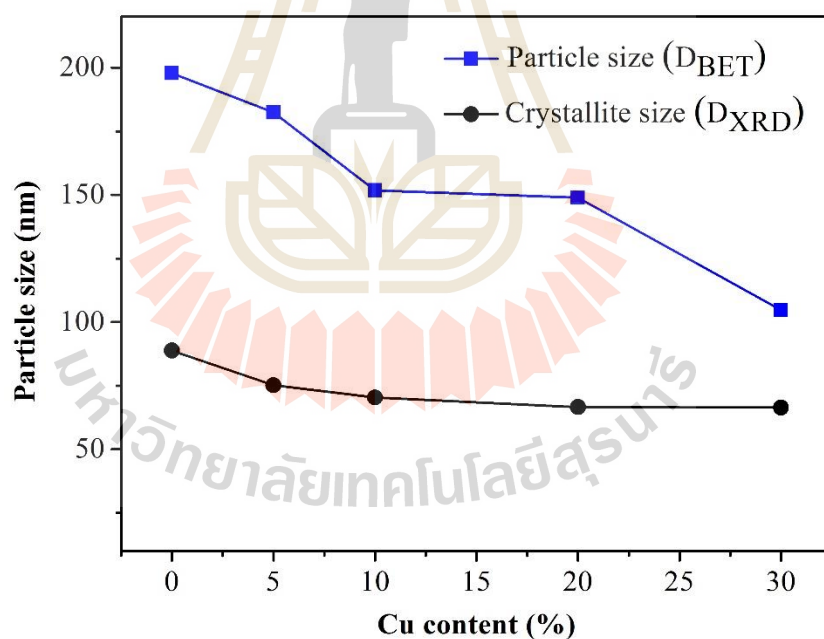


Figure 4.50 Variations of crystallite size calculated by XRD and particle size calculated from BET of $\text{BiFe}_{1-x}\text{Cu}_x\text{O}_3$ nanoparticles as a function of Cu content (%).

4.3.2 Magnetic properties of the Cu-doped BiFeO₃ nanoparticles

Figure 4.51(a)-4.51(d) show the M-H hysteresis loops of the BiFe_{1-x}Cu_xO₃ (x = 0, 0.05, 0.1, 0.2, and 0.3) nanoparticles at 50, 100, 200, 300, and 350 K of temperature. The coercivity (H_c), saturation magnetization (M_s) and remanent magnetization (M_r) values of Cu-doped BiFeO₃ nanoparticles at different temperatures shows in Table 4.28. Clearly, the saturation magnetization (M_s) increases linearly with increasing Cu doping concentrations at all temperatures. The magnetization of BiFeO₃ slightly increases from 0.207 to 0.223 emu/g with increasing in temperatures from 50 to 350 K, respectively, except at 200 K which shows slightly decreases level of magnetization at 0.206 emu/g. Moreover, the magnetization of the Cu-doped BiFeO₃ (x = 0.1, 0.2, and 0.3) samples increases with decreasing in temperature from 350 to 50 K, except x = 0.05 samples at 100 and 200 K of which shows slightly decrease level of magnetization at 0.307 and 0.306 emu/g, respectively. The saturation magnetization (M_s) (from 0.206 to 0.896 emu/g) linearly increases with increasing of Cu doping concentration (from x = 0 to x = 0.3). It is possible that the Cu doping concentration strongly affected the magnetic properties, resulting in enhanced ferromagnetism. This is not due to the presence of the secondary phase of Bi₂Fe₄O₉ nanoparticles in the x = 0 to x = 0.1 samples that exhibit the antiferromagnetic nature with a very low M_s, as reported previously (Wang *et al.*, 2009; Rao *et al.*, 2016; Lin *et al.*, 2015). The magnetization dependence on Cu doping concentration provides strong evidence of the size effect. It is known that particles of the nanoscale exhibit significantly different properties from bulk BiFeO₃ (Zhang *et al.*, 2005). The decrease in particle size causes an increasing in surface-volume ratio, and the long-range antiferromagnetic order is frequently interrupted at the surface. The contribution of uncompensated spins at the surface to the total magnetic moment of the

particles increases. Therefore, an intrinsic spiral spin structure is incompletely suppressed, causing weak ferromagnetism in the nanoparticles (Park *et al.*, 2007; Jia *et al.*, 2009). A slim hysteresis loop is observed in the BiFeO₃ sample and larger loops are seen in the Cu-doped samples with $x = 0.05$ to 0.3. The hysteresis loops of all samples indicated improving ferromagnetism by Cu doping influenced by variations in the coercivity (H_c) between 21.11 to 1116.67 Oe. The H_c increases with increasing of Cu doping concentration and decreasing of the crystallite-size of the nanoparticles. This conform to the variations of H_c , which decreases when the crystallite size is in the multi-domain region (Cullity and Graham, 2011). Moreover, the H_c values increase with decreasing of temperature for all samples. This may occur from two reasons: (1) an increase in H_c is the alignment of the magnetic moment in the direction of the external magnetic field and (2) thermal fluctuations of nanoparticles decrease with decreases in the temperature (Khan *et al.*, 2015). Moreover, the remanent magnetization (M_r) increases with increases of the Cu content due to decreases in the crystallite size of BiFeO₃ and decrease in temperature.

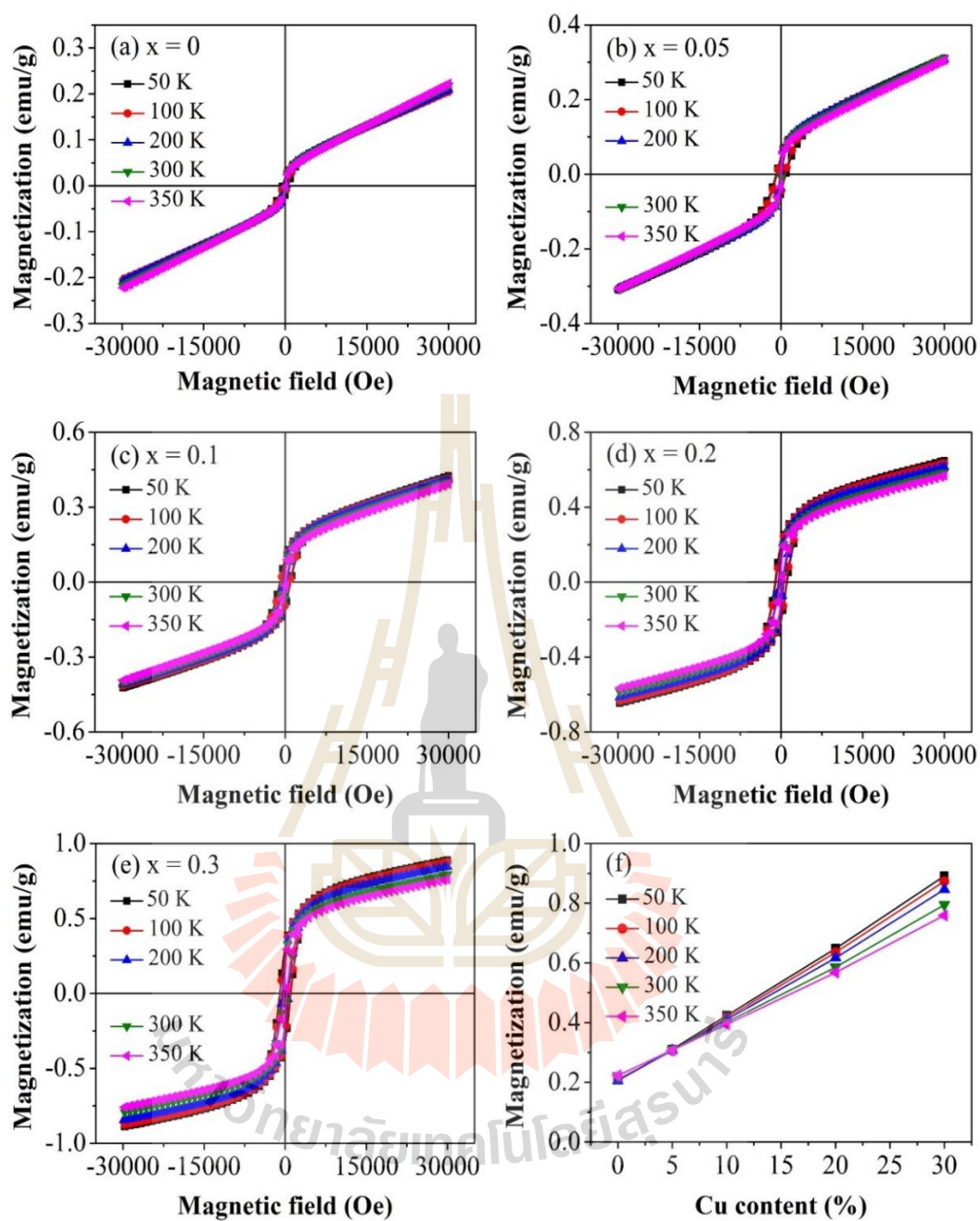


Figure 4.51 Magnetization hysteresis loops at different temperature of $\text{BiFe}_{1-x}\text{Cu}_x\text{O}_3$ nanoparticles: (a) $x = 0$, (b) $x = 0.05$, (c) $x = 0.1$, (d) $x = 0.2$, and (e) $x = 0.3$. (f) Variations in saturation magnetization as a function of Cu content (%).

Table 4.30 Coercivity (H_c), saturation magnetization (M_s) and remanant magnetization (M_r) values of $\text{BiFe}_{1-x}\text{Cu}_x\text{O}_3$ ($x = 0, 0.05, 0.1, \text{ and } 0.2$) samples at different temperatures.

Sample	T (K)	H_c (Oe)	M_s (emu/g)	M_r (emu/g)
x = 0	50	524.35	0.207	0.019
	100	342.73	0.210	0.017
	200	108.14	0.206	0.010
	300	52.85	0.219	0.005
	350	30.59	0.223	0.004
x = 0.05	50	879.190	0.311	0.051
	100	704.808	0.306	0.047
	200	173.951	0.307	0.028
	300	45.867	0.309	0.015
	350	21.111	0.307	0.007
x = 0.1	50	989.272	0.424	0.099
	100	821.427	0.416	0.091
	200	357.531	0.410	0.062
	300	165.219	0.401	0.040
	350	130.720	0.394	0.028
x = 0.2	50	1107.785	0.648	0.207
	100	973.562	0.635	0.191
	200	495.483	0.617	0.144
	300	284.901	0.586	0.079
	350	218.026	0.568	0.079

Table 4.31 Coercivity (H_c), saturation magnetization (M_s) and remanant magnetization (M_r) values of $\text{BiFe}_{1-x}\text{Cu}_x\text{O}_3$ ($x = 0.3$) samples at different temperatures.

Sample	T (K)	H_c (Oe)	M_s (emu/g)	M_r (emu/g)
x = 0.3	50	1116.667	0.891	0.315
	100	980.476	0.873	0.298
	200	574.761	0.846	0.242
	300	325.238	0.795	0.172
	350	258.095	0.759	0.157

Figure 4.52-4.54 shows temperature dependent of the magnetization for the undoped BiFeO_3 and $\text{BiFe}_{1-x}\text{Cu}_x\text{O}_3$ ($x = 0.05, 0.1, 0.2,$ and 0.3) nanoparticles, showing the ZFC (zero field cooling) and FC (field cooling) curves, under 50 K to 350 K with an applied field set at 500 Oe. The FC curves of the Cu-doped BiFeO_3 samples increases in magnetization with a lowering of temperature from 150 to 50 K as shown in Figure 4.50(b)-4.52. This may be attributed to the development of the incommensurate sinusoidal spin structure (Naik and Mahendiran, 2009) and indicates that the Cu-doped BiFeO_3 samples have typical ferromagnetic properties. The decreases in the magnetization of the ZFC curves with a lowering of temperature from 250 to 50 K for $x = 0$ samples and Cu-doped BiFeO_3 samples suggest a antiferromagnetic property (Kumar and Yadav, 2011). A clear broad magnetization maximum of the ZFC curves of $x = 0$ and 0.05 samples in the blocking temperatures (T_B) of ~ 250 K was observed as shown in Figure 4.52. This indicates that there might be magnetic blocking and spin glass behavior (Kumar and Yadav, 2011) (Singh *et al.*, 2008). The Cu doped BiFeO_3 ($x = 0.1, 0.2$ and 0.3) samples show increases in the blocking temperatures (T_B) which are

greater than 350 K. This result conform to other reports of BiFeO₃, which show a magnetic transition below 650 K, indicating that the sample becomes ferromagnetic at the Neel temperature when the particle size is reduced (Vijayanand *et al.*, 2009). The divergence between FC and ZFC magnetization curves more than 350 K is similar to that found for other ferro- and ferrimagnetic materials (Joy and Date, 2000). Moreover, a splitting between FC and ZFC magnetization curves can attributed to an inhomogeneous mixture of AFM and FM (Siwach *et al.*, 2007).

The temperature dependence of the inverse magnetic susceptibility, $1/\chi$, and the fitting curves are shown in the inset of Figure 4.52-4.54. The experimental is fitted data according to the Curie-Weiss law. The Curie constant (C) are 35.73, 41.34, 47.69, 88.09, and 173.19 emu K/g Oe for $x = 0, 0.05, 0.1, 0.2,$ and 0.3 samples, respectively, which increase with increasing of Cu doping concentration. The Curie-Weiss temperature (θ) value obtained from the Curie-Weiss fit of undoped-BiFeO₃ and Cu-doped BiFeO₃ samples are shown in Table 4.32. This negative values of the θ of all samples indicated the antiferromagnetic characteristics with weak FM and without FM component. By fitting with Curie-Weiss law, the theoretical effective moment can compute from Curie constant (C). The effective magnetic moment (μ_{eff}) values from experiment of the undoped BiFeO₃ and Cu-doped BiFeO₃ samples with $x = 0.05, 0.1, 0.2,$ and 0.3 are shown in Table 4.32. The μ_{eff} values are increased with increasing of Cu doping. The μ_{eff} values obtained from experiments for all samples are higher than the theoretical values of high-spin Fe³⁺ (5.92 μ_B). This fitting results from the experiment indicated that Fe³⁺ must be in a high spin configuration.

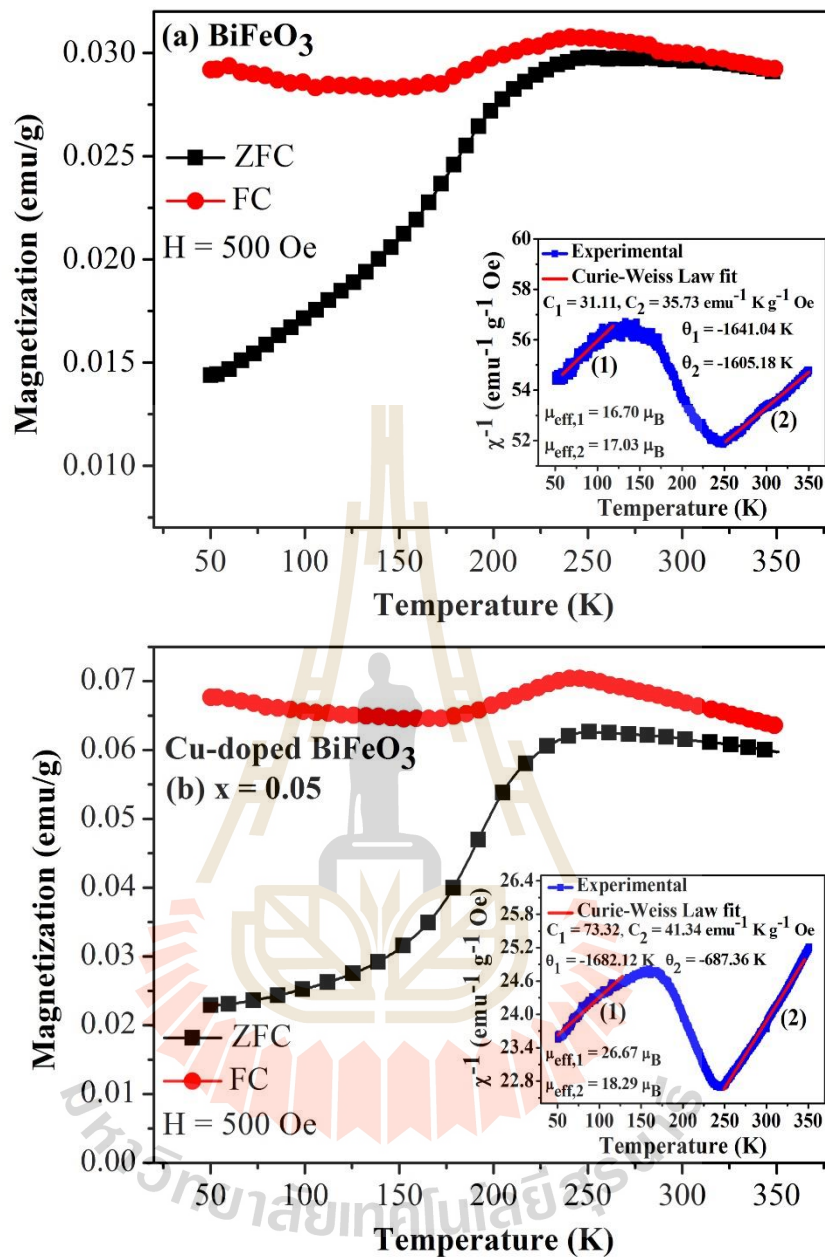


Figure 4.52 ZFC/FC curves and fitting the data to the Curie-Weiss law (inset) for (a) BiFeO₃ and (b) BiFe_{0.95}Cu_{0.05}O₃ nanoparticles.

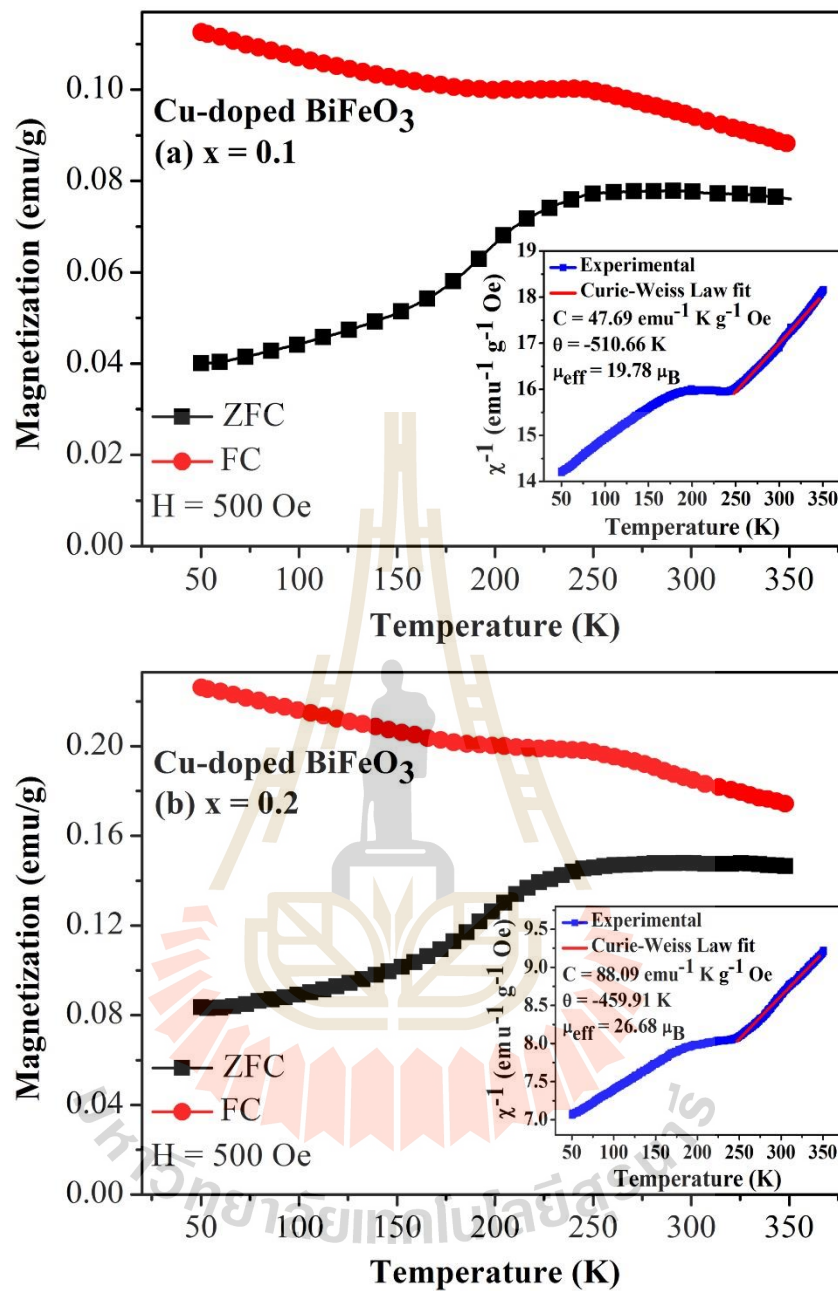


Figure 4.53 ZFC/FC curves and fitting the data to the Curie-Weiss law (inset) for (a) BiFe_{0.9}Cu_{0.1}O₃ and (b) BiFe_{0.8}Cu_{0.2}O₃ nanoparticles.

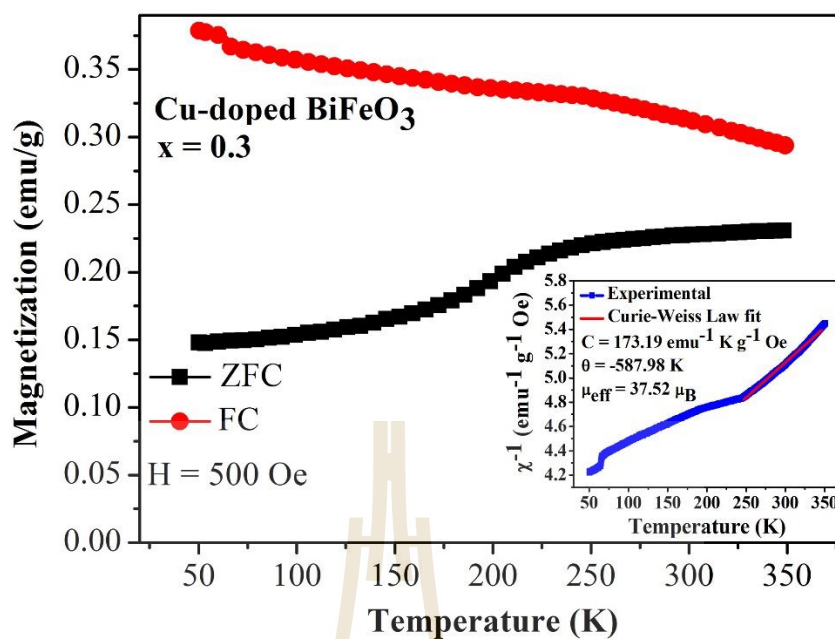


Figure 4.54 ZFC/FC curves and fitting the data to the Curie-Weiss law (inset) for $\text{BiFe}_{0.7}\text{Cu}_{0.3}\text{O}_3$ nanoparticles.

Table 4.32 Effective magnetic moment (μ_{eff}), Curie-Weiss temperature (θ) obtained from Curie-Weiss law fitting results for Cu-doped BiFeO_3 .

Doping level	μ_{eff} (μ_{B})	θ (K)
$x = 0$	16.70 ^a , 17.03 ^b	-1641.04 ^a , -1605.18 ^b
$x = 0.05$	26.67 ^a , 18.29 ^b	-1682.12 ^a , -687.36 ^b
$x = 0.1$	19.78	-510.66
$x = 0.2$	26.68	-459.91
$x = 0.3$	37.52	-587.98

a is fitting at $T = 50\text{-}130$ K, **b** is fitting at $T = 250\text{-}350$ K

4.3.3 Electrochemical properties of Cu-doped BiFeO₃ nanoparticles

4.3.3.1 Cyclic voltammetry measurement

Figure 4.55 shows the CV curves for the BiFe_{1-x}Cu_xO₃ nanoparticles. CV measurements were performed between -1.2 to 0.3 V at different potential scan rates of 5 to 100 mV/s in 6 M KOH solution. The samples exhibited a pseudocapacitive behavior. The redox peaks were observed for all the samples, indicating the redox transitions of the nanoparticles between different valence states. The height of the peak currents varied and a progressive shift in the peaks to higher potentials were observed with increasing scan rates from 5 to 100 mV/s. The specific capacitances of different synthesized samples at different scan rates were calculated from equation 3.13. The calculated specific capacitances vs scan rate are plotted in Figure 4.55(f). The specific capacitances of all the samples decrease with increasing scan rate. This is attributed to the presences of inner active sites, which completely inhibited the redox transitions at higher scan rates of CV, probably owing to the diffusion effect of protons within the electrode (Kötz and Carlen, 2000). At a scan rate of 5 mV/s, all the electrodes exhibited the highest specific capacitance. The maximum specific capacitance of 451.82 F/g at a scan rate of 5 mV/s was obtained in the Cu-doped sample with $x = 0.05$. The specific capacitance of the nanoparticles did not linearly depend on Cu doping concentration. Specific capacitance tended to increase from $x = 0$ to $x = 0.05$ and continuously decrease from $x = 0.10$ to $x = 0.30$.

The number of active sites of the electrodes were calculated using equation 3.14. The calculated number of active sites involved in the redox reaction at different scan rates corresponding to 5-100 mV/s are 1.93-0.89, 2.20-0.96, 2.00-0.77, 1.88-0.77, and 1.77-0.72 in $x = 0, 0.05, 0.1, 0.2,$ and 0.3 samples, respectively as shown in Table 4.33-

4.34. By comparison, the calculated number of active sites of Cu-doped BiFeO₃ (x = 0.05) nanoparticles (2.20-0.96) in this work are slightly higher than Bi₂WO₆ nanoparticles (2.07-0.32) (Nithya *et al.*, 2013) at scan rates of 5-100 mV/s. The number of redox sites participating at lower scan rates is higher compared with the higher scan rates. At slow scan rates, the ions would have enough time to arrive the electrode surface leading to the full utilization of the material. At higher scan rates, the ions would not have enough time to utilize the material and hence the surface adsorption process only takes place (Selvan *et al.*, 2008; Nithya *et al.*, 2013). According to the equation 3.9, the calculated diffusion co-efficient for 6 M KOH electrolyte at different scan rates corresponding to 5-100 mV/s are $2.61-1.38 \times 10^{-16}$, $2.62-2.19 \times 10^{-16}$, $1.93-1.03 \times 10^{-16}$, $1.77-1.02 \times 10^{-16}$, and $1.75-0.85 \times 10^{-16}$ cm²/s in x = 0, 0.05, 0.1, 0.2, and 0.3 samples, respectively as shown in Table 4.33-4.34. The value of diffusion co-efficient depends mainly on the peak current since the other parameters in the equation such as the number of electrons transferred during the redox reaction, concentration and scan rate. The diffusion co-efficient at lower scan rates is higher compared with the higher scan rates. Moreover, since the peak current of x = 0.05 sample is higher than other samples, the diffusion co-efficient value of x = 0.05 sample (2.61×10^{-16} cm²/s) is found to be higher than other samples. By comparison, the calculated diffusion co-efficient of BiFeO₃ and Cu-doped BiFeO₃ (x = 0.05) nanoparticles ($2.61-0.85 \times 10^{-16}$ cm²/s) for 6 M KOH electrolyte at 5-100 mV/s in this work are higher than the diffusion co-efficient of Bi₂WO₆ nanoparticles for 1 M KOH electrolyte (3.6×10^{-17} cm²/s) and 1M KOH electrolyte (1.2×10^{-17} cm²/s) at 2 mV/s (Nithya *et al.*, 2013). The variations of number of active sites and diffusion co-efficient correspond to variations of specific capacitances of the Cu-doped BiFeO₃.

A slight but significant crystallite size decreases from 88 nm in BiFeO₃ to 75 nm after 5 % Cu doping was determined using the Debye-Scherrer equation. This crystallite size decrease led to the sharp increase in the specific surface area (S_{BET}) from 3.6 m²/g in the BiFeO₃ sample to 3.9 m²/g in the BiFe_{0.95}Cu_{0.05}O₃ sample. This slight improvement in crystallinity after 5% Cu doping is likely the main reason for the increase in the specific capacitance from 397.28 F/g in the undoped sample to 451.82 F/g in the Cu-doped sample (at 5 mV/s for CV measurement). However, it was noticed that the specific capacitances decreased when the Cu doping concentration was increased from 5 to 30 %. The surface area increased from 3.9 m²/g in the 5 %-Cu-doped sample to 6.8 m²/g in the 30 %-Cu-doped sample. This indicates that specific capacitance does not only depend on surface area but also on other factors such as the pore size distribution at Cu doping concentrations from 5 to 30% (Long *et al.*, 2001; Reddy and Reddy, 2003).

All the samples have distributions of different sizes of pores, namely, micropores, mesopores, as shown in Figure 4.49, indicating that they have a porous structure, which is specific for supercapacitor materials (Long *et al.*, 2001; Reddy and Reddy, 2003). The improvement in the specific capacitance of the BiFe_{0.95}Cu_{0.05}O₃ sample and the decrease in the specific capacitance of the BiFe_{1-x}Cu_xO₃ samples with increasing x is possibly attributed to mesopore size of the BiFe_{0.95}Cu_{0.05}O₃ sample, which showed the smallest mesopore size of about 2.4 nm. This provides more active sites for chemical reactions (Dubal *et al.*, 2013). The BiFe_{1-x}Cu_xO₃ samples showed smaller pore diameters which tended to decrease with increasing x. Moreover, the edge shift slightly increase above Bi³⁺ position with increasing of Cu doping, except x = 0.05, which is 1.38, 1, 1.40, 1.42, and 1.52 for x = 0, 0.05, 0.1, 0.2, and 0.3 samples,

respectively. This result is in good agreement with reversible redox reaction of Bi^{3+} to Bi_{metal} . Increasing of Cu doping, the oxidation state of Bi is increased higher than $3+$, except $x = 0.05$ were inactive and did not participate in the redox reaction, which may lead to the reduction of height of the peak current and deterioration of specific capacitances. In comparison with those of previously reported BiFeO_3 -based electrodes, the specific capacitances of BiFeO_3 nanoparticles (373.65 F/g) and $\text{BiFe}_{0.95}\text{Cu}_{0.05}\text{O}_3$ (434.45 F/g) tested in 6 M KOH electrolyte are close to that of BiFeO_3 nanorod (450 F/g) tested in 1 M Na_2SO_4 electrolyte at the same scan rate of 10 mV/s. This may be due to difference of electrolyte and a particular structure, that is, an anodized alumina template with a rod form with a high porosity and a large surface area (Rana *et al.*, 2014). Interestingly, the specific capacitance of the BiFeO_3 nanoparticle (342.79 F/g) and $\text{BiFe}_{0.95}\text{Cu}_{0.05}\text{O}_3$ (395.97 F/g) in this work is higher than that of the BiFeO_3 thin film electrode (81 F/g) tested in 1 M NaOH electrolyte at the same scan rate of 20 mV/s (Lokhande *et al.*, 2007). However, thin-film-based supercapacitors also exhibited higher specific capacitances than their bulk electrode owing to their excellent electrical contact to the substrate, fast electron transfer, and electrolyte diffusion (Lokhande *et al.*, 2011).

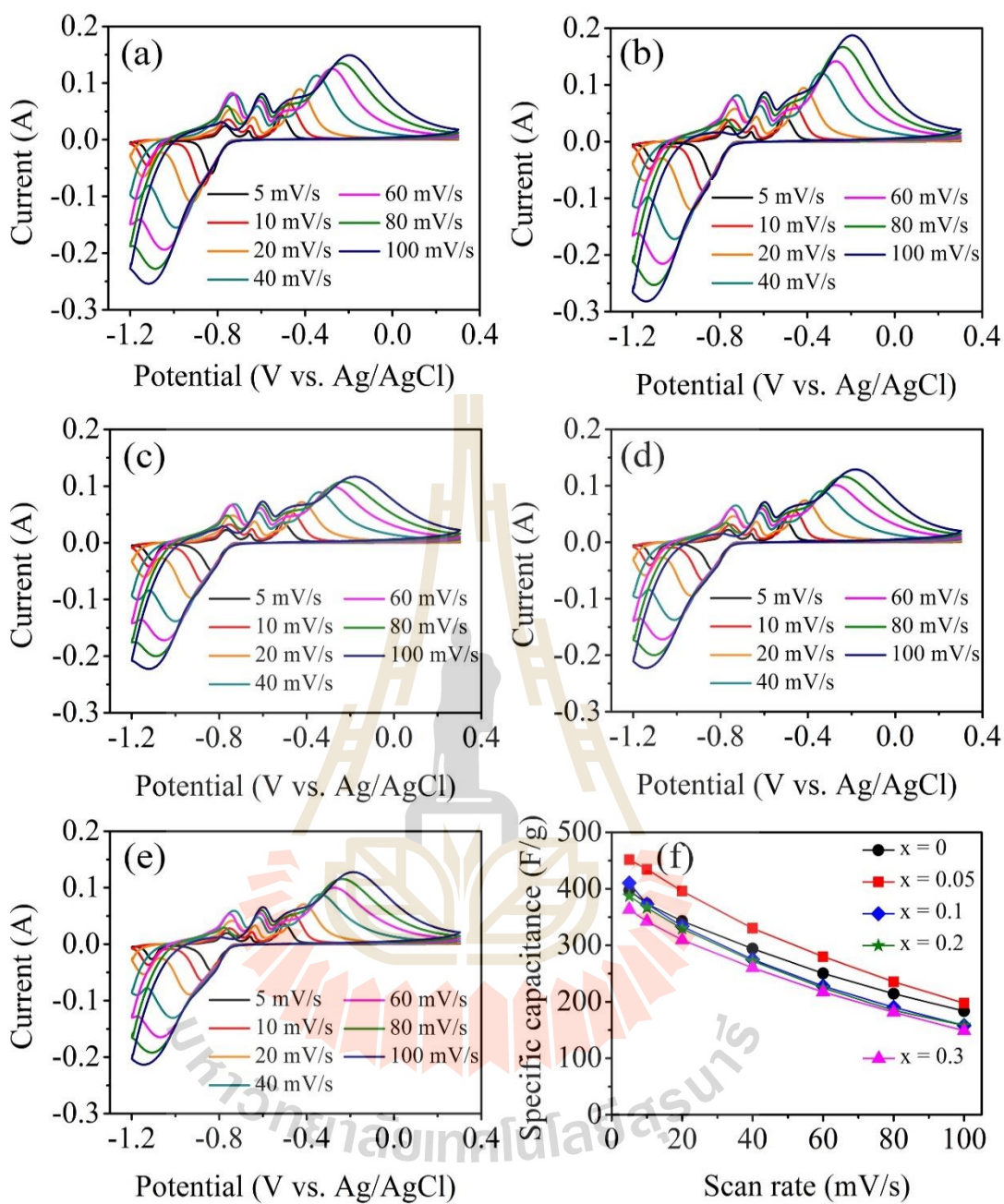


Figure 4.55 CV curves of the $\text{BiFe}_{1-x}\text{Cu}_x\text{O}_3$ nanoparticles: (a) $x = 0$, (b) $x = 0.05$, (c) $x = 0.1$, (d) $x = 0.2$, and (e) $x = 0.3$. (f) Specific capacitance vs scan rate.

Table 4.33 Specific capacitances, number of active sites (N) and diffusion coefficients (D) of $\text{BiFe}_{1-x}\text{Cu}_x\text{O}_3$ ($x = 0, 0.05, \text{ and } 0.1$) samples at various scan rates.

Sample	Scan rate (mV/s)	Specific capacitance (F/g)	Number of active site	Diffusion coefficient (cm^2/s) $\times 10^{-16}$
x = 0	5	397.28	1.93	2.61
	10	373.65	1.82	2.48
	20	342.79	1.67	2.34
	40	294.02	1.43	2.00
	60	250.26	1.22	1.63
	80	214.23	1.04	1.42
	100	183.67	0.89	1.38
x = 0.05	5	451.82	2.20	2.62
	10	434.45	2.11	2.88
	20	395.97	1.93	2.75
	40	330.23	1.61	2.29
	60	279.99	1.36	2.09
	80	235.50	1.15	2.17
	100	197.65	0.96	2.19
x = 0.1	5	410.61	2.00	1.93
	10	372.88	1.81	1.73
	20	333.74	1.62	1.68
	40	275.11	1.34	1.28
	60	227.81	1.11	1.06

Table 4.34 Specific capacitances, numbers of active site (N) and diffusion coefficient of Cu-doped BiFeO₃ (x = 0.1, 0.2, and 0.3) samples at various scan rates.

Sample	Scan rate (mV/s)	Specific capacitance (F/g)	Number of active site	Diffusion coefficient (cm ² /s) × 10 ⁻¹⁶
x = 0.1	80	190.33	0.93	1.05
	100	158.01	0.77	1.03
x = 0.2	5	387.17	1.88	1.77
	10	366.48	1.78	1.59
	20	329.62	1.60	1.60
	40	272.37	1.32	1.22
	60	224.57	1.09	1.04
	80	184.90	0.90	1.03
	100	158.14	0.77	1.02
x = 0.3	5	363.61	1.77	1.75
	10	342.36	1.66	1.58
	20	309.64	1.51	1.56
	40	260.26	1.27	1.18
	60	217.45	1.06	1.01
	80	181.72	0.88	0.90
	100	148.84	0.72	0.85

4.3.3.2 Galvanostatic charge-discharge measurements

Figures 4.56(a)-4.56(e) show the charge-discharge behavior of the electrodes at current densities from 1 to 20 A/g. The nonlinear curves confirm the pseudacapacitance behavior of the material. The discharge curve of the electrodes consists of two parts: a steep voltage drop due to internal resistance and a capacitive component (curved portion) related to the voltage change due to change in energy within the capacitor (Fusalba *et al.*, 1999). The galvanostatic charge-discharge curves tested in all samples show that, with increasing current density, the discharge time reduces. The specific capacitances of different synthesized samples at different current density were calculated from the equation 3.15. The specific capacitance, as shown in Figure 4.56(f), decreases with increasing of current density for all the samples. This decrease in the capacitance suggests that the surface of the electrode is inaccessible at high charging-discharge rates (Lokhande *et al.*, 2007). Therefore, the specific capacitances of the electrodes at a low current density should be suitable for practical applications. At a current density of 1 A/g, all the electrodes exhibited the highest specific capacitance. The maximum specific capacitance of 233.41 F/g at 1 A/g current density was obtained in the Cu-doped sample with $x = 0.05$. The specific capacitance at all current densities increased from $x = 0$ to $x = 0.05$ and continuously decreased from $x = 0.10$ to $x = 0.30$. Performances with energy density and power density in a Ragone plot of the BiFeO₃ and Cu-doped BiFeO₃ electrodes were calculated based on the galvanostatic charge-discharge as shown in Figure 4.57.

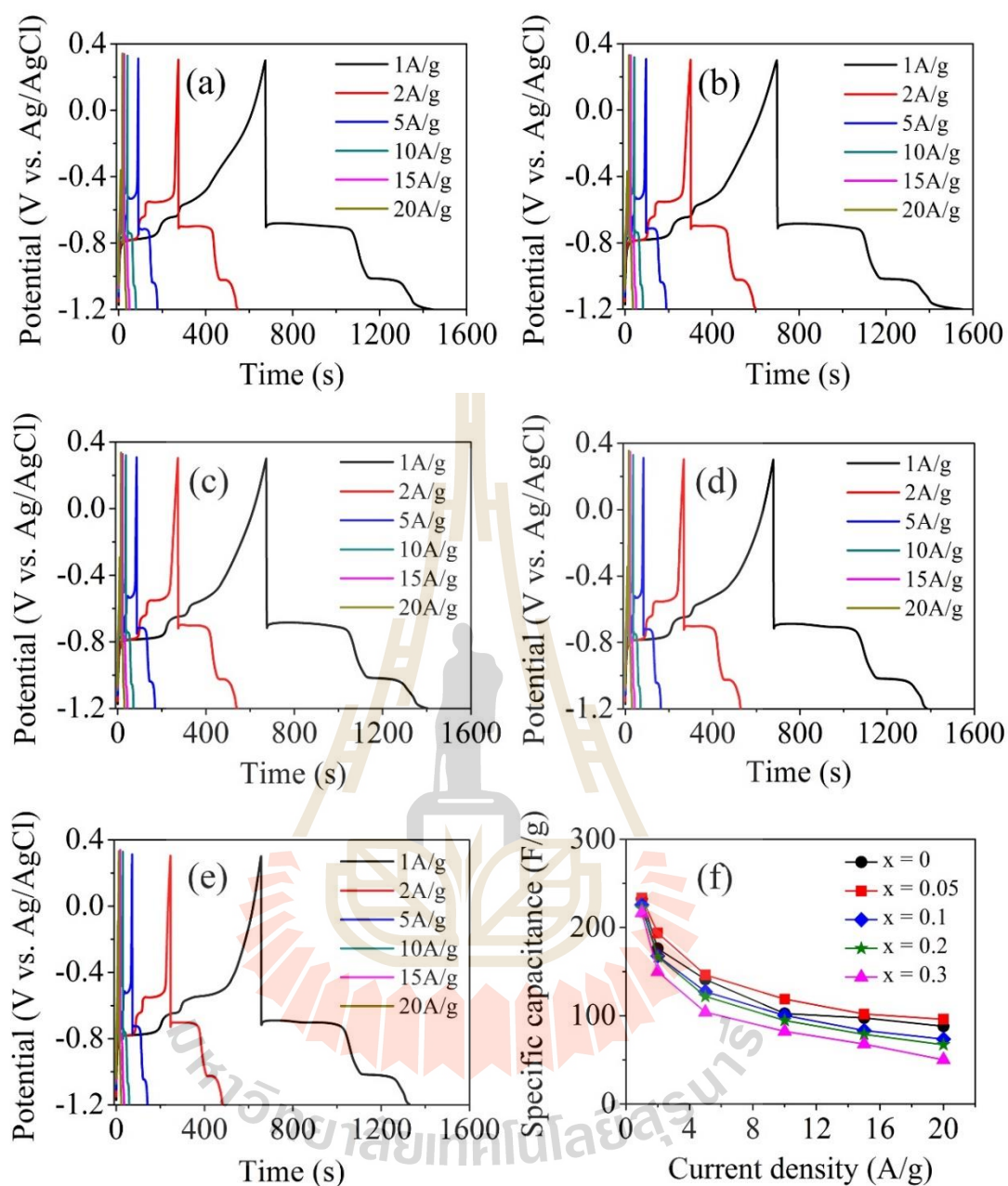


Figure 4.56 Galvanostatic charge-discharge curves of the BiFe_{1-x}Cu_xO₃ nanoparticles:

(a) $x = 0$, (b) $x = 0.05$, (c) $x = 0.1$, (d) $x = 0.2$, and (e) $x = 0.3$. (f) Specific capacitance

vs current density.

The energy densities are decreased with increasing of Cu content and increasing of current density, except $x = 0.05$ sample which can slightly improve energy density, while the power density are increased with increasing of current density as shown in Table 4.35-4.36. Among different electrodes, Cu-doped BiFeO_3 ($x = 0.05$) electrode shows highest energy density (73.03 Wh/Kg) at current density of 1 A/g. Moreover, the highest power density was observed in Co-doped BiFeO_3 ($x = 0.05$) electrode (6413.41 W/Kg) at current densities of 20 A/g. At the current density of 1 A/g, the power density are slightly increased from 308.30 to 360.94 W/Kg with Cu doping concentration for $x = 0.05$ to $x = 0.3$ samples, respectively.

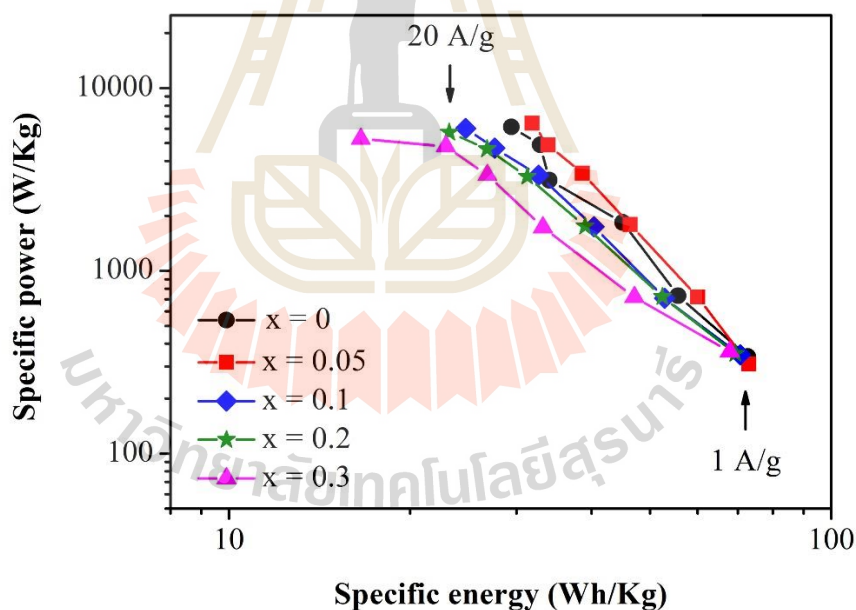


Figure 4.57 Ragone plot showing energy densities and power densities relationship of BiFeO_3 and Cu-doped BiFeO_3 electrodes.

Table 4.35 Specific capacitances, energy densities, and power densities of BiFe_{1-x}Cu_xO₃ (x = 0, 0.05, and 0.1) samples at various current densities.

Sample	Current density (A/g)	Specific capacitance (F/g)	Energy density (Wh/Kg)	Power density (W/Kg)
x = 0	1	232.24	72.71	339.48
	2	176.20	55.67	731.64
	5	141.03	45.05	1838.66
	10	102.48	34.04	3133.76
	15	97.54	32.88	4890.50
	20	88.03	29.44	6127.17
x = 0.05	1	233.41	73.03	308.30
	2	193.78	60.04	716.41
	5	146.21	46.39	1788.01
	10	118.78	38.64	3417.69
	15	101.79	33.92	4884.00
	20	96.00	31.89	6413.41
x = 0.1	1	225.69	70.61	347.11
	2	167.92	52.89	709.46
	5	127.31	40.38	1744.90
	10	100.26	32.67	3331.44
	15	83.13	27.63	4691.04
	20	73.42	24.72	6013.51

Table 4.36 Specific capacitances, energy densities, and power densities of $\text{BiFe}_{1-x}\text{Cu}_x\text{O}_3$ ($x = 0.2$ and 0.3) sample at various current densities.

Sample	Current density (A/g)	Specific capacitance (F/g)	Energy density (Wh/Kg)	Power density (W/Kg)
x = 0.2	1	221.35	69.32	353.12
	2	166.64	52.42	721.61
	5	121.84	39.01	1753.43
	10	94.64	31.28	3282.80
	15	78.83	26.83	4644.23
	20	67.15	23.22	5726.03
x = 0.3	1	216.60	67.85	360.94
	2	149.93	47.13	718.07
	5	103.90	33.22	1728.32
	10	82.25	26.86	3346.02
	15	67.93	22.92	4796.51
	20	49.97	16.56	5274.34

In addition, Figure 4.58 shows the cycling performance of the $\text{BiFe}_{1-x}\text{Cu}_x\text{O}_3$ electrodes at different concentrations of Cu doping with $x = 0, 0.05, 0.1, 0.2,$ and 0.3 at 10 A/g current density. The cycle life (stability) of the electrodes is important for practical applications. Capacity retention can be improved by Cu doping. All of the Cu-doped electrodes except $\text{BiFe}_{0.95}\text{Cu}_{0.05}\text{O}_3$, $\text{BiFe}_{0.9}\text{Cu}_{0.1}\text{O}_3$, and $\text{BiFe}_{0.8}\text{Cu}_{0.2}\text{O}_3$ showed higher capacity retention than the undoped BiFeO_3 electrode. The capacity retention of the $\text{BiFe}_{0.95}\text{Cu}_{0.05}\text{O}_3$ electrode was high. It increased to 120% after 40 cycles, and then

slightly decreased to 77.13 % after 500 cycles. For the $\text{BiFe}_{0.9}\text{Cu}_{0.1}\text{O}_3$ electrode, its capacity retention was increased to 107 % after 60 cycles and decreased to 73.15% after 500 cycles. The capacity retention of over 100 % in this electrode was due to the additional cycles needed to fully activate the sample (Wei *et al.*, 2010; Vivier *et al.*, 2001). This is in agreement with the small mesopore size at low Cu doping concentration, which lead to the suppression of electrolyte diffusion into the inner region of the electrode (Lokhande *et al.*, 2011; Dubal *et al.*, 2013). The capacity retentions of the Cu-doped BiFeO_3 samples with $x = 0, 0.20,$ and 0.30 were 58.59, 61.00, and 52.93 %, respectively, after 500 cycles.

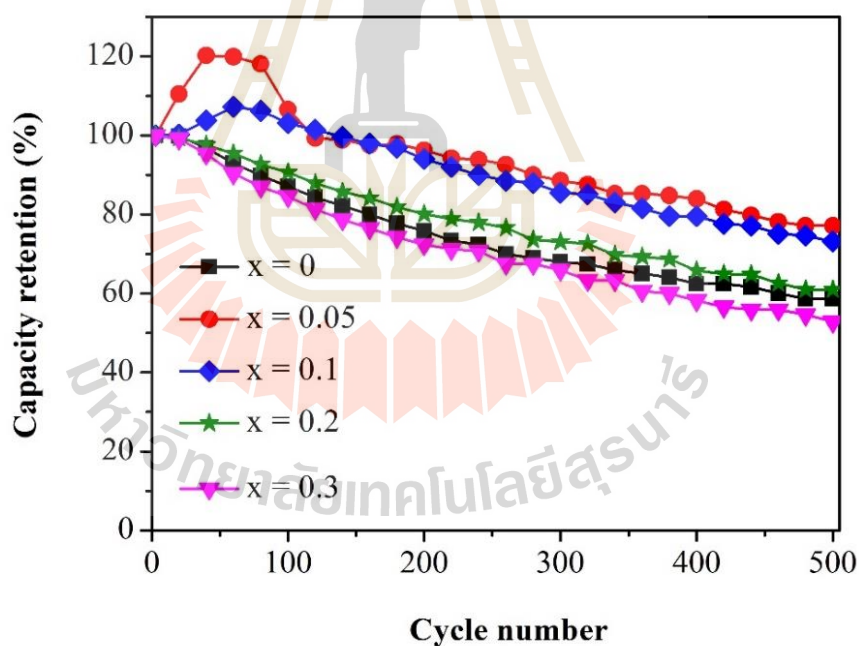


Figure 4.58 Capacity retention (%) of the $\text{BiFe}_{1-x}\text{Cu}_x\text{O}_3$ electrodes after 500 cycles at 10 A/g current density.

4.3.3.3 Electrochemical impedance spectroscopy (EIS) measurements

Figure 4.59 shows Nyquist plots of the $\text{BiFe}_{1-x}\text{Cu}_x\text{O}_3$ ($x = 0, 0.05, 0.1, 0.2,$ and 0.3) electrodes. The small values of solution resistance (R_s) of the $\text{BiFe}_{1-x}\text{Cu}_x\text{O}_3$ ($x = 0, 0.05, 0.1, 0.2,$ and 0.3) electrodes are 0.24, 0.27, 0.26, 0.25, and 0.27 Ω , respectively, which suggest that all electrodes provide good electrical conductivity of the electrolyte. The semi-circle at high frequency corresponds to R_{ct} . The R_{ct} of the $\text{BiFe}_{1-x}\text{Cu}_x\text{O}_3$ ($x = 0, 0.05, 0.1, 0.2,$ and 0.3) electrodes are 0.13, 0.12, 0.09, 0.14, and 0.9 Ω , respectively. The small R_{ct} values indicate that all the electrodes providing the charge transfer performance at the electrode/electrolyte interface are facile (Nithya *et al.*, 2013). The N of the electrodes are in range of 0.711-0.956. This indicated that the electrodes imply the moderate capacitor close to ideal capacitor behavior. In this work, variations in the specific capacitances and capacity retention of the Cu-doped BiFeO_3 electrodes are not attributed to slight increases of surface area and slight differences in the R_{ct} , CPE, W , and R_s values. The straight lines close to 90° are parallel to the imaginary axis at low frequencies which indicate a good capacitive behavior and a low diffusion resistance of the ions in the structure of the electrodes (Guan *et al.*, 2013; Yang *et al.*, 2012; Wang *et al.*, 2011). The more vertical the curve, the more closely the supercapacitor performs as an ideal capacitor. Interestingly, increases in Cu doping concentrations with $x = 0$ to $x = 0.3$ correspond to the curves which move away from the vertical line. Thus, the vertical curve of the BiFeO_3 electrodes close to 90° provides a greater capacitance with low diffusion resistance of ions in the structure of the electrodes than for the Cu-doped BiFeO_3 samples. This leads to decreases in the specific capacitances.

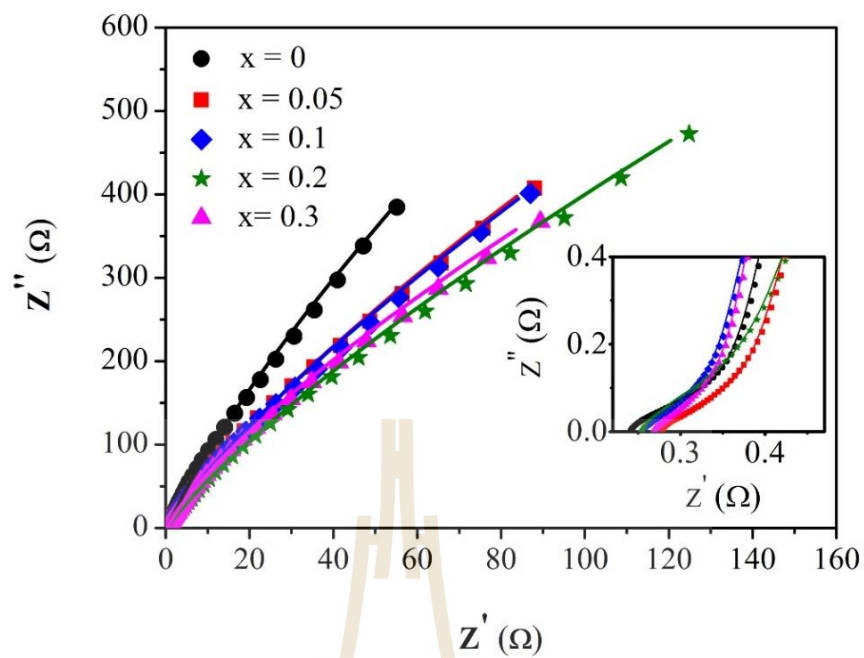


Figure 4.59 Nyquist plots of the BiFe_{1-x}Cu_xO₃ (x = 0, 0.05, 0.1, 0.2, and 0.3) electrodes.

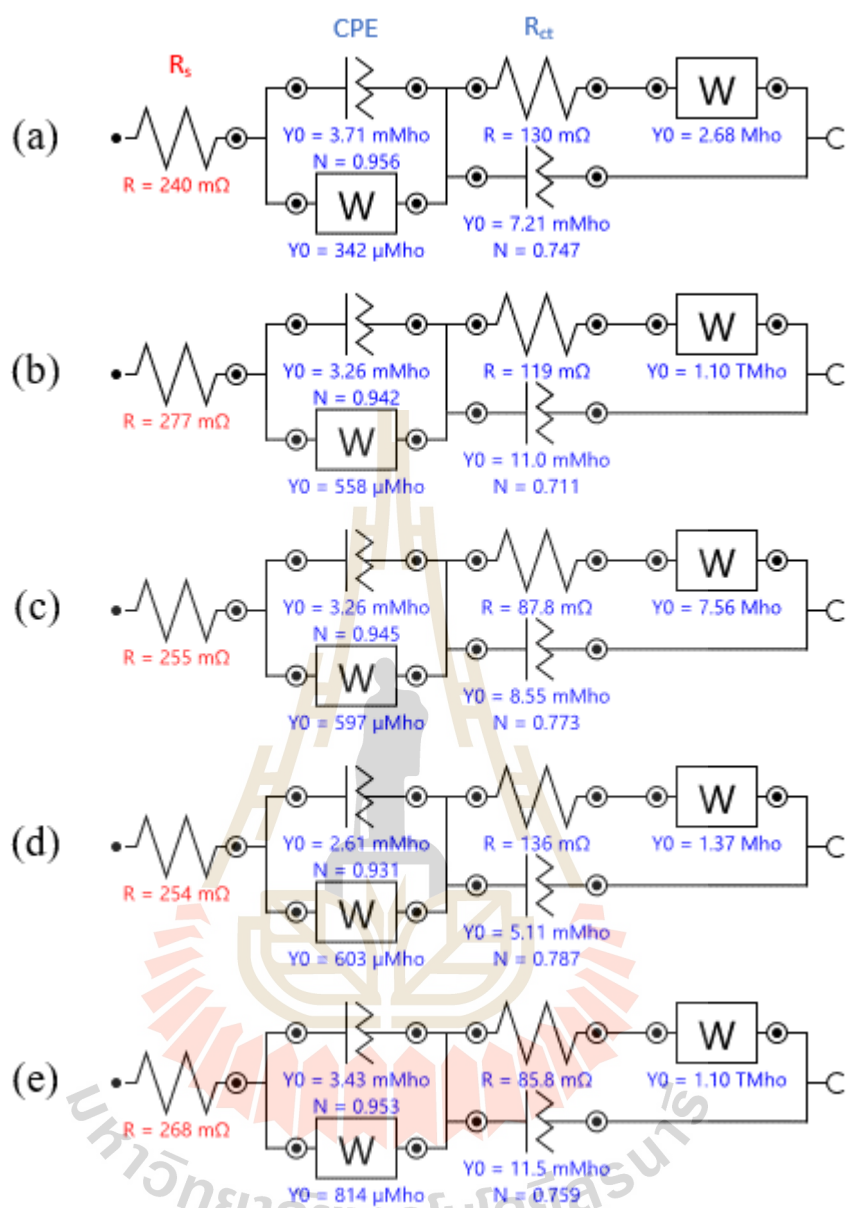


Figure 4.60 Equivalent circuit of the BiFe_{1-x}Cu_xO₃ electrodes: (a) $x = 0$, (b) $x = 0.05$, (c) $x = 0.1$, (d) $x = 0.2$, and (e) $x = 0.3$.

CHAPTER V

CONCLUSIONS AND SUGGESTIONS

In this study, $\text{BiFe}_{1-x}\text{M}_x\text{O}_3$ ($\text{M} = \text{Co}, \text{Ni}, \text{and Cu}$) nanoparticles were successfully synthesized by a simple solution method. In each doping system, five samples have different dopant contents from 0 %, 5 %, 10 %, 20 %, and 30 %, respectively. The structures and morphologies of all the samples were characterized by XRD, SEM, TEM, XAS, and Gas absorption techniques. The magnetic properties were studied by VSM, while the electrochemical properties were studied by CV, GCD, and EIS techniques. Based on the experimental results, it has been demonstrated that understandings of relationship of structure morphology and properties for the $\text{BiFe}_{1-x}\text{M}_x\text{O}_3$ ($\text{M} = \text{Co}, \text{Ni}, \text{and Cu}$) nanoparticles summarized as follows:

5.1 The structure and morphology characterization

The XRD patterns of all samples are found in the main phase which correspond to BiFeO_3 (JCPDS No.86-1518). Small impurity peaks in some samples are present which correspond to different phases such as $\text{Bi}_2\text{Fe}_4\text{O}_9$ (JCPDS No.72-1832), CoFe_2O_4 (JCPDS No.02-1045), Co_3O_4 (JCPDS No.80-1537), and NiFe_2O_4 (JCPDS No.86-2267). The crystallite size of Co-doped BiFeO_3 , Ni-doped BiFeO_3 , and Cu-doped BiFeO_3 nanoparticles (88.8-54.5 nm, 88.8-34.1 nm, and 88.8-66.4 nm, respectively) decreased with increasing of doping content (from un-doped to 30 %). The variation of

lattice constant values of BiFeO₃ conforms to the doping of Co, Ni, and Cu ions. The decrease in lattice constant values of c-parameter with increasing of doping from x = 0 to x = 0.3 for Co-doped BiFeO₃ and Cu-doped BiFeO₃ nanoparticles occur due to Co³⁺ (0.545 Å) and Cu³⁺ (0.54 Å) with a small ionic radius substitutes the Fe³⁺ (0.645 Å) site, respectively. For Ni-doped BiFeO₃ nanoparticles, there is an increase in a parameter in x = 0 to x = 0.3 samples, which related to the increasing of Ni doping concentration. These confirm that the Fe³⁺ (~0.645 Å) site is substituted with higher ionic radius of Ni²⁺ (0.69 Å). This agrees with the oxidation states results from XAS analysis that the oxidation-state of Bi and Fe K edge in all samples is 3+. The oxidation states of Co, Ni, and Cu in Co-doped BiFeO₃, Ni-doped BiFeO₃, and Cu-doped BiFeO₃ nanoparticles are the mixing of 2+ and 3+, 2+, and 3+, respectively. Moreover, the variation of lattice constant values of BiFeO₃ also conform to the variation of crystallize size. According to the morphology observation, the morphology of the nanoparticles was investigated by SEM which showed decreasing (100-200 nm for undoping sample to 50-150 nm for doping samples) in the particle size of the nanoparticles, which is in good agreement with the crystallite size measured by using Scherrer's formula. The TEM bright field images of all samples show that the particles sizes obtained were about 50-200 nm. HRTEM of all samples shows the lattice fringes with interplanar spacing which correspond to the BiFeO₃ structure. Moreover, The SAED patterns of all samples show spotty and ring patterns which indicate the characteristics of nanocrystalline BiFeO₃ (JCPDS No.86-1518). This is in agreement with the XRD and SEM results. In this research, we confirm that all the samples with higher concentrations of Co, Ni, and Cu dopant showed a decrease in particle sizes, which conform to a tendency of increasing their specific surface areas.

5.2 The Magnetic properties

According to the magnetic property study, the room temperature saturation magnetization (M_s) of un-doped BiFeO_3 , $\text{BiFe}_{1-x}\text{Co}_x\text{O}_3$, $\text{BiFe}_{1-x}\text{Ni}_x\text{O}_3$ and $\text{BiFe}_{1-x}\text{Cu}_x\text{O}_3$ with $x = 0.05-0.3$ are 0.219 emu/g, 1.08-8.25 emu/g, 2.51-19.12 emu/g, and 0.31-0.79 emu/g, respectively. The M_s linearly increases with increasing Co, Ni, and Cu doping concentrations ($x = 0$ to 0.3) and trend to increase with higher temperatures of measurement from 50 to 350 K. Clearly, the doping of magnetic materials of Co and Ni can improve the M_s , which correspond to their high magnetic moments per atom of 1.72 and 0.6 μ_B , respectively. Interestingly, the doping of nonmagnetic material of Cu can also improve the M_s . Moreover, the improved magnetization may due to suppression of the spin cycloid structure of the particle size when it is less than 62 nm which causes the intrinsic spiral spin structure to be incompletely suppressed and the decreases in crystallite size with increases of Co, Ni, and Cu doping content results in an increase in surface-volume ratio and the contribution of uncompensated spin at the surface to the total magnetic moment of the particle increases. The magnetic hysteresis (M-H) curves, the M_s of BiFeO_3 slightly increases from 0.207 to 0.223 emu/g with increases in temperature from 50 to 350 K, respectively. Conversely, the magnetization of the Co, Ni, and Cu doping samples increases with decreases in temperature from 300 to 50 K, except at 200 K for Co doping samples and $x = 0.05$ samples at 100-200 K for Cu doping samples. Moreover, the increases in the secondary phases of the CoFe_2O_4 and Co_3O_4 nanoparticles in the $\text{BiFe}_{1-x}\text{Co}_x\text{O}_3$ ($x = 0.2$ to $x = 0.3$) samples and the NiFe_2O_4 nanoparticles in the $\text{BiFe}_{1-x}\text{Ni}_x\text{O}_3$ ($x = 0.05$ to 0.3) samples also cause an increase in saturation magnetization. The coercivity (H_c) of un-doped BiFeO_3 , $\text{BiFe}_{1-x}\text{Co}_x\text{O}_3$ ($x = 0.05-0.3$), $\text{BiFe}_{1-x}\text{Ni}_x\text{O}_3$ ($x = 0.05-0.3$), and $\text{BiFe}_{1-x}\text{Cu}_x\text{O}_3$ ($x = 0.05-0.3$) are 52.82 Oe,

400.74-1003.20 Oe, 13.07-23.09 Oe, and 45.87-325.24 Oe, respectively. The undoped BiFeO₃ and Ni-doped BiFeO₃ display a very slim hysteresis loop with nonzero remnant magnetization and narrow coercive field exhibits antiferromagnetic behavior at room temperature, while Co-doped BiFeO₃ and Cu-doped BiFeO₃ composite samples showed enhanced ferromagnetic behavior. The increasing H_c values of BiFe_{1-x}Co_xO₃ and BiFe_{1-x}Cu_xO₃ correspond to increasing doping concentration and decreasing of the crystallite-size of BiFeO₃ below a critical size when the crystallite size is in the multi-domain region. Not only the size effects of BiFeO₃ but the presence of CoFe₂O₄ and Co₃O₄ are also strongly influenced to the H_c values for BiFe_{1-x}Co_xO₃ (x = 0.2 and 0.3). The increasing of phase composition of NiFe₂O₄ and decreasing of crystallite sizes of NiFe₂O₄ in BiFe_{1-x}Ni_xO₃ (x = 0.05 to 0.3) are related to variations of H_c values, especially, decreasing of H_c values of the x = 0.2 samples. The H_c of all samples increases with measurements at low temperature due to the alignment of the magnetic moment in the direction of the external magnetic field and thermal fluctuations of nanoparticles decrease with decreases in the temperature. Moreover, the remanent magnetization (M_r) of un-doped BiFeO₃, BiFe_{1-x}Co_xO₃ (x = 0.05-0.3), BiFe_{1-x}Ni_xO₃ (x = 0.05-0.3), and BiFe_{1-x}Cu_xO₃ (x = 0.05-0.3) are 0.005 emu/g, 0.35-3.57 emu/g, 0.06-0.65 emu/g, and 0.02-0.17 emu/g, respectively. The M_r values increases due to increases of the Co, Ni, and Cu contents with decreasing of the crystallite size of BiFeO₃ and decreasing of temperature. In order to understanding the effect of doping on the magnetic ordering of BiFeO₃, the temperature dependent zero-field cooled (ZFC) and field cooled (FC) magnetization measurements are carried out from temperature range 50 K-350 K under applied field of 500 Oe. The feature of the ZFC curves of un-doped and Cu-doped BiFeO₃ (x = 0.05) sample shows T_{max} ~ 250 K, which can be attributed

to the magnetic blocking mechanism. However, other doped BiFeO₃ samples show increases in the blocking temperatures (T_B) which are greater than 350 K. The hysteresis loop of undoped BiFeO₃, Ni and Cu-doped BiFeO₃ samples reveal weak ferromagnetic at 50-350 K, except Co-doped BiFeO₃ samples, which reveal ferromagnetic. This correspond to the Curie-Wiess law fitting results. The θ values of all samples are negative indicating antiferromagnetic interactions, except all Co-doped BiFeO₃ samples, which are positive indicating ferromagnetic interactions among magnetic ions. Moreover, this research found that all magnetic ions in all doped-BiFeO₃ samples are in the high spin configuration.

5.3 The Electrochemical properties

According to the electrochemical property studies, the redox behavior of the nanoparticles were studied by CV technique between -1.2 V to 0.3 V at different potential scan rates of 5 to 100 mV/s in 6 M KOH solution. This study indicated that all samples exhibited a pseudocapacitive behavior. The presence of redox peaks for all the samples indicated that the redox transitions of the nanoparticles between different valence states and the capacitance of the electrodes was mainly due to the rapid and faradic reaction on the electrode/electrolyte interface. The anodic and cathodic peak currents in the CV increased with an increase in potential scan rate. The current response of all electrodes was enhanced when increasing of the scan rates (5-100 mV/s) and decreasing of Co, Ni, and Cu doping concentration, except BiFe_{0.95}Cu_{0.05}O₃ samples were increased. In GCD measurement, all samples show the nonlinear form of curves with a steep voltage (IR) drop which exhibit the pseudocapacitive behavior due to internal resistance and a capacitive component. The calculated specific capacitance

of all samples decreases with increasing of Co, Ni, and Cu doping concentration, except $\text{BiFe}_{0.95}\text{Cu}_{0.05}\text{O}_3$ samples showed the improving of specific capacitance (451.82 F/ g) for CV measurement and (233.41 F/g) for GCD measurement at scan rate of 5 mV/s and current density of 1 A/g, respectively. In comparison with those of previously reported BiFeO_3 -based electrodes, the specific capacitances of BiFeO_3 nanoparticles (373.65 F/g) and $\text{BiFe}_{0.95}\text{Cu}_{0.05}\text{O}_3$ (434.45 F/g) tested in 6 M KOH electrolyte are close to that of BiFeO_3 nanorod (450 F/g) tested in 1 M Na_2SO_4 electrolyte at the same scan rate of 10 mV/s (Rana *et al.*, 2014). Interestingly, the specific capacitance of the BiFeO_3 nanoparticle (342.79 F/g) and $\text{BiFe}_{0.95}\text{Cu}_{0.05}\text{O}_3$ (395.97 F/g) is higher than that of the BiFeO_3 thin film electrode (81 F/g) tested in 1 M NaOH electrolyte at the same scan rate of 20 mV/s (Lokhande *et al.*, 2007). Among the three different electrodes in each system, Cu-doped BiFeO_3 showed almost highest specific capacitance compared to undoped BiFeO_3 , Ni-doped BiFeO_3 and Co-doped BiFeO_3 electrodes at all scan rates and current densities. By doping with Co, Ni, and Cu cause to different conditions responded to electrochemical performances as following: (1) 5 % of Cu doping showed the highest of number of active sites of redox reaction and diffusion co-efficient (0.96-2.20 and 22.19-2.62 $\times 10^{-16}$ cm^2/s , respectively). This lead to highest of electrochemical performances such as specific capacitance, energy density, power density and capacity retention. Conversely, the number of active sites of redox reaction and diffusion co-efficient of other samples are decrease with increasing of doping concentration from $x = 0$ to $x = 0.3$, which correspond to decreasing of the electrochemical performances. (2) The increasing composition of the secondary phase with lower capacitance than BiFeO_3 of CoFe_2O_4 in Co-doped BiFeO_3 ($x = 0.2$ to 0.3) and NiFe_2O_4 in Ni-doped BiFeO_3 ($x = 0.05$ to $x = 0.3$). This may lead to decreasing of

the specific capacitance of the samples. (3) By XANES analysis, increasing of the Co, Ni, and Cu doping concentration with slightly increase of oxidation state of Bi more than 3+ may lead to decreasing of the height of the peak current of redox reaction and specific capacitances. (4) The mesopore sizes of the BiFeO₃ samples showed small mesopore sizes (3.28 nm) which were smaller than the Co, Ni, and Cu doping samples, which increase with increasing doping concentration, except 5 % of Ni and Cu doping samples (2.42 nm). The small mesopore provides more active sites for chemical reactions (Dubal *et al.*, 2013), which is in good agreement with the results of calculated number of active site of redox reaction and diffusion co-efficient in this work. This may result in the high specific capacitances in the samples. (5) by EIS analysis, the vertical curve close to 90° at low frequencies indicate ideal capacitor behavior and low diffusion resistance of ions in the structure of the electrode (Guan *et al.*, 2013; Yang *et al.*, 2012; Wang *et al.*, 2011). This corresponds to the high specific capacitances in the BiFeO₃ showed more ideal capacitor behavior with vertical the curve and decrease of the specific capacitances with higher doping concentration, which away from the vertical line in Co and Ni doping samples, except some Cu doping samples. Generally, the high capacitance can be attributed to the high surface area and enhanced electrical conductivity of the electrodes (Guan *et al.*, 2013). But in this work, variations in the specific capacitances of some electrodes are not attributed to slight increases of surface area (3.64-21.85 nm) and slight differences in the R_{ct} (0.06-0.13 Ω) and the R_s (0.24 - 0.28 Ω) values. Performance with energy density and power density calculated based on the galvanostatic charge-discharge are decrease with increasing of Co, Ni, and Cu doping concentration and increasing of current density, except BiFe_{0.95}Cu_{0.05}O₃ samples showed improving of energy density (73.03-31.89 Wh/kg) and power density (308.30-

6413.41 W/kg) at current density of 1-20 A/g. The energy density for all electrodes of 3.33-73.03 Wh/kg were in the range observed between electrochemical capacitor of 1-10 Wh/kg and battery of 10-100 Wh/kg (González *et al.*, 2016). Among the three different electrodes in each system, Cu-doped BiFeO₃ showed almost highest energy density compared to undoped BiFeO₃, Ni-doped BiFeO₃, and Co-doped BiFeO₃ electrodes at all current densities. The power densities for all electrodes of 308.30-6413.41 W/kg were in the range observed between electrochemical capacitor of 500-10000 W/kg. The capacity retention decrease with increasing Co, Ni, Cu doping concentration from $x = 0.05$ to 0.3. But 5 % of Co and Ni doping and 5 % to 20 % of Cu doping can improve the capacity retention. This may due to the electrode needed to fully activate for 5 % or 10 % doping with small mesopore size, which cause the suppression of electrolyte diffusion into the inner region of the electrode (Lokhande *et al.*, 2011; Dubal *et al.*, 2013). This work showed that the Cu-doped BiFeO₃ nanoparticle with $x = 0.05$ has excellent electrochemical performance and can be considered as a good candidate for supercapacitors.

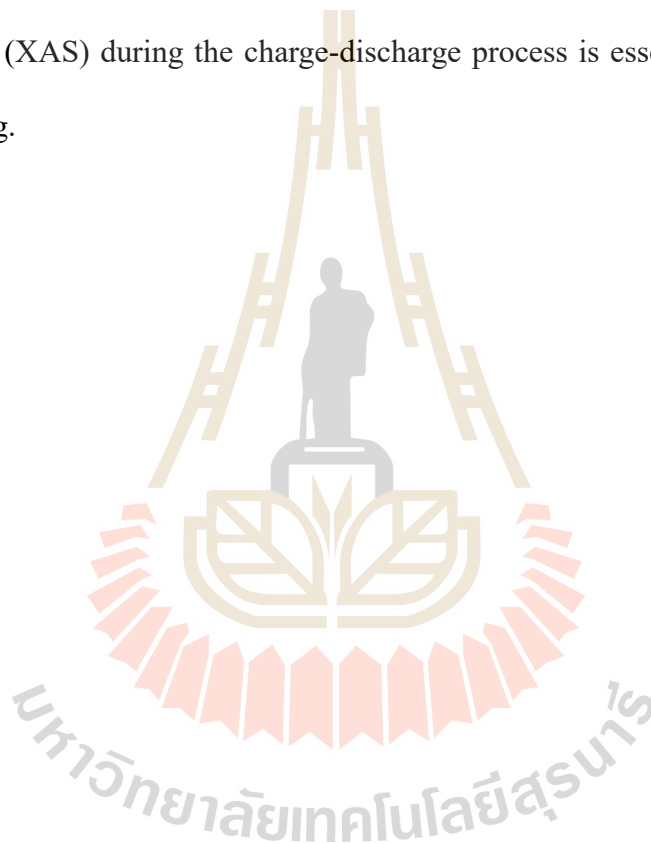
5.4 Suggestions

From the study of the magnetic and electrochemical properties of BiFe_{1-x}M_xO₃ (M = Co, Ni, and Cu) nanoparticles, we have many suggestions for future work to make clear explanation of the results as listed in the followings,

(1) The effect of Co, Ni, and Cu doping with $x = 0.05$ to 0.3 can directly affect the structure and magnetic properties and the doping with $x = 0.5$ can improve the electrochemical properties. This should be studied in more concentrations with x at lower than 0.05 and higher than 0.3.

(2) Study of electrochemical properties in the $\text{BiFe}_{1-x}\text{M}_x\text{O}_3$ ($\text{M} = \text{Co}, \text{Ni},$ and Cu) nanoparticles using various electrolytes in different concentrations and various substrate materials is required to confirm the suitable condition for the fabrication of supercapacitor electrodes.

(3) Investigation of atomic/electronic structure such as redox valency change of the $\text{BiFe}_{1-x}\text{M}_x\text{O}_3$ ($\text{M} = \text{Co}, \text{Ni},$ and Cu) electrodes using in situ X-ray absorption spectroscopy (XAS) during the charge-discharge process is essential to have a better understanding.





REFERENCES

มหาวิทยาลัยเทคโนโลยีสุรนารี

REFERENCES

- Achenbach, G., James, W. and Gerson, R. (1967). Preparation of single- phase polycrystalline BiFeO_3 . **Journal of the American Ceramic Society** 50: 437-437.
- Agrawal, S., Jawad, A., Ashraf, S. and Naqvi, A. (2014). Structural, optical, dielectric and magnetic properties of Cu doped BiFeO_3 nanoparticles synthesized by sol gel method. **Materials Focus** 3: 60-66.
- Bard, A. J., Faulkner, L., Leddy, R. J. and Zoski, C. G. (1980). **Electrochemical methods: fundamentals and applications**. New York: John Wiley & Sons.
- Barrett, E. P., Joyner, L. G. and Halenda, P. P. (1951). The determination of pore volume and area distributions in porous substances. I. Computations from nitrogen isotherms. **Journal of the American Chemical Society** 73: 373-380.
- Battisha, I. K., Farag, I. S. A., Kamal, M., Ahmed, M. A., Girgis, E., Meleegi, H. A. E and Desouki, F. E. (2015). Dielectric and magnetic properties of nano-structure BiFeO_3 doped with different concentrations of Co ions prepared by sol-gel method. **New Journal of Glass and Ceramics** 5: 59-73.
- Bea, H., Bibes, M., Barthelemy, A., Bouzehouane, K., Jacquet, E., Khodan, A., Contour, J. P., Fusil, S., Wyczisk, F. and Forget, A. (2005). Influence of parasitic phases on the properties of BiFeO_3 epitaxial thin films. **Applied Physics Letters** 87: 072508-072508-8.

- Beliakov, A. (2002). Asymmetric type electrochemical capacitors. **Capacitor and Hybrid Power Sources** 7: 12-15.
- Brousse, T., Toupin, M. and Belanger, D. (2004). A hybrid activated carbon-manganese dioxide capacitor using a mild aqueous electrolyte. **Journal of the Electrochemical Society** 151: A614-A622.
- Brownson, D. A. and Banks, C. E. (2014). **The handbook of graphene electrochemistry**. London: Springer.
- Brunauer, S., Emmett, P. H. and Teller, E. (1938). Adsorption of gases in multimolecular layers. **Journal of the American Chemical Society** 60: 309-319.
- Burke, A. and Miller, M. (2011). The power capability of ultracapacitors and lithium batteries for electric and hybrid vehicle applications. **Journal of Power Sources** 196: 514-522.
- Bush, A., Gippius, A., Zaleskii, A. and Morozova, E. (2003). ^{209}Bi NMR spectrum of BiFeO_3 in the presence of spatial modulation of hyperfine fields. **Journal of Experimental and Theoretical Physics Letters**. 78: 389-392.
- Callister, W. D. and Rethwisch, D. G. (2013). **Fundamentals of materials science and engineering**. New York: John Wiley & Sons.
- Castro, R. H., Hidalgo, P., Muccillo, R. and Gouvea, D. (2003). Microstructure and structure of NiO-SnO_2 and $\text{Fe}_2\text{O}_3\text{-SnO}_2$ systems. **Applied Surface Science**. 214: 172-177.
- Catalan, G. and Scott, J. F. (2009). Physics and applications of bismuth ferrite. **Advanced Materials** 21: 2463-2485.

- Chakrabarti, K., Sarkar, B., Ashok, V. D., Chaudhuri, S. S. and De, S. (2015). Enhanced magnetic and dielectric behavior in Co doped BiFeO₃ nanoparticles. **Journal of Magnetism and Magnetic Materials** 381: 271-277.
- Chapman, D. L. (1913). LI. A contribution to the theory of electrocapillarity. **Philosophical Magazine** 25: 475-481.
- Chinnasamy, C., Narayanasamy, A., Ponpandian, N., Chattopadhyay, K., Shinoda, K., Jeyadevan, B., Tohji, K., Nakatsuka, K., Furubayashi, T. and Nakatani, I. (2001). Mixed spinel structure in nanocrystalline NiFe₂O₄. **Physical Review B** 63: 184108-184108-6.
- Conway, B. (1999). **Electrochemical supercapacitors: scientific fundamentals and technological applications**. New York: Springer.
- Conway, B., Birss, V. and Wojtowicz, J. (1997). The role and utilization of pseudocapacitance for energy storage by supercapacitors. **Journal of Power Sources** 66: 1-14.
- Cullity, B. D. and Graham, C. D. (2011). **Introduction to magnetic materials**. New York: John Wiley & Sons.
- Das, R. and Mandal, K. (2012). Magnetic, ferroelectric and magnetoelectric properties of Ba-doped BiFeO₃. **Journal of Magnetism and Magnetic Materials** 324: 1913-1919.
- Dong, S., Cheng, J., Li, J. and Viehland, D. (2003). Enhanced magnetoelectric effects in laminate composites of Terfenol-D/Pb(Zr,Ti)O₃ under resonant drive. **Applied Physics Letters** 83: 4812-4814.
- Donohue, M. and Aranovich, G. (1998). Classification of Gibbs adsorption isotherms. **Advances in Colloid and Interface Science** 76: 137-152.

- Du, B., Jiang, Q., Zhao, X., Huang, B. and Zhao, Y. (2009). Preparation of PPy/CNT composite applications for supercapacitor electrode material. **Materials Science Forum** 610: 502-505.
- Dubal, D. P., Gund, G. S., Holze, R. and Lokhande, C. D. (2013). Mild chemical strategy to grow micro-roses and micro-woolen like arranged CuO nanosheets for high performance supercapacitors. **Journal of Power Sources** 242: 687-698.
- Foner, S. (1959). Versatile and sensitive vibrating- sample magnetometer. **Review of Scientific Instruments** 30: 548-557.
- Frackowiak, E. (2007). Carbon materials for supercapacitor application. **Physical Chemistry Chemical Physics** 9: 1774-1785.
- Frackowiak, E. and Beguin, F. (2001). Carbon materials for the electrochemical storage of energy in capacitors. **Carbon** 39: 937-950.
- Fusalba, F., Mehdi, N. E., Breau, L. and Belanger, D. (1999). Physicochemical and electrochemical characterization of polycyclopenta [2, 1-b; 3, 4-b'] dithiophen-4-one as an active electrode for electrochemical supercapacitors. **Chemistry of Materials** 11: 2743-2753.
- Gaber, A., Rahim, A. M., Latief, A. A. and Salam, A. M. N. (2014). Influence of calcination temperature on the structure and porosity of nanocrystalline SnO₂ synthesized by a conventional precipitation method. **International Journal of Electrochemical Science** 9: 81-95.
- Gao, F., Yuan, Y., Wang, K., Chen, X., Chen, F., Liu, J. and Ren, Z. (2006). Preparation and photoabsorption characterization of BiFeO₃ nanowires. **Applied Physics Letters** 89: 102506-102900.

- Gao, Y., Chen, S., Cao, D., Wang, G. and Yin, J. (2010). Electrochemical capacitance of Co_3O_4 nanowire arrays supported on nickel foam. **Journal of Power Sources** 195: 1757-1760.
- George, M., John, A. M., Nair, S. S., Joy, P. and Anantharaman, M. (2006). Finite size effects on the structural and magnetic properties of sol-gel synthesized NiFe_2O_4 powders. **Journal of Magnetism and Magnetic Materials** 302: 190-195.
- González, A., Goikolea, E., Barrena, J. A. and Mysyk, R. (2016). Review on supercapacitors: technologies and materials. **Renewable and Sustainable Energy Reviews** 58: 1189-1206.
- Goodenough, J. B., Abruna, H. and Buchanan, M. (2007). Basic research needs for electrical energy storage. **Report of the Basic Energy Sciences Workshop for Electrical Energy Storage** 186: 1-77.
- Gopinath, S., Sivakumar, K., Karthikeyan, B., Ragupathi C. and Sundaram, R. (2016). Structural, morphological, optical and magnetic properties of Co_3O_4 nanoparticles prepared by conventional method. **Physica E: Low Dimensional Systems and Nanostructures** 81: 66-70.
- Gouy, G. (1910). Constitution of the electric charge at the surface of an electrolyte. **Journal of Physics** 9: 457-467.
- Griffith, J. S. (1961). **The theory of transition-metal ions**. Cambridge: Cambridge University Press.
- Guan, D., Gao, Z., Yang, W., Wang, J., Yuan, Y., Wang, B., Zhang, M. and Liu, L. (2013). Hydrothermal synthesis of carbon nanotube/cubic Fe_3O_4 nanocomposite for enhanced performance supercapacitor electrode material. **Materials Science and Engineering: B** 178: 736-713.

- Gujar, T., Shinde, V., Lokhande, C. and Han S. H. (2006). Electrosynthesis of Bi_2O_3 thin films and their use in electrochemical supercapacitors. **Journal of power sources** 161: 1479-1485.
- Halper, M. S. and Ellenbogen, J. C. (2006). **Supercapacitors: A brief overview**. Virginia: MITRE Nanosystems Group.
- Hang, B. T., Watanabe, T., Eashira, M., Okada, S., Yamaki, J. I., Hata, S., Yoon, S. H. and Mochida, I. (2005). The electrochemical properties of Fe_2O_3 -loaded carbon electrodes for iron-air battery anodes. **Journal of Power Sources** 150: 261-271.
- Heeg, T., Schubert, J., Buchal, C., Cicerrella, E., Freeouf, J., Tian, W., Jia, Y. and Schlom, D. (2006). Growth and properties of epitaxial rare-earth scandate thin films. **Applied Physics A** 83: 103-106.
- Helmholtz, H. (1853). Some laws of the distribution of electrical currents in material conductors with application to experiments in animal electricity. **Poggendorff's Annals** 89: 211-233.
- Hill, N. A. (2000). Why are there so few magnetic ferroelectrics?. **The Journal of Physical Chemistry B** 104: 6694-6709.
- Hu, C. C. and Chen, W. C. (2004). Effects of substrates on the capacitive performance of $\text{RuO}_x \cdot n\text{H}_2\text{O}$ and activated carbon- RuO_x electrodes for supercapacitors. **Electrochimica Acta** 49: 3469-3477.
- Huang, F., Wang, Z., Lu, X., Zhang, J., Min, K., Lin, W., Ti, R., Xu, T., He, J. and Yue, C. (2013). Peculiar magnetism of BiFeO_3 nanoparticles with size approaching the period of the spiral spin structure. **Scientific Reports** 3: 2907-2907-7.

- Ianculescu, A., Gheorghiu, F. P., Postolache, P., Oprea, O. and Mitoseriu, L. (2010). The role of doping on the structural and functional properties of $\text{BiFe}_{1-x}\text{Mn}_x\text{O}_3$ magnetoelectric ceramics. **Journal of Alloys and Compounds** 504: 420-426.
- Jadhav, V. V., Zate, M. K., Liu, S., Naushad, M., Mane, R. S., Hui, K. and Han, S. H. (2016). Mixed-phase bismuth ferrite nanoflake electrodes for supercapacitor application. **Applied Nanoscience** 6: 511-519.
- Jia, D. C., Xu, J. H., Ke, H., Wang, W. and Zhou, Y. (2009). Structure and multiferroic properties of BiFeO_3 powders. **Journal of the European Ceramic Society** 29: 3099-3103.
- Joy, P. and Date, S. (2000). Effect of sample shape on the zero-field-cooled magnetization behavior: comparative studies on NiFe_2O_4 , CoFe_2O_4 and $\text{SrFe}_{12}\text{O}_{19}$. **Journal of Magnetism and Magnetic Materials** 222: 33-38.
- Khajonrit, J., Phumying, S. and Maensiri, S. (2016). Structure and magnetic /electrochemical properties of Cu-doped BiFeO_3 nanoparticles prepared by a simple solution method. **Japanese Journal of Applied Physics** 55: 06GJ14-06GJ14-8.
- Khan, U., Adeela, N., Javed, K., Riaz, S., Ali, H., Iqbal, M., Han, X. and Naseem, S. (2015). Influence of cobalt doping on structural and magnetic properties of BiFeO_3 nanoparticles. **Journal of Nanoparticle Research** 17: 1-9.
- Kim, I. H. and Kim, K. B. (2006). Electrochemical characterization of hydrous ruthenium oxide thin-film electrodes for electrochemical capacitor applications. **Journal of the Electrochemical Society** 153: A383-A389.

- Kim, Y. I., Kim, D. and Lee, C. S. (2003). Synthesis and characterization of CoFe_2O_4 magnetic nanoparticles prepared by temperature-controlled coprecipitation method. **Physica B: Condensed Matter** 337: 42-51.
- Kirupakar, B. and Vishwanath, B. (2016). Vibrating sample magnetometer and its application in characterisation of magnetic property of the anti cancer drug magnetic microspheres. **International Journal of Pharmaceutics and Drug Analysis** 4: 227-233.
- Kittel, C. (1986). **Introduction to solid state physics**. New York: John Wiley & Sons.
- Kötz, R. and Carlen, M. (2000). Principles and applications of electrochemical capacitors. **Electrochimica Acta** 45: 2483-2498.
- Kumar, A. and Yadav, K. (2011). A systematic study on magnetic, dielectric and magnetocapacitance properties of Ni doped bismuth ferrite. **Journal of Physics and Chemistry of Solids** 72: 1189-1194.
- Kumar, M. and Yadav, K. (2006). Study of room temperature magnetoelectric coupling in Ti substituted bismuth ferrite system. **Journal of Applied Physics** 100: 74111-74111-4.
- Lahmar, A., Habouti, S., Dietze, M., Solterbeck, C. and Souni E. M. (2009). Effects of rare earth manganites on structural, ferroelectric, and magnetic properties of BiFeO_3 thin films. **Applied Physics Letters** 94: 12903-12903-3.
- Lebeugle, D., Colson, D., Forget, A., Viret, M., Bataille, A. and Gukasov, A. (2008). Electric-field-induced spin flop in BiFeO_3 single crystals at room temperature. **Physical Review Letters** 100: 227602-227602-4.
- Lebeugle, D., Colson, D., Forget, A., Viret, M., Bonville, P., Marucco, J. F. and Fusil, S. (2007). Room-temperature coexistence of large electric polarization and

- magnetic order in BiFeO₃ single crystals. **Physical Review B** 76: 024116-024116-8.
- Lee, H. Y. and Goodenough, J. (1999). Ideal supercapacitor behavior of amorphous V₂O₅·nH₂O in potassium chloride (KCl) aqueous solution. **Journal of Solid State Chemistry** 148: 81-84.
- Lee, J. W., Hall, A. S., Kim, J. D. and Mallouk, T. E. (2012). A facile and template-free hydrothermal synthesis of Mn₃O₄ nanorods on graphene sheets for supercapacitor electrodes with long cycle stability. **Chemistry of Materials** 24: 1158-1164.
- Lee, P., Citrin, P., Eisenberger, P. T. and Kincaid, B. (1981). Extended x-ray absorption fine structure-its strengths and limitations as a structural tool. **Reviews of Modern Physics** 53: 769-804.
- Leng, Y. (2009). **Materials characterization: introduction to microscopic and spectroscopic methods**. New York: John Wiley & Sons.
- Li, Y., Fan, Y., Zhang, H., Teng, X., Dong, X., Liu, H., Ge, X., Li, Q., Chen, W. and Ge, Z. (2014). Structural, thermal, and magnetic properties of Cu-doped BiFeO₃. **Journal of Superconductivity and Novel Magnetism** 27: 1239-1243.
- Lin, Y., Kang, P., Yang, H. and Liu, M. (2015). Preparation and magnetic properties of Bi₂Fe₄O₉/CoFe₂O₄ composite powders. **Journal of Materials Science: Materials in Electronics** 26: 1102-1106.
- Lokhande, C., Dubal, D. and Joo, O. S. (2011). Metal oxide thin film based supercapacitors. **Current Applied Physics** 11: 255-270.

- Lokhande, C., Gujar, T., Shinde, V., Mane, R. S. and Han, S. H. (2007). Electrochemical supercapacitor application of pervoskite thin films. **Electrochemistry Communications** 9: 1805-1809.
- Long, J. W., Stroud, R. M. and Rolison, D. R. (2001). Controlling the pore-solid architecture of mesoporous, high surface area manganese oxides with the birnessite structure. **Journal of Non-Crystalline Solids** 285: 288-294.
- Lotey, G. S. and Verma, N. (2012). Structural, magnetic, and electrical properties of Gd-doped BiFeO₃ nanoparticles with reduced particle size. **Journal of Nanoparticle Research** 14: 742-742-2.
- Lou, X., Yang, C., Tang, T., Lin, Y., Zhang M. and Scott, J. (2007). Formation of magnetite in bismuth ferrite under voltage stressing. **Applied Physics Letters** 90: 2908-2908-3.
- Lubk, A., Gemming, S. and Spaldin, N. (2009). First-principles study of ferroelectric domain walls in multiferroic bismuth ferrite. **Physical Review B** 80: 104110-1104110-8.
- Mazumder, R., Devi, P. S., Bhattacharya, D., Choudhury, P., Sen, A. and Raja, M. (2007). Ferromagnetism in nanoscale BiFeO₃. **Applied Physics Letters** 91: 062510-062510-3.
- Mazumder, R., Ghosh, S., Mondal, P., Bhattacharya, D., Dasgupta, S., Das, N., Sen, A., Tyagi, A., Sivakumar, M. and Takami, T. (2006). Particle size dependence of magnetization and phase transition near TN in multiferroic BiFeO₃. **Journal of Applied Physics** 100: 033908-033908-9.
- McElfresh, M. (1994). **Fundamentals of magnetism and magnetic measurements**. San Diego: Quantum Design.

- Montes, G., Perez, P. O., Renteria, B. and Galvez, M. (2010). Synthesis and magnetic properties of pure and cobalt-doped nanocrystalline bismuth ferrite. **Materials Research Society Symposium Proceedings** 1256: 59-64.
- Moreau, J. M., Michel, C., Gerson, R. and James, W. J. (1971). Ferroelectric BiFeO₃ X-ray and neutron diffraction study. **Journal of Physics and Chemistry of Solids** 32: 1315-1320.
- Morr, A. and Haneda, K. (1981). Magnetic structure of small NiFe₂O₄ particles. **Journal of Applied Physics** 52: 2496-2498.
- Naik, V. and Mahendiran, R. (2009). Magnetic and magnetoelectric studies in pure and cation doped. **Solid State Communications** 149: 754-758.
- Nakamura, S., Soeya, S., Ikeda N. and Tanaka, M. (1993). Spin- glass behavior in amorphous BiFeO₃. **Journal of Applied Physics** 74: 5652-5657.
- Nam, K. W., Yoon, W. S. and Kim, K. B. (2002). X-ray absorption spectroscopy studies of nickel oxide thin film electrodes for supercapacitors. **Electrochimica Acta** 47: 3201-3209.
- Newville, M. (2001). EXAFS analysis using FEFF and FEFFIT. **Journal of Synchrotron Radiation** 8: 96-100.
- Ni, C. (2013). **Scanning Electron Microscopy (SEM)**. New York: Springer.
- Nithya, V., R. Selvan, K., Kalpana, D., Vasylechko, L. and Sanjeeviraja, C. (2013). Synthesis of Bi₂WO₆ nanoparticles and its electrochemical properties in different electrolytes for pseudocapacitor electrodes. **Electrochimica Acta** 109: 720-731.

- Palai, R., Katiyar, R., Schmid, H., Tissot, P., Clark, S., Robertson, J., Redfern, S., Catalan, G. and Scott, J. (2008). β phase and γ - β metal-insulator transition in multiferroic BiFeO₃. **Physical Review B** 77: 014110-014110-11.
- Pang, S. C., Anderson, M. A. and Chapman, T. W. (2000). Novel electrode materials for thin- film ultracapacitors: comparison of electrochemical properties of sol-gel- derived and electrodeposited manganese dioxide. **Journal of the Electrochemical Society** 147: 444-450.
- Park, T. J., Papaefthymiou, G. C., Viescas, A. J., Moodenbaugh, A. R. and Wong, S. S. (2007). Size-dependent magnetic properties of single-crystalline multiferroic BiFeO₃ nanoparticles. **Nano Letters** 7: 766-772.
- Patterson, A. (1939). The Scherrer formula for X-ray particle size determination. **Physical Review** 56: 978-982.
- Pradhan, A., Zhang, K., Hunter, D., Dadson, J., Loiutts, G., Bhattacharya, P., Katiyar, R., Zhang, J., Sellmyer, D. J. and Roy, U. (2005). Magnetic and electrical properties of single-phase multiferroic BiFeO₃. **Journal of Applied Physics** 97: 093903-093903-4.
- Prasad, K. R., Koga, K. and Miura, N. (2004). Electrochemical deposition of nanostructured indium oxide: high-performance electrode material for redox supercapacitors. **Chemistry of Materials** 16: 1845-1847.
- Prasad, K. R. and Miura, N. (2004). Electrochemical synthesis and characterization of nanostructured tin oxide for electrochemical redox supercapacitors. **Electrochemistry Communications** 6: 849-852.

- Prashanthi, K., Chalke, B., Bapat, R., Purandare, S. and Palkar, V. (2010). Multiferroic $\text{Bi}_{0.7}\text{Dy}_{0.3}\text{FeO}_3$ thin films directly integrated on Si for integrated circuit compatible devices. **Thin Solid Films** 518: 5866-5870.
- Qu, Q., Zhang, P., Wang, B., Chen, Y., Tian, S., Wu, Y. and Holze, R. (2009). Electrochemical performance of MnO_2 nanorods in neutral aqueous electrolytes as a cathode for asymmetric supercapacitors. **The Journal of Physical Chemistry C** 113: 14020-14027.
- Rai, R., Mishra, S. K., Singh, N., Sharma, S. and Kholkin, A. L. (2011). Preparation, structures, and multiferroic properties of single-phase BiRFeO_3 , $\text{R} = \text{La}$ and Er ceramics. **Current Applied Physics** 11: 508-512.
- Rana, S., Dutta, N., Bandyopadhyay, S., Sen, P. and Himanshu, A. (2014). High capacitance in BiFeO_3 nanorod structure, **AIP Conference Proceedings**. 1591: 254-255.
- Ranjusha, R., Nair, A. S., Ramakrishna, S., Anjali, P., Sujith, K., Subramanian, K., Sivakumar, N., Kim, T., Nair, S. V. and Balakrishnan, A. (2012). Ultra fine MnO_2 nanowire based high performance thin film rechargeable electrodes: Effect of surface morphology, electrolytes and concentrations. **Journal of Materials Chemistry** 22: 20465-20471.
- Rao, P. K., Krishnan, S., Pattabi, M. and Sanjeev, G. (2015). Electron Irradiation Effects on Structural Properties of Multiferroic YMnO_3 . **International Journal of ChemTech Research** 7: 1377-1380
- Rao, P. K., Krishnan, S., Pattabi, M. and Sanjeev, G. (2016). Magnetic and photoluminescence studies of electron irradiated $\text{Bi}_2\text{Fe}_4\text{O}_9$ nanoparticles. **Journal of Magnetism and Magnetic Materials** 401: 77-80.

- Ravel, B. and Newville M. (2005). ATHENA, ARTEMIS, HEPHAESTUS: data analysis for X-ray absorption spectroscopy using IFEFFIT. **Journal of Synchrotron Radiation** 12: 537-541.
- Reddy, R. N. and Reddy, R. G. (2003). Sol-gel MnO₂ as an electrode material for electrochemical capacitors. **Journal of Power Sources** 124: 330-337.
- Richardson, J., Yiagas, D., Turk, B., Forster, K. and Twigg, M. (1991). Origin of superparamagnetism in nickel oxide. **Journal of Applied Physics** 70: 6977-6982.
- Sankar, K. V., Selvan, R. K. and Meyrick, D. (2015). Electrochemical performances of CoFe₂O₄ nanoparticles and a rGO based asymmetric supercapacitor. **RSC Advances** 5: 99959-99967.
- Schwab, R., Spörl, R., Severloh, P., Heidinger, R. and Halbritter, J. (1997). Temperature and orientation dependent dielectric measurements of LaAlO₃-substrates. **Journal of Physics: Conference Series**. 158: 61-64.
- Selbach, S. M., Einarsrud, M. A. and Grande, T. (2008). On the thermodynamic stability of BiFeO₃. **Chemistry of Materials** 21: 169-173.
- Selvan, R. K., Perelshtein, I., Perkas, N. and Gedanken, A. (2008). Synthesis of hexagonal-shaped SnO₂ nanocrystals and SnO₂@C nanocomposites for electrochemical redox supercapacitors. **The Journal of Physical Chemistry C** 112: 1825-1830.
- Senthilkumar, B., Sankar, K. V., Selvan, R. K., Danielle, M. and Manickam, M. (2013). Nano α -NiMoO₄ as a new electrode for electrochemical supercapacitors. **Rsc Advances** 3: 352-357.

- Shami, M. Y., Awan, M. and Rehman, A. U. M. (2011). Phase pure synthesis of BiFeO₃ nanopowders using diverse precursor via co-precipitation method. **Journal of Alloys and Compounds** 509: 10139-10144.
- Simoës, A., Gonzalez, A., Cavalcante, L., Riccardi, C., Longo, E. and Varela, J. A. (2007). Ferroelectric characteristics of BiFeO₃ thin films prepared via a simple chemical solution deposition. **Journal of Applied Physics** 101: 074108-1-074108-6.
- Singh, M. K., Katiyar, R. S., Prellier, W. and Scott, J. (2008). The Almeida-Thouless line in BiFeO₃: is bismuth ferrite a mean field spin glass?. **Journal of Physics: Condensed Matter** 21: 042202-042202-5.
- Singh, M. K., Prellier, W., Singh, M., Katiyar, R. S. and Scott, J. (2008). Spin-glass transition in single-crystal Bi FeO₃. **Physical Review B** 77: 144403-1-144403-5.
- Singh, S., Ishiwara, H. and Maruyama, K. (2006). Enhanced polarization and reduced leakage current in BiFeO₃ thin films fabricated by chemical solution deposition. **Journal of applied physics** 100: 064102.
- Siwach, P., Singh, H., Singh, J. and Srivastava, O. (2007). Anomalous ferromagnetism in spray pyrolysis deposited multiferroic BiFeO₃ films. **Applied Physics Letters** 91: 122503.
- Sosnowska, I., Neumaier, T. P. and Steichele, E. (1982). Spiral magnetic ordering in bismuth ferrite. **Journal of Physics C: Solid State Physics** 15: 4835.
- Stern, O. (1924). The theory of the electrolytic double-layer. **Z. Elektrochem** 30: 1014-1020.

- Taberna, P. L., Portet, C. and Simon, P. (2006). Electrode surface treatment and electrochemical impedance spectroscopy study on carbon/carbon supercapacitors. **Applied Physics A** 82: 639-646.
- Teague, J. R., Gerson, R. and James, W. J. (1970). Dielectric hysteresis in single crystal BiFeO₃. **Solid State Communications** 8: 1073-1074.
- Vanga, P. R., Mangalaraja, R. and Ashok, M. (2015). Effect of (Nd, Ni) co-doped on the multiferroic and photocatalytic properties of BiFeO₃. **Materials Research Bulletin** 72: 299-305.
- Vijayanand, S., Mahajan, M., Potdar, H. and Joy, P. (2009). Magnetic characteristics of nanocrystalline multiferroic BiFeO₃ at low temperatures. **Physical Review B** 80: 064423-064423-6.
- Vivier, V., Regis, A., Sagon, G., Nedelec, J. Y., Yu, L. and Vivier C. C. (2001). Cyclic voltammetry study of bismuth oxide Bi₂O₃ powder by means of a cavity microelectrode coupled with Raman microspectrometry. **Electrochimica Acta** 46: 907-914.
- Wang, G., Cao, D., Yin, C., Gao, Y., Yin, J. and Cheng, L. (2009). Nickel foam supported-Co₃O₄ nanowire arrays for H₂O₂ electroreduction. **Chemistry of Materials** 21: 5112-5118.
- Wang, H., Xu, Z., Yi, H., Wei, H., Guo, Z. and Wang, X. (2014). One-step preparation of single-crystalline Fe₂O₃ particles/graphene composite hydrogels as high performance anode materials for supercapacitors. **Nano Energy** 7: 86-96.
- Wang, J., Gao, Z., Li, Z., Wang, B., Yan, Y., Liu, Q., Mann, T., Zhang, M. and Jiang, Z. (2011). Green synthesis of graphene nanosheets/ZnO composites and electrochemical properties. **Journal of Solid State Chemistry** 184: 1421-1427.

- Wang, L., Xu, J. B., Gao, B., Chang, A. M., Chen, J., Bian L. and Song, C. Y. (2013). Synthesis of BiFeO₃ nanoparticles by a low-heating temperature solid-state precursor method. **Materials Research Bulletin** 48: 383-388.
- Wang, S. Y., Ho, K. C., Kuo, S. L. and Wu, N. L. (2006). Investigation on capacitance mechanisms of Fe₃O₄ electrochemical capacitors. **Journal of the Electrochemical Society** 153: A75-A80.
- Wang, Y. H. and Qi, X. (2012). The effects of nickel substitution on bismuth ferrite. **Procedia Engineering** 36: 455-461.
- Wang, Y., Xu, G., Yang, L., Ren, Z., Wei, X., Weng, W., Du, P., Shen, G. and Han, G. (2009). Low-temperature synthesis of Bi₂Fe₄O₉ nanoparticles via a hydrothermal method. **Ceramics International** 35: 51-53.
- Wei, T. Y., Chen, C. H., Chien, H. C., Lu, S. Y. and Hu, C. C. (2010). A cost-effective supercapacitor material of ultrahigh specific capacitances: spinel nickel cobaltite aerogels from an epoxide-driven sol-gel process. **Advanced Materials** 22: 347-351.
- Williams, D. B. and Carter, C. B. (1996). **Transmission electron microscopy**. New York: Springer.
- Xie, S., Li, J., Proksch, R., Liu, Y., Zhou, Y., Liu, Y., Ou, Y., Lan, L. and Qiao, Y. (2008). Nanocrystalline multiferroic BiFeO₃ ultrafine fibers by sol-gel based electrospinning. **Applied Physics Letters** 93: 222904-222904-3.
- Xu, H., Gao, L., Zhang, Q., Li, J., Diwu, J., Chou, X., Tang, J. and Xue, C. (2014). Preparation method of Co₃O₄ nanoparticles using degreasing cotton and their electrochemical performances in supercapacitors. **Journal of Nanomaterials** 2014: 1-9.

- Yan, J., Liu, J., Fan, Z., Wei, T. and Zhang, L. (2012). High-performance supercapacitor electrodes based on highly corrugated graphene sheets. **Carbon** 50: 2179-2188.
- Yang, C. H., Kan, D., Takeuchi, I., Nagarajan, V. and Seidel, J. (2012). Doping BiFeO₃: approaches and enhanced functionality. **Physical Chemistry Chemical Physics** 14: 15953-15962.
- Yang, W., Gao, Z., Wang, J., Wang, B., Liu, Q., Li, Z., Mann, T., Yang, P., Zhang, M. and Liu, L. (2012). Synthesis of reduced graphene nanosheet/urchin-like manganese dioxide composite and high performance as supercapacitor electrode. **Electrochimica Acta** 69: 112-119.
- Yang, X. H., Wang, Y. G., Xiong, H. M. and Xia, Y. Y. (2007). Interfacial synthesis of porous MnO₂ and its application in electrochemical capacitor. **Electrochimica Acta** 53: 752-757.
- Yang, Z. T., Cheng B. W. and Zhao, Y. N. (2013). Synthesis of NiFe₂O₄ nanoparticles and its supercapacitive properties. **Applied Mechanics and Materials** 275: 1733-1736.
- Yano, J. and Yachandra, V. K. (2009). X-ray absorption spectroscopy. **Photosynthesis Research** 102: 241-254.
- Yin, L., Sun, Y., Zhang, F., Wu, W., Luo, X., Zhu, X., Yang, Z., Dai, J., Song, W. and Zhang, R. (2009). Magnetic and electrical properties of Bi_{0.8}Ca_{0.2}Fe_{1-x}Mn_xO₃ (0 ≤ x ≤ 0.5). **Journal of Alloys and Compounds** 488: 254-259.
- Yu, A., Chabot, V. and Zhang, J. (2013). **Electrochemical supercapacitors for energy storage and delivery: fundamentals and applications**. New York: CRC Press.

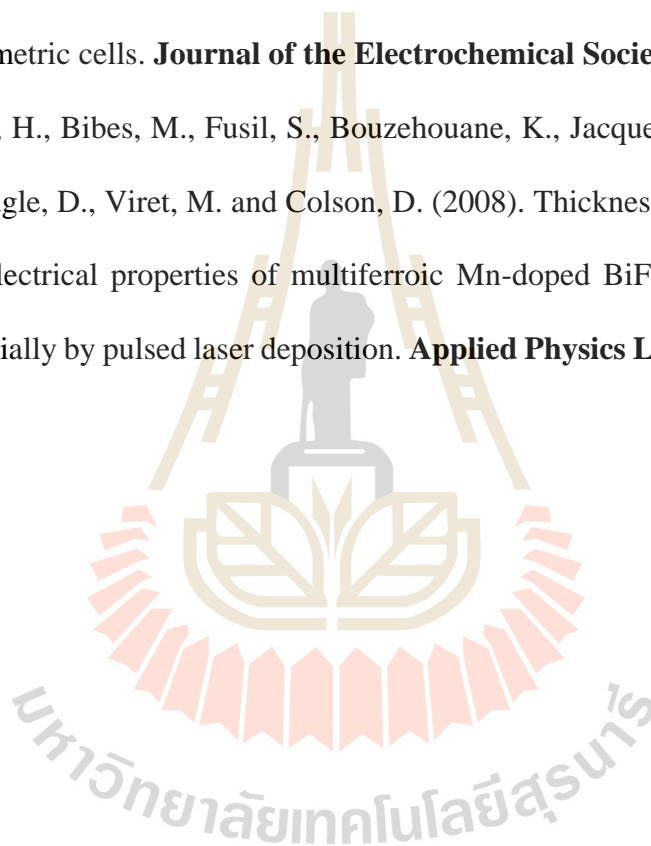
- Yuan, C., Zhang, X. Su, L., Gao, B. and Shen, L. (2009). Facile synthesis and self-assembly of hierarchical porous NiO nano/micro spherical superstructures for high performance supercapacitors. **Journal of Materials Chemistry** 19: 5772-5777.
- Yuan, D., Chen, J. Zeng, J. and Tan, S. (2008). Preparation of monodisperse carbon nanospheres for electrochemical capacitors. **Electrochemistry Communications** 10: 1067-1070.
- Zhang, J., Kong, L. B. Cai, J. J., Li, H., Luo, Y. C. and Kang, L. (2010). Hierarchically porous nickel hydroxide/mesoporous carbon composite materials for electrochemical capacitors. **Microporous and Mesoporous Materials** 132: 154-162.
- Zhang, J., Zhang, L., Liu, H., Sun, A. and Liu, R. S. (2012). **Electrochemical technologies for energy storage and conversion**. Weinheim: John Wiley & Sons.
- Zhang, S. T., Zhang, Y., Lu, M. H., Du, C. L., Chen, Y. F., Liu, Z. G., Zhu, Y. Y., Ming N. B. and Pan, X. (2006). Substitution-induced phase transition and enhanced multiferroic properties of $\text{Bi}_{1-x}\text{La}_x\text{FeO}_3$ ceramics. **Applied Physics Letters** 88: 162901-162901-3.
- Zhang, S., Lu, M., Wu, D., Chen, Y. and Ming, N. (2005). Larger polarization and weak ferromagnetism in quenched BiFeO_3 ceramics with a distorted rhombohedral crystal structure. **Applied Physics Letters** 87: 2907-2907-3.
- Zhao, D. D., Bao, S. J., Zhou, W. J. and Li, H. L. (2007). Preparation of hexagonal nanoporous nickel hydroxide film and its application for electrochemical capacitor. **Electrochemistry Communications** 9: 869-874.

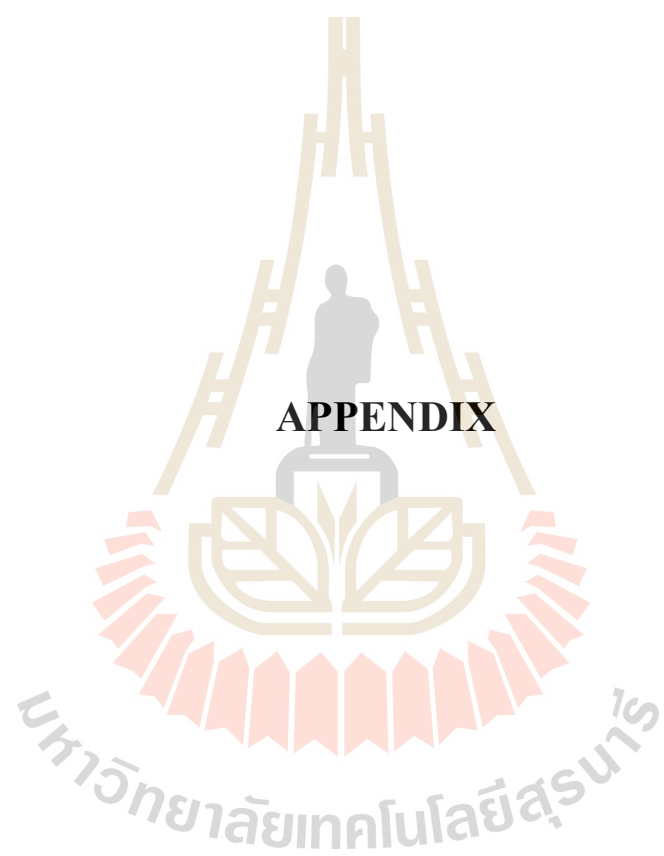
Zhao, J., Zhang, X., Liu, S., Zhang, W. and Liu, Z. (2013). Effect of Ni substitution on the crystal structure and magnetic properties of BiFeO₃. **Journal of Alloys and Compounds** 557: 120-123.

Zheng, J. and Jow, T. (1995). A new charge storage mechanism for electrochemical capacitors. **Journal of the Electrochemical Society** 142: L6-L8.

Zheng, J. P. (2003). The limitations of energy density of battery/double-layer capacitor asymmetric cells. **Journal of the Electrochemical Society** 150: A484-A492.

Zhu, X., Bea, H., Bibes, M., Fusil, S., Bouzehouane, K., Jacquet, E., Barthelemy, A., Lebeugle, D., Viret, M. and Colson, D. (2008). Thickness-dependent structural and electrical properties of multiferroic Mn-doped BiFeO₃ thin films grown epitaxially by pulsed laser deposition. **Applied Physics Letters** 93: 2902-2902-3.





APPENDIX

APPENDIX

PUBLICATIONS AND PRESENTATIONS

A.1 List of publications

Khajonrit, J., Phumying, S., and Maensiri, S. (2016). Structure and magnetic/ electrochemical properties of Cu-doped BiFeO₃ nanoparticles prepared by a simple solution method. **Japanese Journal of Applied Physics** 55: 06GJ14-06GJ14-8.

Khajonrit, J., Prasoetsopha, N., Sinprachim, T., Kidkhunthod, P., Pinitsoontorn, S., and Maensiri, S. (2017). Structure, characterization, and magnetic/ electrochemical properties of Ni-doped BiFeO₃ nanoparticles. **Advances in Natural Sciences: Nanoscience and Nanotechnology** 8: 015010-015010-12.

A.2 List of oral presentations

Khajonrit, J., and Maensiri, S. (November 2014). Synthesis and electrochemical properties of Co-doped BiFeO₃ nanopowders for high performance supercapacitors. **The 27th International Microprocesses and Nanotechnology Conference**. Hilton Fukuoka Sea Hawk, Fukuoka, Japan.

Khajonrit, J., and Maensiri, S. (November 2015). Effects of Cu doping on crystal structure and magnetic properties of BiFeO₃ nanoparticles. **The 41st Congress on Science and Technology of Thailand (STT41)**. Suranaree University of Technology, Nakhon Ratchasima, Thailand.

Khajonrit, J., Prasoetsopha, N., Sinprachim, T., Kidkhunthod, P., Pinitsoontorn, S., and Maensiri, S. (November 2016). Structure, characterization, and magnetic/electrochemical properties of Ni-doped BiFeO₃ nanoparticles. **8th International Workshop on Advanced Materials Science and Nanotechnology**. Halong Grand Halong Hotel, Halong, Vietnam.

Khajonrit, J., Wongpratrat, U., Kidkhunthod, P., Pinitsoontorn, S., and Maensiri, S. (November 2016). Effects of Co doping on magnetic and electrochemical properties of BiFeO₃ nanoparticles. **The 5th Thailand International Nanotechnology Conference**. Greenery Resort Khao Yai Hotel, Nakhon Ratchasima, Thailand.

A.3 List of poster presentations

Khajonrit, J., Phumying, S., and Maensiri, S. (November 2015). Structure and magnetic/electrochemical properties of Cu-doped BiFeO₃ nanoparticles prepared by a simple solution method. **The 28th International Microprocesses and Nanotechnology Conference**. Toyama International Conference Center, Toyama, Japan.

CURRICULUM VITAE

Name Mr. Jessada Khajonrit

Date of Birth July 5, 1985

Place of Birth 34 Moo 15 Tambol Samkha, Kuchinarai District, Kalasin Province, 46110, Thailand.

Education

2012-2016 **PhD candidate in Apply Physics**
School of Physics, Institute of Science Suranaree University of Technology, Nakhon Ratchasima, Thailand.
Structure, Magnetic and Electrochemical Properties of $\text{BiFe}_{1-x}\text{M}_x\text{O}_3$ (M = Co, Ni, Cu) Nanoparticles prepared by a Simple Solution Method.

2008-2011 **M.Sc. (Radiological Science)**
Department of Radiology, Faculty of Medicine Siriraj Hospital, Mahidol University, Bangkok, Thailand.
Determination of the Elemental Contents in Sediments on the Inner Gulf of Thailand by Instrumental Neutron Activation Analysis.

2004-2007 **B. Sc. (Physics)**
Department of Physics, Faculty of Science, Khon Kaen University, Khon Kaen, Thailand.